RADIATION HARDNESS IN FERROELECTRIC THIN FILMS FOR MEMS APPLICATIONS

A Dissertation
Presented to
The Academic Faculty

by

Steven J. Brewer

In Partial Fulfillment
of the Requirements for the Degree
Doctor of Philosophy in the
George W. Woodruff School of Mechanical Engineering

Georgia Institute of Technology
December 2017

RADIATION HARDNESS IN FERROELECTRIC THIN FILMS FOR MEMS APPLICATIONS

Approved by:

Dr. Nazanin Bassiri-Gharb, Advisor
G.W.Woodruff School of Mechanical Engineering
Georgia Institute of Technology

Dr. Josh Kacher
School of Materials Science and Engineering
Georgia Institute of Technology

Dr. Peter Hesketh
G.W.Woodruff School of Mechanical Engineering
Georgia Institute of Technology

Dr. Ronald Polcawich
US Army Research Laboratory

Dr. Chaitanya Deo
G.W.Woodruff School of Mechanical Engineering
Georgia Institute of Technology

Date Approved: August 18, 2017

ACKNOWLEDGEMENTS

An extremely special thank you to Dr. Bassiri-Gharb, for her constant support and continued guidance from the moment I first met with her several years ago. Nazanin's passion for and dedication to science, learning, and doing things the proper way are unrivaled; she has left an indelible mark on who I've become as an engineer and how I approach difficult problems, both in scientific pursuits and in my personal life. Few people have shaped my life in the way she has, and I'm indebted to her for her inspiring leadership and counsel.

I would also like to express my great appreciation to the members of my dissertation committee: Profs. Hesketh, Deo, Kacher; and Dr. Polcawich. Their guidance has extended beyond that of collaborations and research advice – they have acted as tangible examples of scientists and researchers whom I respect and admire. I thank them for selflessly volunteering their time and expertise.

I thank members of my family: my parents have always encouraged me to seek out the best opportunities available to me. My wife Katie has been a constant source of inspiration and impulse toward accomplishing something valuable and lasting, and never settling for less than the best I can achieve.

Finally, I thank all those who graciously aided me in accomplishing the work contained in this thesis, including design of experiments, sample preparation, data collection, image acquisition, intellectual discussions, manuscript writing/editing, and many other tasks. Truly, this thesis would not exist without their contributions: Carmen

Deng, Connor Callaway, Sam Williams, McKinley Paul, Kenzie Fisher, Lee Griffin, Yaser Bastani, Georgia Tech IEN Cleanroom Staff, Eric Woods, Yong Ding, David Tavakoli, Hanhan Zhou, Jonathon Guerrier, Manny Rivas, Ryan Rudy, Ron Polcawich, Jacob Jones, Evan Glaser, Cory Cress, Aaron Naden, Sabine Neumayer, Brian Rodriguez, Amit Kumar, Nazanin Bassiri-Gharb, and any others I may have forgotten to mention.

TABLE OF CONTENTS

LIST OF TABLES

LIST OF FIGURES

samples.[175] The "P_{Si}" show spectra associated with shallow phosphorous donors in the Si substrate. Data and figure courtesy of Evan R. Glaser, US Naval Research Laboratory.

LIST OF SYMBOLS AND ABBREVIATIONS

2-MOE	2-Methoxyethanol
A	Cross-sectional area of parallel plate capacitor, equal to top electrode area
AFM	Atomic force microscopy
Amp	Amplitude of the piezoresponse
ARL	US Army Research Laboratory
BE-PFM	Band-excitation piezoresponse force microscopy
BE-SSPFM	Band-excitation switching spectroscopy piezoresponse force microscopy
BOE	Buffered oxide etch
C	Capacitance
CMOS	Complementary metal-oxide-semiconductor
CSD	Chemical solution deposition
d	Thickness of dielectric media in parallel plate capacitor, *i.e.*, film thickness
D	Flexural rigidity
d'	Real component of the piezoelectric coefficient
d''	Imaginary component of the piezoelectric coefficient
d^*	Complex piezoelectric coefficient
d_{33}	Converse piezoelectric coefficient
$d_{33,f}$	Effective, converse piezoelectric coefficient
$d_{33,f,max}$	Maximum, effective, converse piezoelectric coefficient
$d_{33,f,remanent}$ ($d_{33,f,rem}$)	Remanent, effective, converse piezoelectric coefficient
$d_{33,f,saturation}$ ($d_{33,f,sat}$)	Saturation, effective, converse piezoelectric coefficient

DART	Dual amplitude resonance tracking
DBLI	Double beam laser interferometer
$d_{electrode}$	Electrode diameter
D_i	Electric displacement field
DI	Deionized (water)
d_{ij}	Longitudinal piezoelectric coefficients tensor (reduced engineering notation)
d_{ijk}	Longitudinal piezoelectric coefficients tensor
d_{init}	Reversible Rayleigh piezoelectric parameter
DRIE	Deep reactive ion etching
DSP	Double-side polished
d_{space}	Interatomic spacing of atoms in crystal lattice
E	Electric field
E_{AC}	AC electric field
EBSD	Electron backscatter diffraction
E_C	Coercive field
E_{DC}	DC electric field
EDX	Energy dispersive X-ray spectroscopy
e_{ij}	Transverse piezoelectric coefficients tensor (reduced engineering notation)
e_{kij}	Transverse piezoelectric coefficients tensor
$E_{internal}$	Horizontal shift in polarization-field and piezoelectric response hysteresis loops, equal to internal electrical bias
ESR	Electron spin resonance
E_{th}	Threshold electric field for nonlinear AC dielectric response
E_y	Young's modulus
FEA	Finite element analysis

FeRAM	Ferroelectric random access memory (RAM)
FE-SEM	Field-emission scanning electron microscopy
FIB	Focused ion beam
FWHM	Full width at half maximum
HAADF	High-angle annular dark field
I	Intensity (of collected diffracted X-rays)
IMO	Inverted mixing order
IPA	Isopropyl alcohol
j	$\sqrt{-1}$
k	Effective rate of defect saturation in arbitrarily-defined volume of functional material
LCR	Inductance, capacitance, resistance
LET	Linear energy transfer
M	Molarity
MEMS	Microelectromechanical systems
MIEC	Mixed ionic-electronic conductor
MLA	Multi-layer anneal
MLCC	Multilayer ceramic capacitor
MPB	Morphotropic phase boundary
n	Diffraction order, Bragg's law
N	Defect population in arbitrarily-defined volume of functional material
NRL	US Naval Research Laboratory
P	Polarization response
p	Applied differential pressure
PDF	Powder diffraction file

P-E	Polarization-electric field (hysteresis loop measurement)
PEB	Post-exposure bake
PFM	Piezoresponse force microscopy
p_i	Pyroelectric coefficient
P_{LF}	Lotgering factor peak summations
PR	Photoresist
pR/T	Periodic rhombohedral/tetragonal
P_{rem}	Remanent polarization
P_{sat}	Saturation polarization
PTFE	Polytetrafluoroethylene
PTO	$PbTiO_3$ (lead titanate)
PV	Photovoltaic
PVDF	Polyvinylidene fluoride
PZO	$PbZrO_3$ (lead zirconate)
PZT	$Pb(Zr,Ti)O_3$ (lead zirconate titanate)
R	Radius of curvature
r	Radius
R/T	Rhombohedral/tetragonal (crystallographic phases of PZT)
RF	Radio-frequency
RID	Radiation-induced degradation
RTP	Rapid thermal processor
SEM	Scanning electron microscopy
SHO	Simple harmonic oscillator
SNR	Signal-to-noise ratio
SOFC	Solid oxide fuel cell

SSP	Single-side polished
SS-PFM	Switching spectroscopy piezoresponse force microscopy
STEM	Scanning transmission electron microscopy
T	Temperature
$tan(\delta)$	Dielectric loss tangent; dissipation factor
T_C	Curie (transition) temperature
TEM	Transmission electron microscopy
TID	Total ionization dose
TKD	Transmission Kikuchi diffraction
ToF-SIMS	Time of flight secondary ion mass spectrometry
V	Electrical bias
V_d	Normalized volume affected by defect interactions in arbitrarily-defined volume of functional material, equal to $\frac{V_{def}}{V_T}$
V_{def}	Volume of functional material affected by defect interactions
V_{free}	Free material volume in arbitrarily-defined volume of functional material
V_N	Volume of material impacted by N^{th} defect
V_T	Total material volume in arbitrarily-defined volume of functional material
W	Maximum deflection
$W(N)$	Weighting function
x	Percent composition
x_{ij}	Mechanical strain matrix
XPS	X-ray photoelectron spectroscopy
XRD	X-ray diffraction
YBCO	Yttrium barium copper oxide
α	Irreversible Rayleigh parameter

$\alpha/\varepsilon_{init}$ Rayleigh irreversible:reversible ratio

α_d Irreversible Rayleigh piezoelectric parameter

γ Shear strain

$\Delta P/2$ Vertical shift in polarization-field hysteresis loops

δ_z Membrane deflection

ε Dielectric permittivity

ϵ Strain

ε' Real component of the dielectric permittivity

ε'' Imaginary component of the dielectric permittivity

ε^* Complex dielectric permittivity

ε_0 Permittivity of free space

ε_{DC} Dielectric permittivity from DC tunability hysteresis measurement

ε_{init} Reversible Rayleigh parameter

ε_r Relative dielectric permittivity

θ Diffraction angle

λ Wavelength

Λ Layer periodicity

ν Poisson's ratio

σ_i Mechanical stress matrix (reduced engineering notation)

σ_{ij} Mechanical stress matrix

τ Shear stress

ϕ Piezorespone phase angle

φ_N Normalized change in material volume impacted by N^{th} defect in arbitrarily-defined volume of functional material, equal to $\frac{V_N}{V_T}$

χ_{ij} Dielectric susceptibility

SUMMARY

In recent years, the continuous thrust toward developing microelectronic devices with greater autonomy, reduced footprint size, and large-scale interconnection has necessitated high-performance materials capable of fulfilling multiple functional roles. Ferroelectric materials, and specifically lead zirconate titanate (PZT), boast large dielectric, polarization, and electromechanical responses, making them ideal for microelectromechanical systems (MEMS) sensors and actuators, energy harvesters, multilayer ceramic capacitors (MLCC), ferroelectric logic elements and relays, *etc.* However, many of the most compelling applications for these types of devices – space travel, satellite communications, nuclear energy, and unmanned reconnaissance – concurrently require sustained operation in extremely demanding radiation-hostile environments. Radiation, both ionizing and displacive, has been shown to substantially degrade the functional responses of ferroelectric thin films, thus rendering the development of techniques for increased radiation tolerance of these materials critically important.

In this work, a multifaceted investigation towards increasing radiation hardness was undertaken, focusing on an array of critical interfaces and interactions in the ferroelectric material stack. Generally, the presence of (radiation-modified) oxygen vacancies at these interfaces resulted in substantial degradation of measured functional responses. Oyxgen vacancy motion, accumulation, and self-ordering have long been associated with ferroelectric fatigue, which results in the suppression of polarization and the pinning of domain wall motion in ferroelectric materials. Furthermore, the exposure of oxygen vacancies to ionizing radiation can trap charges, yielding a singly-charged species of

increased mobility. The work in this thesis aims to elucidate the fundamental interactions of radiation-induced defects with the ferroelectric material at critical interfaces, and attempts to discover methods for mitigating the damage caused by these interactions.

First, the hetero-interface between the ferroelectric thin film and top electrode contact was investigated with exposure to 2.5 Mrad gamma radiation, concluding that samples with IrO_2 top electrodes are more radiation hard than those with Pt top electrodes. IrO_2 top electrodes are conductive to ionic motion, especially that of mobile oxygen vacancies; on the other hand, accumulation of mobile oxygen vacancies at the interface between Pt top electrodes and PZT results in ferroelectric fatigue-like effects and greater degradation of functional properties. This critical interaction between radiation, oxygen vacancies, and the ferroelectric material lead to an array of investigations designed to elucidate its fundamental nature, as well as methods for its mitigation.

While single-dose radiation studies provide a glimpse of material and device behavior in radiation-hostile settings, total ionization dose (TID) studies more adequately simulate real-world conditions by probing material behavior across a valuable range of exposure doses. However, comparison of functional properties for multiple design parameters across this range of radiation doses can become cumbersome. A phenomenological model was thus developed to quantify functional behavior with TID, relying on the fact that radiation induces defects and defect-defect interactions that modify functional material response. Fitting of functional response trends as a function of TID with the phenomenological model yields two important parameters describing (i) the global susceptibility to radiation-induced degradation by induced defects and (ii) the rate of defect saturation in the material. Extraction and comparison of these parameters allows for

quantification of defect interactions as a function of microstructural and compositional variations in ferroelectric thin films. Furthermore, the model was applied to other functional materials, including those used for solid oxide fuel cells (SOFCs) and high-temperature superconductors; as well as methods for manipulating defect populations, *e.g.*, radiation, ion implantation, chemical doping, *etc.*

The derived model was employed to study multiple changes to the ferroelectric material stack, including variations in PZT thin film microstructure and crystallization interface frequency, whose effects are closely intertwined and dependent on thermal processing histories of the films. First, investigations comparing PZT thin films with columnar and equiaxed grains showed that, generally, samples with smaller, more uniformly-oriented columnar grains were more resistant to radiation-induced degradation of domain wall motion, and exhibited reduced rates of defect saturation compared to samples with equiaxed grains. Greater grain boundary in the columnar samples resulted in greater defect accumulation at grain boundaries, effectively acting as defect sinks for mobile oxygen vacancies and potentially reducing their deleterious effects with respect to equiaxed-grained samples. The radiation-induced defects were concluded to be of relatively low pinning energy, and overcome at elevated electric field.

Studies of crystallization interface periodicity from a functional response enhancement perspective showed that microstructural discontinuity, compositional fluctuations, crystallographic phase, and potential flexoelectric effects play critical roles in determining the extent of intrinsic and extrinsic contributions to the functional response. This investigation was expanded to include TID studies on the effects of layer crystallization interfaces in PZT thin films, showing that samples with greater frequency

of crystallization through the thickness of the film and more discrete interfaces were more susceptible to radiation-induced degradation, again due to mobile oxygen vacancy accumulation at more numerous internal interfaces. Interestingly, PZT thin films annealed after every one and every three layers both showed small enhancements of dielectric, polarization, and piezoelectric responses at low radiation doses, likely due to the effects of radiation-induced charging on internal bias in the films. Samples with greater frequency of crystallized layers demonstrated greater enhancements and reduced susceptibility to degradation of polarization and piezoelectric responses across the TID range, potentially resulting from increased radiation-induced symmetry of internal bias in samples with more even distribution of layer interfaces through the thickness of the film.

Given the prominent effects of oxygen vacancy concentration on radiation-induced degradation of functional properties in PZT thin films, methods for reducing as-fabricated, pre-irradiation oxygen vacancy populations were investigated. Mn acceptor-doping of the PZT solid solution can effectively consume oxygen vacancies, resulting in a “hard” PZT composition and dramatically increasing radiation tolerance relative to undoped PZT samples. Defect dipoles formed between substituted Mn ions and oxygen vacancies pin domain wall motion and reduce overall sample response prior to irradiation, but diminish the population of mobile oxygen vacancies (relative to undoped PZT), thus increasing radiation hardness of Mn-doped samples across all gamma doses studied.

Finally, components of the lower material stack were studied in order to evaluate their potential effects on ferroelectric functional properties and their tolerance to radiation. The elastic layer and substrate do not directly contact the ferroelectric layer in the material stack, yet modification thereof resulted in substantial impact to measured functional

response. Modification of the elastic layer thickness and material selection produced notable changes in radiation-induced degradation trends, suggesting that residual stress generated in the ferroelectric thin film can significantly affect defect motion and eventual radiation tolerance. Related preliminary work to selectively release the PZT thin film from the substrate via backside plasma etching of the Si substrate demonstrated substantial modification of stress in the ferroelectric material and accompanying changes to its functional response – enormous enhancements to electromechanical properties and minor local modifications to dielectric and ferroelectric response. These results, coupled with those from TID studies on elastic layer variations, suggest that components of the material stack have significant effects on residual stress and film clamping, and thus are likely to affect radiation and defect interactions with the ferroelectric material.

The studies presented in this thesis serve to expand the fundamental scientific understanding of the interaction of radiation with ferroelectric thin films. Such understanding is leveraged to develop direct engineering approaches to mitigate radiation-induced degradation in ferroelectric thin films. Modification of critical interfaces in the ferroelectric material stack can have dramatic effects on the interaction of radiation with the material, defect generation, defect-ferroelectric and defect-defect interactions, and the eventual effects on functional response. This knowledge of radiation-induced defect interactions is beneficial for further development of approaches to fabricating radiation-tolerant ferroelectric thin film material stacks for use in MEMS and microelectronics devices.

CHAPTER 1. INTRODUCTION

This chapter outlines the motivation for the research and the work undertaken, including the main objectives for this thesis. A basic overview of approaches to enhancing radiation hardness in thin film ferroelectric materials for use in MEMS applications is presented.

1.1 Introduction

Since the genesis of the transistor, the continuous development of semiconductor and functional materials has led to extraordinary advances of microelectronics devices. As these devices are driven further towards increased miniaturization and multifunctionality, ferroelectric thin films have assumed a critical role for sensing and actuation in a variety of applications. A diverse range of microelectromechanical system (MEMS) sensors and actuators, non-volatile logic and memory elements (*e.g.*, FeRAM), multilayer ceramic capacitors (MLCC), energy harvesting systems, and various devices for medical and security applications leverage the large dielectric, piezoelectric, and pyroelectric properties inherent to ferroelectric materials. These advantageous properties are in large part owed to hysteretically and nonlinearly mobile internal interfaces, such as domain walls and eventual phase boundaries, *i.e.*, extrinsic contributions, which are the focus of intense research aimed at property enhancement in ferroelectric thin films. The rapid progress of devices that leverage these functionalities has expanded to include devices capable of sustained operation in radiation-hostile environments, such as applications in satellite communications, surveillance, nuclear power, *etc.* However, the accumulation and interactions of defects, either inherent or stimulated by exposure to radiation and high energy beams, have been shown to degrade dielectric and electromechanical response in ferroelectrics by pinning domain wall motion, restricting domain nucleation, and suppressing polarization switching. Furthermore, in sub-micron-thickness films, both extrinsic and intrinsic size effects tend to strongly limit dielectric and electromechanical response, manifest through grain size variation, ferroelectric dead layers, space charge depletion layers, stoichiometric inconsistencies, and residual substrate clamping. Hence, it

is necessary to develop methods for processing ferroelectric thin films that increase radiation hardness and mitigate degradation of functional response during operation in radiation-hostile environments.

This work presents multiple major, multifaceted contributions to the science governing ferroelectric materials for use in multifunctional MEMS sensors and actuators, particularly for those operating in radiation-hostile environments. The methods and studies focus on various critical interfaces in the ferroelectric material stack and the interactions of defects and radiation with them. Initial work on top electrode material in gamma-irradiated PZT thin films highlighted the critical interaction of radiation with defects in the material. Generally, oxygen vacancies and electronic defects are created or activated by exposure to ionizing radiation, resulting in increased defect mobility, defect accumulation at internal interfaces, and substantial modification of the ferroelectric material's functional response. To more comprehensively study the interactions of radiation-induced defects, a phenomenological model was developed and used to quantify defect interactions in ferroelectric materials as a function of total ionization dose (TID) and related to their effects on functional response. The model, coupled with radiation studies, not only helps to quantify radiation-induced degradation of ferroelectric materials, but also allows for investigations of defect interactions in the material, elucidating the fundamental mechanisms responsible for enhanced or suppressed functional response in these materials, and therefore proving beneficial even during operation in low-radiation environments.

Subsequent investigations leveraged increased knowledge of the fundamental interactions of radiation with critical interfaces in the PZT thin film to substantially mitigate radiation-induced degradation of the functional response. Variation of the films'

internal interfaces is achieved through unique processing methods, including deliberate fabrication of anisotropic ferroelectric grain interfaces and modification of the layer crystallization interfaces to induce chemical heterogeneity. However, the strong dependence of the functional response on oxygen-related defect concentration in irradiated PZT thin films cannot be understated – their presence, mobility, and accumulation lead to substantial reduction of dielectric, ferroelectric, and piezoelectric properties. Accordingly, Mn acceptor doping was investigated as a means for reducing as-fabricated *mobile* oxygen vacancy concentration. Mn-doped films demonstrated a high level of radiation tolerance and functional response stability across a large TID range due to the reduction of these mobile oxygen vacancies in the ferroelectric thin film.

Studies to modify the lower material stack (*i.e.*, elastic layer and substrate) were undertaken by changing external electromechanical interfaces in the material stack. Measured changes to in-plane residual stress in the ferroelectric film via elastic layer modification were shown to noticeably affect radiation tolerance. Furthermore, backside etching of the substrate to release the PZT thin film from clamping resulted in vast changes to the stress state in the film. Hence, modification of the lower material stack yields clear changes to residual stress in the ferroelectric thin film, and is expected to affect defect motion and radiation tolerance in future studies.

This multifaceted approach to enhanced radiation hardness of ferroelectric materials stacks leverages an increased understanding of the behavior of irradiated ferroelectric materials at various critical interfaces to achieve higher performance materials and devices. However, while methods for increasing radiation hardness and functional responses in ferroelectric thin films are beneficial in and of themselves, this work primarily

aims to probe the underlying mechanisms that drive ferroelectric functional response. Thus, the overarching goal of this research is to understand the physical phenomena that influence functional responses in ferroelectric thin films, by studying the contributions of both internal and external interfaces, the interaction of radiation with said interfaces and the material stack, and the resulting defect interactions in the ferroelectric material. Increased radiation hardness is anticipated through engineering of electromechanical, electrical, microstructural, chemical, and crystallographic boundary conditions both internally within the film, and externally in the overall material stack.

1.2 Thesis Organization

Literature Review (CHAPTER 2)

Background information is provided regarding ferroelectricity, radiation, defects, and related topics. Approaches to measuring dielectric and electromechanical responses in ferroelectric materials are reviewed, including the Rayleigh method to quantify intrinsic/extrinsic response in ferroelectrics. The general effects of defect concentrations and defect interactions are reviewed, with a specific focus on the effects of radiation on the structural and functional properties of ferroelectric materials.

Approach and Experimental Methods (CHAPTER 3)

Experimental procedures for modifying critical interfaces and boundary conditions in the ferroelectric thin film material stack are discussed in detail in this chapter. These include the experimental methods for fabrication, characterization, and irradiation of the

PZT thin films used in this research. Chemical solution deposition (CSD) is discussed, as well as the suite of functional characterization measurements performed to interrogate dielectric, polarization, and electromechanical responses in the samples. Additional methods, such as piezoresponse force microscopy (PFM) are also presented.

Electromechanical Interface at the Ferroelectric-Electrode Boundary (CHAPTER 4)

This chapter reports the effects of material selection at the ferroelectric-electrode interface on the gamma radiation-induced degradation of PZT thin films. An understanding of defect interactions at the hetero-interface between the top electrode and ferroelectric film contributes to the engineering of highly radiation-tolerant material stacks. Radiation-induced modification of oxygen vacancies and their subsequent effects on functional response are identified as the primary cause of functional response degradation.

Phenomenological Model for Quantifying Defect Interactions in Irradiated Functional Materials (CHAPTER 5)

The prevalence of radiation-induced defect interactions stands to benefit from the quantification of material response trends as a function of radiation dose, which is directly correlated to defect population in ferroelectric materials. A phenomenological model is developed and implemented for such quantification, with the ultimate goal not only of aiding in comparisons of critical ferroelectric-radiation-defect interactions in this thesis, but of becoming a tool in defect engineering and functional response control in functional metal oxides.

Internal Grain Boundary Interfaces (CHAPTER 6)

The previously-identified radiation-induced modification and mobility of oxygen vacancies is investigated in relation to grain boundary configuration in PZT thin films. A range of gamma radiation doses is used to induce elevated levels of defect interactions to explore the function of grain boundary density, grain size, and grain morphology in columnar *vs.* equiaxed grain structures. The phenomenological model from CHAPTER 5 is employed to quantify and compare the effects of material microstructure on response.

Functional and Structural Effects of Internal Layer Interfaces and Chemical Heterogeneity (CHAPTER 7)

The work in CHAPTER 6 demonstrated a strong dependence of radiation tolerance and functional response on ferroelectric microstructural factors. To further investigate these effects, crystallized layer periodicity in CSD PZT thin films is studied with respect to structural and functional changes; in CHAPTER 8, similar films are irradiated and studied. Large chemical heterogeneity from asymmetric nucleation and growth behavior during crystallization of individual PZT layers results in large Zr/Ti oscillations through the thickness of the films. R/T phases are expected to correspond to the Zr-/Ti-rich regions, and resulting changes in extrinsic and intrinsic contributions to the functional response are studied. Variations in response are attributed to large changes to internal microstructure, chemical heterogeneity, and compositional fluctuations relative to the morphotropic phase boundary (MPB).

Layer Crystallization Interfaces: Interaction with Radiation (CHAPTER 8)

The work in CHAPTER 7 demonstrated significant structural and functional effects of varying layer crystallization interfaces in pre-irradiated samples. In this chapter, similar

films are studied as a function of TID and correlated to the periodicity of crystallization interfaces and chemical heterogeneity to radiation-induced defects and their mobility. Radiation interacts strongly with defects, the internal film crystallization interfaces, and grain boundaries, causing nonlinear trends of response degradation with radiation dose. Notable enhancements to the functional response are also observed due to neutralization of internal bias in the films.

Internal Dopant Defect Interactions (CHAPTER 9)

Investigations of top electrode material, microstructure, and layer crystallization interfaces highlighted the significance of oxygen vacancies in ferroelectric thin films exposed to ionizing radiation. To study films with reduced populations of deleterious mobile oxygen vacancies, the PZT solid solution was doped with large quantities of acceptor Mn, which effectively consumes oxygen vacancies by creating $Mn''_{Zr/Ti} - V_O^{\cdot\cdot}$ defect dipoles. These defect dipoles pin domain wall motion and reduce pre-irradiation functional response, but the subsequently lower concentration of *mobile* oxygen vacancies yields much greater stability of functional response in Mn-doped samples over the TID range studied (with respect to undoped samples). Application of the model derived in CHAPTER 5 is used to aid in comparison the 4 wt.% Mn-doped PZT thin films to undoped films as a function of gamma TID.

Elastic Layer Boundary and Effects of Residual Stress (CHAPTER 10)

The final two chapters of this thesis deal with modification of components of the lower material stack that do not directly contact the ferroelectric thin film. These components are particularly important for eventual implementation of the ferroelectric thin

film in MEMS devices, where the substrate may be modified to meet the needs of the intended application. First, in this chapter, trends in gamma-irradiated functional response are investigated as a function residual stress induced by variation of elastic layer thickness and material selection. Both parameters are shown to significantly modify in-plane strain in the PZT thin film. These changes in residual stress are correlated to significant variations in functional response after exposure to radiation, suggesting a strong role of film stress in determining defect motion and radiation tolerance in ferroelectric thin films.

Substrate Mechanical Interface and Residual Film Clamping Effects (CHAPTER 11)

To continue the investigation of the components of the lower material stack, the influence of the mechanical substrate-film boundary in PZT thin films is explored by reducing the degree of substrate-induced film clamping. Reduced mechanical constraint of the film to the substrate yields dramatic enhancement of electromechanical response, and potentially allows for increased long-range domain wall motion with the complex interaction of stress states and material stack components in the substrate-released PZT thin films. As demonstrated in CHAPTER 10, a strong stress variation in the ferroelectric is expected to affect radiation tolerance, and suggests that modification of the substrate, as is common for MEMS devices and packaging, is a critical focus for ongoing work.

Conclusions and Future Work (CHAPTER 12)

A summary of the research performed and recommendations for potential areas of future work regarding increased radiation hardness in ferroelectric thin films for MEMS applications. Avenues toward enhanced scientific understanding and improved engineering methods are discussed.

CHAPTER 2. LITERATURE REVIEW

This chapter outlines background information and essential work from the literature that is relevant to the investigations presented in this thesis. Pertinent theory regarding piezoelectric and ferroelectric materials is discussed, including the origins of spontaneous polarization, hysteretic functional response, ferroelectric domains, and intrinsic/extrinsic contributions to the dielectric and piezoelectric responses. The lead zirconate titanate (PZT) solid solution is introduced, including discussion of the morphotropic phase boundary (MPB). The general effects of radiation on solid matter are outlined, with specific attention placed on ferroelectric materials. Applications of thin-film ferroelectrics are discussed.

2.1 Piezoelectricity

Piezoelectrics are materials that develop a polarization in response to an applied stress or strain. The converse piezoelectric effect describes the development of stress or strain in the material under application of an external electric field. Piezoelectricity arises due to the occurrence of asymmetric electric dipole moments in solid materials, induced primarily by ions in the crystal lattice with asymmetric charge surroundings. Of the 32 crystallographic point groups, 21 are non-centrosymmetric, with 20 of those demonstrating piezoelectricity (Figure 2-1).

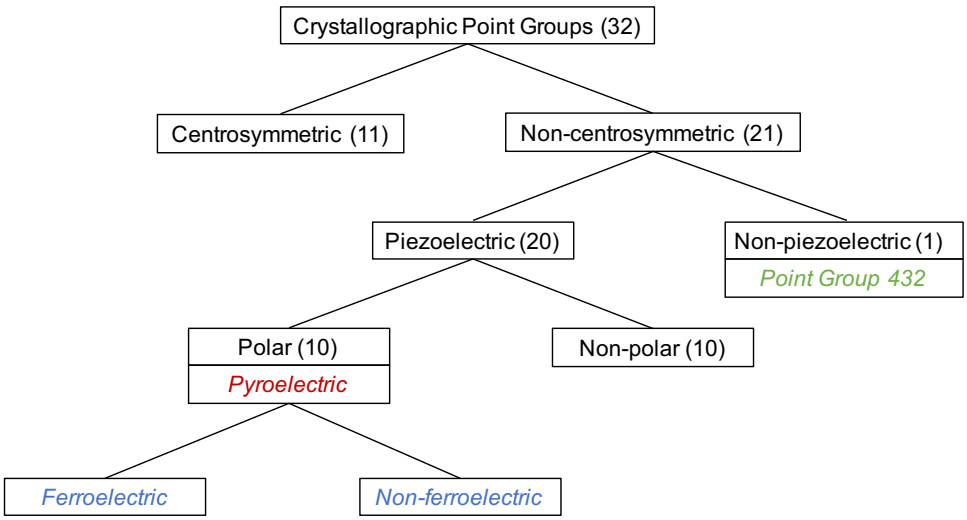

Figure 2-1 Point groups demonstrating relationship between piezoelectricity, pyroelectricity, and ferroelectricity.

The development of an electric displacement field, D_i, in response to an applied stress (σ_{jk}) or strain (x_{jk}) in a piezoelectric material is given by the expression:

$$D_i = d_{ijk}\sigma_{jk} \;\; or \;\; D_i = e_{ijk}x_{jk} \qquad 2\text{-}1$$

where d_{ijk} and e_{ijk} are the piezoelectric coefficients of a third rank tensor, and are related through the appropriate stiffness tensor.[1] The converse piezoelectric effect, on the other hand, describes the development of strain or stress as a function of applied electric field, E_k, and can be expressed similarly:

$$x_{ij} = d_{kij}E_k \ \ or \ \ \sigma_{ij} = e_{kij}E_k \qquad 2\text{-}2$$

For more practical use and reference, the coupling coefficients can also be described in reduced matrix form (engineering notation), d_{ij}, where i is the component of the electric displacement field, D_i, and σ_{jk} and x_{jk} have been reduced to σ_j and x_j, respectively. The index j = 1 to 6 describes the mechanical stress or strain: j = 1, 2, or 3, corresponding to the normal stresses along the Cartesian x_1, x_2, and x_3 directions, respectively.[2] The shear stresses τ_{12}, τ_{13}, and τ_{23} are replaced by σ_4, σ_5, and σ_6, respectively; similar reductions are made to the shear strains: γ_{12}, γ_{13}, and γ_{23} are substituted with x_4, x_5, and x_6, respectively.[2] Thus,

$$D_i = d_{ij}\sigma_j \ \ or \ \ D_i = e_{ij}x_j \qquad 2\text{-}3$$

$$x_i = d_{ij}E_j \ \ or \ \ \sigma_i = e_{ij}E_j \qquad 2\text{-}4$$

Figure 2-2 demonstrates the effects of the piezoelectric and converse piezoelectric effects. The linear relationships in Equations 2-1, 2-2, 2-3, and 2-4 adequately describe functional piezoelectric and converse piezoelectric responses at low applied stress or electric field.[3]

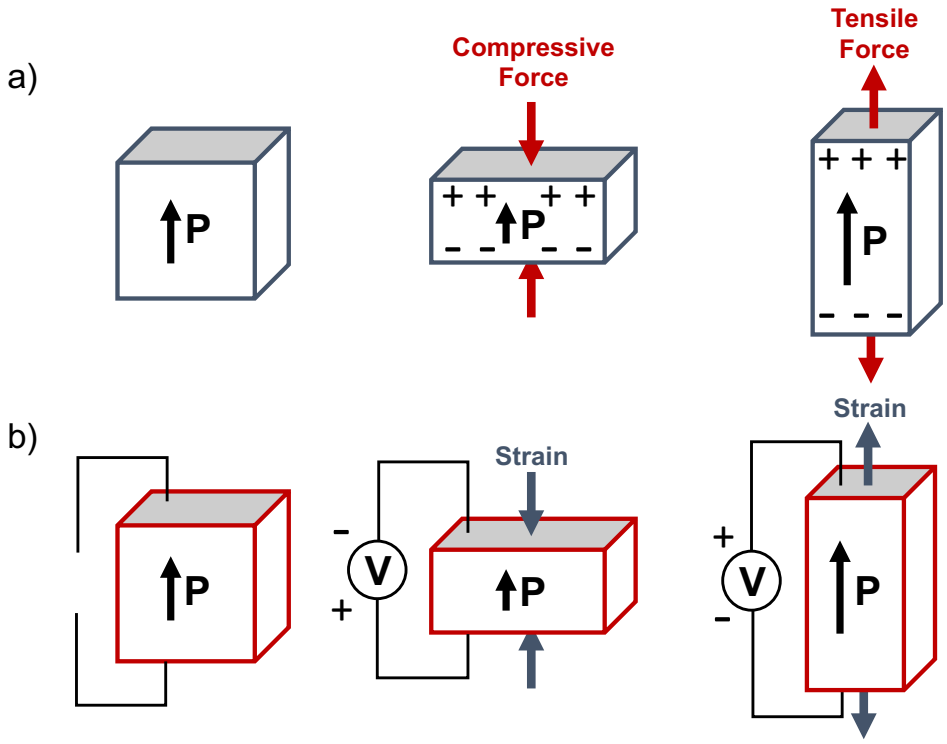

Figure 2-2. Schematic illustrating the (a) piezoelectric and (b) the converse piezoelectric effects. *P* and the accompanying arrow denote the polarization direction.[2]

The classes of piezoelectric materials can be further specified into polar and non-polar groups (Figure 2-1). Polar materials are those which exhibit a spontaneous charge separation or dipole moment in the absence of applied electric field. All polar crystal classes are pyroelectric; a pyroelectric material generates a net polarization as a function of temperature change. The pyroelectric coefficient, p_i, relates this proportional change in electric displacement field to a change in temperature:[4]

$$\Delta D_i = p_i \Delta T \qquad 2\text{-}5$$

Polar materials can be further separated into ferroelectric and non-ferroelectric (Figure 2-1). A ferroelectric material possesses a spontaneous polarization that is re-orientable via application of electric field. Not all polar/pyroelectric materials are ferroelectric due to the fact that the electric field necessary to reorient the spontaneous dipole may exceed the dielectric strength of the material (Figure 2-3), and two or more energetically equivalent polarization directions must exist in the material to constitute ferroelectricity. In the following section, specifics of ferroelectric materials and their fundamental behavior will be discussed.

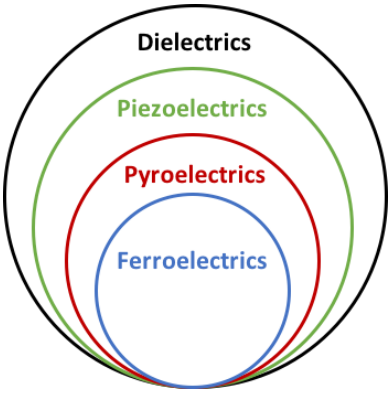

Figure 2-3 Classification of dielectric, piezoelectric, pyroelectric, and ferroelectric materials.

2.2 Ferroelectric Materials

Ferroelectrics are polar materials that possess at least two equivalent, spontaneous polarization states in the absence of an electric field, and are switchable via application of a sufficiently large electric field.[4,5] By virtue of the presence of the spontaneous polarization, they also exhibit (typically strong) pyroelectric, piezoelectric, and dielectric responses.[4] During synthesis or fabrication, most ferroelectric materials undergo a structural phase change from a high-temperature, non-ferroelectric, paraelectric phase, to

a low-temperature ferroelectric phase; the transition temperature between the paraelectric and ferroelectric phases is called the Curie temperature, T_C.

Regions of the material exhibiting (nearly) uniform direction of dipoles are known as ferroelectric domains, and are formed during the cooling process from paraelectric to ferroelectric phases. Their formation minimizes electrostatic energy of depolarizing fields, as well as the electrostatic and elastic energies associated with the appearance of spontaneous polarization and strain during the phase transition (Figure 2-4).[4] Domain walls are the regions between individual domains, and are established by the various axes of polarizability in the crystal lattice: *e.g.*, 90° and 180° for the tetragonal distortion; 71°, 109°, and 180° for rhombohedral. The mobility of these domain walls is determined by the internal energy landscape of the material, owed to electric and elastic fields associated with lattice defects (including vacancy and point defects), other domain walls, dislocations, grain boundaries, and hetero-interfaces with the electrodes and/or substrate.[6,7] For reasons of simplification, domain walls will be considered the major internal interfaces responsible for extrinsic contributions to dielectric and piezoelectric responses, while keeping in mind that phase boundary motion and/or defect dipole reorientation can contribute in a similar manner to functional response, though typically observed to a lesser degree.

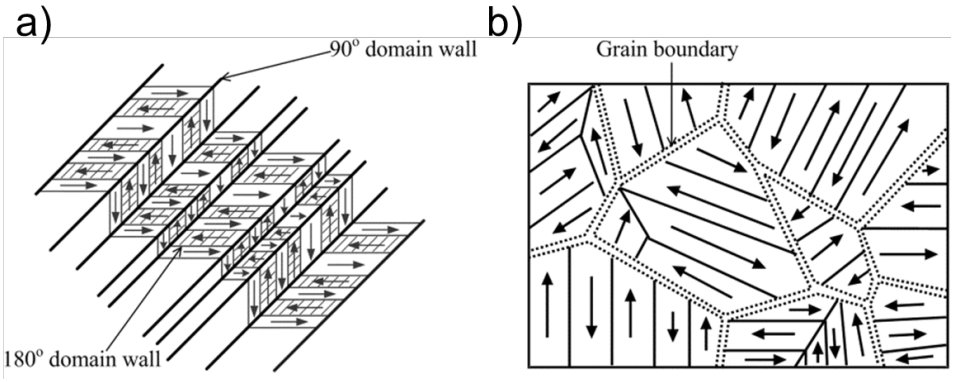

Figure 2-4 Schematic representation of ferroelastic domains. (a) shows 90° and 180° domain walls, (b) shows domains formed within grains.[8]

Ferroelectric materials exhibit a hallmark hysteretic response of polarization. (Figure 2-5). In a virgin, polycrystalline ferroelectric material, the application of a small electric field (E_j) at point (O) (Figure 2-5) results in an initially linear increase to the polarization response (P_i) with increasing electric field, while the dielectric susceptibility (χ_{ij}) remains constant, according to the formula:

$$P_i = \chi_{ij} E_j \qquad 2\text{-}6$$

Increasing the applied electric field results in switching of the domains in order to increase alignment of the spontaneous polarization directions to conform with the direction of the applied electric field, in a nonlinear manner, until saturation of the polarization response occurs at point (A) (P_{sat+}) (Figure 2-5). As the magnitude of the electric field is then reduced, some domains will switch back to their initial polarization direction, but an overall spontaneous polarization, called the remanent polarization, P_{rem+}, persists at point (B) in the absence of applied electric field (Figure 2-5). Small domain nucleation begins as the electric field is inverted and passes (B). As the field is driven in the negative direction, an

eventual net zero polarization is realized at point *C*, the negative coercive field (E_{C-}) (Figure 2-5), where the *macroscopic* polarization is said to "switch". Between this point and the negative saturation polarization, domain nuclei grow, and eventually result in (ideally) a uniformly-polarized domain in a single direction at P_{sat-}. Reducing the magnitude of the negative applied electric field begins the process in the opposite polarization direction, until reaching P_{sat+} again. Subsequent loops driven sequentially will follow the outer path shown in Figure 2-5a, *i.e.*, the path from *O* to *A* is observed only during the initial increase of the positive electric field from zero. If the macroscopic strain is plotted as a function of AC electric field, the hysteretic behavior typically follows a path similar to that shown in Figure 2-6a, also known as the "butterfly loop."

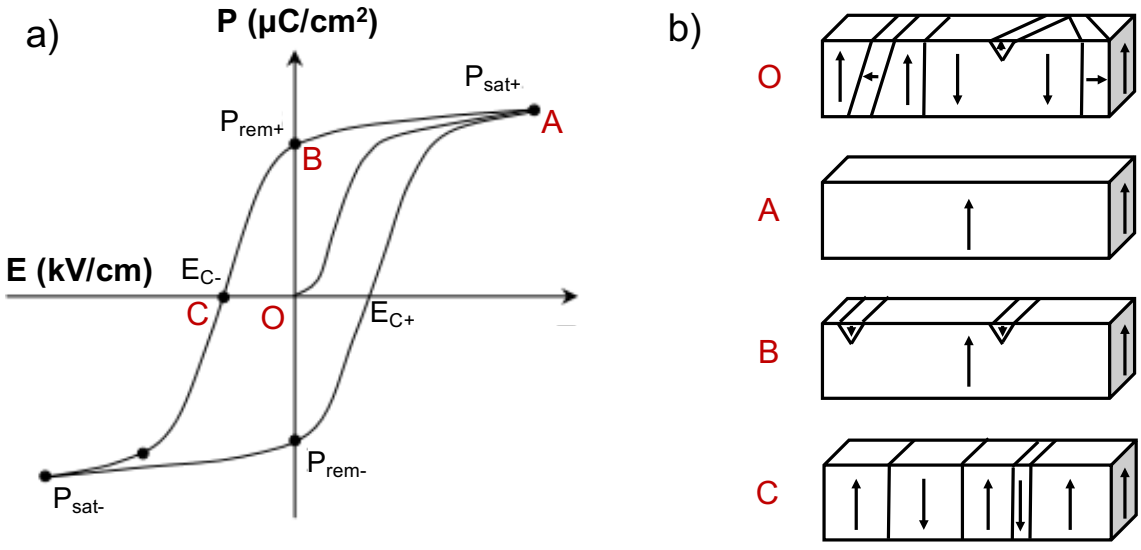

Figure 2-5 Schematic representation of the (a) polarization-electric field (*P-E*) loop and (b) domain states at important points along the hysteresis loop. Adapted from.[9]

With application of a DC electric field (E_{DC}), reorientation of the spontaneous polarization will typically result in a nonlinear hysteretic relationship of the effective converse piezoelectric coefficient, d_{33} (Figure 2-6b). A small AC electric field signal is

typically superimposed on top of the DC bias in order to make this measurement, and the piezoelectric response is measured at discrete intervals of DC bias.

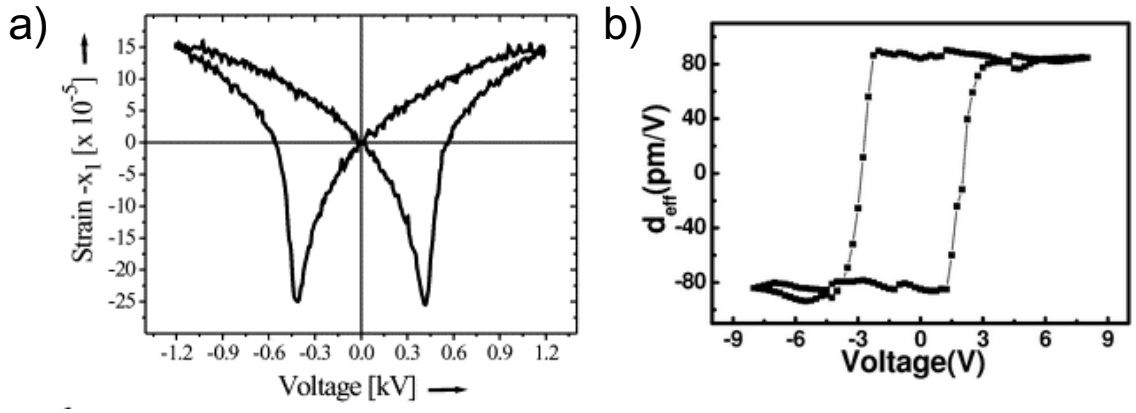

Figure 2-6 Representations of the (a) strain-AC electric field hysteresis loop and the (B) piezoelectric-DC electric field hysteresis loop, in polycrystalline ferroelectric materials.[10,11]

2.3 Perovskite Structure

Multiple crystal structures exhibit ferroelectricity, but perhaps the most commonly studied and technologically important is the perovskite structure. The prototypical perovskite structure consists of the general chemical formula ABO_3 where A and B sites are occupied by cations of typically very different sizes, and O is anionic oxygen bonded to both cations (Figure 2-7). Most generally, the A-site cation forms a body-centered cubic (BCC)-derivative structure with the B-site cation in the body center, and octahedral coordination of the oxygen atoms in the lattice.[12] However, in many perovskite-structured materials, the cubic structure is unstable, especially at low temperatures, leading to distinct distortions and corresponding diversity in the structural phase diagrams. The tetragonal

distortion of the ABO_3 perovskite cell is shown in Figure 2-7b, inducing a spontaneous polarization in the ferroelectric phase. A plethora of perovskite-phase materials have been intensely studied over the years for their diverse range of material properties and functionalities, such as $BaTiO_3$ for ceramic capacitors, $SrTiO_3$ for superconductor substrates, and $PbTiO_3$ for use in transducers, thermistors, and optoelectronics.

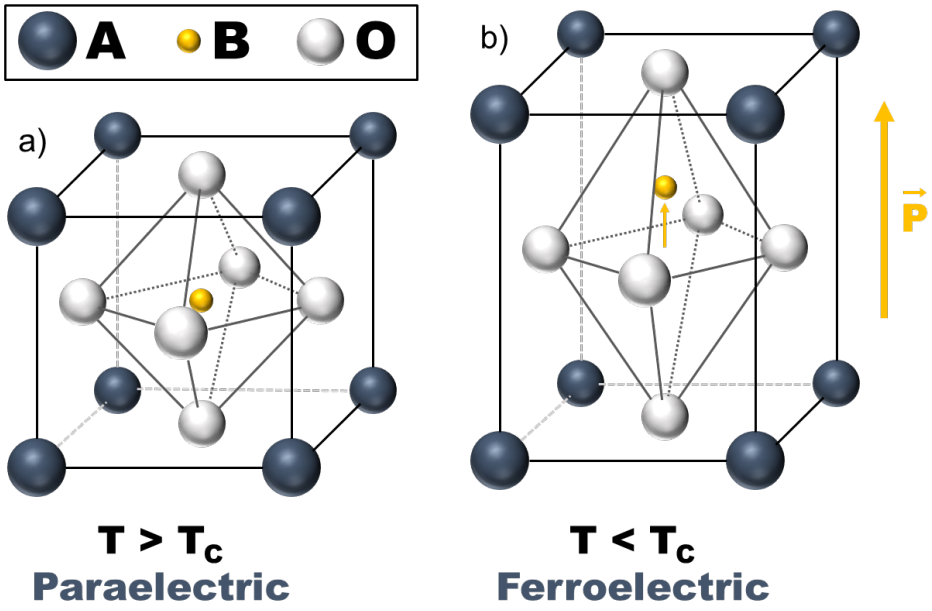

Figure 2-7 Schematic of prototypical perovskite structure, in the phase ABO_3. (a) shows the high-temperature, paraelectric phase with cubic structure, and (b) shows the tetragonal distortion in the low-temperature ferroelectric phase.

2.4 Ferroelectric Poling

Upon fabrication and cooling of a ferroelectric material from the paraelectric phase, the initial directions of spontaneous polarization and domain orientation are nonuniform and randomly distributed in such a manner as to result in nearly net zero (or very small)

polarization. This averaging of spontaneous polarization to zero over the full volume renders the material essentially non-polarized, hence, non-piezoelectric, in that state.[4] "Poling" can be employed to induce a polar state in the material by applying a strong electric field in the range of 10-100 kV/cm, often at elevated temperatures.[4] This process reorients domains within individual grains towards the available polarization direction that is best aligned with respect to the direction of the applied electric field, thereby resulting in a non-zero response (Figure 2-8). The effects of poling can deteriorate with time, when the material is exposed to higher temperatures, or with application of strong alternating electric fields comparable to or larger than the coercive field, E_C. This deterioration process is usually referred to as aging.

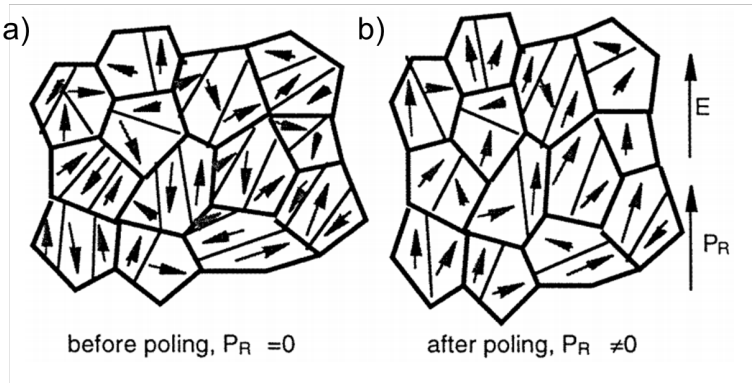

Figure 2-8 Illustration of domain polarization orientations within grains (a) before and (b) after application of an electric field to pole the sample.[4]

2.5 Intrinsic/Extrinsic Contributions and the Rayleigh Law

The strong dielectric and piezoelectric responses exhibited by polydomain ferroelectric materials are composed of both intrinsic and extrinsic contributions to the

response.[4] Intrinsic contributions encompass reversible lattice distortions and vibrations – in other words, the response that a single-crystal, single-domain ferroelectric material would exhibit (Figure 2-9a). Additionally, any *reversible* vibration of domain walls is often grouped in the intrinsic contributions to the response. On the other hand, extrinsic contributions to the dielectric and piezoelectric response entail the *irreversible* motion of domain walls in a polydomain ferroelectric material.[4] Motion of domain walls of all types will affect polarization and dielectric responses of the ferroelectric material, as only the polarization direction vector is changed. On the other hand, the piezoelectric response is typically affected only by the motion of non-180° domain walls, due to their more ferroelastically-active nature (Figure 2-9b and c).[4] However, in thin films where non-180° domain walls are heavily clamped, dynamic poling effects have been shown to lead to contributions from 180° domain walls to the piezoelectric response.[13]

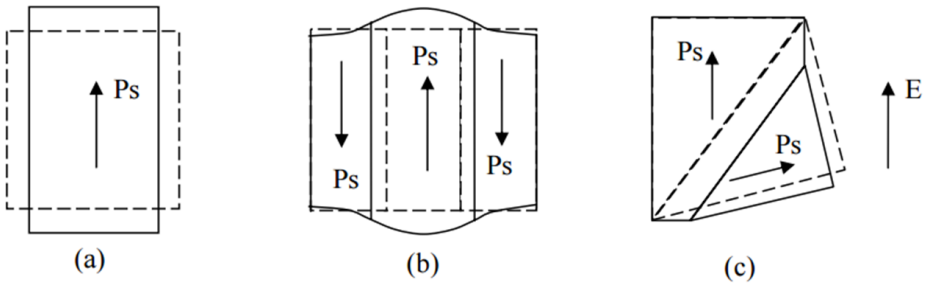

Figure 2-9 Schematic representation of (a) intrinsic contributions from a single domain, (b) dielectric extrinsic contributions from 180° domain walls, and (c) dielectric/piezoelectric extrinsic contributions from non-180° domain walls, all with application of external electric field.[14]

In an ideal polycrystalline, polydomain ferroelectric material, intrinsic and extrinsic mechanisms both contribute to the real components of dielectric and piezoelectric responses, while extrinsic mechanisms can also contribute to the loss component of the

response, which is imaginary. A variety of studies have been undertaken to separate the intrinsic and extrinsic contributions to dielectric and piezoelectric responses, primarily as a function of temperature,[15,16] excitation frequency,[17-20] and aging time dependence.[21-23] These approaches are primarily qualitative, and unable to strictly quantify intrinsic/extrinsic contributions to the dielectric and piezoelectric responses.

The study of the *nonlinear* AC electric field-dependence of the dielectric and piezoelectric responses is another method that has been leveraged to separate intrinsic and extrinsic contributions. As mentioned previously, the relationships defining piezoelectric coefficients and dielectric permittivity are valid at low electric fields,[3] but become progressively nonlinear with increasing applied electric field beyond a threshold value, E_{th}.[14,24] This threshold has been associated with the degree of domain wall pinning in the ferroelectric material, though the value of E_{th} is highly sample-dependent.[25,26] Above the threshold value, domain walls are sufficiently mobile to overcome local pinning centers, and the subsequent behavior of the dielectric permittivity and piezoelectric coefficients for AC electric field excitation can often be described using the Rayleigh Law in a quantitative manner. Specifically, the Rayleigh Law provides a link between the irreversible, hysteretic behavior and the nonlinearity of the electric field-dependent dielectric permittivity.[24] However, the Rayleigh analysis does not take into account rate dependence or thermally-activated processes, and is valid only over a specific range of applied electric field.[24] The Rayleigh method is employed extensively throughout the literature and this thesis.

The Rayleigh Law was initially developed in 1887 by Lord Rayleigh to describe the behavior of ferromagnetic materials at low electric fields.[27] Néel expanded on Rayleigh's observations, demonstrating the motion of ferromagnetic walls between

potential energy wells with application of electric field.[14] Overcoming an initial energy barrier results in pinning and unpinning of the domain walls and subsequent hysteretic behavior. This work was later correlated to defect concentrations in ferromagnetic materials by Kronmuller.[28] The Rayleigh Law has further been applied to analogous behavior of ferroelectric materials (both bulk and thin film) and mobile domains or phase boundaries moving across randomly-distributed pinning centers in a ferroelectric sample (Figure 2-10).[29-31]

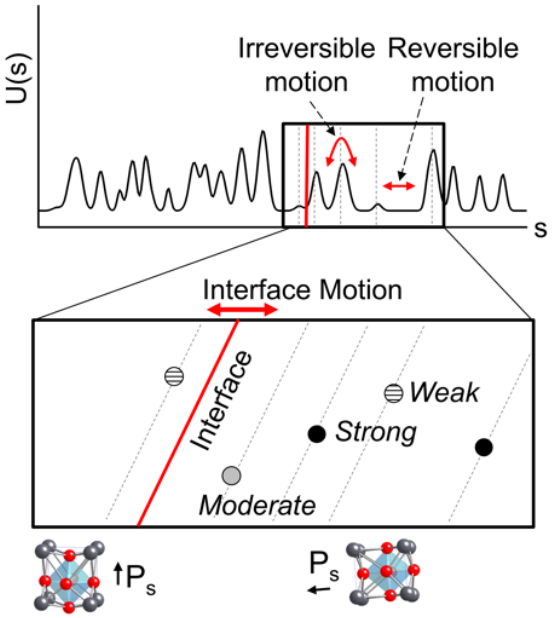

Figure 2-10 Schematic representation of domain wall motion in a ferroelectric material. *U(s)* is the potential energy as a function of domain wall position, *s*, and P_S demonstrates the direction of polarization.[32]

In ferroelectric materials, the Rayleigh Law for dielectric permittivity is given by:[24]

$$\varepsilon' = \varepsilon'_{init} - \alpha' E_0 \quad (real\ dielectric\ permittivity) \qquad 2\text{-}7$$

where

$$\varepsilon^* = \varepsilon' - j\varepsilon'' \ \ (complex\ dielectric\ permittivity) \quad 2\text{-}8$$

$$|\varepsilon^*| = \sqrt{(\varepsilon')^2 + (\varepsilon'')^2} = \varepsilon_r \ \ (dielectric\ permittivity) \quad 2\text{-}9$$

under an applied AC electric field, $E_{AC} = E_0$. A linear dependence for the piezoelectric coefficient as a function of AC electric field can also be developed, similar to Equation 2-7:

$$d' = d'_{init} - \alpha'_d E_0 \quad 2\text{-}10$$

ε'_{init} and d'_{init} terms are independent of electric field, and dominate the dielectric and piezoelectric responses, respectively, at low fields. These terms are typically referred to as the reversible Rayleigh parameters and constitute intrinsic lattice response as well as small contributions of reversible domain wall motion (vibration). The α' and α'_d terms include extrinsic contributions to the dielectric and piezoelectric responses, respectively – *e.g.*, the irreversible motion of domain walls – and are usually called the irreversible Rayleigh parameters. The ratio of irreversible to reversible Rayleigh parameters, $\alpha'/\varepsilon'_{init}$ and α'_d/d'_{init} are often employed as quantitative measures of the extrinsic contributions to the dielectric and piezoelectric responses, respectively.[24,33]

In materials that exhibit Rayleigh-like behavior, the dependence of the dielectric and piezoelectric responses on applied AC electric field can typically be separated into three separate regions – (I) a low-field region of relatively constant dielectric response that precedes the threshold electric field, (II) the region directly following E_{th} characterized by linear dependence of dielectric response, and (III) a region of nonlinear response following the coercive voltage, E_C (Figure 2-11).[34] Fitting a linear curve to the dielectric response in

region (II) allows for extraction of the reversible and irreversible Rayleigh parameters, and comparative analysis thereof (see Section 3.3.3). Extrinsic contributions, and specifically the motion of domain walls, make up a significant portion of the dielectric and piezoelectric responses in polycrystalline ferroelectric thin films, but these contributions are greatly reduced with decreasing thickness of the film, as will be discussed in the following section.[35] The role of extrinsic contributions to the functional response, in the context of fabricating radiation-tolerant ferroelectric thin films, cannot be understated, and plays a major role in the studies in this thesis.

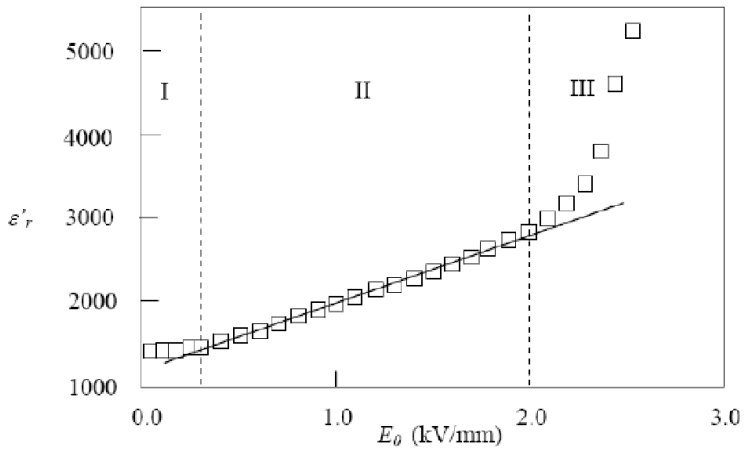

Figure 2-11 Schematic representation of the dielectric response as a function of AC electric field in bulk $Pb(Zr,Ti)O_3$ ceramics. The low-field region, (I), demonstrates relatively constant dielectric permittivity. The Rayleigh region (II) begins after the threshold field, E_{th}, and dielectric permittivity increases linearly with the applied AC field. The high-field region (III) is characterized by a nonlinear dielectric response.[34]

2.6 Size Effects in Ferroelectric Thin Films

As ferroelectric film thickness decreases, especially below one micron, the motion of domain walls and internal interfaces can become severely restricted by extrinsic size effects, thus inhibiting dielectric and electromechanical response.[36,37] Variations in grain morphology and size, chemical heterogeneity, substrate clamping, space charge depletion, defect(-defect) interactions, increased defect concentration in thinner films, *etc.* are responsible for deleterious effects on the response of thin (< 1 μm) and ultrathin (< 200 nm) ferroelectric films. Grain sizes in polycrystalline thin films are typically smaller than those found in bulk samples (50-150 nm compared to 1+ μm), thereby increasing both grain boundary and domain wall density in thin films, and leading to reduced domain wall mobility (Figure 2-12).[24,38] Furthermore, large concentrations of point defects present in polycrystalline thin films give rise to defect interactions that can subsequently pin domain walls and reduce their range of motion and the derived functional response.[24] Residual stress, introduced through substrate clamping, thermal expansion coefficient mismatch between film and substrate during cooling, and various other electromechanical interfaces in the material stack, can result in similar pinning of domain walls, further robbing the material of dielectric and electromechanical response.[24] These effects are considered for investigations of intrinsic and extrinsic contributions to the functional response as a function of layer crystallization interfaces (CHAPTER 7) and work on residual stress resulting from modifying mechanical boundary conditions (CHAPTER 11).

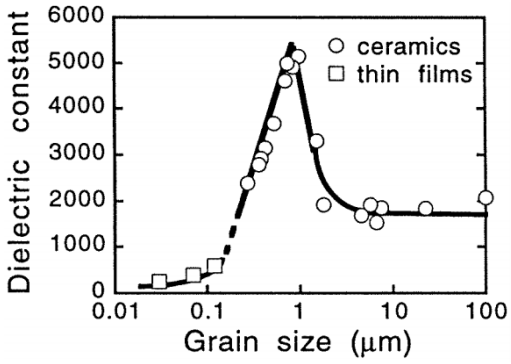

Figure 2-12 Plot showing scaling of the dielectric constant with grain size in $BaTiO_3$ thin films and ceramics.[4]

2.7 Ferroelectric Thin Films for MEMS Applications

With the increasing push of microelectronics devices towards greater functionality at smaller length scales, ferroelectric materials have assumed a critical role in a multitude of applications, ranging from ferroelectric random access memory (FeRAM), multilayer ceramic capacitors (MLCC), and microelectromechanical systems (MEMS). Indeed, the multifunctional properties of ferroelectrics – *i.e.*, large dielectric, piezoelectric, and pyroelectric coefficients – make them ideal candidates for enabling a "More-than-Moore" paradigm in microelectronic devices. Specifically, the excellent piezoelectric response of ferroelectric thin films makes them prime candidates for many MEMS sensors, actuators, and relay applications. Several important piezoelectric materials have been employed for MEMS-related applications, such as AlN, ZnO, and polyvinylidene fluoride (PVDF).[1,39] However, many of these commonly-used piezoelectric materials for MEMS devices do not boast the same electromechanical and dielectric responses inherent to perovskite oxide ferroelectric thin films, and especially PZT (Table 2-1). While studies on PZT and related

ferroelectric compositions have been widespread in recent years, novel devices and increased demand for further scaling of functional materials continuously creates new applications for which the functional response must be considered. The rapid growth in the field of connected microelectronics devices has been met with increasingly robust functional requirements, such as the ability to operate in radiation-hostile environments, *i.e.*, for aerospace, satellite, and nuclear applications (Figure 2-1).[40]

Table 2-1 Comparison of dielectric and electromechanical responses in selected ferroelectric/piezoelectric materials in thin film form for use in MEMS-related applications.[1,41]

Material	Class	d_{31} (pC/N)	d_{33} (pC/N)	ε_{33}
PZT	Ferroelectric	-94 to -274	80 to 593	425 to 1900
$BaTiO_3$	Ferroelectric	78	190	1700
PVDF	Ferroelectric	23	-35	4
ZnO	Piezoelectric	-4.7	6 to 12	8.2
AlN	Piezoelectric	-3	5	10

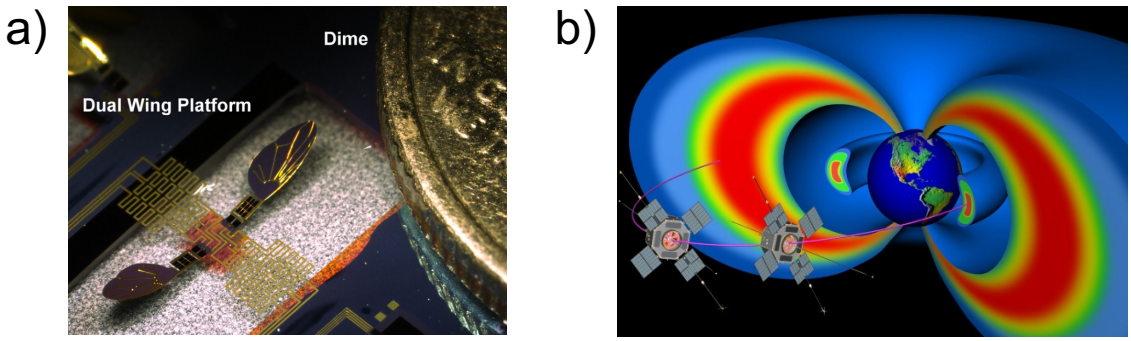

Figure 2-13 Ferroelectric thin films are prime candidates for use in environments exposed to radiation, such as in (a) mm-scale robotics,[42] and satellite applications.[43]

As discussed in the following sections, radiation strongly influences the dielectric, ferroelectric, and piezoelectric responses of ferroelectric materials by creating and/or activating defects that can interfere with the defect energy landscape of the material. Such interactions occur not only in the ferroelectric material, but also throughout the material stack at multiple critical locations. The design and engineering of improved functional ferroelectric materials and material stacks for operation in radiation-hostile environments requires an augmented understanding of the fundamental interactions of radiation with the functional material and supporting substrate, elastic layer, and electrodes. This work takes a multifaceted approach to studying ferroelectric materials for MEMS applications in radiation hostile environments by considering multiple parameters that influence the effects of radiation on a ferroelectric thin film stack. Several methods and interfacial interactions are investigated, including the effects of radiation on top electrode material, ferroelectric microstructure, layer crystallization interfaces, dopant concentration, and mechanical boundaries of the lower material stack. It is expected that the results presented in this thesis not only increase the scientific understanding of ferroelectric materials and their interaction with radiation, but also provide avenues toward increased performance and radiation tolerance for use in MEMS devices and applications.

2.8 Lead Zirconate Titanate (PZT) Solid Solution

While numerous materials demonstrate piezoelectric and ferroelectric properties, lead zirconate titanate, $Pb(Zr_xTi_{1-x})O_3$ (PZT), has found widespread use and technological relevance, primarily due to its large dielectric, ferroelectric, and piezoelectric properties,

and the ability to tune and tailor such properties through a variety of processing methods.[1,42,44] PZT is a solid solution between the two end members lead zirconate ($PbZrO_3$, "PZO") and lead titanate ($PbTiO_3$, "PTO"). $PbZrO_3$ is anti-ferroelectric, *i.e.*, single atomic cells show local spontaneous polarization (ferroelectricity), but adjacent cells show anti-parallel polarization vectors, resulting in net-zero macroscopic ferroelectricity. $PbTiO_3$ is ferroelectric with tetragonally-distorted perovskite (ABO_3) structure. The PZT material system exists in multiple phases, dependent on Zr to Ti ratio, temperature, and pressure (Figure 2-16a). Above the Curie temperature, T_C, PZT exists in a cubic, paraelectric phase. At room temperature, PZT exhibits ferroelectricity in either a rhombohedral (R) or tetragonal (T) phase.[24] A third, monoclinic phase has also been reported between the R and T phases at certain atmospheric conditions.[45,46]

The tetragonal phase of PZT has six equivalent, principal directions along which spontaneous polarization can occur, normal to each of the faces of the unit cell. Due to this four-fold symmetry, domain walls formed in tetragonal-phase exist at 90° (perpendicular polarization direction) and 180° (anti-parallel polarization direction) (Figure 2-4a).[4] The rhombohedral unit cell has eight spontaneous polarization directions, along the body diagonals, resulting in 71°, 109°, and 180° domain walls (Figure 2-14).

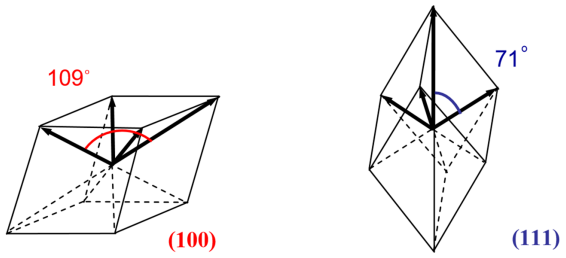

Figure 2-14 Schematic representation of the 71° and 109° angles between body diagonals in the (100)- and (111)-directions of the rhombohedral unit cell of PZT.[14]

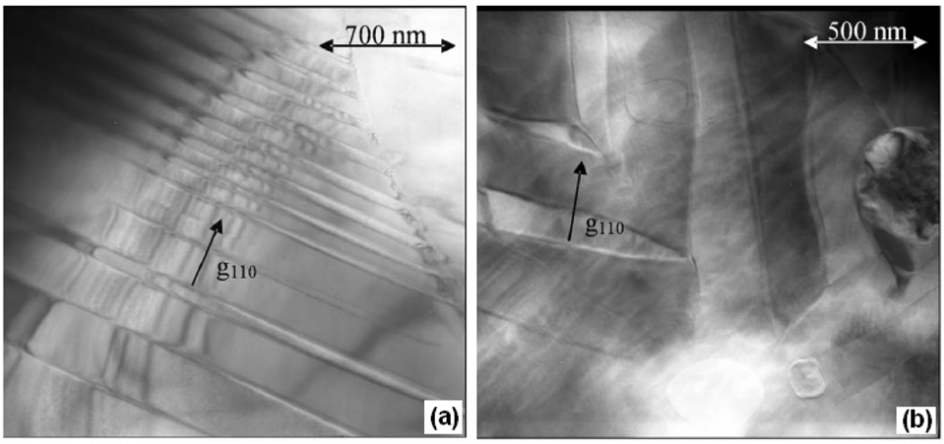

Figure 2-15 Transmission electron microscopy (TEM) images of domain structures for $Pb(Zr_xTi_{1-x})O_3$ with (a) x = 0.4 (tetragonal phase) and (b) x = 0.6 (rhombohedral phase).[47]

The boundary between the rhombohedral and tetragonal phases at which a structural phase change occurs is called the morphotropic phase boundary (MPB). At room temperature, this boundary exists at approximately x = 0.53.[48] Polarizability is enhanced in the vicinity of the MPB, and large enhancements to dielectric and piezoelectric properties occur, making compositions near the MPB very attractive (Figure 2-16b).[49,50] Leveraging both the enhanced properties as well as potential phase transitions in proximity of the MPB

in PZT constitutes a significant portion of this thesis, and will be discussed in detail later. While proximity to the MPB generally results in favorable enhancements of dielectric and electromechanical responses, there are differences in intrinsic and extrinsic contributions for compositions on either side of the MPB. Rhombohedral compositions (Zr > 0.53) generally demonstrate greater extrinsic contributions to the dielectric response than tetragonal compositions at an equal distance from the MPB, due to greater spontaneous strains of the tetragonal distortion compared to the rhombohedral distortion.[48,51] The 90° domain walls that are more prevalent in tetragonal-phase PZT are more likely to be clamped to some degree by this inherent strain, while the 109° and 71° domain walls of the rhombohedral phase are often less strained, and freer to move.[4] The effects of these phenomena are clearly demonstrated in the piezoelectric response of rhombohedral, tetragonal, and MPB PZT compositions (Figure 2-17).[48,51]

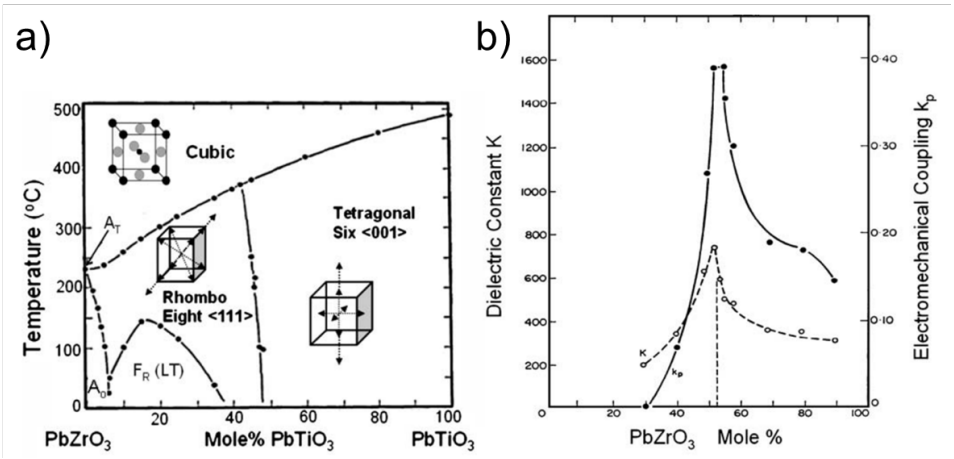

Figure 2-16 a) Temperature-composition phase diagram for PZT and b) dependence of dielectric and electromechanical response on Zr/Ti composition. Morphotropic phase boundary (MPB) is shown as the vertical line in the center of the plot in (a), which separates the rhombohedral (R) and tetragonal (T) phases of perovskite-structure PZT. [49]

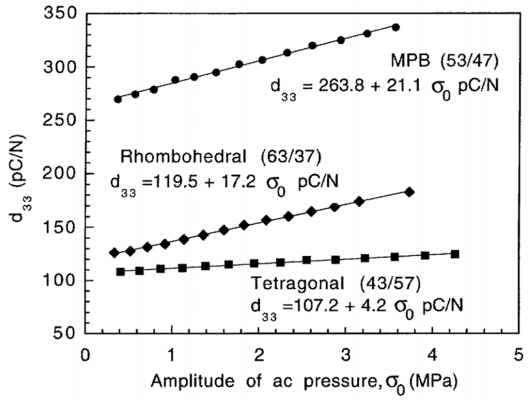

Figure 2-17 Plots of the direct d_{33} piezoelectric coefficient of different compositions of PZT (4 at.% Mn) near the MPB, and in the tetragonal and rhombohedral phases.[48]

Doping, temperature and pressure fluctuations, residual stresses, and a variety of other factors can lead to changes in the effective PZT functional response and proximity-to-MBP-like behavior. Numerous studies have shown that residual stresses, such as those developed during film crystallization, can effectively shift the MPB and modify the transition temperature, T_C.[52-55] In PZT thin films, biaxial tensile/compressive stresses can result in a T/R phase transition; tensile-stressed films have shown shifts of MPB compositions towards the tetragonal phase.[52,53] These potential changes can be both beneficial and harmful for eventual device design. Generally, compositions near the MPB or slightly to the rhombohedral side of the phase diagram are preferred, due to the large increase in extrinsic contributions to the dielectric and piezoelectric response.

Crystal anisotropy can also play an important role in the dielectric and piezoelectric response of PZT thin films. Figure 2-18 shows the phenomenologically-calculated dielectric and piezoelectric responses of PZT compositions near the MPB in both tetragonal and rhombohedral phases.[56] For the majority of the work in this thesis, 100-textured MPB PZT compositions are targeted, due to their large piezoelectric response.

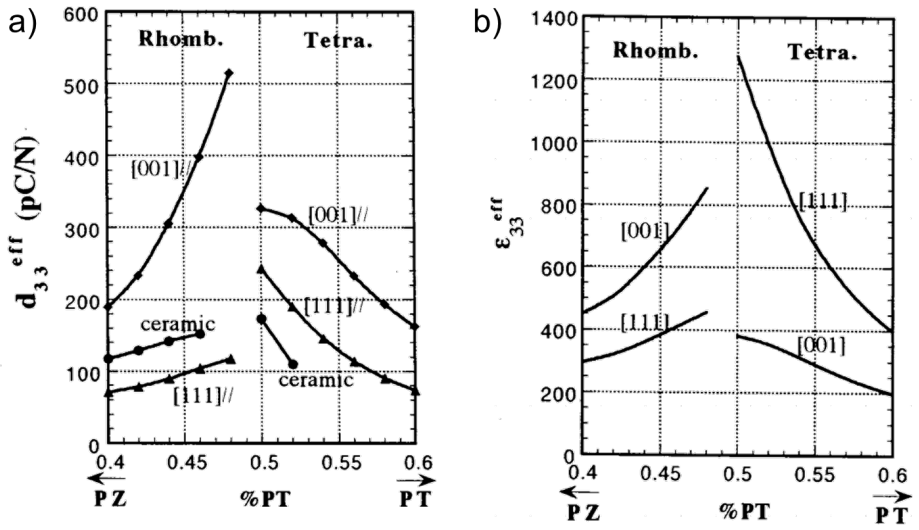

Figure 2-18 Phenomenologically-calculated responses of PZT compositions near the MPB show strong dependence (a) piezoelectric and (b) dielectric responses on crystallographic orientation.[56]

2.9 Defects in Ferroelectric Thin Films

Crystallographic defects are present in virtually all solid materials, and especially prevalent in polycrystalline materials, existing as point, line, planar, and bulk defects. In ferroelectric thin films, the presence and interaction of a variety of different types of defects can be both beneficial and deleterious to material properties and functional response. The interactions between domain walls (2D defects), grain boundaries (2D defects), and point defects (0D) are often considered when discussing defect-defect interactions in ferroelectrics. The mobility of domain walls is affected by both point defects and defect dipoles, which consist of a strong polar interaction between a cationic defect (such as an acceptor ion at the B-site in the PZT lattice or a Pb-vacancy) and an oxygen vacancy. On one hand, the electric field-induced pinning and unpinning of domains walls to/from other

defects contributes to the dielectric and piezoelectric responses.[4] On the other hand, higher concentrations of defects can result in stronger or more ubiquitous pinning of domain wall motion, and ultimately degrade functional response.

Ferroelectric fatigue is often discussed in relation to defects in ferroelectric thin films. Ferroelectric fatigue is defined as the loss of the spontaneous, switchable polarization with an increasing number of bipolar switching cycles.[4] Multiple factors have been shown to contribute to ferroelectric fatigue, including defect concentrations, electrode material selection, temperature, electric field strength, surface treatment, porosity, and grain size.[4] The interaction of mobile oxygen vacancies, both with the ferroelectric itself, as well as with internal interfaces (*e.g.*, grain boundaries, layer interfaces, electrode interfaces, *etc.*), and the effects on ferroelectric fatigue has been a topic of extensive research, especially for applications in memory devices.[4,32,57-73] Oxygen vacancies, both within a single grain, and accumulating at interfaces, can effectively screen part of the ferroelectric film from the applied electric field and lead to loss of polarization switching.[74-77] It has been suggested that oxygen vacancies can serve as pinning centers for domain walls in ferroelectric thin films, reducing or completely restricting their motion, and leading to suppression of polarization and reduced functional response.[78]

In addition to oxygen vacancies, electronic defects can also suppress polarization and inhibit domain wall motion. Free electronic charge carriers can pin domain walls by becoming trapped in the domain-wall region, to which they are attracted due to the inherent polarization discontinuities at those locations.[4] Such charge carriers can be injected into the material through electric field cycling at the electrodes, during fabrication of the material, and even with exposure to radiation (including UV).[4] Application of electric field

can induce domain wall motion and overcome the pinning caused by defects (oxygen vacancies, trapped charges, *etc.*). However, point defects can also become mobile and/or recombine with other defects, resulting in subsequently-increased motion of domain walls.[4] Generally, ferroelectric fatigue results in reduction of ferroelectric, dielectric, and piezoelectric properties by restricting domain wall motion and suppressing polarization switching (Figure 2-19b).

Ferroelectric aging can also play a critical role in determining the functional properties of ferroelectric thin films over extended periods of time. Several primary effects contribute to aging – all are attributable to defect interactions in the ferroelectric. First, elastic and/or electronic defects are formed within domains upon fabrication of a ferroelectric thin film and are, for the most part, randomly oriented. Over time, these defects can reorient to assume more energetically-favorable positions or orientations, thus making subsequent attempts to switch their polarization more difficult.[4] Second, diffusion driving forces in the ferroelectric film, such as residual mechanical stresses or uncompensated electrical charges, can result in defect motion into domain walls over time, inhibiting their future motion.[4] Third, space charges are often accumulated at regions such as grain boundaries due to phase separation or dopant segregation at these locations. These uncompensated space charges – if distributed asymmetrically – can result in a preferential bias of the entire grain and stabilize local domains, thus reducing the motion of the corresponding domain walls.[4] Each of these three effects results in some degree of internal bias in the sample, which can act as an additional energy barrier to be overcome when switching the polarization in the ferroelectric. Aging is often manifest via a pinching of the

polarization-field hysteresis loops (Figure 2-19a).[62] This pinching is indicative of the defect interactions discussed above, and their generally deleterious effects on the polarization.

The terms endurance, retention, and imprint are often used when referring to the effects of fatigue and aging on ferroelectric materials, specifically in memory device applications. Endurance refers to the resistance of a ferroelectric material to fatigue, while retention designates an analogous resistance to the effects of aging on ferroelectric properties. Imprint describes the tendency of a ferroelectric memory to develop a preferential bias state, *i.e.*, a strong asymmetrical internal bias.[4]

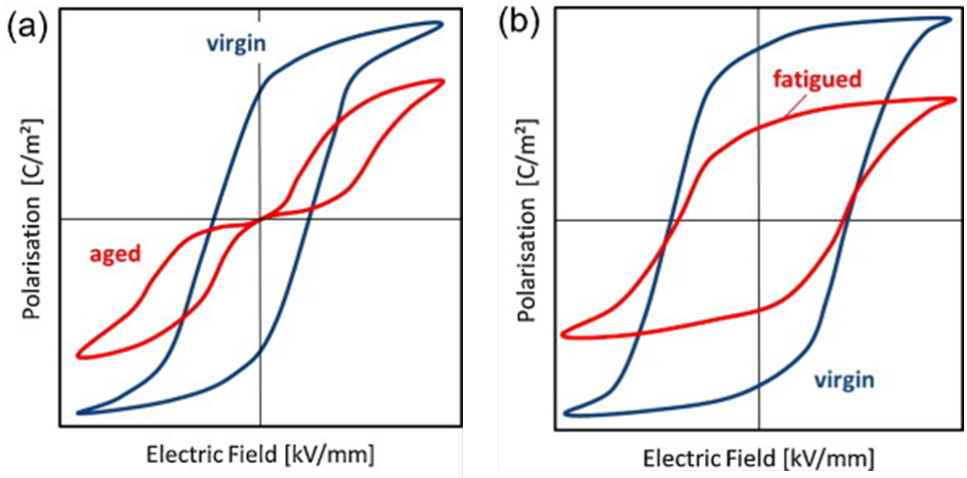

Figure 2-19 Schematic showing the effects of (a) aging and (b) fatigue on the ferroelectric hysteresis loops.[62]

2.10 Defect Engineering and Chemical Doping

Defect engineering refers to the modification of the type, charge, concentration, spatial distribution, or mobility of defects in a crystalline solid, typically to control and tailor material properties and functional response.[79] Such techniques have been used for

decades in semiconductor materials, resulting in enormous advances to microelectronics devices and entire industries. A variety of methods have been used to study and manipulate defect concentrations in semiconductors, including irradiation, ion-implantation, heating protocols, epitaxial growth methods, and photostimulation, among others.[79] Similar approaches to defect engineering of ferroelectric materials have been undertaken, especially the use of chemical doping of the solid solution to improve functional properties.[80] However, defect chemistry and engineering in most perovskite-phase ferroelectrics can be quite complex, due to the inclusion of multiple chemical elements, potential phase separation, diffusion, and the interactions of defects with extrinsic contributions to the functional response.[81-83]

Donor doping substitutes ionic species such as La^{3+} or Nb^{5+} (larger positive charge than Pb) into the Pb position in the PZT lattice, resulting in a "*soft*" PZT. These substitutions typically introduce excess positive charge, which is compensated by additional Pb vacancies, as well as reduced number of oxygen vacancies and defect dipoles in the material.[81,84] This reduction often leads to enhanced domain wall motion and greater electromechanical response, but also larger dielectric losses and low conductivity.[81,84] Additionally, doping with La or Nb can lead to changes in the crystal structure of PZT – removing oxygen from the perovskite unit cell can result in an effective contraction of the lattice, thus reducing tetragonality (smaller *c*/*a* ratio, *i.e.*, more cubic, when *a* is constrained to the substrate).[81]

On the other hand, acceptor doping with ions such as Fe^{3+} or Mn^{3+} into B-site cation sites results in "*hard*" PZT, creating oxygen vacancies and defect dipoles. Such defects can pin domain wall motion and reduce electromechanical response, while lowering dielectric

and piezoelectric losses in the material.[84] Figure 2-20 shows the effects of Fe- and La-dopant concentrations on the *P-E* hysteresis loops for ceramic PZT.

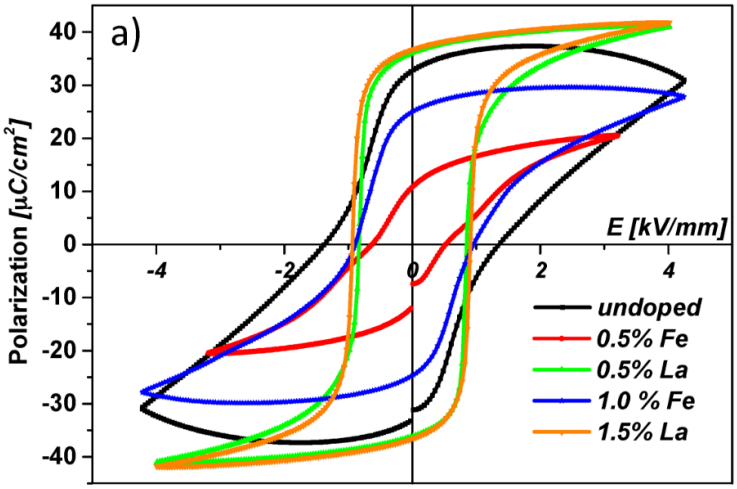

Figure 2-20 *P-E* loops for undoped, Fe-, and La-doped $PbZr_{0.6}Ti_{0.4}O_3$ ceramics. La-doping results in increased polarization with slimmer, more square hysteresis curves. Fe-doped samples develop slanted, pinched hysteresis loops.[85]

While chemical doping of ferroelectric materials results in distinct modifications to functional properties and enhances their utility for a variety of applications, phase separation, dopant segregation, and chemical heterogeneity can pose challenges to doping of ferroelectric thin films and the PZT solid solution.[4,81,86]

2.11 Radiation-Material Interactions

This thesis deals with the interaction of radiation with ferroelectric PZT thin films for MEMS applications. Radiation transfers energy to a material via ionization, *i.e.*, electron excitation and generation of electron-hole pairs; or via nuclear interactions, resulting in lattice vibrations and atomic displacements. Low-energy photons, such as X-

rays, gamma rays, and electrons, do not usually have sufficient energy to result in atomic displacements, and therefore interact with materials by exciting electrons, eventually leading to the formation of electron-hole pairs and electron trapping at defect centers.[87] Higher-energy radiation can ionize the material, and is energetic enough to directly (electrons) or indirectly (gamma ray Compton-scattered electrons) form Frenkel defects.[88] Charged particles, such as protons and heavy ions, also transfer energy to the material via electron and nuclear interactions, in much the same way that photons/electrons do. However, their greater mass and reduced velocities increase their interaction time with the material, and can result in greater rates of ionizing energy transfer, even at similar doses. Their larger mass also increases the possibility of displacement events. Displaced atoms, also called recoils, will also lose energy through (secondary) ionization, and may create additional defects (with sufficient energy) to form a defect cascade. Subsequent defect cascades can in turn lead to defect clustering and high-dose amorphization of the material.[89]

2.11.1 Radiation-Ferroelectric Interactions

In ferroelectric materials, radiation-induced ionization and displacement events can potentially augment (stable) defect population and modify the energy of preexisting defects, thus changing the local energy landscape for defect-defect interactions (such as those responsible for the mobility of internal interfaces) in the ferroelectric material. Prior work on the effects of radiation on ferroelectric materials has shown a direct correlation between radiation dose and degradation of functional properties.[32,90-96] Bastani *et al.* demonstrated substantial degradation of ferroelectric, dielectric, and electromechanical

response in PZT thin films exposed to 2 Mrad X-ray and proton irradiation.[97] Others have shown substantial changes in both the structural properties and the functional response in ferroelectric thin films exposed to neutron irradiation.[40,98,99] A variety of studies on the effects of gamma irradiation on ferroelectric bulk ceramics and thin films have reported measurable reductions to domain wall motion, thus degrading dielectric and ferroelectric responses.[92,93,100-107]

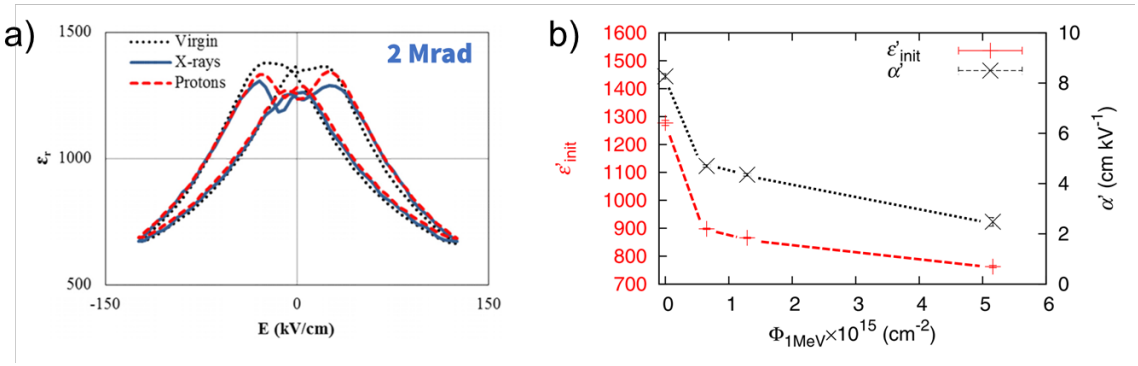

Figure 2-21 Effects of (a) X-ray and proton radiation on the permittivity-electric field response ($\varepsilon_r - E_{DC}$ curves) of PZT thin films,[97] and (b) the effects of neutron fluence on the intrinsic and extrinsic contributions to the AC electric field dielectric response.[40] Lines in (b) have been added to guide the eye.

Generally, radiation-generated trapped charges can result in degradation of polarization, dielectric, and electromechanical response, primarily through increased pinning of domain wall motion.[32,40,97,98,100] In addition to ionizing energy transfer to the material, high-energy electrons and more energetic particles (protons, neutrons, heavy ions, *etc.*) also transfer energy via nuclear interactions that lead to direct atomic displacement. These radiation-induced displacements may degrade the functional ferroelectric response in a way that is relatively similar to that of ionization-related defects (especially for defects like Frenkel pairs) or may result in unique modes of response degradation in the case of multi-atom defects (defect clusters) that affect larger volumes.[32,96,101] In many cases, the

effects of radiation, both due to ionization and displacement events, are similar to those brought on by ferroelectric fatigue: pinned domain walls and suppressed polarization.[96] Ultimately, radiation-induced modification of functional response in ferroelectrics is the result of changes in defect concentration and energy in the material.

In this work, the interaction of radiation with ferroelectric materials is studied from multiple perspectives, with the intent of making valuable scientific contributions regarding the role of defects – especially the modification, mobility, and accumulation of radiation-modified oxygen vacancies – and offer potential methods for reducing such damage. These methods for damage mitigation include variations in electrode material, film microstructure, and film layer crystallization interfaces. Additionally, chemical doping is leveraged as a way to reduce mobile oxygen vacancy concentration in pre-radiation PZT thin films, resulting in samples exhibiting a high degree of radiation hardness. Finally, work on modification of the mechanical boundaries and interfaces in the lower material stack (*i.e.*, elastic layer and substrate), demonstrate strong changes to the stress state in the ferroelectric film, and a correlation between residual stress and radiation tolerance. The methods studied here seek to expand the current knowledge of the interaction of radiation with ferroelectric thin films, focusing on methods for quantifying defects and material performance, and attempting to mitigate the deleterious effects wrought by exposure to radiation.

CHAPTER 3. EXPERIMENTAL PROCEDURES

This chapter details the specific processing, fabrication, and characterization methods for the ferroelectric $Pb(Zr_xTi_{1-x})O_3$ (PZT) thin films and material stacks studied in this thesis. Included are procedures for precursor solution preparation, substrate preparation, thin film deposition/crystallization, and top electrode photolithography processes. Post-fabrication imaging and microstructural characterization techniques, macroscopic functional response characterization, and various other experimental methods used throughout this work are discussed.

3.1 Chemical Solution Deposition

Since being implemented in the mid-1980s, chemical solution deposition (CSD) has proven to be a highly attractive method for large-area, cost-effective processing of perovskite-phase ferroelectric thin films.[44,108-110] Ferroelectric thin films processed via CSD typically demonstrate favorable compositional homogeneity, good thickness uniformity, and a large amount of microstructural and compositional control, allowing for fine-tuning of material properties and eventual functional performance.[110,111] On the other hand, the superlative sensitivity and control over properties can often make consistent processing of ferroelectric thin films a difficult task.[112-117] Minor changes to precursor chemistry, deposition protocols, heat treatment parameters, substrate roughness, *etc.*, can greatly influence nucleation and growth behavior, ferroelectric material microstructure, and the defect landscape of the material.[112,117-125] It is thus imperative to document in detail all aspects of the film-fabrication procedures used in this work.

CSD fabrication of ferroelectric thin films is typically comprised of four basic steps: (i) precursor solution synthesis; (ii) deposition of precursor solution on an appropriate substrate; (iii) low-temperature pyrolysis (300-400 °C) (thermal ("pyro") decomposition ("lysis")) to remove solvent and residual organic compounds from the precursor solution, resulting in an amorphous film; and (iv) crystallization of the amorphous film via high-temperature (600-850 °C) heat treatment.[111] Nucleation events of the ferroelectric phase may be initiated during pyrolysis (iii) to some degree, but full crystallization of the material is realized only at the elevated annealing temperatures (iv).[111,126] A schematic overview of this process is shown in Figure 3-1. In many implementations, steps (i) to (iii) are repeated multiple times to obtain a thicker film before

crystallization in (iv). The entire crystallization process can be repeated until films of the desired thickness are obtained. Each of the four steps for CSD processing is discussed in the following sub-sections.

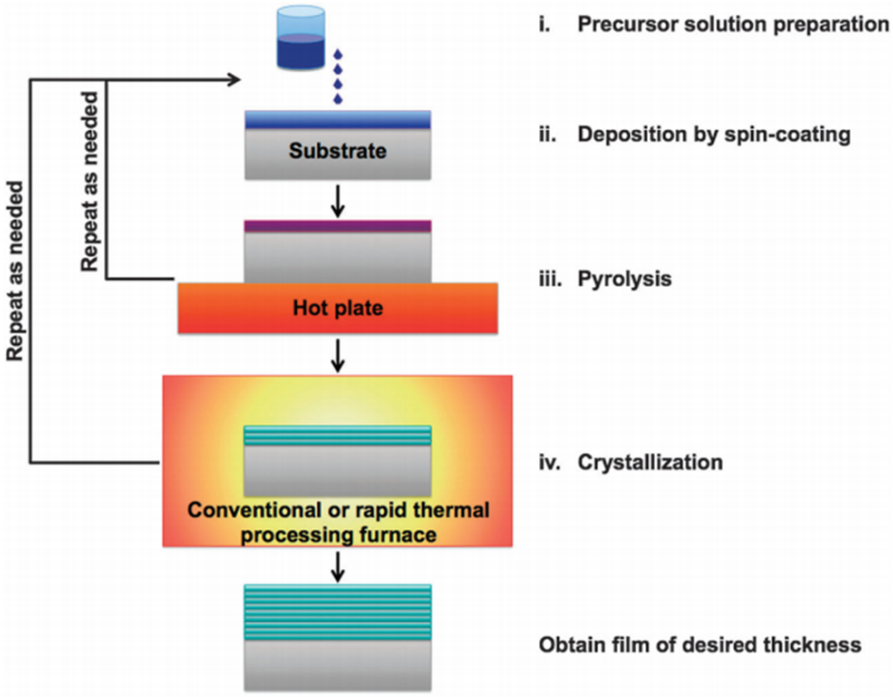

Figure 3-1 Schematic illustration of the basic steps of chemical solution deposition (CSD) of ferroelectric thin films.[111]

3.1.1 Sol-gel Precursor Solution Synthesis

The solvent and chemical precursors selected for preparation of the precursor solution significantly affect the final microstructure and functional properties of the ferroelectric-phase material, and dictate the appropriate deposition and thermal processing conditions for optimal material properties.[111] Numerous methods and precursors have been employed in the literature to address a number of processing concerns, including as-

crystallized material properties, solution longevity, resistance to precipitation, toxicity, and process simplicity.[111] Of these methods, solutions employing 2-methoxyethanol (2-MOE) as the solvent are the most commonly used, due to their high level of solution stability (resistant to precipitation up to months or even years), minimal aging effects, and reproducibility of the process chemistry.[111,127] However, 2-MOE-based precursor solutions require long synthesis times, and the relative toxicity and carcinogenicity of 2-MOE are primary concerns.[111] Chelate-based processing, also commonly known as inverted mixing order (IMO), employs (relatively safe) methanol as the solvent and is faster to prepare, but synthesized solutions are sensitive to humidity and age quickly.[110 120,128] In this thesis, all but one of the sets of PZT thin films that were studied were prepared with 2-MOE-based precursor solutions. The notable exception is a set of methanol-based IMO deposited PZT thin films that demonstrated large equiaxed grains, used in the case study for developing a phenomenological model (CHAPTER 5) and a more in-depth study of the effects of grain structure on radiation tolerance of PZT thin films (CHAPTER 6). All other precursor solutions were synthesized at Georgia Tech or the US Army Research Laboratory using 2-MOE-based methods.

3.1.1.1 2-MOE-based PZT precursor solutions (Georgia Tech)

This process outlines precursor solution preparation for the studies found in CHAPTER 7, CHAPTER 8, and CHAPTER 11. The PZT (53/47) precursor solutions were synthesized with 2-MOE solvent, generally following the routes described by Wolf and Trolier-McKinstry, [129] and Bastani with minor modifications.[130] Zirconium (IV) propoxide

solution, $Zr(OCH_2CH_2CH_3)_4$ 70 wt.% in 1-propanol (Sigma Aldrich) and titanium (IV) isopropoxide, $Ti[OCH(CH_3)_2]_4$ 97% (Sigma Aldrich) were dissolved in 2-MOE, ($CH_3OCH_2CH_2OH$) 99.9% (Sigma Aldrich) in an Ar-purged glove box, and subsequently stirred continuously (Heidolph Laborota 4000 efficient rotary evaporator) at ~115 °C (oil bath on hot plate) for 30 minutes in an Ar-purged environment. Separately, lead (II) acetate trihydrate, $Pb(CH_3CO_2)_2 \cdot 3H_2O \geq 99.99\%$ on a trace metals basis (Sigma Aldrich) was dissolved in 2-MOE in an Ar-purged glove box, and vacuum distilled (IKA RV 05 basic rotary evaporator, ~180 Torr) at 120 °C (oil bath in IKA HB4 basic) until the 2-MOE was evaporated and a white foamy matter was achieved (~30-60 minutes depending on the quantity of 2-MOE in which the lead acetate tri-hydrate is dissolved). The 2-MOE-lead acetate trihydrate solution was continuously chilled with flowing ethylene glycol coolant set to ~18 °C (REMCOR chiller). When the foamy Pb solution was achieved, both separate solutions were removed from their respective rotary evaporators and oil baths, and allowed to cool for approximately 5 minutes, before the Zr/Ti solution was added to the Pb solution. This final solution was stirred for 4 hours at 120 °C (oil bath in IKA HB4 basic), and the solution molarity was adjusted by adding 2-MOE or additional vacuum distillation to evaporate excess solvent. PZT solutions of molarities (M) ranging from 0.1M to 0.4M were used throughout this work. An outline of this process is shown in Figure 3-2.

In Pb-based ferroelectric oxides, the high crystallization temperatures can cause Pb instability and diffusional loss through the surface of the film. In order to compensate for this loss, PZT solid solutions are frequently synthesized with over-batched Pb content relative to the stoichiometric formula. The amount to which they were over-batched in this thesis depends on the specifics of the process and layer thicknesses, but was typically

between 8 and 20 M% excess. The PZT solutions used in CHAPTER 7, CHAPTER 8, and CHAPTER 11 contained 20 M% excess Pb.

Thin PZT or $PbTiO_3$ seed layers are often employed as the first deposited layer in order to induce a preferential texture in the subsequent layers.[131] For the films studied in CHAPTER 7, CHAPTER 8, and CHAPTER 11, a 0.15M PZT seed solution with 30 M% excess Pb was used, processed identically to the PZT layer solutions, as described above.

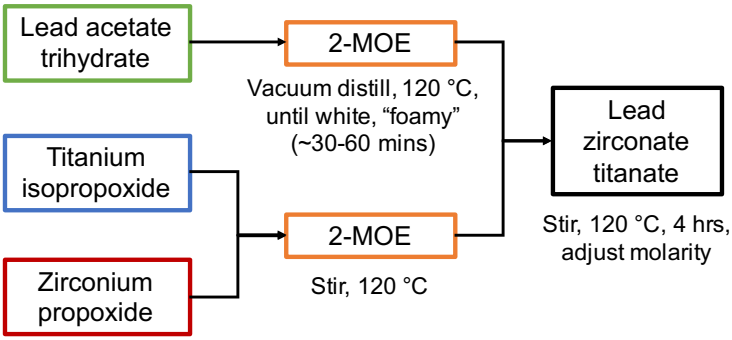

Figure 3-2 Schematic showing the general outline of PZT sol-gel precursor solution preparation.

3.1.1.2 2-MOE-based PZT precursor solutions (ARL)

A portion of this work was done in collaboration with the US Army Research Laboratory (ARL), including the processing of PZT precursor solutions and sample preparation for the work in CHAPTER 4, CHAPTER 5, CHAPTER 6, CHAPTER 9, and CHAPTER 10. Solutions prepared at ARL follow the process outlined by Sanchez *et al.*[131] 0.4M PZT (52/48) solutions with 8 M% excess Pb were prepared by mixing lead (III) acetate trihydrate (Puratronic) with 2-MOE (Sigma Aldrich) before refluxing for 20 min at 120 °C with flowing N_2 in a Heidoph Laborota 4000 rotary evaporator. Vacuum distillation

was performed to remove impurities by reducing the internal pressure of the rotary evaporator to between 280 and 330 mbar (dependent on humidity level), until the solution appeared as a white foam. Appropriate amounts of zirconium (IV) n-propoxide precursor (Alfa Aesar) and titanium (IV) isopropoxide 70 wt% in n-propanol (Alfa Aesar) were mixed with 2-MOE and stirred on a magnetic spinner while the Pb solution was refluxed and distilled. The Ti/Zr solution was then combined with the Pb solution in a glove box, and the combined solution refluxed for 210 min. A second vacuum distillation at 925 mbar and N_2 purge were performed and the solution transferred to a storage container where 4 vol% formamide was slowly added to the solution to act as a drying control agent. The final solution was stirred overnight with a magnetic stirrer. For all samples prepared at ARL, a 0.17M $PbTiO_3$ (PTO) seed solution with 30 M% excess Pb was prepared using the same process above without the addition of the Zr precursor.

3.1.1.3 IMO PZT precursor solutions (Sandia)

The work in CHAPTER 5 and CHAPTER 6 compares PZT thin films with columnar and equiaxed grain structures – columnar samples were prepared via 2-MOE-based CSD at ARL, and equiaxed samples were fabricated with methanol-based IMO CSD PZT thin films prepared at Sandia National Laboratories. The IMO precursor solutions were prepared following a method outlined by Assink and Schwartz,[110] and is reproduced below. Quantities for chemical precursors of PZT (53/47) are available in the report by Assink and Schwartz, but are not reported here.[110] A 0.35M PZT (52/48) with 5 M% excess Pb precursor solution was used in this thesis. Purified titanium isopropoxide was added to

zirconium butoxide (80% in n-butanol). After 5 min, the acetic acid was added to the mixed alkoxide solution. After 6 min, methanol was added, and after 5 additional min, lead (IV) acetate 90% was added to the solution and heated to ~85 °C in order to dissolve the Pb precursor (~16 min to dissolution). The hot plate was turned off and methanol immediately added to rapidly cool the solution to 70 °C. Acetic acid, methanol, and (again) acetic acid in appropriate amounts were added at 2-min intervals. After 5 min, deionized water was added to the solution, reducing the temperature to ~50 °C. Stirring was maintained throughout the entire preparation process. The first part of the process up until the first addition of acetic acid was carried out under Ar-purged conditions, after which the remainder of the process was carried out under ambient laboratory conditions. This general process is shown in Figure 3-3, and available elsewhere.[110]

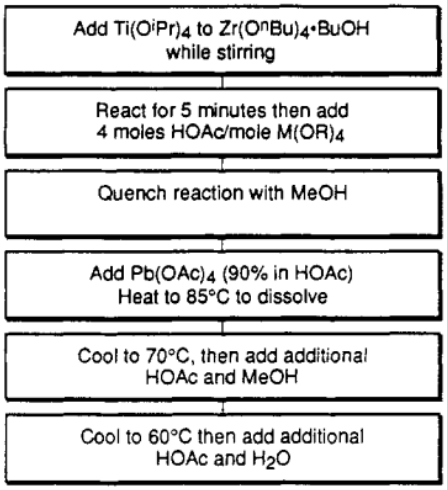

Figure 3-3 Flowchart showing the IMO process for PZT precursor solution prepartion, as described by Assink and Schwartz, and employed for multiple samples fabricated for this work at Sandia National Laboratories.[110] Reprinted with permission from Assink and Schwartz, *^{1}H and ^{13}C NMR Investigations of Pb(Zr,Ti)O_3 Thin-Film Precursor Solutions*. Copyright 1993 American Chemical Society.

3.1.2 Substrate/Bottom Electrode Selection and Preparation

A critical aspect of processing PZT thin films is selection of appropriate substrate and bottom electrode materials, as they can result in vast modifications to deposited ferroelectric film microstructure and eventual functional properties. A multitude of work has been undertaken to elucidate the effects of clamping, stress, substrate texture, diffusion barriers or elastic layers, and electrode materials.[131-135]

All substrates and bottom electrode stacks used in this work (with the exception of one set of samples, see CHAPTER 11) were prepared according to work by Potrepka *et al.*, and Sanchez *et al.*[131,132] 500 to 2035 nm (specified in each individual work) of dry thermal SiO_2 were grown on 100 mm- or 150 mm-diameter *p*-type (boron-doped) 100-Si wafers (500 μm or 625 μm thick, respectively). A bottom electrode was sputtered onto the SiO_2 barrier/elastic layer with a Unaxis Clusterline 200 (CLC) deposition system. The bottom electrode consisted of 35 nm Ti sputtered at room temperature, and annealed in oxygen at 750 °C (Bruce Technologies tube furnace), thus converting the layer to TiO_2. TiO_2 serves as an adhesion layer for the Pt electrode layer, and also acts to induce a 111-texture with a full width half maximum (FWHM) range of 1.7 to 2.3°.[131,132] 100 nm of Pt was then sputter-deposited at 500 °C, yielding a highly 111-textured bottom electrode contact and growth template for the subsequently-deposited PZT thin films. Throughout this work, these substrates are often referred to as "platinized substrates."

As mentioned, one set of samples in CHAPTER 11 utilizes slightly different processing conditions for the substrate and material stack (sample set M1). These samples were fabricated on 100 mm-diameter, 300 μm thick, double-side polished (DSP) *p*-type

(boron-doped) 100-Si wafers, upon which 1300 nm of wet/dry (final ~15 nm of growth are dry) thermal SiO_2 (Tystar Tytan Mini). Prior to oxide growth, wafers were prepared via standard CMOS protocols, *i.e.*, 10 min at 120 °C in Piranha bath (6:1 mixture of H_2SO_4:H_2O_2); 10 min at 70 °C in SC-2 bath (5:1:1 mixture of H_2O:HCl:H_2O_2); and 30 s in dilute hydrofluoric acid (10:1 mixture of H_2O:HF (49%)) at room temperature; followed by a spin-rinse in deionized water and spin-drying. A 20-nm Ti adhesion layer and 80-nm Pt bottom electrode layer were sputter deposited (Unifilm Sputterer), both at ~200 Å/min without breaking vacuum between the two depositions. The Pt bottom electrode showed a strong 111-texture, providing an ideal growth template for subsequently-processed PZT thin films.

3.1.3 PZT Thin Film Deposition

The PZT thin film deposition process proved to be one of the more difficult aspects of the material stack fabrication, as minor variations in spin speed, ambient conditions, pyrolysis temperature, wait times between deposition steps, and final crystallization temperature profiles can translate to large variations in film microstructure, phase, texture, and functional properties.[111,136] As discussed previously, the collaborative nature of much of this work means that multiple deposition processes were used, and are outlined below.

3.1.3.1 PZT thin film deposition (Georgia Tech)

The PZT film deposition process presented in this section was performed at Georgia Tech and used for the work in CHAPTER 7, CHAPTER 8, and CHAPTER 11. The platinized substrates described in 3.1.2 were rinsed with acetone and isopropyl alcohol (IPA) before deposition to remove any residual organics or water. Care was taken to ensure that acetone was not allowed to dry on the substrate (or cleaved pieces thereof) before rinsing with IPA, and then dried with nitrogen or compressed air. Solutions were loaded into 5 to 6 mL veterinarian syringes, after which large air bubbles were pushed out of the syringe, and a 0.1 μm PTFE filter and a 16- or 18-gauge needle (depending on availability) were connected to the syringe. The precursor solution was then dispensed onto the stationary wafer or chip, which was previously positioned in the spin coater (Laurell Technologies) with the vacuum chuck activated. Care was taken to dispense the solution slowly to avoid formation of any bubbles on the chip surface. The tip of the needle was positioned such that the solution was not allowed to form discrete drops onto the substrate (*i.e.*, the surface of the substrate and the needle are "connected" by the surface tension of the sol-gel solution), but the tip of the needle was not permitted to touch the surface of the substrate. This method allows for a smooth stream of sol-gel solution to be deposited and reduces bubbles and surface perturbations. The viscosity of the solution and speed of the advancing front of sol-gel solution are primary concerns in the formation of bubbles, and has been studied in relation to a variety of polymer applications.[137,138] As a rough estimation of deposition time, the dispensing of solution on a 4 cm^2 chip takes ~10 s, and ample solution is dispensed to cover the entire surface of the chip, and even enough to allow for substantial surface tension to build up at the edges of the chip. Care must be taken

not to impact the spin coater after dispensing the sol-gel, thus breaking the surface tension – for this reason the vacuum chuck is activated prior to dispensing the solution. The chip was spun at 3000 rpm for 30 s, with a ramp rate of approximately 500 rpm/s. For PZT solutions of 0.4M concentration, this process results in layer thickness of ~60 nm, with thickness scaling roughly linearly to molarity down to 0.15M solutions. For solutions lower than 0.15M, layers become increasingly thin at a nonlinear rate.

Deposited films were pyrolyzed on a hot plate at ~390 to ~400 °C for 1 min. Pyrolysis temperatures were noted to have substantial effects on the eventual crystallographic texture of the crystallized PZT thin films: at temperatures below ~360 °C, development of the PZT 111-orientation was greatly augmented; and above ~405 °C, the PZT 110-orientation was noted, though these effects are reported only anecdotally. An in-depth study of pyrolysis parameters and the effects on eventual microstructure and functional properties is provided by Ihlefeld *et al.*[136] After pyrolysis, the sample was allowed to cool (20 to 30 s), and the deposition/pyrolysis process repeated as many times as desired to obtain the individual layer crystallization thickness (Figure 3-1). After repeating the deposition/pyrolysis process the desired number of times, the amorphous film was quickly transferred to a rapid thermal annealer (SSI Rapid Thermal Processor (RTP)) and crystallized at a target temperature of 700 °C for 1 min in air, with a heating rate of approximately 120 °C/s. No flowing oxygen or nitrogen was present during crystallization or during the ramp down cooling step. Small samples were annealed on a Si (most commonly) or Si/SiO_2 carrier wafer in the SSI RTP; the carrier wafer material is unimportant, given that temperature calibration with dummy samples is performed before actual crystallization runs. After 1 min at 700 °C, the sample was allowed to ramp down to

< 180 °C before sample retrieval. Figure 3-4a shows the heating and radiation intensity profiles as a function of time, and the resulting temperature. Note that the plot has been cut off at 100 °C due to the fact that films were typically at that temperature after pyrolysis and the RTP process was started with the samples at approximately 80 to 100 °C. Minor overshoot (5 to 10 °C) was often programmed into the recipe, as the eventual film phase and microstructure are (anecdotally) more susceptible to undershooting 700 °C than overshooting. However, overshoots of ~25+ °C should be avoided, as Pb loss becomes a problem with rising temperatures. Figure 3-4b shows specifics of the recipe used, with the strong caveat that these are a recommended baseline – accurate calibration of the tool is required before each session of film deposition, as the temperature profile is extremely susceptible to variability from Si carrier-wafer warpage with successive heat treatments, heated-sample size/mass/reflectivity, and the current maintenance state of the tool. Following crystallization, the previous process is repeated until the desired film thickness is achieved (Figure 3-1). For films processed with multiple layers in a single crystallization step, the term “multi-layer anneal” (MLA) is used.

a)

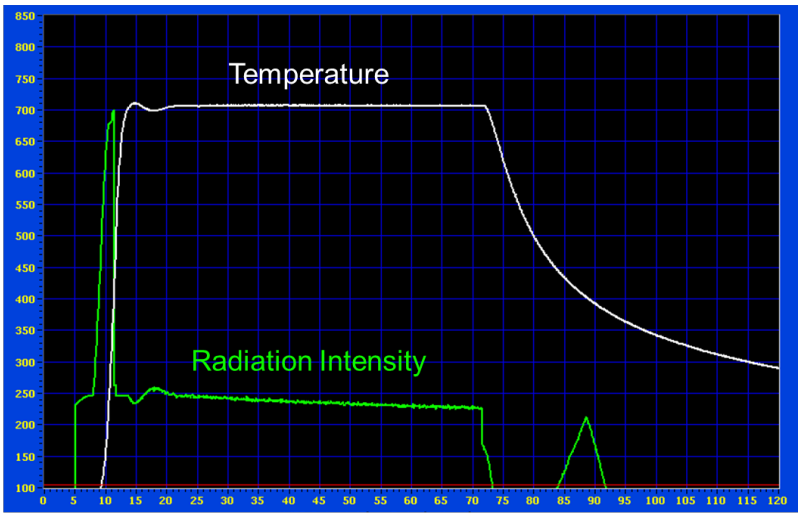

b)

Step#	Operation	Control Temp	Ramp Rate/ Step Time	REM/ Intensity	Control Device	Nitrogen	Oxygen	% Forming G	N/A	P Value	I Value	D Value	LRLP	LFLP	LLP
1	Purge	0.0	5.0	0.00	Tray TC	0.0	0.0	0.0	0.0	0.0	0.0	0.0	0.0	0.0	0.0
2	Ramp Up	710.0	60.0	296.00	Tray TC	0.0	0.0	0.0	0.0	5.0	0.0	0.0	100.0	100.0	100.0
3	Hold	705.0	60.0	24.00	Tray TC	0.0	0.0	0.0	0.0	40.0	0.0	0.0	100.0	100.0	100.0
4	Ramp Down	180.0	20.0	0.00	Tray TC	0.0	0.0	0.0	0.0	0.0	0.0	0.0	0.0	0.0	0.0
5	Hold	20.0	20.0	5.00	Tray TC	0.0	0.0	0.0	0.0	0.0	0.0	0.0	0.0	0.0	0.0
6	Finish	20.0	10.0	0.00	Tray TC	0.0	0.0	0.0	0.0	0.0	0.0	0.0	0.0	0.0	0.0

Figure 3-4 (a) Temperature and radiation profiles for the heating routine employed for PZT thin film crystallization in the SSI RTP (Georgia Tech). (b) specifics of the recipe used; these were constantly adjusted based on pre-processing calibrations, but serve as a baseline.

3.1.3.2 PZT thin film deposition (ARL)

The samples used for the work in CHAPTER 4, CHAPTER 5, CHAPTER 6, CHAPTER 9, and CHAPTER 10 were prepared according to processing conditions outlined by Sanchez *et al.* at ARL.[131] Any deviations from the following general process are noted specifically in the experimental procedures of individual chapters. A single $PbTiO_3$ (PTO) seed layer approximately ~17 nm thick was spin coated onto the platinized substrate to induce 001-texture in the subsequent PZT layers. The solution was dispensed from a 10 mL syringe through a 0.1 μm filter onto the stationary substrate, then spun with a Bidtec SP100 spin coater at 3000 rpm for 45 s. The as-deposited layer was pyrolyzed on

a Wentworth Laboratories vacuum hot plate at 350 °C for 2 min to remove organic species and solvent, resulting in a film with some mid-range order.[126] The pyrolyzed films were then crystallized in a rapid thermal annealer (AG Associates Heatpulse 610 RTA) at 700 °C with a ramp rate of 4 °C/s. This process was repeated for the groups of 0.4M PZT (52/48) layers used in this work, except with a spin speed of 2500 rpm for 45 s, resulting in individual layer thickness of approximately 60 nm. Unless otherwise noted in the experimental process of each chapter, films were deposited with a total target thickness of 500 nm and annealing after every 2 layers.

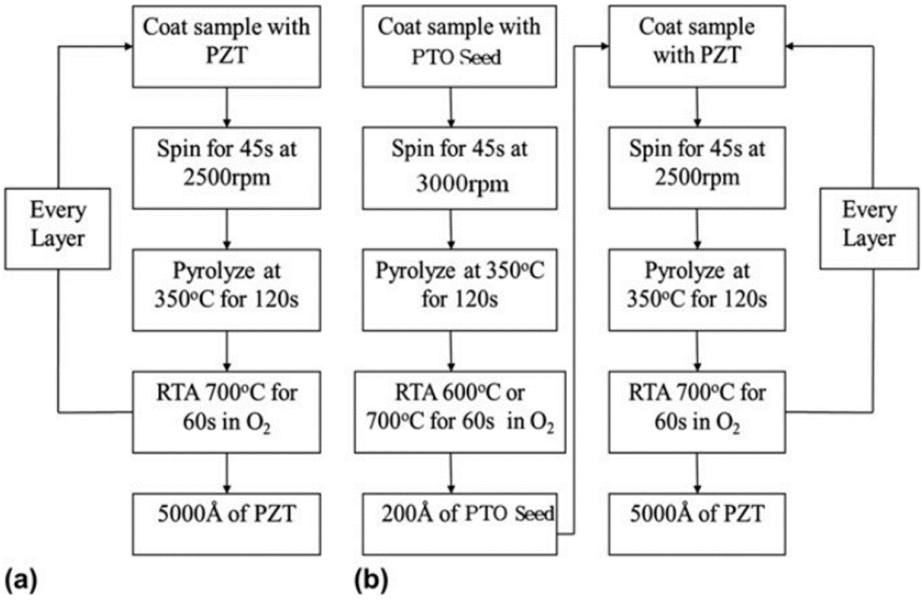

Figure 3-5 Flowchart detailing PZT thin film deposition procedures for samples prepared at ARL. (a) details the PTO seed layer, and (b) shows the process for subsequent PZT layers.[131]

3.1.4 Electrode Contact Fabrication

While not explicitly a part of the CSD process, the crystallized films must undergo macroscopic dielectric, ferroelectric, and piezoelectric characterization, the specifics of which are discussed later in this chapter. Accordingly, top electrode contacts must be deposited to create a metal-ferroelectric-metal capacitor sandwiched between the bottom- and top electrode contacts, and the continuous bottom electrode must be exposed for proper contact (Figure 3-6). These process is performed either via photolithography or Ar-ion milling of deposited metal layers to create the contacts. This section is divided into two procedures done at Georgia Tech and ARL.

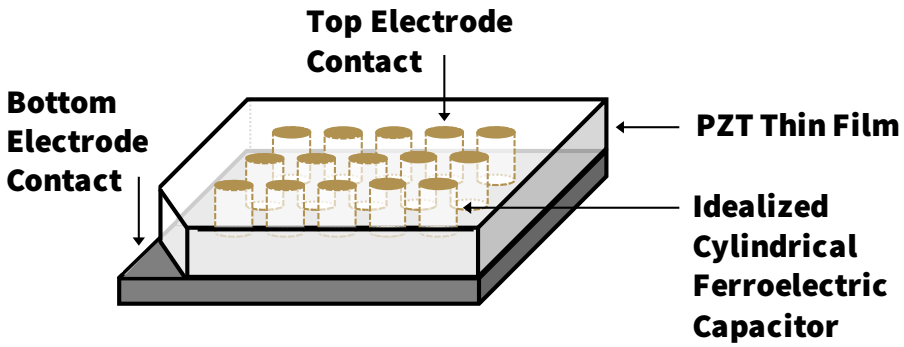

Figure 3-6 Schematic illustration of the ferroelectric thin film sandwiched between the top and bottom electrode contacts, creating an idealized cylindrical capacitor to be probed electronically.

3.1.4.1 Pt electrode contacts (Georgia Tech)

The following process was used for the samples prepared at Georgia Tech and used in CHAPTER 7, CHAPTER 8, and CHAPTER 11. A light-field mask consisting of 100 μm-, 500 μm-, and 1 mm-diameter circular electrodes in a grid pattern was used. NR9-

1500PY negative photoresist (Futurrex) was spun onto the film at 2000 rpm for 40 s with a ramp time of 2 s (SCS G3 spin coater), and baked on a hot plate at 150 °C for 1 min. Ultra violet (UV) *i*-line (365 nm) exposure was performed using a Karl Suss MA6 mask aligner, with the exposure time calculated to result in a dose of 300 mJ/cm^2 (*dose/intensity = time*). A post-exposure bake (PEB) was performed at 100 °C for 1 min on a hot plate, and the resist was developed in RD6 resist developer (Futurrex) for ~20 s, before rinsing with deionized (DI) water. The samples were then cleaned with a plasma "descum" process consisting of 50 sccm O_2, platen power of 250 W, RF frequency 13.56 MHz, and 60 mTorr chamber pressure for 30 s (Advanced Vacuum Vision RIE) to remove any residual photoresist (PR) from the developed patterning and to increase future top electrode metallization continuity with the film. Approximately 80 nm of Pt was sputter-deposited on the samples (Unifilm Sputterer) at ~200 Å/min. The samples were submerged in acetone to lift off the residual Pt, and if necessary, an ultrasonic bath (VWR) was used for ~1 min to accelerate/complete the lift-off process.

Bottom electrode contacts are formed by etching a corner of the sample with buffered oxide etch (BOE), a 1:6 ratio of 49% HF buffered with ammonium fluoride (NH_4F) (J.T. Baker). A small piece of Kapton polyimide adhesive tape is laid over the corner to protect the center of the film from the BOE. The exposed corner of the chip is a triangular region with sides approximately 2 mm in length. A small cleanroom swab is used to apply a small amount of the BOE solution the corner, and rubbed until it etches through the PZT film to the bottom Pt electrode. This process usually takes several minutes and requires multiple applications of the BOE solution.

3.1.4.2 IrO_2 and Pt top electrode contacts (ARL)

The following processes were used to prepare the top electrode contacts at ARL for the work in CHAPTER 4, CHAPTER 5, CHAPTER 6, CHAPTER 9 and CHAPTER 10. IrO_2 or Pt top electrodes were 100 nm-thick and sputter-deposited onto the wafer at 500 °C. The IrO_2 electrodes were also processed with a post-deposition furnace anneal at 650 °C in flowing O_2 for 30 minutes. The electrode and PZT were patterned via Ar-ion milling, and completed through a series of additional metallization steps for creating proper interconnects to device structures and capacitors. The overall process flow for creation of the test devices is discussed by Proie *et al.*[100] Bottom electrode contacts were also patterned via Ar-ion milling, but were pre-fabricated in the stack before PZT deposition and exposed at the end of the process.

3.2 Structural Characterization Methods

Following the CSD process and fabrication of the necessary components of the material stack, a number of methods are utilized for observing the (micro)structural characteristics of the films, such as X-ray diffraction (XRD), scanning electron microscopy (SEM), and atomic force microscopy (AFM).

3.2.1 X-ray Diffraction Phase Characterization

X-ray diffraction (XRD) methods are rapid, non-destructive analytic techniques typically used for phase identification of crystalline materials, and allowing for quantification of unit cell dimensions and material strain. An incident X-ray beam is generated from a cathode ray tube and filtered to produce a monochromatic radiation, which is then collimated and directed toward the sample. These incident rays interact with the sample to produce constructive interferences and a diffracted ray when the conditions of Bragg's law are satisfied:

$$n\lambda = 2d_{space} \sin\theta \qquad 3\text{-}1$$

where n is the diffraction order (integer), λ is the X-ray wavelength, d_{space} is the lattice spacing of the interrogated solid material, and θ is the diffraction angle. The diffracted X-rays are collected at an angular position equal to two times that of the incident beam, processed, and counted. The counted intensity is plotted as a function of the diffraction angle, and the position of the peaks in the plot correspond to a specific family of atomic planes in the interrogated sample. Using Bragg's law and the locations of the peaks in the XRD trace, the d_{space} can be calculated (Figure 3-7). Generally, powder samples that have been finely ground and homogenized are studied via XRD. However, in the case of ferroelectric thin films studied in this work, their highly-textured nature can make common XRD measurements more difficult, such as determining lattice strain (see CHAPTER 10).

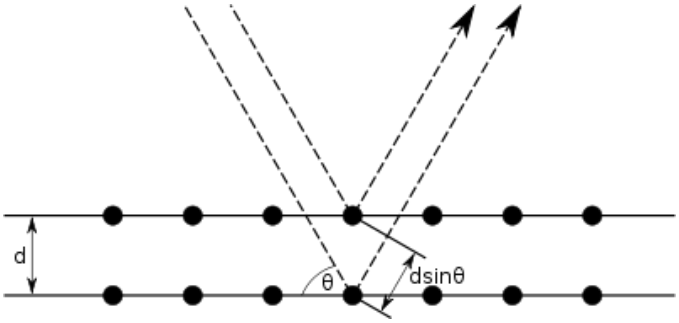

Figure 3-7 Schematic representation of Bragg diffraction with the lattice of an arbitrary material. Incident X-rays are scattered when in contact with atoms, and the diffracted rays are collected and counted for plotting and later phase identification. Image credit: Furiouslettuce.[139]

Standard baseline 2θ XRD scans were performed with a PANalytical Alpha-1, using Cu-Kα radiation. The X-ray source was operated at 45 kV and 40 mA. PZT thin films were scanned across a range of 2θ from 20° to 70°, with a step size ranging from ~0.002° to ~0.02°, depending on the desired resolution, and at a rate of ~10 s/deg. Incident beam optics typically included a 10 mm mask (adjusted larger or smaller as necessary to correspond to sample size), fixed anti-scatter slit at 1°, and a computer controlled divergence slit of 0.5°. The diffracted beam optics employed a 5.5 mm anti-scatter slit, and both the incident and receiving beams were controlled for lateral divergence with a 0.04 radian Soller slit. The 400-Si peak from the substrate was typically used for calibration of the XRD profiles when comparing films' scans, due to the fact that sample tilt on the stage can result in minor variations in raw data.

The Lotgering factor (LF) is a commonly used evaluation of XRD phase data to quantify the degree of orientation and distribution in a polycrystalline sample.[140,141] It is given by:

$$LF = \frac{P_{LF} - P_{LF,0}}{1 - P_{LF,0}} \quad 3\text{-}2$$

where

$$P_{LF} = \frac{I_{(100)} + I_{(200)}}{\sum I_{(hkl)}} \quad 3\text{-}3$$

where $I_{(100)}$ is the intensity of the PZT 100-peak, $I_{(200)}$ is the intensity of the PZT 200-peak, and $\sum I_{(hkl)}$ is the summation of the intensities of all of the PZT peaks in the probed diffraction range. P_{LF} is calculated from the textured PZT thin film samples as measured from the XRD traces, and $P_{LF,0}$ is calculated from unstressed power diffraction files (PDF) for PZT. The PDFs used throughout this work are reported in Table 3-1.

Table 3-1 Table of material and corresponding powder diffraction files (PDF) for materials used in this work.

Material	PDF Number
$Pb(Zr_{0.53}Ti_{0.47})O_3$ (*Tetragonal*)	04-016-2735, ref:[45]
$Pb(Zr_{0.53}Ti_{0.47})O_3$ (*Rhombohedral*)	04-012-8156, ref:[142]
$Pb(Zr_{0.52}Ti_{0.48})O_3$ (*Tetragonal*)	01-070-4060, ref:[143]
$Pb(Zr_{0.52}Ti_{0.48})O_3$ (*Rhombohedral*)	04-011-8861, ref:[144]
Pt (*Cubic*)	04-001-0112, ref:[145]
Ti	00-044-1288, ref:[146]
TiO_2 (*Tetragonal, Anatase*)	01-070-6826, ref:[147]
IrO_2 (*Cubic*)	00-058-0335, ref:[148]
IrO_2 (*Tetragonal*)	04-009-8479, ref:[149]
Au	00-002-1095, ref:[150]

3.2.2 Film Thickness Measurements

The previously-discussed method of exposing the continuous bottom electrode contact via BOE (see Section 3.1.4.1) leaves a physical step from the bottom electrode directly to the surface of the film, allowing for accurate thickness measurements using contact profilometry. Tencor KLA P15 and Veeco Dektak 150 profilometers were used, typically with a scan speed of ~50 μm/s, a sampling rate of ~50 Hz, and taking care to scan a long enough distance to reach a region of the sample towards the center with uniform thickness (on the order of several mm scan distance). Multiple scans were averaged at different locations. Film thickness can also be confirmed via scanning electron microscopy (see Section 3.2.3).

3.2.3 Scanning Electron Microscopy Microstructural Characterization

Films' cross-sectional grain morphology was studied using field-emission scanning electron microscopy (FE-SEM) with a Zeiss Ultra-60 FE-SEM in both in-lens and secondary-lens modes. FE-SEM was performed at accelerating voltages ranging from 2 to 5 kV and current of 10 μA. Samples were often coated with 10 to 20 nm of sputtered Au (Unifilm Sputterer) to mitigate sample charging.

3.2.4 Atomic Force Microscopy Microstructural Characterization

Surface microstructure and morphology was observed using an Asylum Research MFP-3D in contact and tapping modes. Scan sizes ranged from 2 to 20 μm, with scan rates from 0.5 to 1 Hz. 800 mV to 1 V was used as the contact set point. Pt- or Ir-coated tips from Budget Sensors, Olympus, and NanoSensors were used, given that many of the AFM surface scans were performed directly before piezoresponse force microscopy (PFM), which requires an electrically-conductive tip.

3.2.5 X-ray Photoelectron Spectroscopy Depth Profiling

X-ray photoelectron spectroscopy (XPS) is a destructive analysis technique used to determine chemical composition and chemical bonding states of elements present in a sample. XPS spectra are gathered by irradiating the material with a monochromatic X-ray beam and simultaneously measuring the kinetic energy and number of electrons that escape from the surface of the measured material, typically at depths ranging from 1 to 10 nm.[130] This method is often combined with Ar-ion beam etching to iteratively etch to a given depth of the sample, perform XPS measurements, and repeat, thereby effectively probing the chemical composition and elemental species through the thickness of a film. XPS depth profiling was performed on periodically-layered PZT thin films in CHAPTER 7. Data was collected on a ~400 μm-diameter spot size, under vacuum of 10^{-7} Torr. Ar-etching was carried out with a spot size of 1 to 2 mm diameter and an etch rate of ~2 nm/min (depending on desired resolution). Samples were periodically rotated during ion-etching, but rotation was determined not to largely affect the flatness and symmetry of the etched surface.

3.2.6 Transmission Electron Microscopy

The previously-mentioned methods of microstructural characterization (SEM and AFM) allow for observation of surface or cross-sectional microstructure, but are not capable of directly probing individual lattice and ferroelectric domain structures. Transmission electron microscopy does so by transmitting a beam of electrons through a thinned sample (typically < 100 nm thick) and observing the scattering behavior and electron interactions of the sample (Figure 3-8). The work in CHAPTER 5, CHAPTER 6, CHAPTER 7, CHAPTER 10, and CHAPTER 11 employs TEM to observe domain structures, layer crystallization interfaces, and variations/discontinuities in crystallite size and orientation. The individual sample preparation and experimental methods vary in each chapter, and are documented appropriately, but generally involve focused ion beam (FIB) lift-out normal to the surface of the PZT layer. A variety of methods associated with TEM are also employed, including scanning TEM (STEM), energy dispersive X-ray spectroscopy (EDX) to measure compositional fluctuations, high-angle annular dark field (HAADF) imaging, and transmission Kikuchi diffraction (TKD).

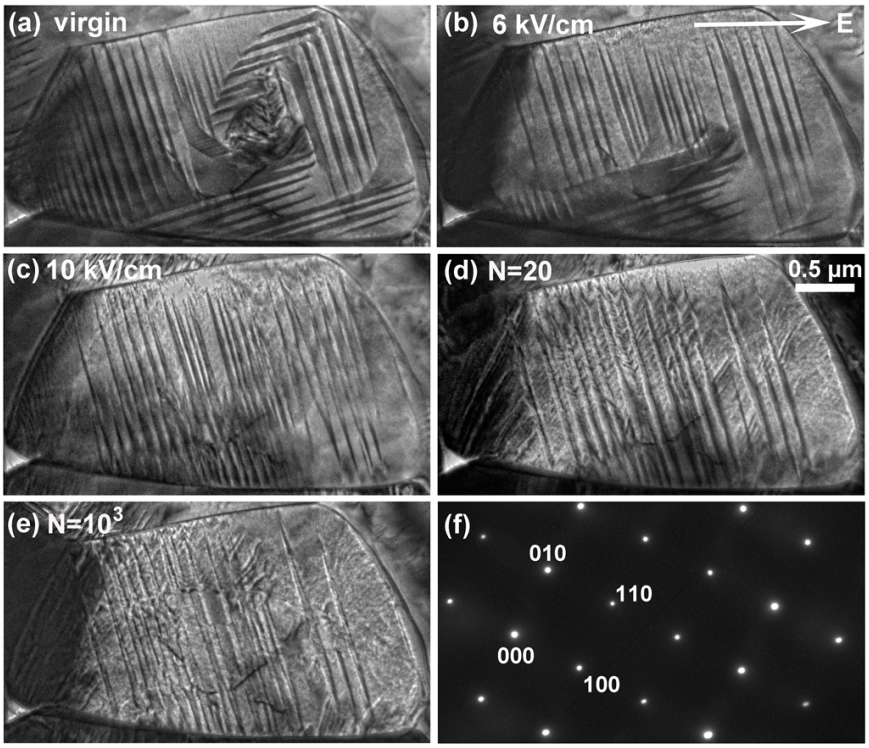

Figure 3-8 Transmission electron microscopy (TEM) observation of a ferroelectric grain along the 001-axis of PZT with clearly-visible domains.[151]

3.2.7 Transmission Kikuchi Diffraction

While TEM is typically used to study structure and chemical composition of a material, it is not able to spatially evaluate grain distribution and orientation, which can be highly beneficial for quantifying and drawing conclusions regarding material microstructure. Electron backscatter diffraction (EBSD) can be performed in an SEM, but spatial resolution is limited to ~20 nm, and insufficient for quantifying many of the fine structures in ferroelectric thin films.[152] Transmission Kikuchi diffraction (TKD), also known as transmission-electron backscatter diffraction (t-EBSD) or transmission electron forward scatter diffraction (t-EFSD), is a method that improves spatial resolution over

EBSD by measuring the forward-scattering near the back surface a specimen typically prepared in a similar manner to TEM samples, *i.e.*, thinned to < 100 nm for transmission and diffraction of electrons. TKD provides much better spatial resolution than EBSD, down to 2 to 5 nm. Inelastic scattering of the electron beam by the sample produces electrons traveling in all directions, but those traveling in specific (*hkl*) directions are called Kikuchi bands. Indexing the Kikuchi bands can resolve orientation and crystal structure in the sample. Figure 3-9 shows band contrast images and the indexed TKD images, showing distinct grain orientations and distributions in CeO_2 thin films. This information can be very useful for studying the in-plane uniformity of grains in thin films (see CHAPTER 6).

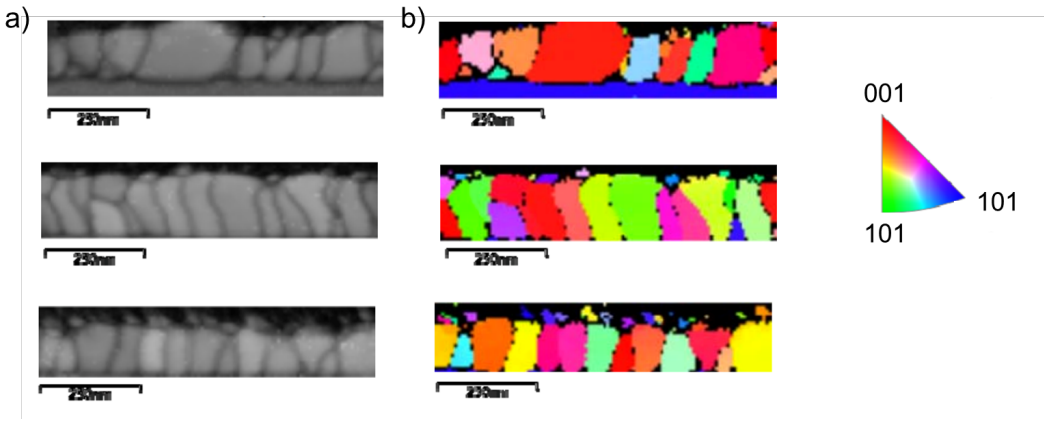

Figure 3-9 (a) Cross-sectional band contrast maps and (b) transmission Kikuchi diffraction (TKD) maps in the out-of-plane direction of CeO_2 thin films. Images courtesy of Hanhan Zhou, North Carolina State University.

For the TKD measurements in this work, focused ion beam (FIB) milling was used to prepare thin specimens, after which they were sputter-coated with 20 nm of Au to increase sample conductivity and mitigate drift during imaging. A 3 µm-thick Pt layer was also deposited on the sample surface before FIB milling under FEI Quanta 3D FEG to protect the sample surface from potential electron and ion damage. Cross-sectional TKD

samples were prepared using FEI Quanta 3D FEG which employs both electron and ion beam guns (SEM/FIB). TKD imaging was performed on the FIB samples using an Oxford Instruments NordlysNano Electron Backscatter Diffraction (EBSD) detector. Kikuchi diffraction patterns were acquired at 30 kV with the Oxford Instruments Aztec software. TKD data was processed using the HKL CHANNEL5 program Tango. Kikuchi images for the PZT were indexed to both cubic and tetragonal phases of the perovskite structure, showing details of the grain orientation in the probed films.

3.3 Functional Response Characterization

The widespread implementation of ferroelectric thin films in a vast array of MEMS and microelectronics applications is primarily due to their large multifunctional dielectric, ferroelectric, and piezoelectric responses. The characterization of these functional responses as a function of processing parameters, material stack variations, and experimental radiation conditions is thus paramount to the work in this thesis. Both macroscopic and microscopic methods are discussed in detail, with general measurement parameters outlined here, but further detailed in the individual chapters. Characterization methods are presented in the order in which they are generally performed on fabricated PZT samples in all chapters of this thesis. All measurements were performed at room temperature and ambient conditions.

3.3.1 Low-field Relative Dielectric Permittivity and Loss Tangent

The relative dielectric permittivity, ε_r, and loss tangent, *tan(δ)*, are measured at low applied AC electric field, before the onset of irreversible extrinsic contributions to the dielectric response, such as those by nonlinearly- and hysteretically-mobile domain walls (see Section 2.5). At low electric field, intrinsic lattice effects and the reversible vibration of domain walls dominate the dielectric response. All measurements of the low-field dielectric permittivity in this work were performed at 100 mV and 1 kHz using an Agilent 4284A precision LCR meter with a long integration time. The LCR meter measures the capacitance of the parallel-plate metal-ferroelectric-metal sandwiched capacitor (Figure 3-6), which is then converted to dielectric permittivity using the expression for capacitance of a parallel plate capacitor:

$$C = \frac{\varepsilon_r \varepsilon_0 A}{d} \qquad 3\text{-}4$$

where C is the measured capacitance, ε_r is the relative dielectric permittivity, ε_0 is the permittivity of free space, A is the cross-sectional area of the (typically cylindrical) ferroelectric capacitor being interrogated, and d is the thickness of the dielectric media (ferroelectric thin film).

The dielectric loss tangent quantifies a dielectric material's intrinsic dissipation of electromagnetic energy (as opposed to storage as a capacitor in the dielectric media). δ is the loss angle, and refers to the phasor in the complex plane whose real component is resistance (lossy) and imaginary component is reactive (lossless). *tan(δ)* is also often called the dissipation factor. Measurements of *tan(δ)* were performed simultaneously with the

capacitance measurements at 100 mV and 1 kHz using an Agilent 4284A precision LCR meter with a long integration time, and recorded to the thousandth place. The loss tangent is often reported as a percentage.

3.3.2 Polarization-Electric Field Hysteresis Loops

Polarization hysteresis loops are the hallmark feature of ferroelectric materials. In this work, polarization-AC electric field (*P-E*) hysteresis loops were obtained using a Radiant Technologies P-PM2 ferroelectric test system, using a bipolar sine wave at 100 Hz or 1 kHz, up to fields ranging from 100 to 1000 kV/cm. The *P-E* loops were analyzed to determine the remanent polarization (P_{rem}), saturation polarization (P_{sat}), positive and negative coercive fields (E_{C+} and E_{C-}), and loop areas. The vertical shift in the *P-E* loop, $\Delta P/2$, is calculated using the formula

$$\Delta P/2 = \frac{P_{rem+} + P_{rem-}}{2} \qquad 3\text{-}5$$

where P_{rem+} and P_{rem-} are the values of the positive and negative remanent polarization, respectively. Similarly, the horizontal shift of the electric field in the *P-E* (and $d_{33,f}$-E_{DC}, discussed later) hysteresis loops is determined by

$$E_{internal\ bias} = \frac{E_{C+} + E_{C-}}{2} \qquad 3\text{-}6$$

where E_{C+} and E_{C-} are the positive and negative coercive fields, respectively. Notably, when running a single period of the applied waveform, prior relaxation of the sample's polarization can result in a loop that starts at $\sim P = 0$, but the loop terminates at a nonzero value of P, resulting in an open loop discontinuity and making extraction of polarization properties and coercive field difficult or unreliable. This effect is rectified by running two consecutive loops on the tool (without breaking in between), and analyzing the continuous loop from the second period of the applied waveform.

3.3.3 Nonlinear AC Electric Field-Dependent Dielectric Permittivity

The AC electric field dependence of the dielectric permittivity response elucidates the intrinsic and extrinsic contributions to the response, as discussed in Section 2.5. The capacitance and dissipation factor of the films were measured at AC electric field from ~1 kV/cm up to the coercive field (E_C) (typically 20 to 50 kV/cm) at 1 kHz. The capacitance was converted to dielectric permittivity using Equation 3-4 and plotted as a function of applied AC electric field. From the plot, the sub-coercive, linear, Rayleigh region was identified (see Figure 2-11) and fitted with a least-squares linear regression, and the slope and intercept extracted, according to Equation 2-7. This analysis yields the reversible Rayleigh parameter, ε_{init}, the intercept of the linear permittivity curve; and the irreversible Rayleigh parameter, α, the slope curve. ε_{init} describes intrinsic contributions to the dielectric response such as lattice vibration as well as low field, reversible extrinsic contributions; while α designates extrinsic contributions to the dielectric response, *e.g.,* from irreversible domain wall and phase boundary motion.

3.3.4 DC Electric Field-Dependent Dielectric Permittivity

Measurements of the dielectric permittivity as a function of applied DC electric field allow for further investigation of domain wall motion and extrinsic contributions to the dielectric response. Ferroelectric domain walls move with application of a DC field, and by superimposing a small AC amplitude over the DC bias, small oscillatory motions of the walls (*i.e.*, vibrations) will result.[153] Additionally, measurements of the dielectric permittivity as a function of DC electric field allow for extraction of the dielectric tunability, a useful parameter for gauging the versatility of a dielectric material for use in filters and frequency-agile radio-frequency (RF) circuits, which leverage the pronounced variability in dielectric permittivity as a function of applied DC field.

Measurements of the DC electric field-dependent dielectric permittivity (ε_r-E_{DC}) were typically performed up to maximum fields of 200-400 kV/cm with an overlapping small-signal 100 mV at 1 kHz. The overlapping small signal should not exceed the coercive voltage of the sample. If these measurements are combined with the converse, effective longitudinal piezoelectric response (Section 3.3.5), an overlapping small-signal voltage of ~1 V is typically appropriate. The dielectric tunability is calculated using the expression

$$dielectric\ tunability = \frac{\varepsilon_{DC,max} - \varepsilon_{DC,min}}{\varepsilon_{DC,max}} \tag{3-7}$$

where $\varepsilon_{DC,max}$ and $\varepsilon_{DC,min}$ are the maximum and minimum values of the dielectric permittivity under DC field measurements, respectively. The dielectric tunability is often reported as a percent, and a value approaching unity signifies greater utility for filter

applications. In the literature, the ε_r-E_{DC} hysteresis loops are often called *C-V* loops, derived from the raw capacitance-voltage data obtained from the measurement.

3.3.5 Macroscopic Converse, Effective Longitudinal Piezoelectric Response

Measurements of the piezoelectric response in ferroelectric thin films can be performed by quantifying either the direct or converse piezoelectric effects, through charge measurements or strain/displacement measurements, respectively. In this thesis, the converse piezoelectric effect is measured with high-resolution double beam laser interferometry (DBLI). For measurements of the piezoelectric coefficients, a coordinate system is defined, where the *x*-, *y*-, and *z*-directions are conventionally referred to by the numbers 1, 2, and 3, respectively.[2] Subscripts of the measured piezoelectric coefficient (d_{ij}, e_{ij}, g_{ij}, h_{ij}) can be defined in a Cartesian coordinate system where *i* corresponds to poling axis and *j* refers to the measurement axis (Figure 3-10). In this work, the converse longitudinal piezoelectric coefficient, d_{33}, was measured to quantify piezoelectric response in the out-of-plane direction, *i.e.*, normal to the surface of the substrate/thin film. However, polycrystalline ferroelectric thin films contain a wide array of domain structures, grain orientations, defects, residual substrate clamping, *etc.* that affect the measurements of the pure piezoelectric coefficients.[2] Thus, the piezoelectric measurements on thin films are denoted as "effective" measurements thereof, and the converse, effective longitudinal piezoelectric response is accordingly designated as $d_{33,f}$. From the measurements of $d_{33,f}$ are extracted the remanent ($d_{33,f,remanent}$ or $d_{33,f,rem}$) and mean saturation values ($d_{33,f,saturation}$

or $d_{33,f,sat}$) of the piezoelectric response, and in certain cases, the horizontal shift of the coercive field in the $d_{33,f}$-E_{DC} hysteresis loops is calculated according to Equation 3-6.

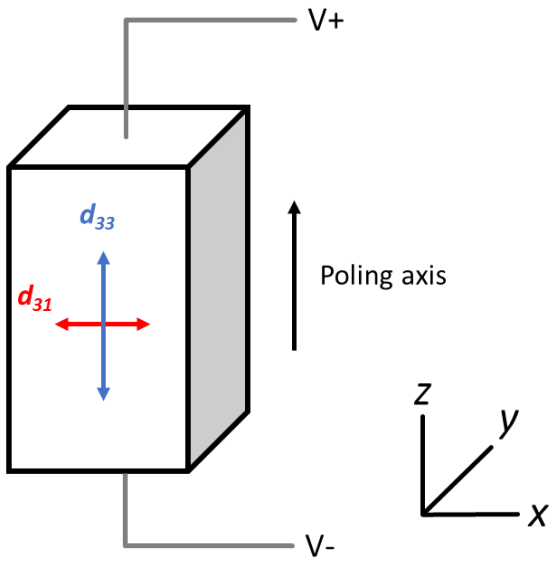

Figure 3-10 Schematic representation of a sample with electrodes on the top and bottom faces, showing the poling and measurement axes and corresponding subscripts for the piezoelectric coefficients. Note that d_{ij}, is shown, but could be substituted for the other three piezoelectric coefficients.

Measurements of the converse, effective longitudinal piezoelectric response ($d_{33,f}$) as a function of DC field ($d_{33,f}$-E_{DC}) were performed on an aixACCT double beam laser interferometer (DBLI), typically to maximum electric field of ~200 to 400 kV/cm with an overlapping AC signal $V_{AC} \approx 0.5V_C$ (~1 V in most cases). The DBLI system measures the electric field-induced differential displacement of the two major surfaces of the sample (top electrode and bottom surface of the substrate). A laser is split and merged at several critical locations (see Figure 3-11) in the path, and the constructive/destructive interference of the beam is calibrated to displacement of the sample with application of electric field. Compared to single beam interferometry, which only measures the top surface

displacement, DBLI effectively eliminates contributions from the bending of the substrate induced by the piezoelectric thin film. A measurement of the total hysteretic displacement as a function of applied AC electric field also leverages the DBLI method and is often called a "butterfly loop."

The use of DBLI requires that the two measurement surfaces of the sample are highly reflective. The sputtered Pt top electrodes satisfy this condition, as does the use of double-side polished (DSP) wafers during the CSD process for the bottom surface. However, samples prepared on single-side polished (SSP) wafers must be backside-polished prior to testing. Polishing was performed after the CSD and top electrode patterning, by masking the top side with SPR-220 photoresist (PR), spun at ~1000 rpm for 1 min, and baked for ~4 min, or until the PR is hard to the touch with tweezers after removing from the hot plate and allowing to cool. The samples were then polished manually on a rotary polishing wheel with 1 μm, 0.3 μm, and 0.05 μm Al_2O_3 powders, until a mirror polish was achieved. Photoresist was stripped in acetone and rinsed with IPA.

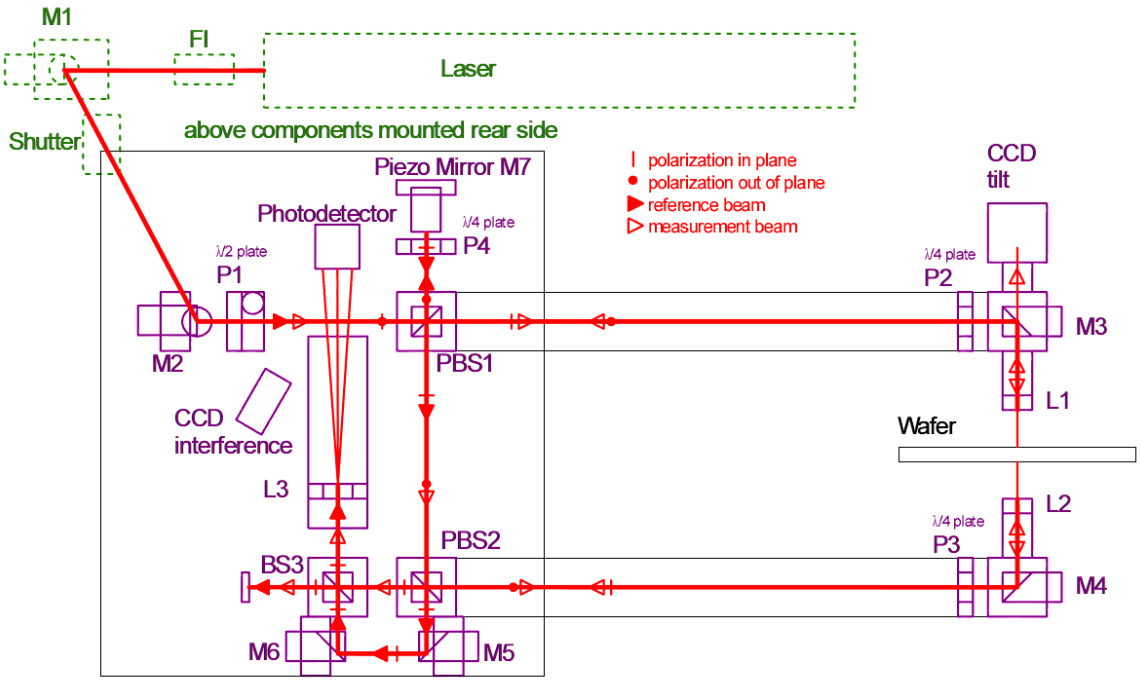

Figure 3-11 Schematic diagram of the aixACCT double beam laser interferometer (DBLI). M = mirror, BS = beam splitter, PBS = polarizing beam splitter, P = plate, L = lens, CCD = charge coupled device. Image credit: aixACCT Systems GmbH.[154]

3.3.6 Piezoresponse Force Microscopy

While measurements of the macroscopic piezoelectric response allow for an effective measurement of the "aggregated" macroscopic material properties,[2] characterization of the local piezoelectric response at individual grain and domain locations can provide an interesting picture of local functional response as a function of microstructure and morphology (Figure 3-12).

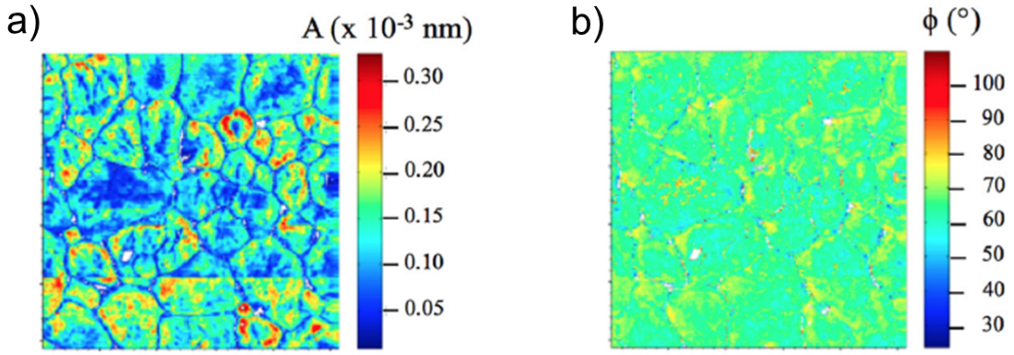

Figure 3-12 Band-excitation piezoresponse force microscopy (BE-PFM) (a) amplitude and (b) phase performed on highly 100-textured relaxor ferroelectric PMN-PT thin films, showing distinct grain morphology and the enhancement of local piezoresponse in annular regions near individual grain boundaries.[155]

Piezoresponse force microscopy (PFM) is performed on an AFM system with an applied bias through a conductive probe tip to interrogate the sample. The displacement of the PFM probe tip as it responds with the film and the applied tip bias allows for characterization of a variety of dielectric and piezoelectric properties, including local polarization state/direction (Figure 3-13). However, PFM is not able to accurately quantify the magnitude of material strain, as the tip/film contact is heavily affected by the surface topography, nonuniform electric field distribution, probe tip wear, *etc.* The continuous bottom Pt electrode is electrically grounded and used as the bottom electrode for PFM. Multiple types of PFM measurements are performed in the work presented in this thesis, including those at a single measurement frequency, dual amplitude resonance tracking (DART) PFM, band-excitation PFM (BE-PFM), switching spectroscopy PFM (SS-PFM), and band-excitation switching-spectroscopy PFM (BE-SSPFM).

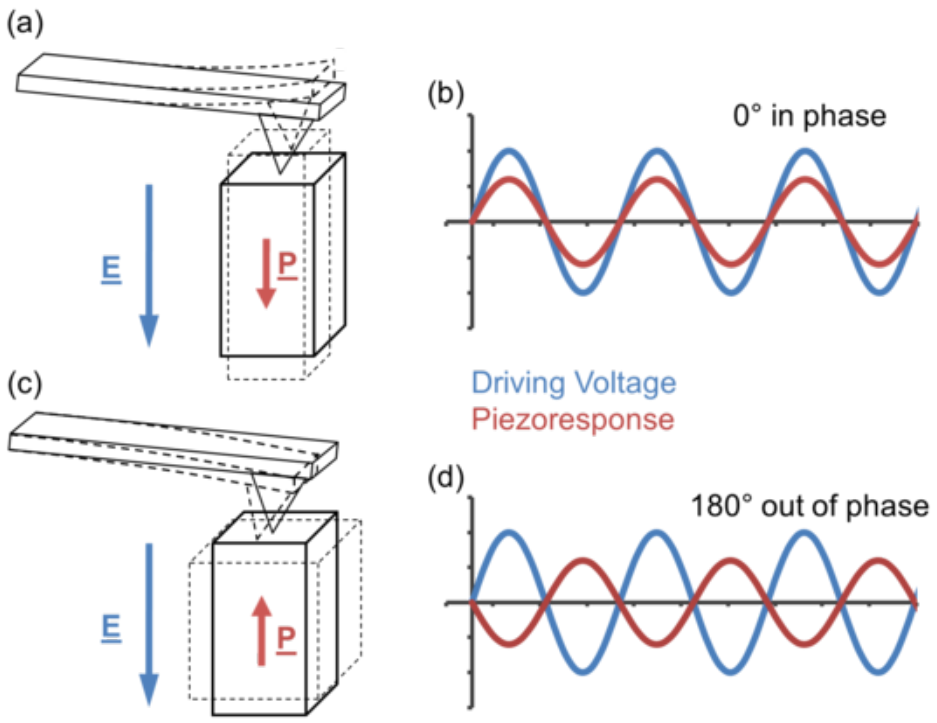

Figure 3-13 Schematic representation of PFM probe tip interaction with a piezoresponsive material. (a) shows the interaction of the tip where the applied electric field (*E*) vector aligns with the polarization direction (*P*), and resulting (b) in-phase measurement. (c) shows the case where the applied field direction is anti-parallel to the polarization direction, resulting in an (d) out-of-phase response. Image credit: Tertib64.[156]

3.3.6.1 Single-frequency PFM

The interaction between the ferroelectric material and the conductive PFM probe tip is frequency-dependent, and results in a resonant mode with an applied bias, typically on the other of several hundred kHz for the PZT thin films studied in this work. This resonance can be leveraged to increase the signal-to-noise ratio (SNR) of the piezoresponse measurement. Single-frequency PFM applies the tip bias at a given frequency near resonance, but the resonant frequency is subject to change based on sample morphology

and local response variability, potentially making the SNR inconsistent, and rendering the phase of the piezoresponse difficult to track in some cases. Single-frequency PFM was performed on the same Asylum Research MFP-3D used for AFM measurements, (Section 3.2.4), typically with Pt- or Ir-coated PFM probe tips from BudgetSensors, Olympus, and NanoSensors. Contact set point was 800 mV to 1 V, scan frequency was 0.5 to 1 Hz, and scan area was 2 to 20 μm.

3.3.6.2 Dual Amplitude Resonance Tracking PFM

Dual amplitude resonance tracking (DART) PFM relies on tracking the resonance of the PFM tip-ferroelectric interaction with two lock-in amplifiers, allowing for dynamic monitoring and more consistent scans of the piezoresponse (Figure 3-14). DART mode measurements were performed on Asylum Research MFP-3D, with similar measurement parameters to those used for single-frequency PFM. DART PFM provides a significant improvement over single-frequency PFM, with no time penalty. However, the system can lose track of the resonance peak, or it can become weak in samples of low response.

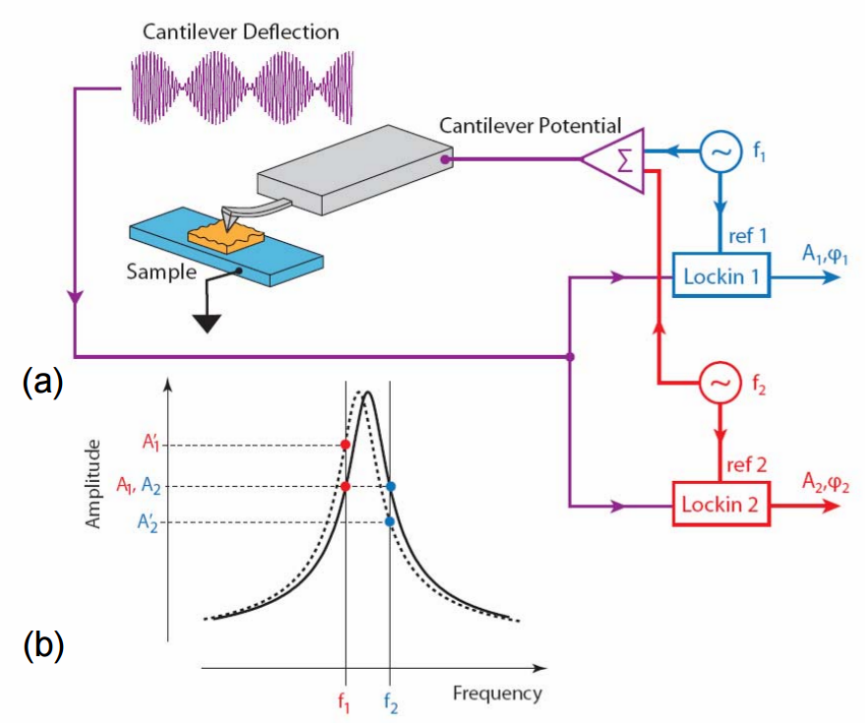

Figure 3-14 (a) Schematic representation of the DART PFM system set up with two lock-in amplifiers to track the tip-ferroelectric resonance. (b) The resonance peak and the tracking thereof by the two lock-in amps is shown.[157]

3.3.6.3 Band-excitation PFM

Interrogation of the sample with an AC electric field across a band of frequencies (band-excitation, BE-PFM) is a more reliable way to study the piezoresponse behavior in PFM measurements, and can provide striking information regarding the local piezoresponse (Figure 3-12). The BE waveform is generated and applied to the sample. The cantilever response is collected and the Fourier transform at each pixel/tip location is performed, yielding the transfer function of the cantilever response. This response is fit to a simple harmonic oscillator (SHO) and yields the amplitude, phase, resonance frequency, and quality factor of the interaction.[158] BE-PFM requires expensive equipment, robust

fitting software, and is more time-consuming than DART and single-frequency methods. BE-PFM was performed at Oak Ridge National Laboratory Center for Nanophase Materials Sciences, and at University College Dublin; the specifics of such experiments are outlined in respective chapters.

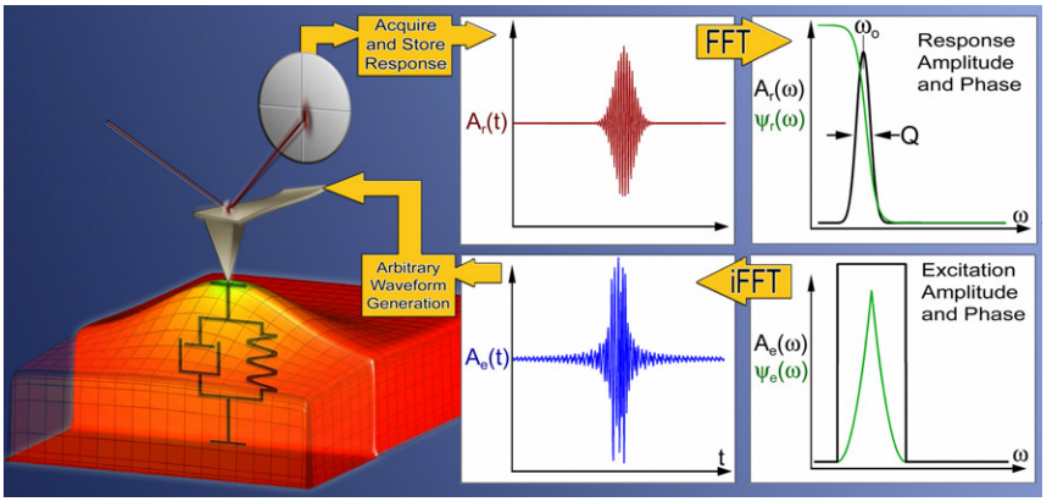

Figure 3-15 Schematic demonstrating the principle of band-excitation piezoresponse force microscopy (BE-PFM). An electric field is generated and applied to the sample across a band of frequencies. The cantilever response is collected and the Fourier transform at each pixel/tip location is performed, yielding the transfer function of the cantilever response. This response is fit to a simple harmonic oscillator (SHO) and gives the amplitude, phase, resonance frequency, and quality factor of the interaction. [158]

3.3.6.4 Switching Spectroscopy PFM

The previous methods pertaining to PFM are useful for areal scans of the material and observing the amplitude and phase of the piezoresponse across those regions, allowing for correlation of the piezoresponse to microstructure and morphology. However, the local hysteretic switching behavior, including coercive field, imprint, and remanent/saturation

responses are important for studying and engineering materials at the micro-/nano-scale. Switching spectroscopy PFM (SS-PFM) applies a bias to a local region of the material and collects the hysteretic piezoresponse strain at that point with the PFM cantilever, allowing for extraction of local response parameters, as well as construction of an area map of the material showing changes in local responses.[159] SS-PFM can be integrated with both DART PFM and BE-PFM methods; details of these experiments are discussed in appropriate chapters.

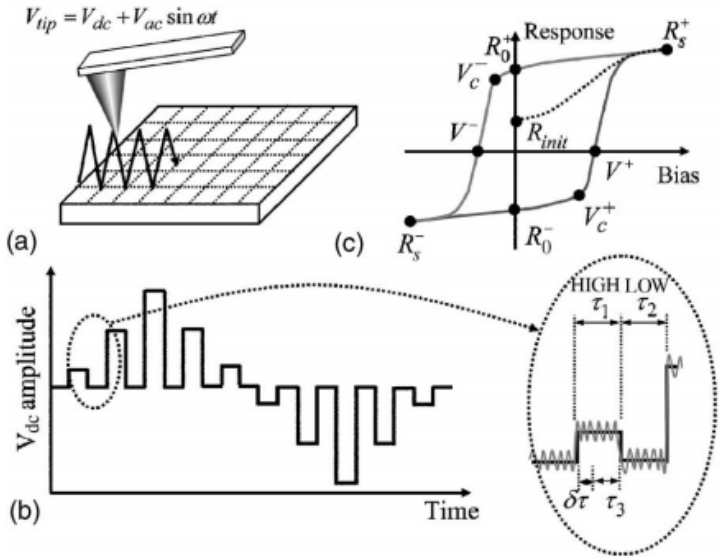

Figure 3-16 Diagram illustrating switching-spectroscopy piezoresponse force micrsocopy (SS-PFM). (a) shows the interaction of the tip with the material surface, and the application of (b) electric field waveform, allowing for extraction of (c) the local hysteresis behavior and related response parameters.[159]

3.4 Gamma Radiation Exposure

The majority of the work in this thesis deals with the effects of ionizing radiation and total ionization dose (TID) studies involving gamma radiation. Gamma rays are photons generated from the radioactive decay of atomic nuclei, and are the most energetic form of electromagnetic radiation (> 100 keV). Typical wavelengths are less than 10 picometers and frequencies above 10 exahertz (10^{19} Hz). Due to the prevalence of gamma radiation in space (related to satellite and communications applications) and as the most energetic form of photonic, penetrating irradiation, it was selected for the studies in this thesis. Gamma irradiations were performed at the US Naval Research Laboratory, using a ^{60}Co source (Figure 3-17), which produces radiation with energies of approximately 1.25 MeV. The geometry of the ^{60}Co gamma source surrounds the sample, resulting in an isotropic exposure, thus eliminating any effects of radiation directionality. Doses were typically spaced semi-logarithmically, at 0.2, 0.5, 1.0, 2.0, 5.0, 10.0, and (in one experiment in CHAPTER 8) 20 Mrad equivalent Si dose, at a dose rate of ~600 rad(Si)/s. All electrodes were left floating during radiation exposure. All samples were functionally characterized within one week of irradiation to minimize the transient effects of aging or recovery in the samples.

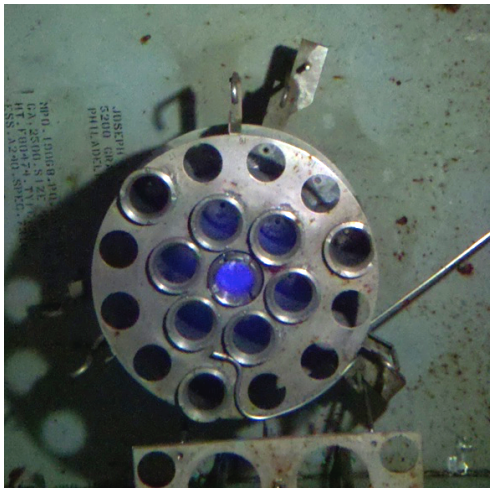

Figure 3-17 Image of the ^{60}Co source used in this work, located at the US Naval Research Laboratory (NRL). Image courtesy of Cory D. Cress, US Naval Research Laboratory

3.5 Membrane Microfabrication Process

The microfabrication process for preparation of the "membrane" samples used in CHAPTER 11 is a relatively complex process with multiple fabrication steps that are documented here for completeness and future work reference.

3.5.1 Substrate Preparation

Specifics of individual substrates used are available in CHAPTER 11. Both 300 µm- and 500 µm-thick, 100 mm-diameter 100-Si p-type, double-side polished (DSP) wafers with 500 nm to ~1.3 µm thermal SiO_2 (Tystar Tytan Mini) were used. A 20 nm Ti adhesion layer and 80 nm Pt bottom electrode layer were sputtered (Unifilm Sputterer) at ~200 Å/min. The platinized top side of the wafer was spin-coated with SPR-220 photoresist

(PR) (MicroChem) at 300 rpm for 20 s and 1000 rpm for 45 s in a continuous step (SCS G3 spin coater). The wafer was baked at 115 °C for 5 min, and Mask 1, consisting of parallel dicing marks and topside alignment marks, was exposed to a dose of 1200 mJ/cm^2 (Karl Suss MA-6, *i*-line 365 nm). No post-exposure bake was performed, but a wait step of ~60 min was necessary to allow for proper cross-linking of the PR polymer. The wafer was then developed in MF 319 developer (MicroChem) for ~4-5 min, and a final oven bake at 100 °C for 30 mins was performed. The dicing marks were etched through the Pt layer, using a PlasmaTherm inductively coupled plasma (ICP) tool with 8 sccm Cl and 32 sccm Ar, a chamber pressure of 10 mTorr, coil power of 600 W, platen power of 250 W, and 5 min etch time. Residual photoresist was dissolved in acetone. This process created the topside dicing marks and alignment marks for the backside alignment (Figure 3-18a)

The backside alignment process opened the windows in the backside SiO_2 for eventual backside Si plasma etching. The bottom side of the wafer (SiO_2 only) was spin-coated with SPR-220 photoresist (PR) (MicroChem) at 300 rpm for 20 s and 1000 rpm for 45 s as a continuous step (SCS G3 spin coater). The wafer was baked at 115 °C for 5 min, and Mask 2, consisting of large backside openings (approximately 1 cm × 1 cm) was exposed to a dose of 1200 mJ/cm^2 (Karl Suss MA-6, *i*-line 365 nm). The mask was aligned to alignment marks at positions indicated in Figure 3-18b. No post-exposure bake was performed, but a wait step of ~60 minutes was again necessary to allow for proper cross-linking of the PR polymer. The wafer was then developed in MF 319 developer (MicroChem) for ~4-5 min, and a final bake in an oven at 100 °C for 30 min was performed. At this point, the wafer shows square openings in the PR to the SiO_2 layer on the backside (Figure 3-18b).

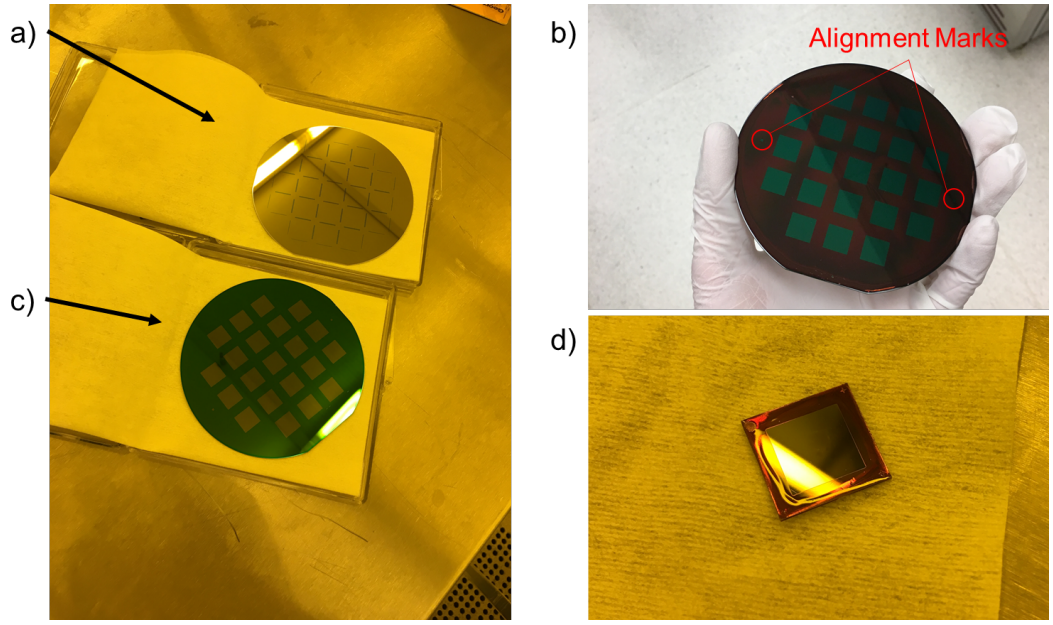

Figure 3-18 Images of intermediate steps of the membrane processing. (a) shows the topside dicing marks after etching in the Pt/Ti layer. (b) shows the backside of the wafer with SPR-220 photoresist (PR), after backside alignment and PR development, but before the SiO_2 etch. (c) shows the backside of the wafer after plasma etching of SiO_2 and PR removal, directly before the dicing step. (d) shows an individual PR-masked chip before backside DRIE etching of the Si substrate.

The backside of each wafer was then etched to selectively remove the SiO_2 from the patterned square openings using an Advanced Vacuum Vision RIE with 45 sccm CHF_3, 5 sccm O_2, platen power of 250 W, RF frequency 13.56 MHz, and 45 mTorr chamber pressure, resulting in an etch rate of approximately 20 nm/min. Residual PR was removed in acetone; an image of the wafer at this point in the process is shown in Figure 3-18c.

At this point, the wafer is either (i) diced, then PZT deposited via CSD, and top electrodes fabricated, or (ii) PZT deposited on the whole wafer, top electrodes fabricated, then diced. Dicing was done by GT IEN cleanroom staff; the wafer was protected beforehand from residual Si particles by spinning a thin layer of NR9-1500PY on Pt topside and hardening, according to the process in Section 3.1.4.1. Specifics of the PZT depositions

can be found in CHAPTER 11; multi-layer anneal (MLA) films with a target thickness of ~1 μm were deposited. Top electrodes were fabricated via photolithography using Mask 3. In the case of the remote electrode map (see CHAPTER 11), SC 1827 photoresist (Microposit) was used, spun at 1000 rpm for 10 s with a 1.5 s ramp, transition to 3000 rpm for 40 s with a 2.5 s ramp (SCS G3 spin coater), soft baked for 60 s at 115 °C, exposed to a dose of 240 mJ/cm^2 (Karl Suss MA-6, *i*-line 365 nm), and developed in MF 319 for 40 s. In case (i), alignment marks exist in all 4 corners of each individual die, and top side alignment is possible. In case (ii), the standard alignment marks for the whole-wafer process, as indicated in Figure 3-18b, were used for topside alignment.

Individual chips were, at this point, nearly ready for backside etching of the Si substrate. However, the thickness of the Si substrate was 300 to 500 μm, and the SiO_2 mask around the edges of the backside of each chip was 500 nm to 1.3 μm thick. The selectivity of the Si plasma etch is ~100:1 Si to SiO_2, meaning that there is not enough SiO_2 thickness to act as a hard-mask for the full backside through-etch of the Si substrate. Thus, SPR-220 was again applied to the back side of each chip, according to the same process as described above for backside patterning. Individual chips were then exposed, again using Mask 2 to open a window in the PR directly above the window that was previously etched in the SiO_2, thus leaving a thick layer of SPR-220 directly over the SiO_2, to act as a mask during the Si etching (Figure 3-18d). This masking process via alignment of Mask 2 was performed only for the first backside Si etch. The first Si etch typically resulted in enough of a depth differential that subsequent masking was possible by simple brushing of SPR-220 around the frame with a cleanroom swab, and hardening on the hot plate, in order to avoid the lengthy photolithography process. This PR hard mask was eventually discovered to

contribute to re-deposition of the etched PR on the backside of the membrane during etching, resulting in a pitted and/or "grass-like" surface. In later experiments, the edges of the chip were masked with Kapton tape instead of PR, which alleviated this problem.

3.5.2 Backside Plasma Etching of the Si Substrate

The PR-hard-masked samples were adhered using Cool Grease vacuum grease to a Si carrier wafer with a thick layer of grown thermal SiO_2. Samples were etched in an STS ICP using both a Bosch process deep reactive ion etch (DRIE) as well as a nearly isotropic DRIE Si etch for later experiments. The Bosch process, also known as a "pulsed" or "time-multiplexed" etch, alternates cycles between a nearly isotropic plasma etch of SF_6 and a chemically inert passivation layer (C_4F_8, similar to Teflon), which coats the sidewalls and base of the etch. The semi-directional nature of the ions from the subsequent cycle of SF_6 essentially sputters off the base of the chemically inert layer, while the sidewalls remain relatively intact (Figure 3-19a). The cyclic process results in scalloped sidewalls shown in Figure 3-19b. Parameters of the etch process used for this work are shown in Table 3-2, and experimental data estimating the etch rate is available in Figure 3-20.

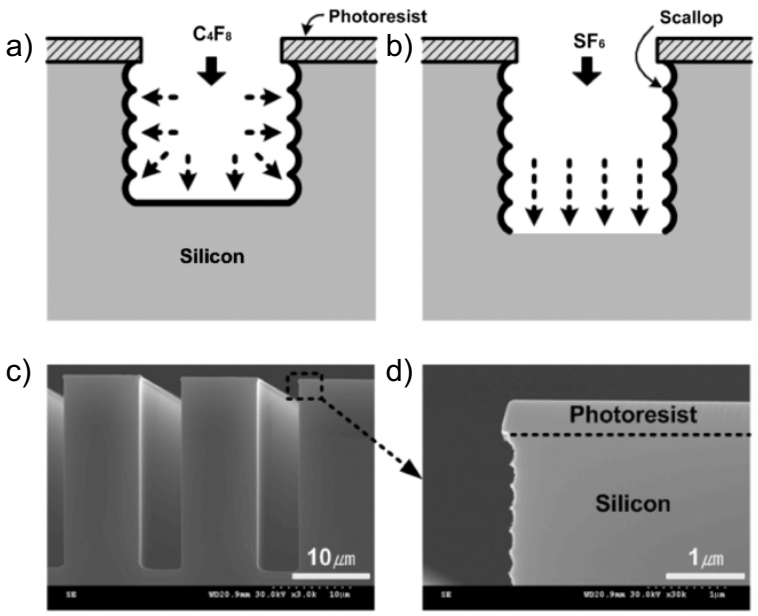

Figure 3-19 Schematic of the Bosch DRIE process, showing (a) organofluorine passivation layer, (b) the semi-isotropic SF_6 etch, (c) high aspect ration trenches, and (d) scalloped sidewalls resulting from the iterative process.[160]

After several iterations of membrane samples using the Bosch DRIE process, it was observed that the interior corners of the backside of the membrane were etching through before the center portion of the membrane. It was hypothesized that this effect was observed due to the cyclic etch process. A pure SF_6 etch was employed for remaining experiments, with somewhat improved results. Notably, the pure SF_6 etch resulted in a smoother backside surface and more rounded edge transitions from the vertical sidewall to the horizontal backside surface of the membrane, potentially resulting in less intense stress risers at those locations. Parameters of the etch process used for this work are available in Table 3-2, and experimental data estimating the etch rate is shown in Figure 3-20. Measurements of the etch depth were performed with the Tencor KLA P15 and Veeco Dektak 150 profilometers (see Section 3.2.2). Measurements of membrane deflection and

bowing due to strain induced by the electrodes was performed with a Veeco Wyko NT2000 white light, non-contact interferometer (see CHAPTER 11).

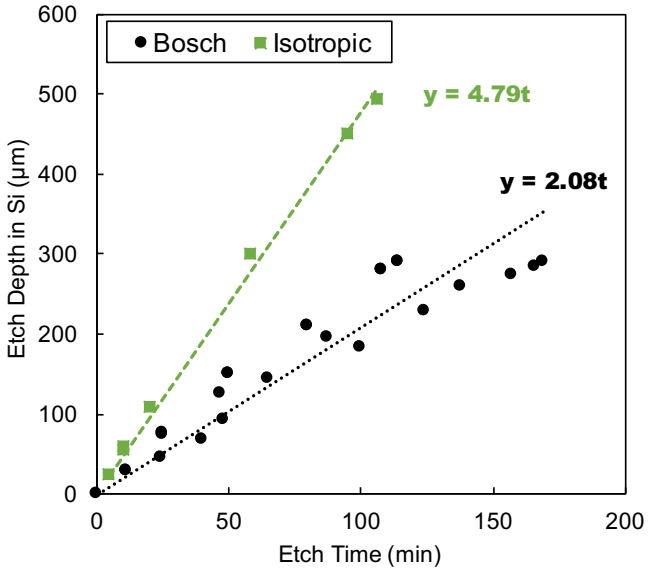

Figure 3-20 Plots of measured etch depth in Si as a function of etch time for both the anisotropic Bosch process and isotropic DRIE etches used in this work, with trendlines fitted to estimate the etch rate.

Table 3-2 Parameters for the isotropic and Bosch process DRIE etches, and the estimated etch rate per minute derived from experimental data.

	Isotropic DRIE	Bosch Process DRIE	
	Etch	Etch	Passivation
Cycle time (s)	∞	11	8
Pressure (mTorr)	0.1	0.1	0.1
SF_6 flow (sccm)	130	130	--
C_4F_8 flow (sccm)	--	--	90
O_2 flow (sccm)	13	13	--
Coil power (W)	600	800	800
Platen power (W)	10	17	0
Etch rate (µm/min)	**4.8**	**2.1**	

CHAPTER 4. ELECTROMECHANICAL INTERFACE AT THE FERROELECTRIC-ELECTRODE BOUNDARY

The content in this chapter has been published in the *Journal of Applied Physics*.[32]

Effect of Top Electrode Material on Radiation-Induced Degradation of Ferroelectric Thin Film Structures

Steven J. Brewer, Carmen Z. Deng, Connor P. Callaway, McKinley K. Paul, Kenzie J. Fisher, Jonathon E. Guerrier, Ryan Q. Rudy, Ronald G. Polcawich, Jacob L. Jones, Evan R. Glaser, Cory D. Cress, Nazanin Bassiri-Gharb

Journal of Applied Physics, vol. 120, no. 2, (2016), doi: 10.1063/1.4955424

4.1 Summary

The effects of gamma irradiation on the dielectric and piezoelectric responses of $Pb(Zr_{0.52}Ti_{0.48})O_3$ (PZT) thin film stacks were investigated for structures with conductive oxide (IrO_2) and metallic (Pt) top electrodes. The samples showed, generally, degradation of various key dielectric, ferroelectric, and electromechanical responses when exposed to 2.5 Mrad(Si) ^{60}Co gamma radiation. However, the low-field, relative dielectric permittivity, ε_r, remained largely unaffected by irradiation in samples with both types of electrodes. Samples with Pt top electrodes showed substantial degradation of the remanent polarization and overall piezoelectric response, as well as pinching of the polarization hysteresis curves and creation of multiple peaks in the permittivity-electric field curves post irradiation. The samples with oxide electrodes, however, were largely impervious to the same radiation dose, with less than 5% change in any of the functional characteristics. The results suggest a radiation-induced change in the defect population or defect energy in PZT with metallic top electrodes, which substantially affects motion of internal interfaces such as domain walls. Additionally, the differences observed for stacks with different electrode materials implicates the ferroelectric-electrode interface as either the predominant source of radiation-induced effects (Pt electrodes) or the site of healing for radiation-induced defects (IrO_2 electrodes).

4.2 Introduction

Perovskite ferroelectrics offer large dielectric, piezoelectric, and pyroelectric response, which can be simultaneously leveraged to create multifunctional devices and enable miniaturization in various applications.[1] Among such devices are concepts for autonomous, millimeter-scale robotics where the ferroelectric components fulfill multiple tasks; these include environmental energy harvesting, logic elements, acoustic and optical sensors and transducers, and precision positioners and locomotion units, all performed by the ferroelectric material.[42] Such units are of particular interest for performing duties in hostile environments that are either difficult to reach or otherwise dangerous for humans. Space is a quintessential example of one such environment, along with facilities that use or process radioisotopes. Thus, it is necessary to characterize the multifunctional properties of ferroelectric oxides as a function of radiation exposure, in order to evaluate device performance and functionality in harsh environments.

Prior work studying radiation effects on ferroelectric materials has primarily concentrated on applications in memory devices and capacitors, showing radiation-induced degradation of dielectric and polarization responses in ferroelectric thin films.[90,92-94,96,161] While degradation of functional properties due to high doses of X-rays, gamma rays, neutrons, and protons has been previously reported, ferroelectric thin films behave largely as radiation-hard materials (retaining critical functionality in the material) at radiation doses up to hundreds of krad, and often several Mrad.[40,97,98,100,103] However, there is evidence, even at the lowest doses, that radiation exposure creates defects or activates existing defects, causing measurable changes in the fundamental material properties.

Radiation transfers energy to a material via electron excitation and ionization, generating electron-hole pairs; or through nuclear interactions, giving rise to lattice vibrations and atomic displacements. Low energy (below ~75 keV) photons (X-rays, gamma rays) and electrons do not have sufficient energy to directly create atomic displacements and therefore interact with materials by exciting electrons, ultimately leading to trapping at defect centers.[87] At higher energies, these particles ionize the material with which they interact and have sufficient energy either directly (electrons) or indirectly (gamma ray Compton scattered electrons) to form Frenkel defects, *i.e.*, vacancies and interstitial pairs.[88] The displaced atom, or recoil, will also lose energy through ionization and may have sufficient energy to create additional defects, forming a defect cascade. Charged particles including protons and ions, similar to electrons, transfer energy to the material via electron and nuclear interactions, yet their greater mass and concomitantly lower velocities increase their interaction time with the material, yielding much higher rates and more localized tracks of ionizing energy transfer. The larger mass also increases the probability of displacement events and subsequent defect cascades, ultimately leading, in some cases, to defect clustering and amorphization for high doses.[89]

In a ferroelectric material, defects are of particular importance, as the elastic and electric energies associated with defects (point, line, surface, or volume) are responsible for changes in the energy landscape and resulting motion of internal interfaces across this landscape.[4,37] The substantial ferroelectric and electromechanical responses in ferroelectric thin films, such as lead zirconate titanate (PZT), are in large part due to extrinsic contributions of hysteretically and nonlinearly mobile internal interfaces, such as domain walls and phase boundaries (see Figure 4-1).[4,162] The mobility of these interfaces is

determined by the internal energy landscape of the material, owing to electric and elastic fields associated with lattice defects, including vacancy and dopant point defects, grain boundaries, and other internal interfaces (such as other domain walls), as well as hetero-interfaces with the electrodes and/or the substrate.[6,7] To simplify the following discussion, domain walls will be considered as the representative internal interfaces responsible for the extrinsic contributions, while noting that motion of phase boundaries or defect dipoles can similarly contribute to the functional response in ferroelectrics.

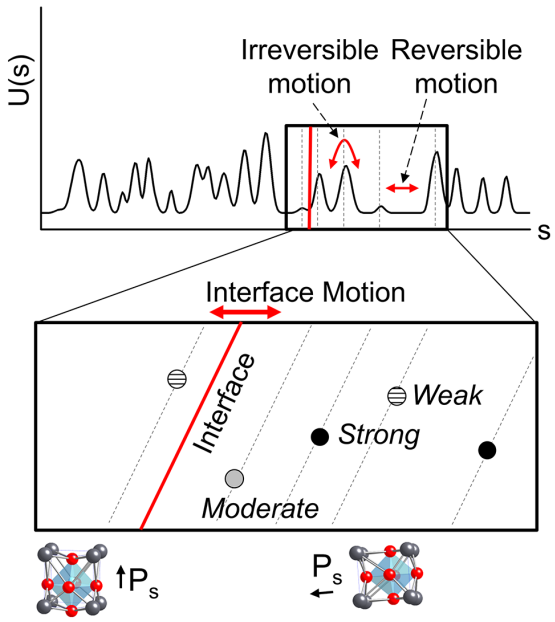

Figure 4-1 Representation of reversible and irreversible interface motion in ferroelectrics, such as the PZT thin films studied here. *U(s)* represents potential energy as a function of interface (domain wall) position *s*, while P_s shows polarization direction. Reversible motion contributes to the low-field response, while irreversible motion of interfaces over pinning centers is mostly observed at increasing fields (larger activation energy).

Radiation-induced ionization and displacement events can potentially provoke deleterious effects in ferroelectrics by increasing defect concentrations and leading to changes in the defect energy landscape of the material. Changes in both concentration and

energy of defects can increase pinning of internal boundaries and interfaces, thereby restricting their mobility and ultimately the functional response of the material. Bastani *et al.* and Proie *et al.* demonstrated substantial degradation in polarization response and changes in permittivity-electric field (ε_r-E) characteristics in PZT thin films, due to trapped charges introduced by X-rays, protons, and gamma irradiation.[97,100] Neutron irradiation, which predominantly transfers energy through nuclear interactions, has been shown to introduce defect dipoles, and result in measureable increases in O and Pb vacancies in ferroelectric PZT.[40,98]

Of particular interest for studies of defect accumulation and their effects is the interface between PZT and the electrodes. In studies of fatigue and retention loss in PZT thin films, the role of the ferroelectric-metal electrode interface has been previously highlighted: defects can move, accumulate, and self-order near the interface, resulting in large volumes of domain wall pinning and inhibited ferroelectric response.[72,163-165] Prior research also supports formation and/or thickening of existing non-ferroelectric layers near the PZT-metal electrode interface, the presence of which is a primary source of degradation of response in ferroelectric thin films, via restriction of domain nucleation and switching.[63,64,166-168] Conversely, using conductive transition metal oxides as electrodes helps to reduce fatigue in ferroelectric thin films, suppressing polarization back-switching.[71] The improvement has been attributed to the reduced concentration of charged defects at the oxide-oxide (ferroelectric-conductor) interface compared to oxide-metal interfaces.[57,63,64,163,164,166,169]

While the interface between either the top or bottom electrode and the ferroelectric material can act as a site for defect accumulation and fatigue, the bottom electrode acts as

a building block for film orientation. For instance, Pt is typically employed due to its compatibility with the high temperature crystallization of the PZT thin films and can serve as template layer for (111)-textured PZT. Alternatively, the Pt layer enables thin seed layers to be used to induce a (001) texture in PZT thin film crystallization.[131] As such, studying various *top* electrode materials presents a convenient method to investigate the effects of defect accumulation at the PZT-electrode interface while decoupling the experiment from any changes in film texture. Here we discuss the role of top electrode material on the radiation-induced degradation of ferroelectric properties of PZT thin film stacks by comparing the effects of gamma radiation on films with IrO_2 and Pt top electrodes.

4.3 Experimental Procedure

$Pb(Zr_{0.52}Ti_{0.48})O_3$ (PZT) thin films were fabricated at the US Army Research Laboratory using 150 mm diameter platinized 100-silicon wafers consisting of 100 nm Pt / 35 nm TiO_2 / 500 nm of SiO_2 / Si. A $PbTiO_3$ seed layer was used to induce 001-texturing of the PZT films, which were prepared via chemical solution processing and spin coating deposition. The films were 529 nm and 527 nm thick (for samples with IrO_2 and Pt, respectively) and showed strong 001-crystallographic texturing. Further details for the substrate and film processing are reported elsewhere.[109,131] IrO_2 or Pt top electrodes were 100 nm-thick and sputter-deposited onto the wafer at 500 °C. The IrO_2 electrodes were also processed with a post-deposition furnace anneal at 650 °C in flowing O_2 for 30 minutes. The electrode and PZT were patterned through argon ion milling, followed by a series of additional metallization steps for creating proper interconnects to device structures. The

overall process flow for creation of the test devices is discussed by Proie *et al.*[100] Figure 4-2 shows baseline characterization of the PZT thin films with IrO_2 and Pt top electrodes via time of flight secondary ion mass spectrometry (ToF-SIMS) (Figure 4-2a and Figure 4-2d), scanning electron microscopy (SEM) (Figure 4-2b and Figure 4-2e), and X-ray diffraction (XRD) (Figure 4-2 and Figure 4-2f).

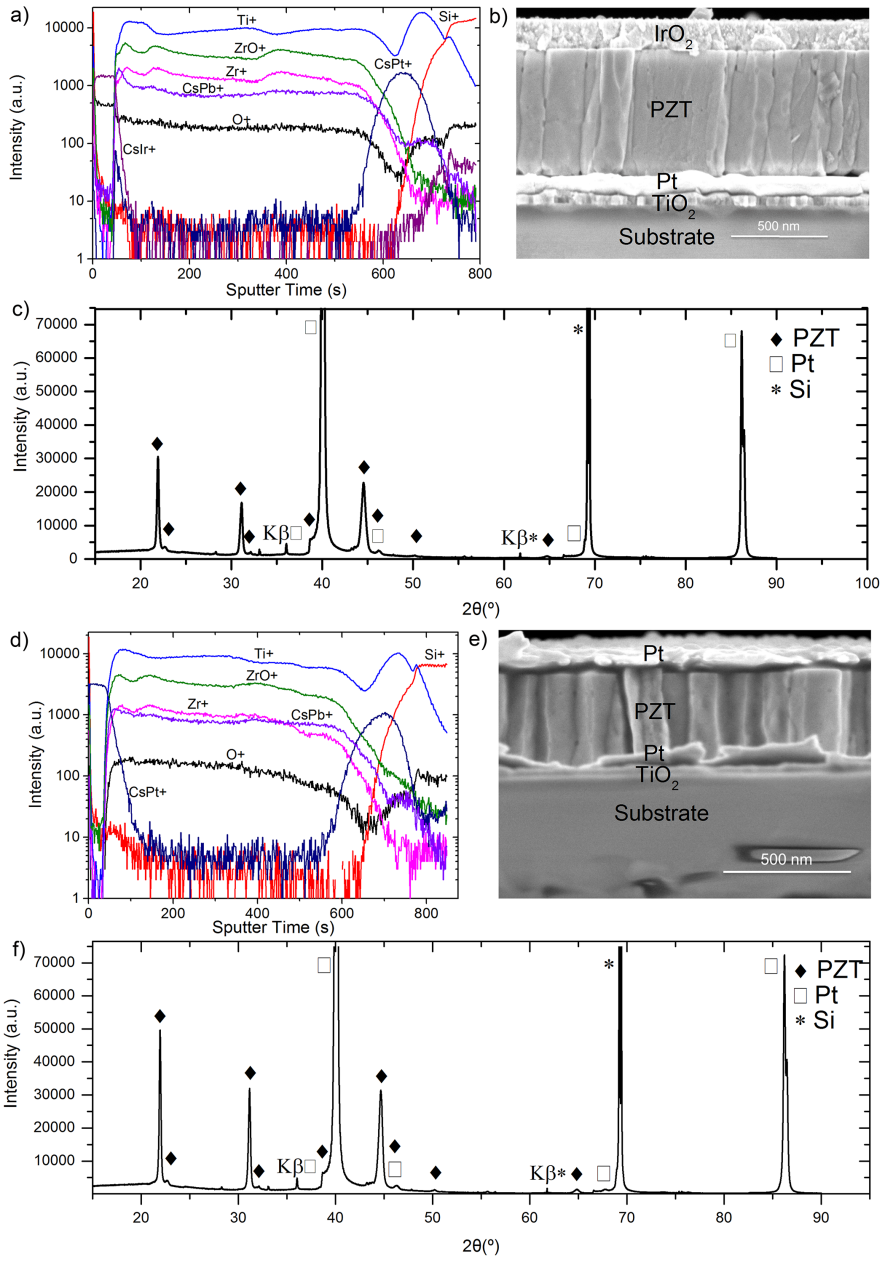

Figure 4-2 Baseline characterization of PZT thin film stacks with IrO_2 and Pt top electrodes. ToF-SIMS characterization for PZT films with a) IrO_2 and d) Pt top electrodes, respectively; SEM images of PZT microstructure near an electrode for b) IrO_2 and e) Pt, respectively; and crystallographic phase identification via XRD for stacks with c) IrO_2 and f) Pt top electrode, respectively. The presence of Cs in ToF-SIMS is noted due to the use of Cs^+ ions in the depth profile analysis, leading to implantation and bonding in the material, often with heavy metals, such as Pb and Pt in PZT.[170]

All samples were irradiated with 2.5 Mrad (equivalent Si dose), using a ^{60}Co gamma radiation source at a dose rate of approximately 600 rad(Si)/s at the Naval Research Laboratory (NRL). The electrodes were left floating during radiation exposure. The dielectric and electromechanical responses of the samples were fully characterized before and after irradiation and are summarized in (Table 4-1). The measurements included, in order, low-field permittivity, polarization response (to identify the coercive field), nonlinear dielectric response, DC electric field-dependent permittivity response, and DC electric field-dependent electromechanical response, followed by irradiation, and repeat of the experiments. Early experiments to pole the samples with DC bias at 2 to 3 times V_C (coercive voltage) for extended periods of time resulted in no change in polarization, dielectric, or electromechanical responses, and were therefore abandoned for this research, effectively confirming that experiments on virgin samples would have no effect on experiments taken after irradiation due to changes in the material. Low-field dielectric (ε_r) measurements were performed at 100 mV and 1 kHz, using an Agilent 4284A precision LCR meter. Polarization-electric field (*P*-*E*) hysteresis experiments were carried out at 1 kHz at fields up to 400 kV/cm using a P-PM2 Radiant ferroelectric test system. AC-nonlinear dielectric permittivity measurements were taken at 1kHz with AC electric field up to approximately the coercive voltage of all samples. ε_r-E_{DC} measurements were performed up to 200 kV/cm DC electric field with an overlapping small signal DC voltage of 500 mV. Measurements to probe the converse, effective longitudinal piezoelectric response ($d_{33,f}$) were performed on an aixACCT double-beam laser interferometer (DBLI) system at 1 kHz and $V_{AC} = 0.25V_C$ with DC electric field up to 200 kV/cm. All reported measurements are subject to up to 3-5% total experimental error, due to sample variability.

These errors are independent and in addition to those shown in the experimental values reported in Table 4-1.

Synchrotron XRD was performed using beamline 33-BM-C with an energy of 15 keV (λ = 0.82613 Å) at the Advanced Photon Source (APS) at Argonne National Laboratory. The samples were mounted on the standard beam-line stage and electrical signals were applied via tungsten microprobes in contact with the top and bottom electrodes of the sample, with the voltage being driven through the bottom electrode. The voltage through the micro-probes was applied using a Keithley 2450, 200V source meter. A Keysight E4980A LCR meter was used to ensure electrical contact with the samples (by measuring capacitance) and to monitor the leakage current in the sample throughout the experiments. The beam size used was 0.3 mm in the horizontal direction by 1.0 mm in the vertical direction. Alignments were performed for the x, y, and z positions to ensure that the diffraction patterns were obtained solely from PZT experiencing the electric field. Diffraction data was measured on a Pilatus100K area detector using θ-2θ scans, with the incident angle (θ) being kept to half of the diffracted angle (2θ) throughout the measurements. Line scans (Intensity *vs.* 2θ) were extracted from the area data by integrating through the azimuthal angle of the detector image. Data presented in results (Figure 4-8) is the section of the scattering data containing the 002- and 200-PZT reflections.

It should be noted that comparisons in results and discussion do not offer conclusions with respect to either top electrode material or the PZT thin film in isolated conditions, but rather the whole material stack (PZT, similar bottom electrode stack and

substrate, and differing top electrode material), as described above, and include any inherent and necessary differences in processing conditions.

4.4 Experimental Results

The low-field, relative dielectric permittivity of virgin PZT films with IrO_2 and Pt electrodes was approximately 950 and 1000, respectively. A representative sampling of the dispersion of the measured relative dielectric permittivity for virgin and irradiated samples with Pt and IrO_2 electrodes is shown in Figure 4-3. Exposure to irradiation resulted in a negligible degradation of relative permittivity for samples with both IrO_2 and Pt electrodes, only 1%. We note that while these changes are statistically relevant, they were within the range of measurement error. The reduction of dissipation factor (*tan δ*) upon irradiation was more substantial: from 1.7% to 1.6% (~6% reduction) for samples with IrO_2 electrodes, and from 3% to 2.4% (~20% reduction) for samples with Pt electrodes (Table 4-1). Reduction in dissipation factor indicates a reduction in the overall conductivity of the dielectric material or reduced amounts of free charges, and could potentially indicate reduced domain wall motion, as such motion contributes to both dielectric permittivity *and* dielectric losses.[171]

Table 4-1 Quantitative data for ferroelectric and electromechanical response of virgin and irradiated samples with IrO_2 and Pt top electrodes, with percent change (from before to after irradiation) noted. Uncertainties expressed represent standard error expressed to one significant figures, except in some cases when the first significant digit is a 1, in which case uncertainty is expressed to two significant figures for consistency between measurements. Measurement values are reported to the same decimal place as uncertainty for said measurement.[172]

	IrO_2			Pt		
	Virgin	2.5 Mrad	% change	Virgin	2.5 Mrad	% change
Low-field Dielectric						
ε_r	954 ± 1	946 ± 1	-1%	998 ± 9	986 ± 7	-1%
tan(δ)	1.7 ± 0.1	1.6 ± 0.1	-5%	3.0 ± 0.2	2.4 ± 0.1	-20%
Rayleigh Analysis						
ε_{init}	1100 ± 40	1130 ± 10	+3%	920 ± 70	1020 ± 20	+11%
α (cm/kV)	52 ± 2	48 ± 1	-8%	35 ± 3	22 ± 1	-37%
$\alpha/\varepsilon_{init}$ x10^{-3} (cm/kV)	49 ± 4	43 ± 2	-12%	40. ± 7	22 ± 1	-45%
Polarization						
P_r (μC/cm^2)	20.4 ± 0.2	19.6 ± 0.4	-4%	16.6 ± 1.6	10.7 ± 0.4	-36%
P_{sat} (μC/cm^2)	48.1 ± 0.1	48.1 ± 0.2	--	48.7 ± 0.6	46.6 ± 0.1	-2%
E_c (kV/cm)	28.6 ± 0.3	27.4 ± 0.3	-4%	41.8 ± 1.2	28.5 ± 1.4	-32%
C-V Response						
% tunability	75.6 ± 0.2	73.5 ± 0.2	-3%	68.1 ± 0.4	67.4 ± 0.2	-1%
Electromechanical						
$d_{33,f,saturation}$ (pm/V)	45.5 ± 0.7	46.1 ± 0.8	+1%	68.2 ± 3.3	61.1 ± 1.2	-10%

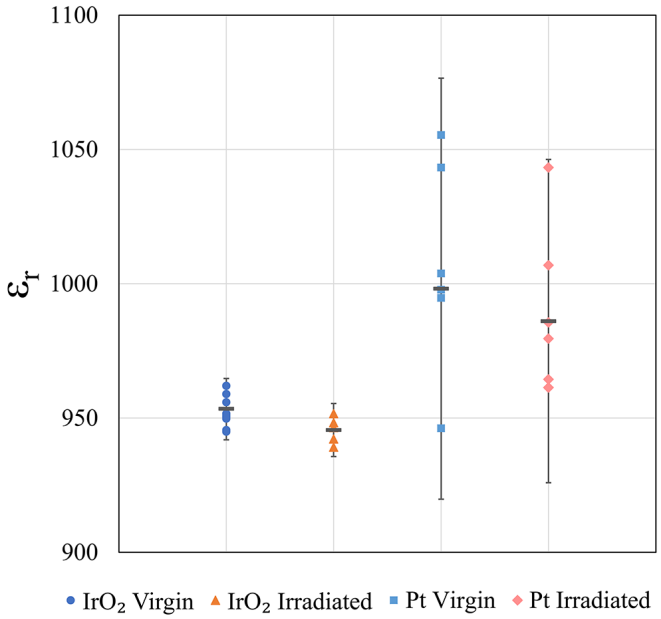

Figure 4-3 Dot plot showing distribution of low-field relative permittivity (ε_r) for samples with either oxide or metal top electrodes, both before and after irradiation. Points shown represent measurements taken on different electrodes. Error bars indicate 95% confidence interval from the mean for all measurements. Mean is shown as dark horizontal bar for each set of measurements. Measurements taken at 100 mV, 1 kHz.

The nonlinear dielectric response of the samples is shown in Figure 4-4. To quantify potential changes in extrinsic contributions, the nonlinear dielectric response was analyzed through the Rayleigh formalism.[24] Specifically, of interest are the reversible Rayleigh parameter, ε_{init}, the intercept of linear field-dependent relative dielectric permittivity, and the irreversible Rayleigh parameter, α, *i.e.* the slope of the field-dependent permittivity. ε_{init} describes mostly contributions from the intrinsic lattice deformation and reversible motion of internal interfaces, while irreversible contributions (represented by α) describe larger-scale, irreversible domain wall motion. Therefore, α and the ratio of the irreversible to reversible Rayleigh parameters are considered a quantitative measure of the extrinsic contributions to the functional response.[25]

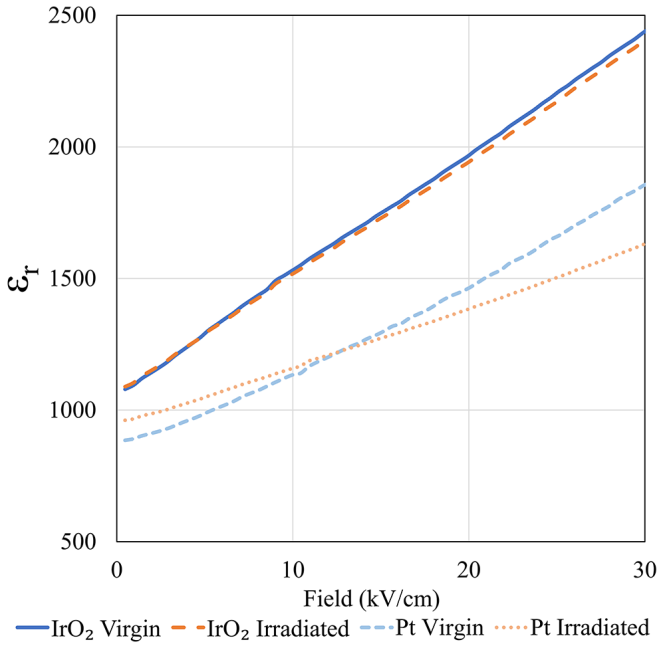

Figure 4-4 Nonlinear dielectric response at low to intermediate fields, probed with 1 kHz AC waveform. Rayleigh analysis fits a line to the linear region of the plots (from 10 kV/cm up to 30 kV/cm for these samples) to extract ε_{init} (intercept) and α (slope).

Irradiation of film stacks with either electrode material resulted in degradation of α. However, films with Pt electrodes showed degradation in excess of four times (37% *vs.* 8% degradation) the degradation observed in samples with IrO_2 electrodes (Table 4-1). This implies that the irreversible motion of internal interfaces is severely reduced by irradiation, with greater effects seen in samples with Pt electrodes. Conversely, ε_{init}, or reversible contributions to the response, showed enhancements of ~3% (within experimental error, Table 4-1) and 11% for samples with IrO_2 and Pt electrodes, respectively (Table 4-1). The above results suggest that intrinsic response and/or reversible domain wall motion were augmented at the expense of irreversible domain wall mobility, which will be discussed hereafter. Finally, the ratio of $\alpha/\varepsilon_{init}$ showed reduction for samples with both electrode

compositions, although the reduction was smaller for samples with IrO_2 electrodes (12%) compared to Pt electrodes (45%) (see Table 4-1 for details).

The effects of irradiation on the polarization-electric field (*P-E*) hysteresis curves are shown in Figure 4-5. Saturation polarization remained largely unaffected for samples with IrO_2 electrodes, while those with Pt electrodes resulted in a modest 4% reduction, which is similar to the range of sample variability (Table 4-1). The remanent polarization was reduced by over 35% in samples with Pt top electrodes after irradiation, compared to essentially no change for films with oxide electrodes (Table 4-1). Additionally, at lower fields, a slight pinching of the hysteresis loops is observed in irradiated samples with Pt electrodes (Figure 4-5).

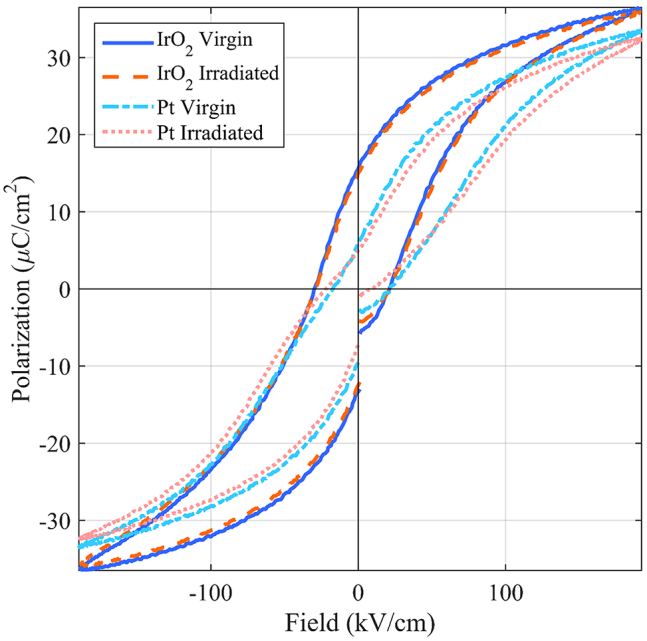

Figure 4-5 Ferroelectric response of virgin and irradiated samples with oxide and metallic electrodes, illustrating radiation-induced pinching of loops in samples with Pt electrodes. The measurements were performed at 1 kHz.

Figure 4-6 shows the permittivity *vs.* DC electric field (ε_r-E_{DC}) tunability curves for films with both electrode compositions. The tunability suffered minor degradation in both samples upon irradiation. However, the changes were once again within the experimental error, at -3% and -1% for samples with IrO_2 and Pt top electrodes, respectively. Furthermore, irradiated samples with metal electrodes showed a slight horizontal peak shift as well as creation of a new peak, which will be discussed in the following section.

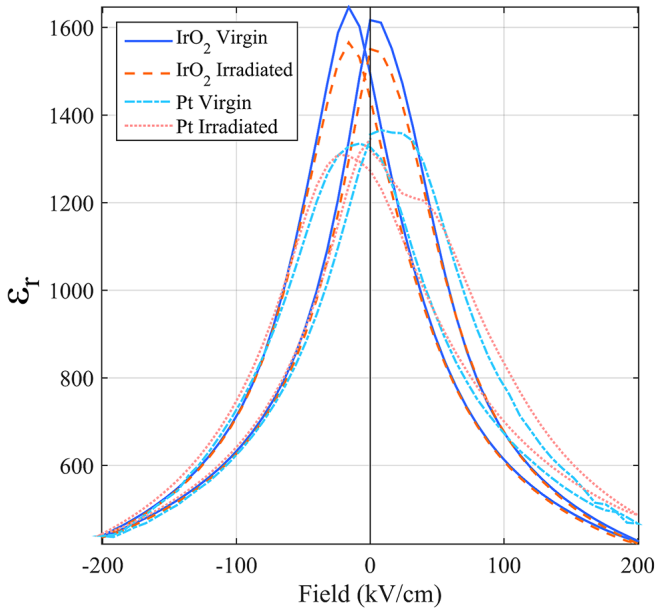

Figure 4-6 DC electric field-dependent permittivity curves for virgin and irradiated samples with IrO_2 and Pt top electrodes, showing horizontal peak shift and creation of a new peak in samples with Pt top electrodes. The measurements were performed up to 200 kV/cm DC field with overlapping 500 mV, 1 kHz AC voltage.

Negligible changes in electromechanical response, $d_{33,f}$, were observed in samples with oxide electrodes, while samples with metallic electrodes suffered 10% degradation in saturation electromechanical response and 48% degradation in remanent electromechanical response. For samples with Pt electrodes, a reduction of approximately 66% in the dispersion of $d_{33,f}$ values was seen post-irradiation (Figure 4-7). It should be noted that the measured electromechanical response was, on average, approximately 20% lower for samples with IrO_2 top electrodes compared to samples with Pt top electrodes, possibly due to tool limitations or sample variances. It should also be noted that the application of DC field to measure electromechanical response can result in lower $d_{33,f}$ values when compared to AC-field measurements of similar parameters, due to possible time dependence of nonlinear domain wall behavior.[173,174]

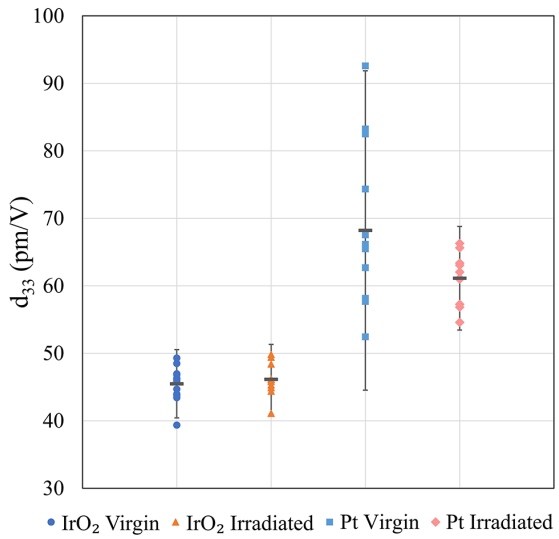

Figure 4-7 Dot plots showing distribution of electromechanical response ($d_{33,f,sat}$) for virgin and irradiated samples with both IrO_2 and Pt top electrode. Points shown represent measurements taken on different electrodes. Error bars indicate 95% confidence interval from the mean for all measurements. Mean is shown as dark horizontal bar for each set of measurements. The measurements were performed at up to 200 kV/cm DC field with overlapping 1 V AC voltage.

Finally, in order to further analyze the effects of gamma irradiation on ferroelectric PZT film stacks and the process by which degradation of functional properties occurs, synchrotron XRD and electron spin resonance (ESR) were performed on virgin and irradiated samples with IrO_2 top electrodes after exposure at 10 Mrad (Si). Prolonged exposure experiments were undertaken in an effort to enhance the changes that could be observed using these techniques.

The diffraction data from the virgin sample is shown in Figure 4-8a and Figure 4-8b. While the two reflections cannot be seen independently in the diffraction profile, profile fitting to the pattern was successful at extracting the respective contributions of the 002- and 200-reflections to the overall diffraction profile. Profile fitting was completed using a least squares refinement approach and two pseudo-Voigt functions, allowing for

the extraction of peak positions (2θ). Using the extracted peak positions, lattice strain was calculated for the 200-reflection using the following equations and plotted in Figure 4-8c:

$$d_n = \frac{\lambda}{2\sin(\theta)} \quad 4\text{-}1$$

$$\varepsilon_{200} = \frac{d_1 - d_0}{d_0} \quad 4\text{-}2$$

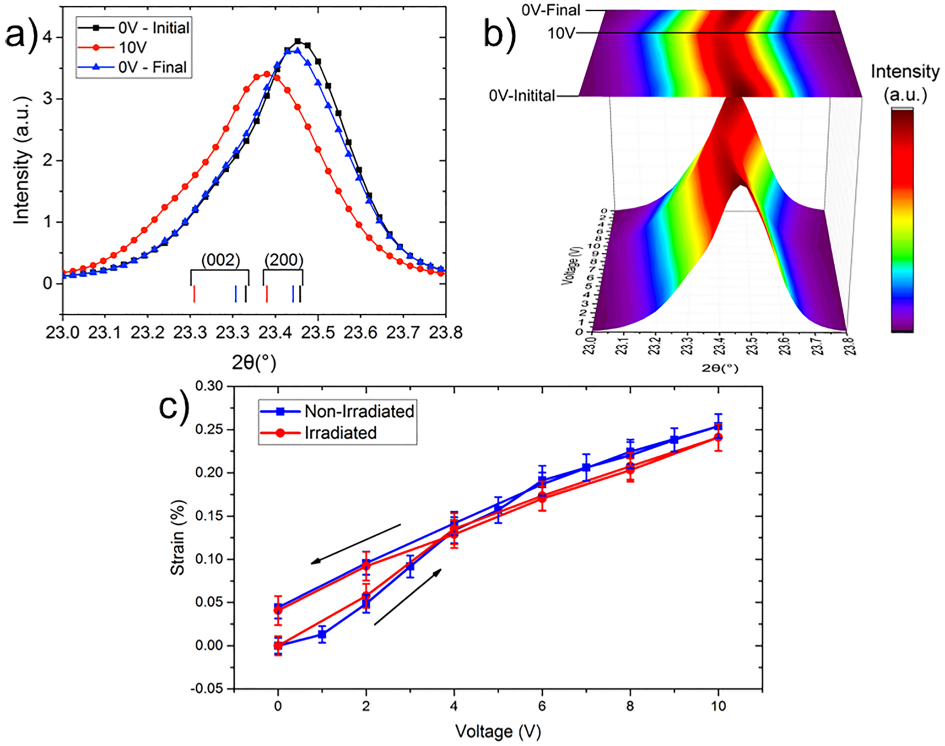

Figure 4-8 a) and b) Representative intensity *vs.* 2θ XRD profiles acquired from the non-irradiated sample and c) 200-lattice strain plotted as a function of voltage for both non-irradiated and irradiated samples, both with IrO_2 top electrodes.

There are consistencies in the 200-lattice strain between virgin and irradiated samples: similar hysteresis is observed in both samples, similar maximum values at maximum field, and similar remanent strain values after removal of the field. The data

shows that there are no significant differences in the 200-lattice strain between the virgin and irradiated samples within the error of the peak position. This indicates that the high electric fields utilized in this experiment may overcome any influence of weak pinning centers that are induced by radiation (*e.g.*, defect creation, domain wall pinning by weak pinning centers).

Electron spin resonance (ESR) is a well-established microwave technique used to identify and quantify native and radiation-induced defects in a variety of materials. Experiments at 9.5 GHz on virgin PZT samples reveal a signal with Zeeman splitting *g*-value of ~2.005 and full width at half maximum (FWHM) of ~10 G (Figure 4-9). These parameters are very similar to those for resonances attributed to oxygen vacancy-related defects in PZT powder samples.[175] After application of 10 Mrad (Si) gamma irradiation, this ESR signal is observed to be approximately twice as broad, indicating differences in the defect-energy landscape, which will be discussed hereafter.

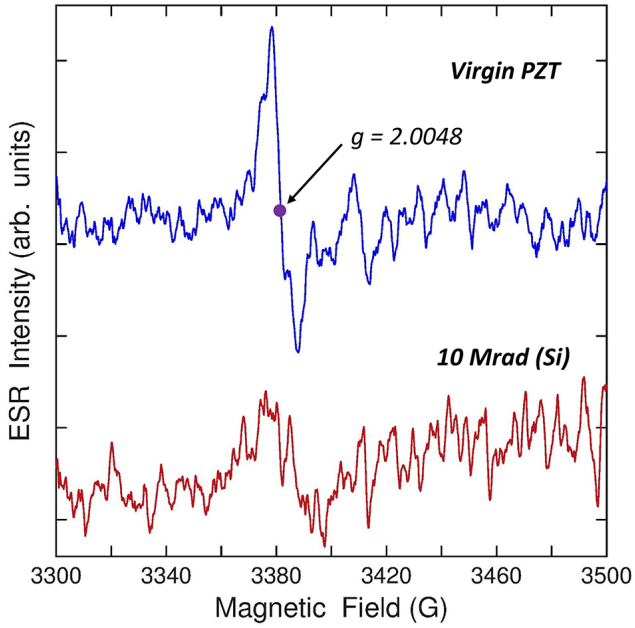

Figure 4-9 Electron spin resonance (ESR) spectra at 9.5 GHz for virgin and irradiated (10 Mrad (Si)) PZT samples, displaying a broadening of the signal at g ~ 2.005 observed post-irradiation.

4.5 Discussion

Gamma irradiation of PZT thin films with both oxide and metal top electrodes resulted in degradation of functional properties. However, a clear trend is observed in the dielectric, ferroelectric, and electromechanical responses for samples with IrO_2 compared to Pt top electrodes: PZT thin films with oxide top electrodes show a higher tolerance to ionizing radiation-induced degradation than films with metallic top electrodes.

A radiation-induced reduction in motion of the internal interfaces is highlighted by the reduction of the irreversible Rayleigh parameter (α), counterpointed by the increasing reversible Rayleigh component (ε_{init}), indicating either enhanced vibration of the same

interfaces or intrinsic lattice strain (assuming that a subset of domain walls are completely pinned after irradiation).[176] However, results from XRD analysis show consistent strain profiles for virgin and irradiated films, suggesting that the lattice strain response change with irradiation is low. It is therefore unlikely that the lattice strain response changes significantly after irradiation and, therefore, the change in ε_{init} is more likely due to contributions of domain wall motion.

These observations suggest radiation-induced, "high energy" pinning sites (defects) for the motion of the internal interfaces, resulting in increased vibration and decreased overall motion of these interfaces, in terms of contributions to the overall dielectric response. We note that such higher-energy defects are consistent primarily with radiation-induced creation of trapped charges as a consequence of ionization events, *i.e.* deepening of the potential energy wells corresponding to pre-existing defects. These trapped charges can result in stabilization of domain walls at pinning sites or accumulation of charges trapped at grain boundaries, thereby resulting in additional pinning.[177]

The above observations are also consistent with the appearance of a new maximum in the post-irradiation ε_r-E_{DC} curves for samples with Pt electrodes (Figure 4-6). The local maxima in ε_r-E_{DC} curves correspond to the average switching DC fields. Therefore, the appearance of a new peak can be associated with the creation of a new family of defects or change of the energy of a subset of the defects already present in the samples. If the energy change in defects affected by radiation differs substantially from the pre-existing defects, the switching fields associated with the defects will also be different and will appear as a separate peak in the ε_r-E_{DC} curves. Similarly, the pinching observed in the *P-E* loops (Figure 4-5) for samples with metallic electrodes – exacerbated after irradiation – is

consistent with pinning of internal interfaces and presence of oriented defect dipoles. Various defects, such as domain wall pinning due to diffusion of charged defects and alignment of dipolar defects, are typically associated with pinching of hysteresis loops in previous studies.[62,178-182] It is also possible that irradiation locally disrupts polarization through the generation of electron-hole pairs. When these unbiased pairs equilibrate, the domain polarization randomly orients, leading to effects similar to those in aging of unpoled PZT.[178] This proposed mechanism is further corroborated by the ESR data presented in Figure 4-8, at elevated levels of irradiation.[175] The broadening of the ESR spectrum in irradiated PZT samples may indicate changes to oxygen vacancies already present in the system, where the gamma irradiation excites electrons that subsequently become trapped at these sites ($i.e.\ V_O^{\cdot\cdot} \rightarrow V_O^{\cdot}$).[177] The singly charged $V_O^{\cdot}$ are known to be more mobile; therefore, their formation could lead to domain depolarization via strain-driven reorientation, even if the charged state is short-lived.[177] At longer time scales, these newly-reoriented defects can move towards the top electrode interface where they will play a particularly critical role on the functional properties of the PZT thin films studied here. However, as point defects, they are not strong enough to affect large-scale domain wall motion, as evidenced by the *in situ* XRD results.

The overall electrode-dependence of the radiation-induced degradation suggests that the PZT-electrode hetero-interface is particularly susceptible to changes in the population and/or energy of defects that act as pinning sites. In general, any interface in the sample is likely to act as a pinning site and affect domain wall motion.[37] The effect of the top electrode on the overall functional response of the ferroelectric material has been addressed by various hypotheses in the literature, including through movement and

ordering of defects at interfaces.[63,64,72,73,163-165] Specifically, oxygen vacancies can become mobile and/or $V_O^{\cdot\cdot} - V_{Pb}^{''}$ defect dipoles reorient under a sufficiently-strong applied electric field, towards the ferroelectric-electrode interface. As oxygen vacancies accumulate and self-order at the interface, they pin domain wall motion, suppress nucleation, and inhibit polarization.[72,165] Prior studies for ferroelectric capacitor and memory applications have reported a more closely matching work-function of PZT with oxide electrodes compared to metallic ones, resulting in improved conductivity at the interface and potential for oxygen vacancy migration and annihilation.[169,183-185] For samples with oxide top electrodes, ion conduction and partial annihilation of defects results in reduced susceptibility of the ferroelectric to degradation-induced defect accumulation, domain wall pinning and polarization switching restriction. Conversely, samples with metal electrodes do not offer sites for healing of defects. Therefore, defect accumulation (and subsequent ordering) at the interface will be viable at lower total ionization doses, resulting in negative consequences on the ferroelectric and electromechanical responses of the samples.[98]

In addition to degradation induced by defect ordering and accumulation, the presence or enlargement of ferroelectrically-inactive layers are pertinent here. The defect-stimulated formation/enlargement of ferroelectric dead layers results in decreased ionic motion and thereby exacerbates defect accumulation and domain wall pinning near the interface.[166-168] These ferroelectric dead layers will theoretically become increasingly more prevalent with compounding defect motion and accumulation stimulated, in this research, by irradiation. The deleterious effects of irradiation on the polarization response of samples with Pt electrodes supports the presence of a ferroelectric dead layer, characterized by non-switchable regions near the interface.[168] Incorporation of oxide electrodes has previously

shown increased fatigue resistance and superior ferroelectric switching behavior due to reduced defect formation in the PZT.[166]

Finally, the difference in density and electron concentration between IrO_2 and Pt must be considered: the greater density of metallic electrodes could lead to a radiation dose enhancement near the PZT-Pt electrode interface, further exacerbating the effects of oxygen vacancy ordering and aging.[186] Based on available data from NIST, the mass energy attenuation coefficients (in units of cm^2/g) for Pt metal, Ir metal, and lead glass are all within approximately 10% of each other for 1 MeV and 100 keV photons, respectively. However, since Pt is approximately twice as dense as IrO_2 (21.5 *vs.* 11.7 g/cm^3) and nearly three times as dense as PZT (7.5 g/cm^3), one would estimate a significant dose enhancement in excess of 50% in the region beneath the Pt electrode as compared with the PZT covered by the IrO_2 electrode.[187,188] The greater total ionizing dose at the metal electrode-PZT interface may contribute to the greater radiation-induced degradation observed in devices with Pt electrodes.

4.6 Conclusions

PZT thin films with metallic Pt and metal-oxide IrO_2 top electrodes were exposed to 2.5 Mrad (Si) ^{60}Co gamma radiation. For material stacks with both types of electrodes, minimal changes in low-field relative permittivity (~1%), saturated polarization (< 5%), and electromechanical response (≤ 10%) were observed. However, irradiated samples with IrO_2 electrodes showed substantially smaller changes of dielectric and electromechanical responses than those with Pt electrodes, suggesting that the hetero-interface between the

PZT thin film and electrode plays a critical role in either the radiation-material interaction or in the subsequent stages for reaching a new equilibrium. The degradation in response was associated with the deepening of the present defects' potential energy wells that resulted in increased reversible contributions to the dielectric response and decreased motion of internal interfaces (*e.g.*, domain walls, phase boundaries, *etc.*), as well as pinching of the polarization hysteresis loops and appearance of new peaks in the ε_r-E_{DC} curves for platinized samples. Changes in the defect landscape are less damaging to the functional response of ferroelectric films and material stacks incorporating a metal-oxide top electrode, due to the closer match of the work function of the oxide *vs.* metal conductor with the ferroelectric, as well as the oxide nature of the IrO_2, which allows for partial annihilation of oxygen defects at the film/conductor hetero-interface. These results suggest a promising avenue for creation of radiation-hard devices based on ferroelectric materials.

4.7 Acknowledgements

This work was supported by the Defense Threat Reduction Agency, Basic Research Award # HDTRA1-15-1-0035, to Georgia Institute of Technology. The contents do not necessarily reflect the position or the policy of the federal government, and no official endorsement should be inferred. The authors acknowledge the contributions of Joel Martin and Brian Power of the Army Research Laboratory and Steven Isaacson of General Technical Services for their roles in the fabrication of the PZT thin films and MEMS devices. The authors acknowledge the use of the Analytical Instrumentation Facility (AIF)

at North Carolina State University, which is supported by the State of North Carolina and the National Science Foundation.

CHAPTER 5. PHENOMENOLOGICAL MODEL FOR QUANTIFYING DEFECT INTERACTIONS IN IRRADIATED FUNCTIONAL MATERIALS

The content in this chapter has been published in *Scientific Reports*.[189] The text has been slightly modified from the original manuscript to accommodate the Supplementary Information.

Phenomenological Model for Defect Interactions in Irradiated Functional Materials

Steven J. Brewer, Cory D. Cress, Samuel C. Williams, Hanhan Zhou, Manuel Rivas, Ryan Q. Rudy, Ronald G. Polcawich, Evan R. Glaser, Jacob L. Jones, Nazanin Bassiri-Gharb

Scientific Reports, vol. 7, no. 5071, (2017), doi: 10.1038/s41598-017-05071-z

5.1 Summary

The ability to tailor the performance of functional materials, such as semiconductors, via careful manipulation of defects has led to extraordinary advances in microelectronics. Functional metal oxides are no exception – protonic-defect-conducting oxides find use in solid oxide fuel cells (SOFCs) and oxygen-deficient high-temperature superconductors are poised for power transmission and magnetic imaging applications. Similarly, the advantageous functional responses in ferroelectric materials that make them attractive for use in microelectromechanical systems (MEMS), logic elements, and environmental energy harvesting, are derived from interactions of defects with other defects (such as domain walls) and with the lattice. Chemical doping has traditionally been employed to study the effects of defects in functional materials, but complications arising from compositional heterogeneity often make interpretation of results difficult. Alternatively, irradiation is a versatile means of evaluating defect interactions while avoiding the complexities of doping. Here, a generalized phenomenological model is developed to quantify defect interactions and compare material performance in functional oxides as a function of radiation dose. The model is demonstrated with historical data from literature on ferroelectrics, and expanded to functional materials for SOFCs, mixed ionic-electronic conductors (MIECs), He-ion implantation, and superconductors. Experimental data is used to study microstructural effects on defect interactions in ferroelectrics.

5.2 Introduction

Modification of the type, charge, concentration, spatial distribution, and mobility of defects in a material can result in dramatic effects on functionality.[79] Semiconductor materials are a prime example, where strict control over defect type and density is used to modify electronic and optical properties,[79,190] resulting in the design of devices that we use and interact with on a daily basis, from modern *pn*-junction transistors to photovoltaic (PV) cells and photoactive image sensors.[190,191] Similar control in functional oxides is substantially more challenging to implement, where local charge balance and phase stability are intertwined with material functionality. For example, in high-temperature superconducting ceramics, localized material defects can interact with and pin magnetic vortices, thus enhancing superconducting properties.[192] Strong interactions between oxygen-related defects in proton-conducting oxides result in crucial changes to conduction behavior for mixed ionic-electronic conductors (MIECs) and solid oxide fuel cells (SOFCs).[193] In ferroelectric materials, defect interactions, such as those between domain walls (2D defects) and point defects (0D) are often the major contributor to substantial dielectric, ferroelectric and piezoelectric responses. Various methods have attempted to elucidate such interactions, both theoretically and empirically.[194,195] In this work we demonstrate a universal approach for quantifying defect interactions in functional materials, and specifically ferroelectrics, without chemical doping, but rather achieved through total ionization dose (TID) studies. A phenomenological model is implemented for such quantification, with the ultimate goal of becoming a tool in defect engineering and functional response control of these oxides. The proposed model is successfully demonstrated for direct comparison of defect-defect interactions in a range of ferroelectric

compositions in both thin film and bulk form. Further applicability is demonstrated by fitting the model to data on functional materials for applications in solid oxide fuel cells (SOFC), mixed ionic-electronic conductors (MIECs), He-ion implantation, and superconducting oxides. Subsequently, the model is employed to compare the effects of grain structure on the interaction of domain walls with defects in polycrystalline lead zirconate titanate (PZT) thin films.

5.3 Background

Since the inception of the transistor, defect engineering of semiconductor materials has undergone momentous advancements, leading to a continuous revolution in electronic devices. The transformative nature of precise defect control and design in these materials has resulted in an abundant manipulation of the resulting material functionalities, which has in turn allowed for vast reductions of length scales for resulting devices. Metal oxide materials offer a substantially wider range of functionalities, with many of them coexisting in the same material. However, these materials suffer from a greater degree of complexity that has hindered similar levels of control over impurity-driven properties.[79,192] Inclusion of more than one elemental component, chemical instability, and diffusion often result in complex interactions of defects with oxides' functional properties,[134,192,196] making such material systems increasingly difficult to control and optimize, specifically in polycrystalline thin films.[79] Such challenging control of defects in functional oxides has often translated into the notion that defects are deleterious to material functionalities.[197] This is particularly relevant in ferroelectric oxides, where defects are often considered to

be a source of degradation of dielectric, ferroelectric, and electromechanical responses.[4] Indeed, the elastic and electrical energies associated with defects can affect the motion of internal interfaces, such as hysteretic and nonlinearly-mobile domain walls and phase boundaries: *i.e.*, the pinning energy for the motion of domain walls is defined by the local defects, resulting in elastic and electrical fields in the lattice.[4,6,7] The mobility of these internal interfaces is largely responsible for the very large functional responses exhibited by ferroelectric materials, and the restriction thereof by defect interactions results in considerable degradation of functional properties.[4,6,7,162] However, recent reports have demonstrated that the introduction of defects via ion bombardment in near-perfect single-crystal ferroelectrics can, in fact, *enhance* ferroelectric properties.[198] Likewise, defects in yttrium barium copper oxide (YBCO) can pin magnetic flux, resulting in increased supercurrent properties.[192] As such, it is imperative to further develop methods for investigating and manipulating structure-property relationships wrought by defect interactions in complex functional oxides.

Traditionally, the effects of defect concentrations in functional materials are studied via impurity doping, an approach historically used for manipulation of material functionalities.[82,83] For example, in PZT, acceptor dopants (*e.g.,* Fe^{3+}, Mn^{3+}) create oxygen vacancies and defect dipoles which can pin domain wall motion, degrading electromechanical response, while reducing dielectric, dynamic mechanical, and piezoelectric losses in the material.[84] Conversely, donor dopants (*e.g.,* La^{3+}, Nb^{5+}) introduce excess positive charge, compensated by Pb vacancies, as well as reduced number of oxygen vacancies and defect dipoles in the material.[81,84] Such reduction leads to

increased domain wall motion and results in greater electromechanical response, but also larger dielectric losses.[81,84]

A variety of work has been carried out to quantify interactions between defects and the resulting effects on the functional response of ferroelectrics. First and foremost, the Rayleigh analysis, originally introduced for ferromagnetic materials and adapted to ferroelectrics in late-1990s by Taylor and Damjanovic, is currently widely employed to quantify contributions of domain wall (2D defects) motion to dielectric responses in ferroelectric materials.[31,195] However, while the Rayleigh analysis allows a quantification of the overall extrinsic contributions to the functional response, it does not directly quantify trends in functional response as a function of defect concentration. In the late 1980s, Kronmüller showed an approximately inverse proportionality between domain wall motion and defect concentration in ferromagnetic materials; Boser expanded this work to ferroelectric $BaTiO_3$, demonstrating a similar inverse relationship between dielectric permittivity and dopant concentration.[28,194] While the changes associated with dopant-induced defects can be substantial, it is often difficult to distinguish whether changes to material properties are the result of the complex effects of compositional heterogeneity, defect interactions, or a combination of both. Manipulation and study of defect interactions via irradiation provides a method that forgoes chemical doping and its associated complications, *e.g.*, due to phase separation and instabilities arising from chemical heterogeneity in the material.[86] Radiation-induced ionization and displacement events can increase defect concentrations, causing changes in defect energy and potentially modifying functional responses of functional oxides.[4,7,199] The ability to quantify these radiation-induced defect concentrations and accurately predict material response as a function

thereof has enormous implications not only for ferroelectric materials, but also for defect engineering of a variety of other functional metal oxides,[200] for applications ranging from multiferroic multistate memory devices and optoelectronics,[201,202] to mixed ionic-electronic conductors,[193,203,204] superconductors,[192,205] and even nuclear fusion materials and X-ray applications.[206]

5.4 Phenomenological Model for Defect Interactions in Functional Oxides

Prior work on irradiation of functional materials has generally shown a direct correlation between radiation dose and degradation of functional properties.[32,90-92,96,207-209] Specifically, trapped charges and ionic displacements – activated or generated as a result of X-ray, gamma, electron, proton, neutron, and heavy-ion irradiation at intermediate and high doses – can result in degradation of functional responses through changes to defect concentration, defect interactions, and the defect energies in the material.[32,40,97,100,198,199,210]

Here, we present a phenomenological model to quantify such defect interactions by assuming that defects, either generated or activated in the material by irradiation, will eventually result in measurable changes to the overall material response. We consider active defect interactions to encompass both an interaction between a created/activated defect and functional material volume, as well as interaction between defects that result in modifications of extrinsic contributions to the functional response (such as domain wall motion in ferroelectric materials, proton-conducting perovskites, *etc.*).[211] Such interactions will inevitably impact a given region of the material, defined here as the volume V_{def}. Conversely, a "free" material volume is defined, V_{free}, corresponding to regions where

defects are either not present or are present but do not result in measurable changes to the functional response. We further assume that the number of defects in an arbitrary volume of the sample, N, changes in proportion to radiation dose, thus allowing for correlation of degradation/enhancement of functional response to changes in V_{def} from an easily-quantifiable and manageable external "stimulus." We can relate the change in V_{def} to changes in the number of defects, N, as a function of: (1) the volume fraction of the material where defect interactions are free to occur: V_{free}/V_T, where V_T is the total material volume; and (2) the mean change in material volume impacted per new defect created/activated, V_N.

$$\frac{dV_{def}}{dN} = V_N \frac{V_{free}}{V_T} \tag{5-1}$$

Equation (1) expresses the fact that the volume of material impacted by new defects is proportional to the fraction of free volume in a given material – larger free volume yields a greater volume influenced by a new defect, due to more free "sites" (Figure 5-1). However, the presence of internal interfaces and material nonlinearities, such as grain boundaries, pre-existing defects, chemical heterogeneity, *etc.*, may result in deviations from the mean volume that a new defect will impact. Thus, we introduce a generalized weighting function, $W(N)$ to account for material-specific fluctuations to the actual volume impacted by each new defect created/activated, V_N, and the resulting modifications of extrinsic contributions to the functional response. The weighting function is also expected to depend on the number of defects created/activated, N, which is proportional to the radiation dose. Thus,

$$\frac{dV_{def}}{dN} = V_N W(N) \frac{V_{free}}{V_T} \tag{5-2}$$

Using the relationship that accounts for the total interrogated volume:

$$V_{def} + V_{free} = V_T \tag{5-3}$$

we can substitute for the free volume, V_{free}, arriving at

$$\frac{dV_{def}}{dN} = V_N W(N) \frac{V_T - V_{def}}{V_T} = V_N W(N) \left(1 - \frac{V_{def}}{V_T}\right) \tag{5-4}$$

This expression is difficult to solve analytically without further simplification. We thus convert the expression for volume fraction to a normalized volume, thus eliminating the variable V_T and constraining the normalized volume impacted by active defect interactions, V_d to the range from 0 to 1:

$$\frac{V_{def}}{V_T} = V_d$$
$$V_d \in [0,1] \tag{5-5}$$

Substituting this result into Expression (5-4) requires multiplying the left-most part by V_T/V_T in order to convert the differential to the appropriate relation of dV_d:

$$\frac{V_T dV_d}{dN} = V_N W(N)(1 - V_d) \quad 5\text{-}6$$

Dividing V_T to the right-hand side of (S6) allows for normalization of the mean change in material volume impacted by defect interactions per new defect created/activated:

$$\frac{dV_d}{dN} = \frac{V_N}{V_T} W(N)(1 - V_d) \quad 5\text{-}7$$

The constant V_N is normalized per total volume V_T, yielding φ_N, the normalized mean change in material volume impacted by defect interactions per new defect created/activated. The result is

$$\frac{dV_d}{dN} = \varphi_N W(N)(1 - V_d) \quad 5\text{-}8$$

Separation of variables and integration results in:

$$V_d = 1 - e^{-\varphi_N \int W(N) dN} \quad 5\text{-}9$$

Given the large dependence of the functional properties on the extrinsic contributions, we can expect the changes in functional response as a function of TID to be directly dependent on the material volume affected by defect-defect interactions. The resulting relationship is a generalized form that can be applied to a variety of functional materials that rely on active/inactive defects within the material volume to drive their functional properties.[192,193,198] We note that similar expressions have been previously derived for

defect motion and interactions in various semiconductor and insulator materials, including Si, SiO_2, and graphene.[208,209,212] Additionally, Equation 5-9 bears resemblance to the sigmoid function used to describe phase transition behavior in solids from the Johnson-Mehl-Avrami-Kolmogorov equation.[213]

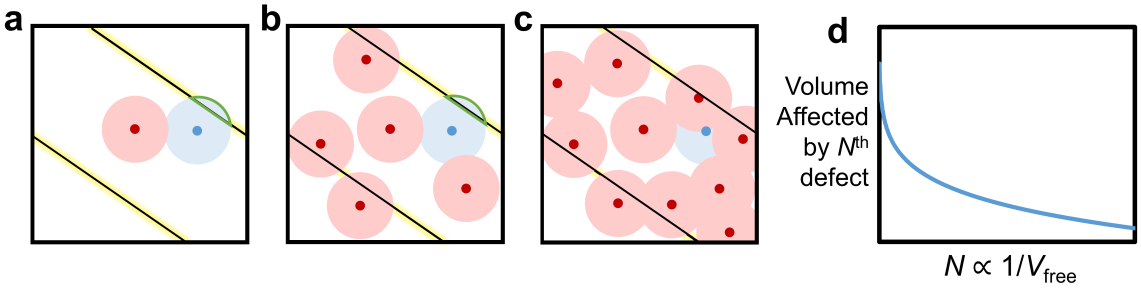

Figure 5-1 Schematic 2D simplification of 3D samples, illustrating the relationship between material volume, volume affected by defects, and the effects of new defects. a) Shown is a single grain with three domains, separated by two domain walls. Free material volume is shown in white, pre-existing defects and the volume they affect in red, and a newly-introduced defect in blue. A larger free volume results in greater mean volume pinned by the new defect. (b, c) With increasing number of pre-existing defects (d) the volume pinned per new defect is reduced. Furthermore, the weighting function is employed to account for nonlinear defect interactions, such as those between defects and domain walls shown in green in (a) and (b). As available sites for new defects to impact domain walls are reduced with greater numbers of pre-existing defects, the weight of new-defect impact on free material volume is modified. The available domain wall area for interactions with new defects is highlighted in yellow.

To further develop Expression 5-9, a knowledge of the weighting function is needed. The proposed expression that relates material nonlinearities to the magnitude of material volume impacted by a new defect (either created or activated by irradiation), thus resulting in modification of the functional response is:

$$W(N) = \frac{1}{N^k} \qquad 5\text{-}10$$

where k is a fitting coefficient related to the rate of defect saturation in the material, which is discussed hereafter. We note that the proposed weighting function is consistent with prior work in both ferroelectric and ferromagnetic materials, for defect interactions between domain walls and chemically-induced (dopant) point defects. Kronmüller originally demonstrated an N^{-1} relationship for degradation of domain wall motion in multiaxial ferromagnetic crystals as a function of density of point defects.[28] Boser expanded this work to ferroelectric $BaTiO_3$, showing an inverse (N^{-1}) relationship of the irreversible Rayleigh parameter (a measure of domain wall mobility) on defect concentration as a result of Fe doping.[194]

Compared to the above work, we introduce an effective, fitted coefficient, k, in order to account for more complex material variations, which implies, for ferroelectric materials, domain size and orientation, grain boundary density and morphology, the effects of defect-influenced volumes on neighboring regions, number of defects necessary to modify response in a given volume, *etc.* Thus, k encompasses the variety of inherent material effects that will lead to deviations from an exact N^{-1} relationship of new defects contributing to response-altering defect interactions in a given discrete ferroelectric material volume. Furthermore, while Boser and Kronmüller demonstrated N^{-1} dependencies of domain wall motion on defect concentrations, thus implying only degradation of properties, previous work on chemical doping as well as recent radiation work by Saremi *et al.*, has shown enhancements to functional properties of ferroelectric materials, suggesting that deviations from a perfectly inverse decay are possible.[171,198] Thus, the use of the effective parameter k offers relative flexibility regarding material

behavior as a function of the number of defects (and specifically, TID). Inserting the weighting function into Equation 5-9, and solving, we arrive at a functional form:

$$V_{d,func} = 1 - e^{-\varphi_N\left(\frac{N^{1-k}}{1-k}\right)} \quad 5\text{-}11$$

For example, using the above expression, a virgin ferroelectric sample with no defects introduced by radiation (N = 0) yields $V_{d,func}$ = 0, meaning that the functional material volume affected by newly-created defect interactions is zero in the pristine, virgin state. This model can be used to study the degradation trend data as a function of radiation dose or other external "stimulus" (dopant concentration, for example) that changes the number of defects per arbitrary volume (concentration, assumed proportional to external "stimulus"). We observe that while newly-created or -activated defects are assumed to interact with a constant volume, φ_N, this parameter does not account for factors such as proximity to pre-existing defects or material anisotropy, *etc.* The effective rate of saturation, k, is able to account for these deviations from linear degradation of response. This effect is typically observed as an asymptotic trend in the response, where subsequently-formed defects result in reduced contributions to the overall change in response.

To correlate the above expression with the functional response of the material, we again consider the specific case of ferroelectric materials. The major contributor to the reduced functional response in irradiated ferroelectric materials has been shown to be degradation of the extrinsic response, *i.e.* increase in defect interactions with ferroelectric material volume through increased pinning of the domain walls by radiation-induced

defects.[32] We note that active defect interactions resulting in measurable changes to material response do not necessarily pin all functional response, but "pinned volume" is used hereafter to refer to volumes of the material in which defect interactions produce quantifiable changes in functional response.

If exposure to radiation results in defect creation, which translates into degradation of the functional properties, such degradation can be measured as a function of TID (where degradation is plotted as a positive value) (Figure 5-2). Hence, φ_N is positive for a degradation trend, and thus results in positive values of pinned volume, $V_{d,func}$, when substituted into Equation (5-11). Conversely, a negative value for φ_N represents an enhancement of response (due to an effective "reduction" of pinned volume. A flat degradation curve would correspond to $\varphi_N = 0$, indicating no decay in properties due to irradiation. A larger magnitude of φ_N signifies a greater interaction of the radiation-induced defects with the material, and increased degradation/enhancement of the functional properties. Therefore, φ_N can generally be considered as the global susceptibility of the material to radiation-induced defects.

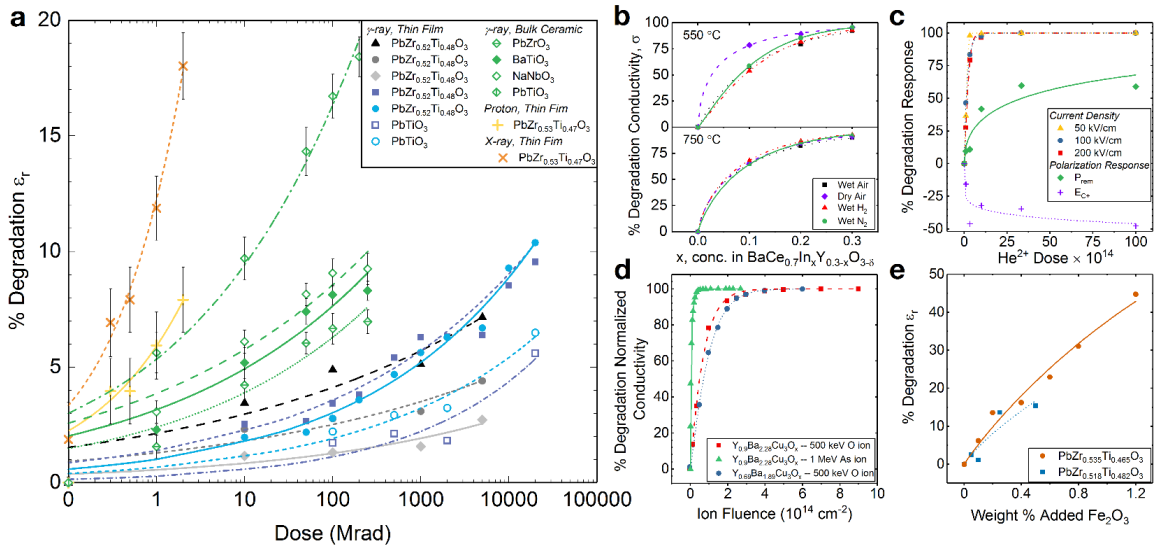

Figure 5-2 Application of the proposed model to previously-reported total ionizing dose (TID) studies in ferroelectrics and to dopant/radiation studies on various functional materials. (a) The effects of gamma, X-ray, and proton irradiation on the dielectric permittivity of various bulk and thin film ferroelectrics are shown. Data in gray/black shows gamma dose rate studies.[106] Blue symbols indicate degradation of the dielectric permittivity at positive and negative coercive voltages for PZT and lead titanate.[102] Green symbols show experiments on bulk ferroelectrics performed.[107] X-ray and proton irradiation of PZT shown in orange and yellow symbols, respectively.[97] (b) Indium doping in $BaCe_{0.7}In_xY_{0.3-x}O_{3-\delta}$ at different atmospheric conditions.[204] (c) He-ion implantation in epitaxial perovskite $PbTiO_3$ films.[198] (d) O- and As-ion irradiation of superconducting yttrium barium copper oxide (YBCO).[199] (e) Fe_2O_3 doping of ferroelectric lead zirconate titanate (PZT).[80] All data reproduced with permission.

We further note that both the φ_N and k parameters can be highly dependent on the specific microstructure, grain morphology, existing defects and charge, *etc.* In order to demonstrate the viability of the proposed model and weighting function to study radiation-induced defect interactions and defect engineering of functional oxides, we apply the model to prior literature reports on the effects of various types of radiation on multiple functional materials. Figure 5-2a shows the applicability of the proposed model to degradation of the dielectric permittivity in a range of ferroelectric materials exposed to irradiation under various measurement conditions.[97,102,106,107] The φ_N and k fitting parameters for the data are

reported in detail in Table 5-5 to Table 5-10. We note that the model is therefore applicable to a variety of radiation types – both ionizing (*e.g.*, gamma, X-ray) and heavy particles (*e.g.*, protons, neutrons) – as well as multiple functional properties, including dielectric, polarization, and electromechanical responses, as demonstrated in Figure 5-7 to Figure 5-12. The model is further expanded to include a broader class of defects in functional materials, demonstrating extensive applicability to doped barium cerate proton conductors for use in solid oxide fuel cells (SOFCs) (Figure 5-2b),[204] He^{2+}-ion implantation in epitaxial perovskite lead titanate (Figure 5-2c),[198] and heavy ion irradiation/implantation of yttrium barium copper oxide (YBCO) high-temperature superconductors (Figure 5-2d).[199] The model is also applicable for defect generation via chemical doping, as shown for examples of various impurity-doped ferroelectric ceramics (Figure 5-2e, Figure 5-13, and Figure 5-14, Table 5-11 and Table 5-12)[80,214] and X-ray synchrotron characterization of functional metal oxide memory cells (Figure 5-18).[210]

We note that the use of this phenomenological model allows for a quantitative comparison of the effects of various irradiation experiments on the materials' properties. For example, as evident by the qualitative data trends, the large degradation in the properties of PZT thin films exposed to X-ray and proton radiation translates into greater effective pinning of ferroelectric material volume, φ_N, compared to those exposed to gamma irradiation (Figure 5-2, Table 5-5 to Table 5-10). The result is a potentially greater number of radiation-induced defects that lead to increased pinning of material volume in X-ray-irradiated samples (compared to gamma), reflected by the greater material volume affected by defect-defect interactions, φ_N (Table 5-9). Further discussion of linear energy

transfer (LET) of various radiation types and its relation to defect generation/activation is available in Section 5.8 (Supplementary Information).

It is also interesting to note that the bulk ferroelectric samples' dielectric permittivity is more susceptible to gamma radiation exposure than thin film ferroelectric samples. We note that both end members of lead zirconate titanate solid solution are studied in the bulk form, and therefore the effects of Zr:Ti ratio (relative to other ferroelectric compositions) might be minimal. However, in general, the bulk ceramics show a larger value of φ_N (Table 5-8) than the thin films exposed to gamma-rays. Additionally, the values of *k* for gamma-irradiated bulk samples are among the highest shown in Figure 5-2a, with the exception of the work from Zhang *et al.*[106] The average grain size in polycrystalline thin films is typically smaller than in bulk ceramics (50-150 nm in thin films, compared to micron-sized grains in bulk ceramics), thereby increasing both grain and domain density in thin films.[38] The extent of pinning of newly-created/activated defect centers in samples with smaller grains/domains is potentially more contained than in samples with larger grains, *i.e.* smaller morphological features enact physical constraints on growth of defect-pinned regions. In other words, in bulk ferroelectrics with larger areas of (nearly) homogenous crystallinity, newly-formed defects may result in greater interactions and longer range effects on domain wall motion (Figure 5-1b and Figure 5-1c). Thus, in bulk samples with larger grains, not only should the volume pinned per new defect be greater, but saturation of response degradation should occur more quickly, as new defects are free to affect a larger volume without "containment" by grain boundaries.

Additionally, Daniels *et al.* have previously shown minimization of electrostatic potentials at grain boundaries in ferroelectric materials due to interactions of domains at

the same locations.[215] In irradiated ferroelectrics, such minimization could potentially reduce the deleterious effects on functional properties caused by radiation-generated charged defects. In polycrystalline samples with smaller grains and higher grain boundary density, this effect is enhanced relative to bulk samples with larger grains, and trends of milder degradation are observed. Namely, the mean volume pinned per new defect can be reduced, as charged defects are annihilated or compensated at the grain boundaries.

The above data support the fact that microstructural features play a critical role in defect interactions in ferroelectrics. To further elucidate this observation, in the following section we compare the effects of gamma radiation on polycrystalline PZT films with columnar and equiaxed grains.

5.5 Case Study: Effect of Microstructure on Defect Interactions in Ferroelectric Thin Films

PZT thin films with columnar and equiaxed grain structures were fabricated via chemical solution deposition (CSD) and exposed to ^{60}Co gamma radiation, from 0.2 to 10 Mrad, at a dose rate of approximately 600 rad(Si) s^{-1}. Measurements to probe the low-field relative dielectric permittivity (ε_r) as well as the remanent and saturated converse, effective, longitudinal piezoelectric responses ($d_{33,f,remanent}$ and $d_{33,f,saturation}$, respectively) were performed before and, at discrete dose intervals, after irradiation. Scanning electron microscopy (SEM), transmission electron microscopy (TEM), and transmission Kikuchi diffraction (TKD) were carried out (Figure 5-3) to observe and quantify grain orientation and size statistically (Table 5-2). Interpretation of the TKD results indicates primarily 100-

texture in samples with columnar grains (Figure 5-3c), while the samples with equiaxed grains are more randomly oriented, *i.e.* weaker texture (Figure 5-3f). The degradation trends for dielectric permittivity, ε_r, and effective longitudinal piezoelectric coefficient, $d_{33,f}$, as a function of TID, as well as the corresponding phenomenological models for the defect-defect interactions they represent are shown in Figure 5-4. The corresponding fitting parameters φ_N and k are reported in Table 5-1; full data sets are available in Table 5-3 and Table 5-4.

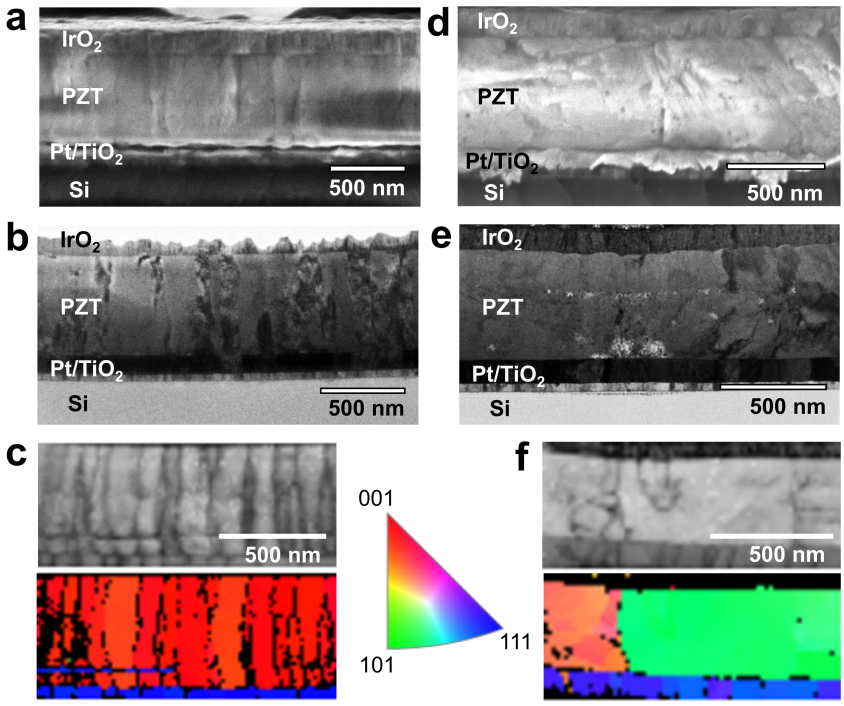

Figure 5-3 Microstructural characterization of PZT thin films with columnar and equiaxed grains. (a, d) SEM, (b, e) TEM, and (c, f) TKD cross-sectional images of columnar-grained films (a, b, c) processed using 2-methoxyethanol-based precursor PZT solution, and equiaxed-grained films (d, e, f) prepared using a methanol-based inverted mixing order PZT precursor solution. Note that the crystallographic poles noted for the pole figure are relative to the film normal (vertical direction in the image).

Table 5-1 Extracted parameters from application of phenomenological model to TID studies. Shown are dielectric permittivity and effective longitudinal piezoelectric response in gamma-irradiated PZT thin films. Data is extracted by fitting Equation (5-11) to percent change of given functional response measurement *vs.* radiation dose. Note that values of φ_N are multiplied by three orders of magnitude to make interpretation more manageable.

	Columnar		Equiaxed	
	$\varphi_N \times 10^3$	k	$\varphi_N \times 10^3$	k
ε_r	19	0.48	26	0.79
$d_{33,f,\text{remanent}}$	185	0.66	142	0.77
$d_{33,f,\text{saturation}}$	7	0.60	1	0.62

A comparison of the TID trend quantification for dielectric and electromechanical responses shows that the values for the change in volume pinned per defect, φ_N, are comparable (same order of magnitude) for individual measurements on samples with columnar and equiaxed grains. However, focusing on response-specific trends, large effective volume pinned is observed for measurements of ε_r and $d_{33,f,remanent}$ in both samples, while φ_N of $d_{33,f,saturation}$ is somewhat negligible comparatively, for both samples. We note that the saturation values are measured under high DC electric fields, while the remanent values and the dielectric permittivity are measured under zero DC bias and low AC electric fields. The observed trend in φ_N, therefore, suggests that defects activated via gamma irradiation are likely of relatively low energy. That is, at the low applied electric field used to measure remanent response, the pinning strength of the defects is sufficient to result in large degradation of functional properties. At the elevated applied electric field used to measure saturated electromechanical response (250 kV cm^{-1} DC bias), the drive for domain wall motion exceeds that of the defect, and the degradation of functional response is, at least partially, overcome, even at higher TID levels. Indeed, the values of φ_N for $d_{33,f,saturation}$

measurements, are very similar to those extracted from work by Gao *et al.*, for measurements of dielectric permittivity of irradiated PZT thin films with an applied 133 kV cm^{-1} DC bias.[216] The implication that applied electric field potentially negates the deleterious effects of defects created by gamma irradiation is not new. However, the ability to quantify and compare high- and low-field degradation behavior of ferroelectrics with distinct morphologies across a range of radiation doses is particularly advantageous for tailoring material response to meet a variety of distinct operational requirements.

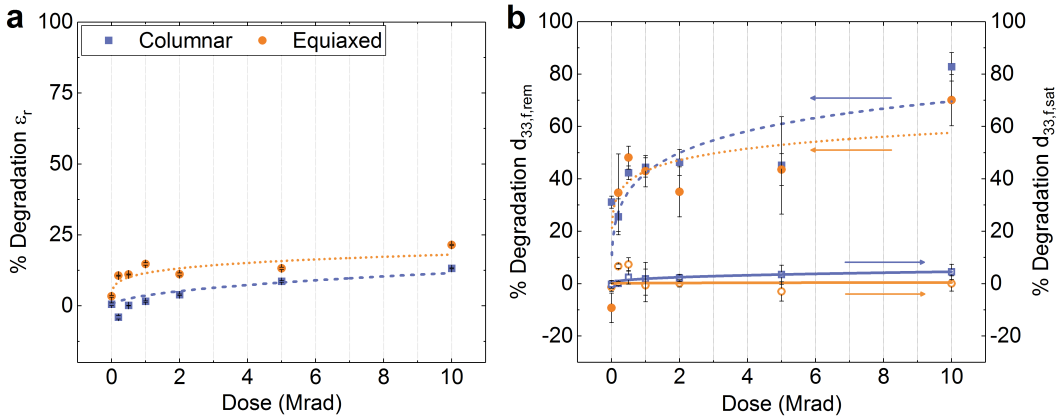

Figure 5-4 Application of the proposed model (curves) to experimental data from PZT thin films with columnar and equiaxed grain structure. (a) Plots of relative, low-field dielectric permittivity, and (b) saturation and remanent piezoelectric as a function of radiation dose,[217] and the fitted model to each data set. Error bars show standard error of the sample mean. Fitted parameters are detailed in Table 5-1.

Interestingly, the effective rate of defect saturation, *k*, is consistently greater for samples with equiaxed grains than those with columnar grains. Claeys and Simoen have previously suggested that defects created or activated in functional materials by exposure to ionizing radiation are proportional to the surface area of grain boundaries with which they interact.[218,219] A variety of reports on irradiation of functional oxide materials have shown increased radiation hardness for materials with increasingly small grain structures,

and thus, higher grain boundary density.[220,221] The samples with columnar grains in this work have a smaller volume than the samples with equiaxed grains, and a surface-area-to-volume ratio that is more than twice as large (Table 5-2). Increased grain boundary density yields a greater number of sites for defect accumulation, acting as effective defect "sinks," and potentially reducing their deleterious effects on functional response. The result is a slower rate of saturation of response degradation, as the effects of a portion of newly-formed defects are neutralized by the grain boundaries. Furthermore, the smaller grains and greater surface-area-to-volume ratio for columnar-grained samples may translate to better "compartmentalization" of functional material volume, thus limiting the effects of newly-created defects to smaller ferroelectric material volumes, and reducing the rate of defect saturation. These effects are both emphasized for samples with columnar grains, where k is observed to be closer to zero (linear decay), and is especially apparent in the decay of dielectric permittivity ($k = 0.48$) (Figure 5-4a). Also noteworthy is the fact that the mean value of k for equiaxed samples ($k = 0.73 \pm 0.09$) is in close agreement with the work by Kronmüller and Boser, as well as prior work published on irradiation of ferroelectrics, as discussed previously.[28,194]

5.6 Conclusions

In summary, we have demonstrated a phenomenological model for quantification of the effects of defect interactions in functional materials. While we have specifically demonstrated applicability to ferroelectric thin films to study the effects of microstructure on defect interactions with the material, the model presented is adaptable to a multitude of

functional materials, *i.e.*, wherever the functional response is derived from and/or is affected by some degree of defect interactions. We have further displayed the proposed model's versatility by comparing data from the literature not only on bulk and thin film ferroelectrics, but also on a variety of functional oxides, including doped barium cerate for SOFCs, He^{2+}-ion implanted epitaxial perovskite lead titanate, and heavy ion-bombarded superconducting YBCO. Furthermore, we show that irradiation of materials can be a strong alternative approach to chemical doping, due to the relative simplicity and favorable additive nature of radiation dose experiments. Correlation of materials' properties to radiation dose allows for careful, on-demand modifications to properties and the ability to tailor functional response to the intended application. Ideally, the demonstrated method for quantification of defect interactions will stimulate further advances in defect engineering of functional materials. Studies on various grain morphologies, preferred crystallographic orientation, radiation types, measurement conditions, *etc.*, will offer further application and refinement of the model proposed here. However, more important are the implications of radiation studies for direct evaluation and quantification of defect-defect interactions in functional materials without the complicated effects of chemical doping. The resulting theoretical and empirical knowledge regarding defect interactions encourages methods for defect engineering of a broad class of functional metal oxide materials.

5.7 Experimental Methods

5.7.1 PZT Thin Film Preparation

$PbZr_{0.52}Ti_{0.48}O_3$ (PZT) thin films were fabricated at the US Army Research Laboratory using 150 mm-diameter 100-silicon wafers consisting of 100 nm Pt/35 nm TiO_2/500 nm SiO_2/Si.[132] A seed layer of $PbTiO_3$ was deposited to induce 001-texture of the PZT thin films.[131] Two separate PZT sol-gel solutions were prepared, one via a 2-methoxyethanol (2-MOE) route at the US Army Research Laboratory, and the other using a methanol-based inverted mixing order (IMO) process at Sandia National Laboratories.[110,131] Both 2-MOE-based and IMO solutions were deposited via chemical solution deposition, resulting in films with thicknesses of 500 ± 14 nm. IrO_2 top electrodes were selected for continuity with prior work;[32] 100 nm thick electrodes were sputter-deposited onto the wafer at 500 °C and processed with a post-deposition anneal at 650 °C in flowing O_2 for 30 min. The top electrode and PZT layer were patterned using argon ion milling and a series of additional metallization steps to create interconnects to device structures. This general process is outlined elsewhere.[100]

5.7.2 Irradiation

The fabricated samples were exposed to radiation from a ^{60}Co gamma source at doses ranging from 0.2 to 10 Mrad (equivalent Si dose) at a dose rate of approximately 600 rad(Si) s^{-1} at the US Naval Research Laboratory. All electrodes were left floating during radiation exposure.

5.7.3 Functional Response Characterization

Dielectric, polarization, and electromechanical responses of the samples were fully characterized at Georgia Institute of Technology both before and after irradiation, including measurements of low-field permittivity and DC electric field-dependent piezoelectric response, followed by irradiation and repetition of all experiments. A detailed summary of these measurements for samples with both columnar and equiaxed grain structures as a function of radiation dose is shown in Table 5-14 and Table 5-15. A 600 second poling step at 10 V, approximately five times the coercive voltage, V_C, was performed directly before the electromechanical measurements in both pre- and post-irradiation measurement sets in order to eliminate anisotropic polarization contributions to electromechanical response. All measurements were performed on the same sample/electrode both before and after irradiation in order to monitor precise changes in response behavior. Low-field dielectric permittivity (ε_r) measurements were conducted at 100 mV and 1 kHz using an Agilent 4284A precision LCR meter. Measurements of the converse, effective longitudinal piezoelectric response ($d_{33,f}$) were performed on an aixACCT double beam laser interferometer (DBLI) measurement system up to 300 kV cm^{-1} DC bias with an overlapping AC signal $V_{AC} \approx 0.5V_C$. All measurements reported are subject to experimental error up to 3-5%, due to sample variability.

5.7.4 SEM/TEM/TKD Analysis

Cross-sectional scanning electron microscopy (SEM), transmission electron microscopy (TEM), and transmission Kikuchi diffraction (TKD) (Figure 5-3) were performed at North Carolina State University (NC State). Samples were sputter coated with a 20 nm-thick Au layer to increase sample conductivity during SEM imaging. Cross-sectional characterization was performed using an FEI Verios field-emission scanning electron microscope.

Before milling the samples under focused ion beam (FIB) for TEM and TKD, they were sputter coated with a 20 nm-thick Au layer to increase sample conductivity and to avoid drift. A 3 μm-thick Pt layer was deposited under FEI Quanta 3D FEG to protect the sample surface from electron and ion damage. Cross-sectional TKD samples were prepared under FEI Quanta 3D FEG using both electron and ion beam guns (SEM/FIB). TEM imaging was performed on the FIB samples using a JEOL 2000-FX scanning transmission electron microscope. Using an Oxford Instruments NordlysNano electron backscatter diffraction (EBSD) detector, Kikuchi diffraction patterns were mapped out under 30 kV with Oxford Instruments Aztec software. TKD data was processed using the HKL CHANNEL5 program Tango.

5.7.5 Crystallographic Phase Analysis

Crystallographic phase analysis was performed to confirm the texture of PZT samples prepared via 2-methoxyethanol-based (2-MOE) and acetic acid-based inverted

mixing order (IMO) chemical solution deposition (CSD) processes (see Experimental Section). Figure 5-5 shows baseline X-ray diffraction (XRD) phase analysis of the films deposited using 2-MOE-based and IMO-prepared solutions, and the resulting columnar and equiaxed grain morphologies, respectively.

Noteworthy are the large 100- and 200-textures in the columnar sample, indicating highly-textured samples; and the relatively large 101-peak in the equiaxed sample compared to the 100- and 200-peaks, indicating their more equiaxial nature and random orientation.

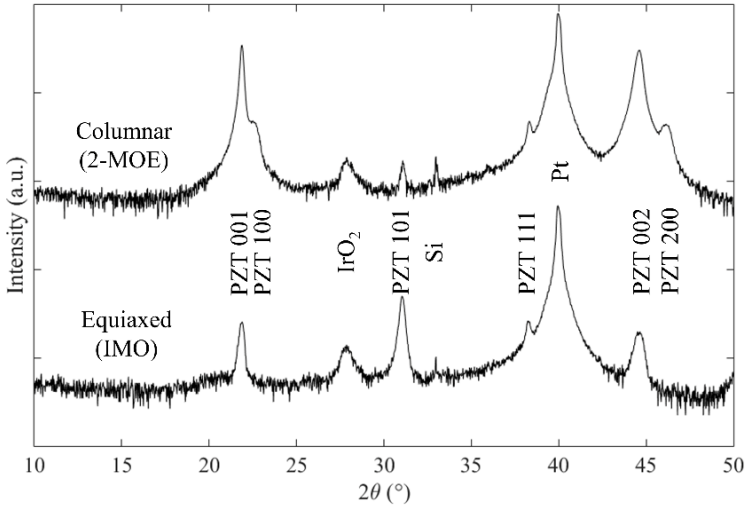

Figure 5-5 X-ray diffraction crystallographic phase analysis comparing representative samples with columnar (top) and equiaxed (bottom) grain structures prepared using 2-MOE and IMO PZT solutions, respectively. Note the large relative intensity of the 100-peak for samples with columnar grains while the opposite behavior for the 101-peak is found for samples with equiaxed structure.

5.7.6 TEM/TKD Statistical Analysis

Cross-sectional transmission electron microscopy (TEM) and transmission Kikuchi diffraction (TKD) were performed at North Carolina State University (NC State) to observe domain and grain structure in the samples (Figure 5-3b, Figure 5-3e). The regions of mottled contrast, primarily visible in the sample with columnar grains (Figure 5-3b), indicate potential nanodomains or striated 90° domain walls.[222,223]

TKD and TEM images were analyzed to calculate statistical values of several grain size characteristics, including mean in-plane grain size, mean out-of-plane grain height, and mean size of multi-grain regions of similar dimension (Table 5-2). These statistics aid in analysis of samples with columnar *vs.* equiaxed grains.

Table 5-2 Statistical size measurements for samples with columnar and equiaxed grain structures, based on measurements of mean grain height and width (in-plane size). Columnar grains are assumed to be cylindrical, with the axis normal to the substrate, while equiaxed grains are assumed to be ellipsoidal, with the longest axis normal to the substrate and the remaining two axes equal to the in-plane grain size.

Grain structure	Mean grain height (nm)	Mean in-plane grain size (nm)	Mean grain surface area (cm^2)	Mean grain volume (cm^3)	Surface area per volume	Number of electron-hole pairs (ehp) per grain·Mrad
Columnar (cylindrical)	391 ± 220	66 ± 27	8.8×10^{-10}	1.3×10^{-15}	6.8×10^{5}	1.2×10^{5}
Equiaxed (ellipsoidal)	215 ± 109	177 ± 160	11.3×10^{-10}	3.6×10^{-15}	3.1×10^{5}	3.4×10^{5}

5.7.7 Functional Response Characterization

Dielectric, polarization, and electromechanical responses of the samples were fully characterized at Georgia Institute of Technology both before and after irradiation, including measurements of low-field permittivity and DC electric field-dependent electromechanical response, followed by irradiation and repetition of experiments (see Experimental Section). A summary of these measurements for samples with both columnar and equiaxed grain structures as a function of radiation dose is shown in Table 5-3. A 600 second poling step at 10 V, approximately five times the coercive voltage, V_C, was performed directly before the electromechanical measurements in both pre- and post-irradiation measurement sets in order to eliminate anisotropic polarization contributions to the electromechanical response. All measurements were performed on the same sample/electrode both before and after irradiation in order to monitor precise changes in response behavior. Low-field dielectric permittivity (ε_r) measurements were conducted at 100 mV and 1 kHz using an Agilent 4284A precision LCR meter. Measurements of the converse, effective longitudinal piezoelectric response ($d_{33,f}$) were performed on an aixACCT double beam laser interferometer (DBLI) measurement system up to 300 kV cm^{-1} DC bias with an overlapping AC signal $V_{AC} \approx 0.5\ V_C$. All measurements reported are subject to experimental error up to 3-5%, due to sample variability.

Table 5-3 Measured dielectric, polarization, and electromechanical responses at increasing radiation doses, for PZT thin films with columnar and equiaxed grain structures. Percent change is measured from 0 to 10 Mrad radiation exposure. Uncertainties expressed represent standard error from the mean to one significant figure. Measurement values are reported to the same decimal place as uncertainty for said measurement.[172]

	Dose (Mrad)	Virgin	0.2	0.5	1.0	2.0	5.0	10.0
ε_r	Col	1222 ± 6	1297 ± 10	1229 ± 4	1208 ± 4	1188 ± 3	1127 ± 4	1083 ± 2
	Eqx	1357 ± 4	1323 ± 2	1215 ± 6	1284 ± 4	1284 ± 5	1262 ± 6	1175 ± 2
$d_{33,f,remanent}$ (pm V^{-1})	Col	34 ± 4	28 ± 1	25 ± 1	22 ± 1	23 ± 2	24 ± 6	7 ± 2
	Eqx	43 ± 3	48 ± 6	25 ± 3	33 ± 3	30 ± 4	30 ± 2	19 ± 5
$d_{33,f,saturation}$ (pm V^{-1})	Col	79 ± 2	76 ± 1	75 ± 0	76 ± 3	78 ± 1	76 ± 1	77 ± 2
	Eqx	68 ± 3	64 ± 1	63 ± 1	64 ± 1	59 ± 2	64 ± 1	64 ± 6

From the data inTable 5-3, degradation trends were extracted by calculating the percent change in response from the virgin control sample. This data has been tabulated in Table 5-4.

Table 5-4 Mean percent change in measured dielectric, polarization, and electromechanical responses as a function of radiation dose, relative to virgin control sample, for PZT thin films with columnar and equiaxed grain structures. Negative numbers represent a degradation of response. All measurements are subject to a 3 to 5% standard measurement error.

	Dose (Mrad)	Virgin	0.2	0.5	1.0	2.0	5.0	10.0
	% Change	%	%	%	%	%	%	%
ε_r	Col	-1	4	0	-2	-4	-9	-13
	Eqx	-3	-11	-11	-15	-11	-13	-22
$d_{33,f,remanent}$	Col	-31	-26	-42	-44	-46	-45	-83
	Eqx	9	-35	-48	-43	-35	-44	-70
$d_{33,f,saturation}$	Col	0	0	-2	-2	-2	-3	-5
	Eqx	1	-7	-7	1	0	3	0

5.7.8 Electron-Hole Pairs Generated by Gamma Irradiation

Exposure to gamma radiation results in the formation of electron-hole pairs (ehp) in ferroelectric PZT. Work by Leray *et al.*, showed that radiation dose in PZT is 1.23 times that of the dose felt in Si, *i.e.,* 1 Mrad(Si) = 1.23 Mrad (PZT).[101] Using a mean density of PZT as 7.6 g cm^{-3} and 100 rad = 1 Gy = 1 J kG^{-1} we can calculate the total energy deposited:

$$Energy\ Deposited = 5.84{\times}10^{20}\ eV\ cm^{-3}\ Mrad(Si)^{-1}$$

Using 6.25 eV as the mean energy per ehp, we arrive at

$$Number\ of\ ehp = 9.34{\times}10^{10}\ ehp\ cm^{-3}\ Mrad(Si)^{-1}$$

We can apply this result to calculate the number of ehp per grain. Assuming that columnar grains are roughly cylindrical (with axis normal to substrate), and equiaxed grains are ellipsoidal (with a = grain height and $b = c$ = in-plane grain size), we can calculate the number of ehp per grain from data extracted from Figure 5-3. Table 5-2 shows these calculations and resulting number of ehp per grain—the results indicate that over twice as many ehp are generated per equiaxed grain compared to columnar grains (3.5×10^5 ehp/equiaxed *vs.* 1.4×10^5 ehp/columnar).

5.8 Supplementary Information

5.8.1 Ferroelectric-Specific Defect Interactions

Generally, radiation interacts with a material by causing either ionization or displacement events. Lower-energy sources – *e.g.*, X-rays and gamma rays – transfer energy to a material via electron interactions, ionizing the material with which they interact to form electron-hole pairs, and at higher energies, vacancy-interstitial pairs.[87,88] Irradiation with massive particles, such as protons and neutrons, transfers energy to a material through both electron interactions, as described previously, and atomic interactions, potentially resulting in displacement of atoms (vacancy-interstitial pairs) and subsequent defect cascades.[89]

In a ferroelectric material, radiation-induced ionization and displacement events can potentially increase the stable defect concentrations, including the trapping of charges at preexisting defects, thus modifying the energy associated with such defects' energy, their mobility, and other forms of interaction with the material. Prior work on the effects of radiation on ferroelectric materials has shown a direct correlation between total radiation dose and degradation of functional properties.[32,90,92-96] Specifically, trapped charges generated as a result of X-ray, proton, gamma and neutron irradiation can result in degradation of polarization, dielectric, and electromechanical response, primarily through changes to the energies of defects of the ferroelectric material.[32,40,97,98,100] In addition to ionizing energy transfer to the material, high-energy electrons and massive energetic particles (protons, neutrons, alpha-particles, *etc.*) also transfer energy via nuclear interactions that lead to direct atomic displacement. These radiation-induced displacements

may degrade the functional ferroelectric response in a fashion that is qualitatively similar to that of ionization-related defects (especially for point defects like Frenkel pairs) or may give rise to unique degradation modes in the case of multi-atom defects (defect clusters) that span over larger volumes. Ultimately, radiation-induced modification of functional response in ferroelectrics is the result of changes in defect concentration and energy in the material. Therefore, irradiation can be leveraged as a method for controlled introduction and/or activation of defects in these material, thus modifying material properties and functional response, to meet the needs of a variety of applications. Such methods stand to benefit from robust quantification and phenomenological modeling to more adequately and conveniently compare material performance as a function of radiation.

5.8.2 Specifics of Fitting the Model to Data

The derivation of the phenomenological model describing radiation-induced defect interactions, as described above, results in the final functional form describing the normalized volume of functional material affected by stimulated defect interactions:

$$V_{d,func} = 1 - e^{-\varphi_N\left(\frac{N^{1-k}}{1-k}\right)} \qquad 5\text{-}11$$

We can then use this to fit the degradation trend data and extract the φ_N and k parameters. Figure 5-6 shows the effects of arbitrary changes to the φ_N and k parameters as a function of a given radiation dose. It is worth noting that fittings are done to the decimal value of

degradation in response, *e.g.*, for 5% degradation, a value of 0.05 is used for the fitting. Additionally, degradation is assumed to be positive, as it is the result of increases to the volume impacted by defect interactions. The result in Equation 5-11 is robust and capable of fitting both degradation and enhancement data. This derivation assumes that the degradation trend data begins at zero change in response for zero defects/radiation dose. Realistically, materials contain inherent defects prior to irradiation. However, given the nature of percent changes in measured response of control samples, degradation trend data should conceivably show minimal change at zero exposure to radiation.

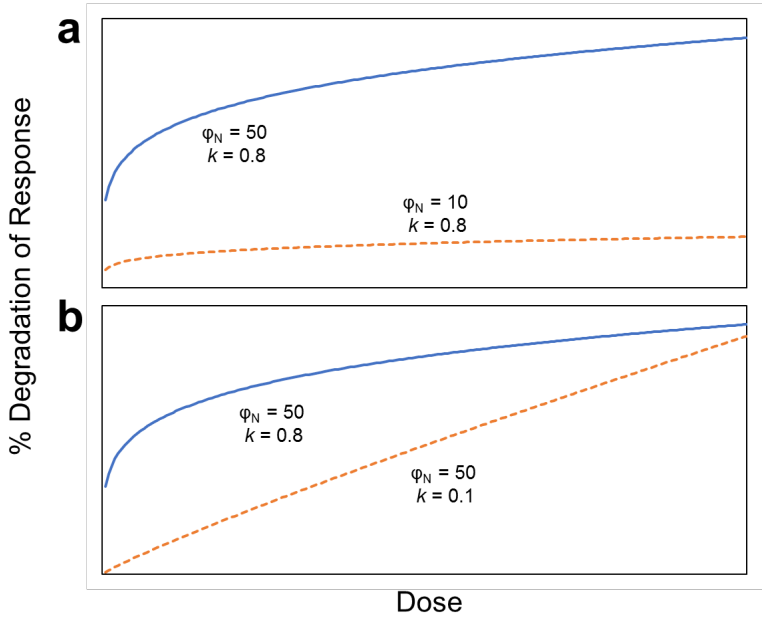

Figure 5-6 Representative plots showing the effects of changes to the effective volume impacted by defect interactions, φ_N, and the effective rate of defect saturation, *k*, for degradation of an arbitrary response parameter. (a) shows changes to φ_N while holding *k* constant, and (b) shows the effects of changing *k*, while holding φ_N constant.

5.8.3 Application of Phenomenological Model to Literature Data

We apply the phenomenological model developed in this work to data reported in the literature from X-ray, gamma, proton, and neutron irradiation studies of various ferroelectric materials, both in thin films and bulk forms.[40,92,97,102,106,107,216] The results of fitting the model are tabulated in Table 5-5 to Table 5-10, and results from individual studies are also shown in Figure 5-7 to Figure 5-12. Notably, by comparing the values of φ_N within individual publication data from the literature, the phenomenological model is able to consistently and accurately reflect the conclusions of the authors when studying a variety of processing and measurement conditions, including dose rate, bias conditions, and different radiation types. We have also applied the model to the results of chemical doping in various ferroelectric materials (Table 5-11 and Table 5-12, Figure 5-13 and Figure 5-14),[80,214] as well as ion irradiation of yttrium barium copper oxide (YBCO) superconductors (Table 5-13, Figure 5-15), He^{2+}-ion implantation of epitaxial ferroelectric thin films (Table 5-14, Figure 5-16), and In-doping of yttrium barium cerate proton conductors for solid oxide fuel cells (SOFC) (Table 5-15, Figure 5-17). Error bars are reproduced when available.

Studying the effects of various radiation types on ferroelectric thin films from Figure 5-11 and Table 5-9, we note that linear energy transfer (LET) in PZT for X-rays (10 keV), protons (3 MeV), and gamma rays (1.25 MeV) are 0.77 keV μm^{-1}, 38.25 keV μm^{-1}, and 0.05 keV μm^{-1}, respectively.[224-226] Notably, the LET for gamma radiation in PZT is much lower than both X-rays and protons. Comparing X-ray and gamma irradiation, the number of incident photons will be greater for gamma rays, but with a greater mean

distance between them. Thus, fewer X-rays may impact the sample, but of those that do, more electron-hole pairs are generated. Additionally, at the lower energy of X-rays, there are many photoelectric lines (*e.g.*, K, L, M, *etc.*) that potentially result in diverse ionization states of affected atoms, compared to simply ejecting outer shell electrons in the case of gamma irradiation.

On the other hand, the LET of protons is two orders of magnitude greater than that of X-rays. A greater dose rate conceivably translates to greater charge generation per unit volume, which could potentially increase the rate of recombination. Evidence of this effect is present in observed local enhancement of functional properties measured by Bastani *et al.*, in samples irradiated with protons (Figure 5-11).[97] Furthermore, smaller values of φ_N, the effective volume affected by radiation-induced defect interactions, in samples irradiated with protons compared to X-rays, support this hypothesis. Defects that could potentially degrade functional response are annihilated or their charge reduced to less-deleterious states, and the volume they pin is reduced. Additionally, the dose rate of protons is approximately 300 times that of X-rays, meaning 300 times fewer protons impact the surface than X-rays per unit time. Data from Oldham and McLean on irradiated MOS oxides demonstrated that the fractional hole yield for ionizing radiation (gamma, X-ray, electrons) was much greater than that of proton and alpha particle radiation, suggesting a more exaggerated interaction of ionizing radiation with the exposed material compared to particles.[227] The net result is a smaller mean volume affected by radiation-induced defect interactions in samples irradiated with protons compared to X-rays or gamma rays, where the fractional charge yield is greater (than that of proton irradiation) (Table 5-9).

Table 5-5 Extracted φ_N and k parameters from fitting equation (S10) to degradation data of various parameters from Zhang *et al.*[106] Note that values of φ_N are multiplied by three orders of magnitude to make interpretation more manageable.

Zhang *et al.*	0.5 kGy hr^{-1}		2.5 kGy hr^{-1}		25 kGy hr^{-1}	
	$\varphi_N \times 10^3$	k	$\varphi_N \times 10^3$	k	$\varphi_N \times 10^3$	k
ε_+	3	0.85	2	0.85	1	0.82

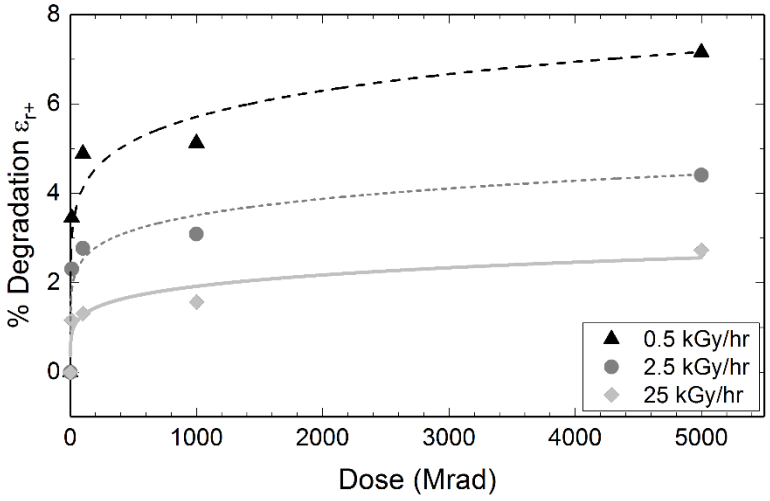

Figure 5-7 Application of phenomenological model (curves) to work on the effects of gamma irradiation dose rate on degradation of dielectric permittivity measured at the positive coercive field (ε_{r+}) of PZT thin films.[106]

Table 5-6 Extracted φ_N and k parameters from fitting Equation 5-11 to degradation data of various parameters from Gao *et al.*[216] Note that values of φ_N are multiplied by three orders of magnitude to make interpretation more manageable.

Gao *et al.* (1999)	0V Bias		4V Bias	
	$\varphi_N \times 10^3$	k	$\varphi_N \times 10^3$	k
ε_+	13	0.55	3	0.78
ε_-	16	0.57	4	0.77

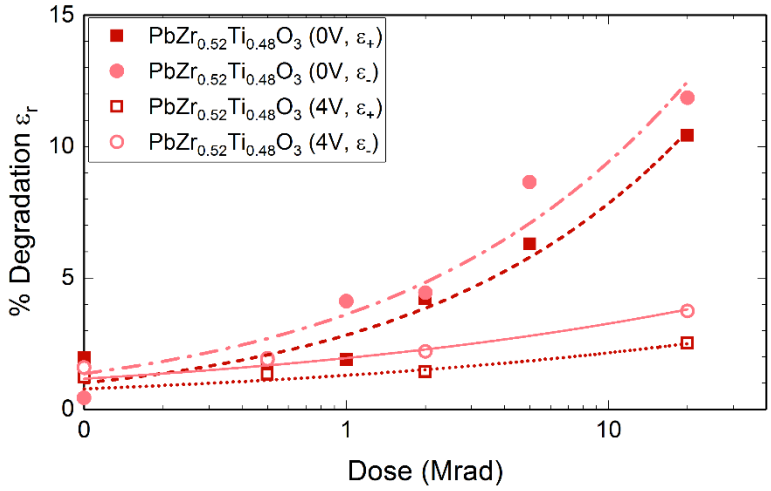

Figure 5-8 Application of phenomenological model (curves) to work done by on the effects of bias conditions on gamma radiation-induced degradation of dielectric permittivity measured at the positive and negative coercive fields (ε_{r+} and ε_{r-}) of PZT thin films grown via pulsed laser deposition (PLD).[216]

Table 5-7 Extracted φ_N and k parameters from fitting Equation 5-11 to degradation data of dielectric permittivity measurements on $PbZr_{0.52}Ti_{0.48}O_3$ and $PbTiO_3$.[102] Note that values of φ_N are multiplied by three orders of magnitude to make interpretation more manageable.

Gao *et al.* (1998)	ε_+		ε_-	
	$\varphi_N \times 10^3$	k	$\varphi_N \times 10^3$	k
$PbZr_{0.52}Ti_{0.48}O_3$	3	0.79	2	0.76
$PbTiO_3$	1	0.70	2	0.77

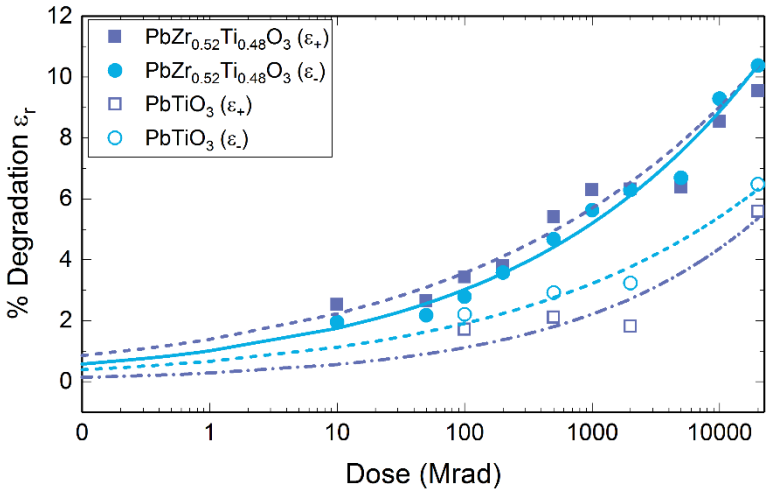

Figure 5-9 Application of phenomenological model (curves) to work done on the effects of gamma irradiation on degradation of dielectric permittivity measured at the positive and negative coercive fields (ε_{r+} and ε_{r-}) in ferroelectric PZT and lead titanate thin films.[102]

Table 5-8 Extracted φ_N and k parameters from fitting Equation 5-11 to degradation data of various parameters from Solovev *et al.*[107] Note that values of φ_N are multiplied by three orders of magnitude to make interpretation more manageable.

Solovev *et al.*	ε_r	
	$\varphi_N \times 10^3$	k
$SrTiO_3$	-1	0.95
$PbZrO_3$	5	0.79
$BaTiO_3$	6	0.80
$NaNbO_3$	6	0.82
$PbTiO_3$	14	0.75

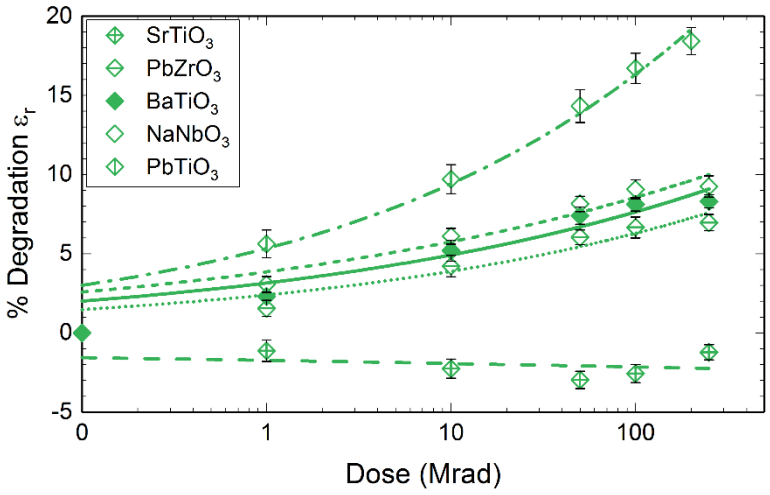

Figure 5-10 Application of phenomenological model (curves) to work done on gamma irradiation of bulk ceramic ferroelectrics and corresponding changes to dielectric permittivity.[107]

Table 5-9 Extracted φ_N and *k* parameters from fitting Equation 5-11 to degradation data of various parameters from Bastani *et al.*[97] Note that values of φ_N are multiplied by three orders of magnitude to make interpretation more manageable.

Bastani *et al.*	X-rays		Protons	
	$\varphi_N \times 10^3$	*k*	$\varphi_N \times 10^3$	*k*
ε_r (low-field)	76	0.41	26	0.57
$P_{remanent}$	79	0.57	50	0.40
ε_{init}	74	0.24	36	0.53
α	244	0.44	90	0.59
$\alpha/\varepsilon_{init}$	251	0.38	110	0.54
$d_{33,f,saturation}$	126	0.37	70	0.51

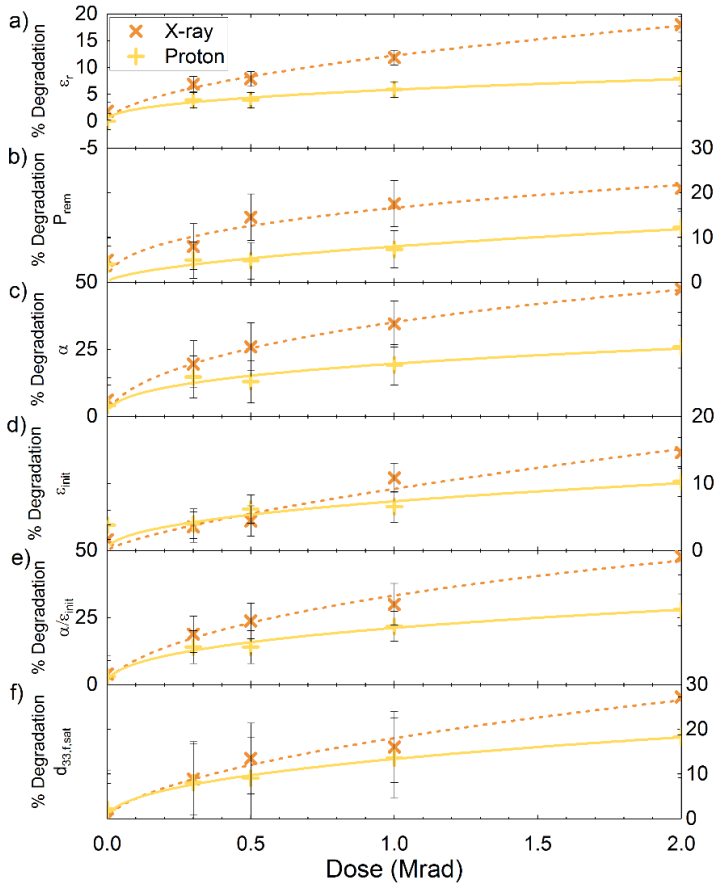

Figure 5-11 Application of phenomenological model (curves) to degradation of various functional responses of PZT films subjected to X-ray and proton irradiation.[97]

Table 5-10 Extracted φ_N and k parameters from fitting Equation 5-11 to dielectric degradation data as a function of neutron irradiation in PZT thin films by Graham *et al.*[40] Note that values of φ_N are multiplied by three orders of magnitude to make interpretation more manageable, and that fitting was done with neutron flux × 10^{15} cm^{-2}.

Graham *et al.*	$PbZr_{0.52}Ti_{0.48}O_3$ - CSD		$PbZr_{0.52}Ti_{0.48}O_3$ - IMO	
	$\varphi_N \times 10^3$	k	$\varphi_N \times 10^3$	k
ε_r (~5 kV cm^{-1})	75	0.81	47	-0.20
ε_r (~16 kV cm^{-1})	82	0.79	43	-0.36

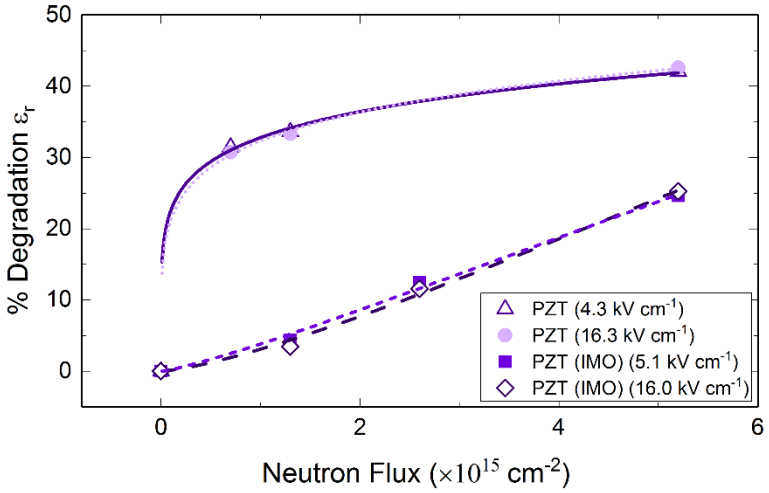

Figure 5-12 Application of phenomenological model (curves) to historical data on dielectric permittivity of neutron-irradiated in PZT thin films prepared via chemical solution deposition (CSD). Inverted mixing order (IMO) methods were used on two of the films. Non-IMO films are 350 nm thick and IMO films are 320 nm thick.[40]

Table 5-11 Extracted φ_N and k parameters from fitting Equation 5-11 to dielectric degradation data as a function of Ho_2O_3 dopant concentration in $BaTiO_3$ ceramics by Paunovic *et al.*[214] Note that values of φ_N are multiplied by three orders of magnitude to make interpretation more manageable.

Paunovic *et al.*	1320K sinter				1380K sinter			
	300K measure		T_C measure		300K measure		T_C measure	
	$\varphi_N \times 10^3$	k	$\varphi_N \times 10^3$	k	$\varphi_N \times 10^3$	k	$\varphi_N \times 10^3$	k
ε_+	623	0.40	963	0.17	483	0.06	1682	0.03

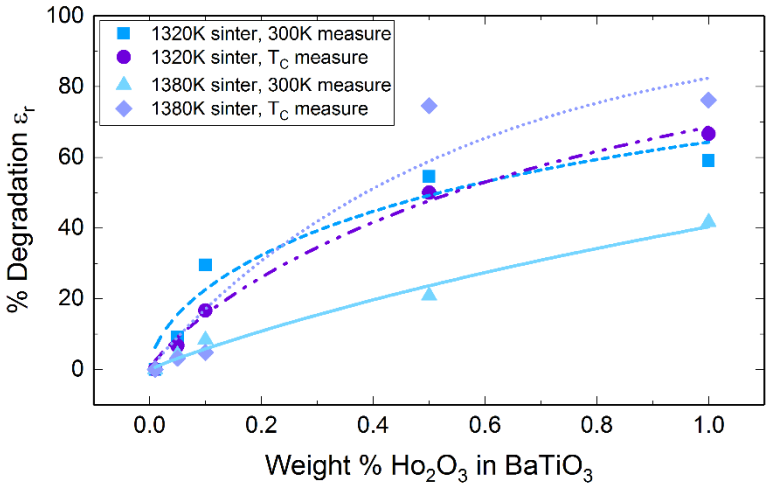

Figure 5-13 Application of phenomenological model (curves) to historical data on dielectric permittivity as a function of Ho_2O_3 dopant concentration in $BaTiO_3$ ceramics. Trends are shown for various sinter temperatures and measurement temperatures, including the Curie temperature, T_C.[214]

Table 5-12 Extracted φ_N and k parameters from fitting Equation 5-11 to dielectric degradation data as a function of Fe dopant in PZT by Weston *et al.*[80] Note that values of φ_N are multiplied by three orders of magnitude to make interpretation more manageable.

Weston *et al.*	$PbZr_{0.518}Ti_{0.482}O_3$		$PbZr_{0.535}Ti_{0.465}O_3$	
	$\varphi_N \times 10^3$	k	$\varphi_N \times 10^3$	k
ε_r	279	0.15	445	0.06

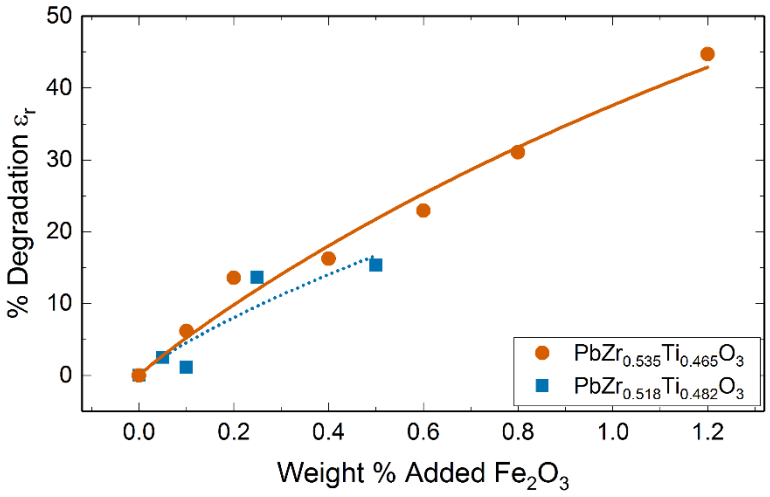

Figure 5-14 Application of phenomenological model (curves) to historical data on dielectric permittivity as a function of Fe_2O_3 dopant concentration in PZT ceramics.[80]

Table 5-13 Extracted φ_N and *k* parameters from fitting Equation 5-11 to degradation of conductivity in superconducting yttrium barium copper oxide (YBCO) by Clark *et al.*[199] Notably, the range of exposure doses for As ions is shorter than that of the O ions, but results in greater degradation and higher φ_N, suggesting that As ion bombardment is likely associated with a different degradation mechanism compared to O ions. Note that values of φ_N are multiplied by three orders of magnitude to make interpretation more manageable.

Clark *et al.*	$Y_{0.9}Ba_{2.28}Cu_3O_x$ (500 keV O ion)		$Y_{0.9}Ba_{2.28}Cu_3O_x$ (1 MeV As ion)		$Y_{0.69}Ba_{1.89}Cu_3O_x$ (500 keV O ion)	
	$\varphi_N \times 10^3$	k	$\varphi_N \times 10^3$	k	$\varphi_N \times 10^3$	k
Normalized Conductivity	1330	0.01	3540	0.44	1020	0.03

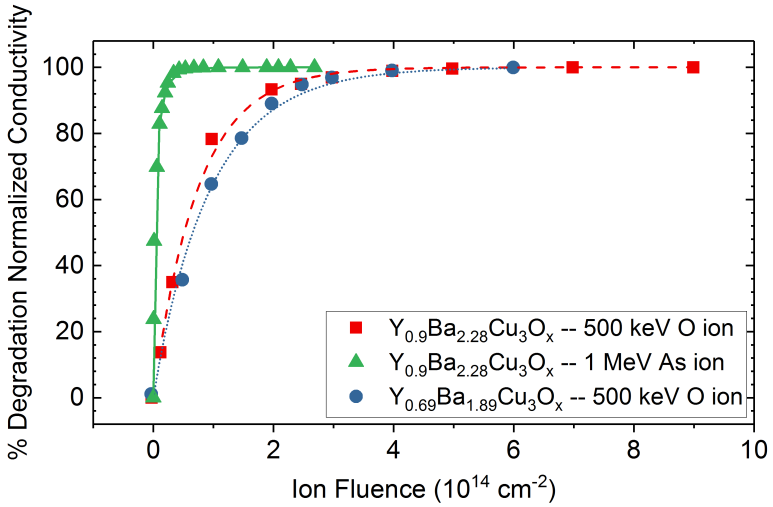

Figure 5-15 Application of phenomenological model (curves) to data on irradiation of yttria barium copper oxide (YBCO) in multiple stoichiometries, irradiated with O and As ions.[199]

Table 5-14 Extracted φ_N and k parameters from fitting Equation 5-11 to current density and polarization response degradation data as a function of He^{2+}-ion bombardment in ferroelectric thin films by Saremi *et al.*[198] Note that values of φ_N are multiplied by three orders of magnitude to make interpretation more manageable.

Saremi *et al.*	*Current Density*						*Polarization Properties*			
	50 kV/cm		100 kV/cm		200 kV/cm		P_{rem}		E_{C+}	
	$\varphi_N \times 10^3$	k	$\varphi_N \times 10^3$	k	$\varphi_N \times 10^3$	k	$\varphi_N \times 10^3$	k	$\varphi_N \times 10^3$	k
ε_+	611	0.004	547	0.13	410	0.00	64	0.55	-25	0.89

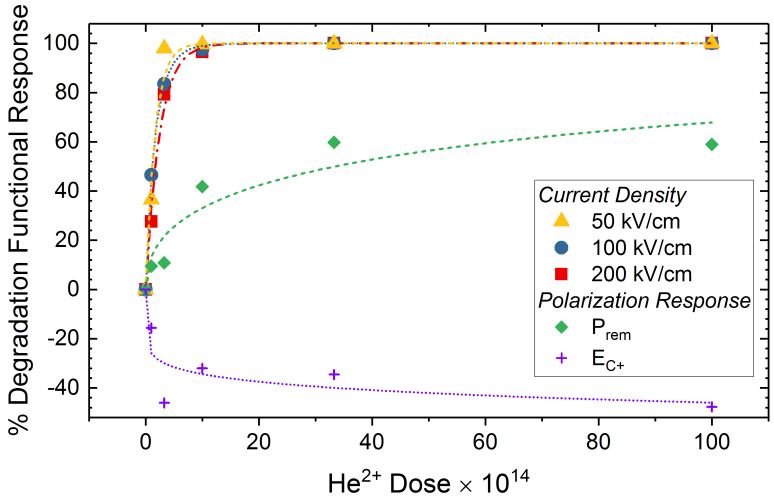

Figure 5-16 Application of phenomenological model (curves) to data on He^{2+}-ion bombardment of epitaxial ferroelectric thin films.[198]

Table 5-15 Extracted φ_N and k parameters from fitting Equation 5-11 to degradation of total conductivity of In dopant yttrium barium cerate, compiled by Medvedev.[204] Note that values of φ_N are multiplied by three orders of magnitude to make interpretation more manageable.

Medvedev	σ (550 °C)		σ (750 °C)	
	$\varphi_N \times 10^3$	k	$\varphi_N \times 10^3$	k
Wet Air	7200	0.05	3917	0.28
Dry Air	3590	0.40	4538	0.25
Wet H_2	11682	-0.13	5424	0.22
Wet N_2	13390	-0.13	6313	0.15

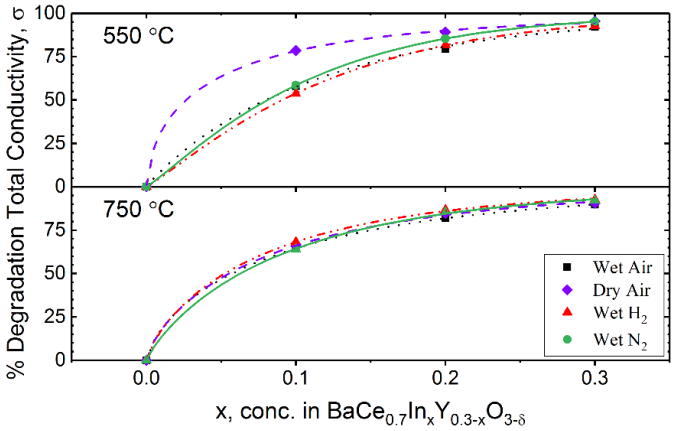

Figure 5-17 Application of phenomenological model (curves) to In-doping of yttrium barium cerate at multiple atmospheric conditions, for use in solid oxide fuel cell (SOFC) applications.[204]

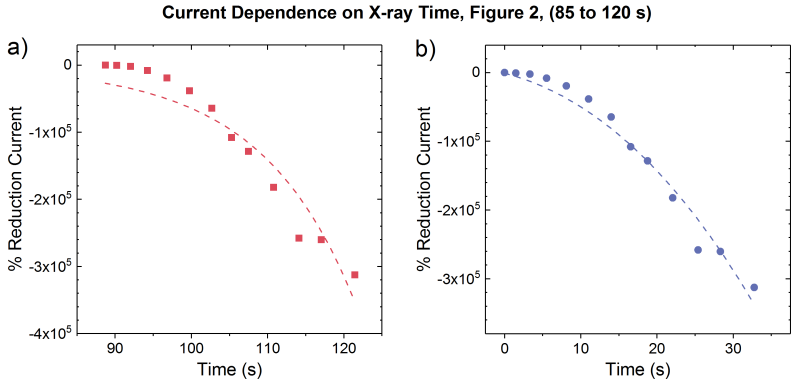

Figure 5-18 Application of phenomenological model (curves) to the effects of X-ray synchrotron experiments on current in Pt/TiO_2/Pt memory cells.[210] Data is extracted Figure 2 of the work by Chang *et al.*, from approximately 85 to 120 seconds, due to the continuous set of data at that location. Data has been normalized to the first point of the selected set, and the percent change from that point as the baseline plotted. The model fits well in (a), but does encounter some difficulty due to the starting point at 85 s and resulting discontinuity from 0 to 85 s. By shifting the initial point to 0 s (b), the model provides a better fit. We note that the model requires fitting the degradation/reduction of a property as a positive value (as explained in the manuscript), thus the negative trends here represent an increase to the electric current.

5.9 Acknowledgements

This work was supported by the Defense Threat Reduction Agency, Basic Research Award No. HDTRA1-15-1-0035 to Georgia Institute of Technology. The contents do not necessarily reflect the position or the policy of the federal government, and no official endorsement should be inferred. The authors gratefully acknowledge Jon Ihlefeld and Elizabeth Paisley for providing IMO PZT solutions and samples. They further acknowledge the contributions of Joel Martin and Brian Power of the Army Research Laboratory and Steven Isaacson of General Technical Services for their roles in the fabrication of the PZT thin films. This work was performed in part at the Analytical Instrumentation Facility (AIF) at North Carolina State University, which is supported by the State of North Carolina and the National Science Foundation (award number ECCS1542015). The AIF is a member of the North Carolina Research Triangle Nanotechnology Network (RTNN), a site in the National Nanotechnology Coordinated Infrastructure (NNCI).

CHAPTER 6. INTERNAL GRAIN BOUNDARY INTERFACES

The content in this chapter has been published in the *Journal of Applied Physics*.[217]

Effect of Microstructure on Irradiated Ferroelectric Thin Films

Steven J. Brewer, Hanhan Zhou, Samuel C. Williams, Ryan Q. Rudy, Manuel Rivas, Ronald G. Polcawich, Cory D. Cress, Evan R. Glaser, Elizabeth A. Paisley, Jon F. Ihlefeld, Jacob L. Jones, Nazanin Bassiri-Gharb

Journal of Applied Physics, vol. 121, no. 24, (2017), doi: 10.1063/1.4987032

6.1 Summary

This work investigates the role of microstructure on radiation-induced changes to the functional response of ferroelectric thin films. Chemical solution-deposited lead zirconate titanate (PZT) thin films with columnar and equiaxed grain morphologies are exposed to a range of gamma radiation doses up to 10 Mrad and the resulting trends in functional response degradation are quantified using a previously-developed phenomenological model. The observed trends of global degradation as well as local rates of defect saturation suggest strong coupling between ferroelectric thin film microstructure and material radiation hardness. Radiation-induced degradation of domain wall motion is thought to be the major contributor to the reduction in ferroelectric response. Lower rates of defect saturation are noted in samples with columnar grains, due to increased grain boundary density offering more sites to act as defect sinks, thus reducing the interaction of defects with functional material volume within the grain interior. Response trends for measurements at low electric field show substantial degradation of polarization and piezoelectric properties (up to 80% reduction in remanent piezoelectric response), while such effects are largely diminished at increased electric fields, indicating that the defects created/activated are primarily of low pinning energy. The correlation of film microstructure to radiation-induced changes to the functional response of ferroelectric thin films can be leveraged to tune and tailor the eventual properties of devices relying on these materials.

6.2 Introduction

Chemical solution deposition (CSD) of perovskite ferroelectric thin films has proven to be a cost-effective, large-area processing method for a variety of applications since it was first implemented by Budd *et al.* in the mid-1980s.[44,108] The fine microstructural control inherent to CSD has led to efficient processing of ferroelectric materials that demonstrate exceptional multifunctional dielectric, polarization, and piezoelectric responses without the need for expensive and size-limiting substrates and/or processing equipment.[1,228] Modification of CSD processing parameters can influence grain and domain morphology, chemical heterogeneity, defect concentrations, stress states, *etc.*, and thus leads to a wide range of functional material responses. Accordingly, many CSD-processed ferroelectrics, especially lead zirconate titanate (PZT), have found use in ferroelectric random access memories (FeRAM), multilayer ceramic capacitors, infrared (IR) detectors, acoustic and ultrasound devices, and microelectromechanical systems (MEMS) sensors and actuators.[118,127,128,229-233] However, new generations of novel microelectronics devices require operation in increasingly-demanding environments, including radiation-hostile settings like space or facilities managing radioisotopes. While many studies on the microstructure of CSD ferroelectric thin films have centered around (multi-) functional response enhancement, the coupling between microstructural variations and radiation tolerance is still unclear. In this work, we investigate the effects of grain morphology on radiation tolerance in gamma-irradiated ferroelectric PZT thin films.

Many ferroelectric thin films, such as $PbZr_{0.60}Ti_{0.40}O_3$, $PbZr_{0.52}Ti_{0.48}O_3$, and $BaTiO_3$ with columnar grain structure exhibit greater dielectric and electromechanical responses compared to similar compositions with equiaxed grains.[118,125,234] Furthermore, changes to

grain morphology can modify the energy landscape of the material, affecting the motion of internal interfaces, *e.g.*, domain walls and phase boundaries.[4,6,7,37] The nonlinear and hysteretic motion of these internal interfaces is largely responsible for the large magnitude of the functional response of ferroelectric thin films. Hence, any restriction to the motion of these interfaces can potentially result in degradation of the functional properties.[4,162] Interactions of lattice, vacancy, and point defects with internal interfaces like domain walls, can pin domain wall motion and result in degradation of the ferroelectric response.[6,7] Exposure to radiation can further aggravate these effects, resulting in additional dependencies of the functional response on microstructural and morphological factors.

Generally, the effects of irradiation on the functional response are strongly correlated with grain size (and thus, grain boundary density) in the material. Greater grain boundary density potentially results in increased interaction of radiation-induced perturbations (electron-hole pairs, defect dipoles, vacancies) with defective interfaces, thus yielding greater radiation-induced degradation (RID).[218] However, grain boundaries can act as effective defect "sinks," and counteract to a large degree the deleterious effects of RID in the material.[221] In a ferroelectric material, radiation-induced ionization and displacement events can increase stable defect concentrations and cause changes in the defect energy landscape. Specifically, trapped charges generated by X-ray, gamma, and proton irradiations, as well as defect dipoles activated by neutron irradiation, have been shown to cause degradation of polarization, dielectric, and electromechanical responses.[32,40,97,98,100] Work by Leray *et al.* suggested that irradiation of PZT thin films mimics and/or exacerbates the effects of ferroelectric aging and fatigue, and hypothesized

that gamma radiation-induced space charges are likely proportional to grain boundary density across the thickness of interrogated samples.[101]

While prior work on irradiated ferroelectric materials has shown considerable amounts of RID of functional properties, very little research has been undertaken to specifically correlate such variations in ferroelectric response to grain morphology and microstructure.[32,90-96] Variations in grain morphology and microstructure will inevitably alter the fundamental interaction between radiation and the ferroelectric material. Modifying parameters such as grain size, orientation, and degree of anisotropy can potentially alter the effects of radiation interaction, defect creation and mobility, and even the extent of degradation that defects can impart. In this work, we investigate the role of grain morphology on radiation-induced changes to the functional response of ferroelectric materials by studying gamma-irradiated PZT thin films with columnar and equiaxed grain structures.

6.3 Experimental Procedure

Two separate $PbZr_{0.52}Ti_{0.48}O_3$ (PZT) precursor solutions were prepared, one via a 2-methoxyethanol-based (2-MOE) route, and the other using a methanol-based inverted mixing order (IMO) process.[109,110,120,131,235] Both 2-MOE and IMO PZT solutions were deposited by spin coating on 150 mm-diameter 100-silicon wafers consisting of 100 nm Pt, 35 nm TiO_2, 2035 nm SiO_2, Si, and resulting in PZT films with thicknesses of 500 ± 14 nm.[120,131,132] A seed layer of $PbTiO_3$ was deposited for the 2-MOE films to induce 100-texture.[131] 2-MOE-PZT films were deposited with a target thickness of 500 nm using 0.4M

solutions, pyrolysis temperatures of 365 °C for 60 s for each spin layer, and a crystallization anneal at 700 °C for 60 s after every 2 layers in a rapid thermal anneal furnace. IMO-PZT films were deposited to a target thickness of 500 nm using 0.35M solutions. IMO-PZT films were pyrolyzed at a temperature of 350 °C for 60 s for each spin layer and subsequently crystallized in a preheated furnace at 700 °C for 10 minutes; the crystallization step was repeated halfway through the film thickness and again at 500 nm. IrO_2 top electrodes were selected for continuity with prior work.[32] 100 nm-thick electrodes were sputter-deposited onto both the 2-MOE- and IMO-films at 500 °C and processed with a post-deposition anneal at 650 °C in flowing O_2 for 30 min. The top electrode and PZT layer were patterned using argon ion milling and a series of additional metallization steps to create interconnects to the device structures. This general process is outlined elsewhere.[100] Figure 6-1 shows baseline X-ray diffraction (XRD) phase analysis of the films deposited using 2-MOE- and IMO-prepared solutions, and the resulting columnar and equiaxed grain morphologies, respectively. Additionally, scanning electron microscopy (SEM) was performed to observe grain size and porosity in the films deposited with each precursor solution (Figure 6-2).

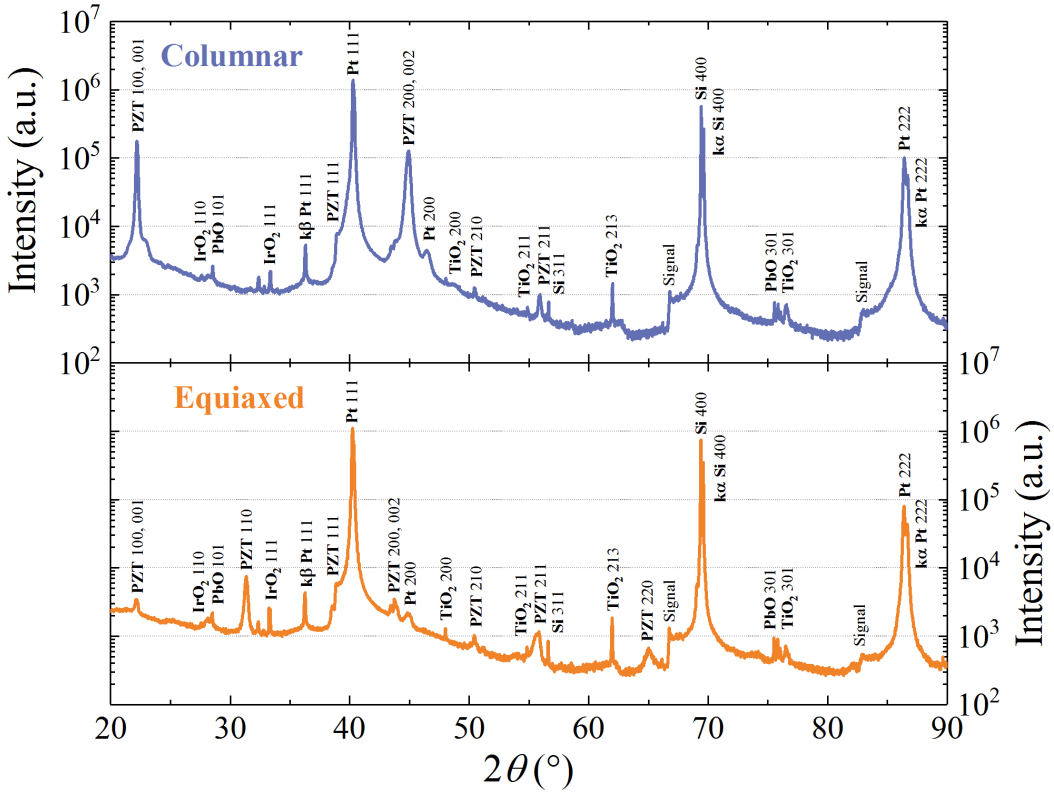

Figure 6-1 X-ray diffraction (XRD) crystallographic phase analysis comparing representative samples with columnar and equiaxed grain structures that were prepared using 2-MOE and IMO PZT solutions, respectively. Noteworthy is the large 100-peak in samples with columnar grains, compared to the large presence of 110-texture in samples with equiaxed grains. "Signal" indicates artifacts of rapid increases to XRD signal intensity.

The fabricated samples were exposed to radiation from a ^{60}Co gamma source at doses ranging from 0.2 to 10 Mrad (equivalent Si dose) at a dose rate of approximately 600 rad(Si)/s at the US Naval Research Laboratory (NRL). The geometry of the ^{60}Co gamma source surrounds the sample, resulting in an isotropic exposure, and thus eliminating any effects of radiation directionality. All electrodes were left floating during radiation exposure. Dielectric, polarization, and piezoelectric responses of the samples were fully characterized both before and after irradiation, including (in order) measurements of low-field dielectric permittivity, polarization response, nonlinear AC dielectric response, DC

electric field-dependent permittivity response, and DC electric field-dependent piezoelectric response. All measurements were performed on the same sample/electrode both before and after irradiation in order to accurately monitor changes in response. A summary of these measurements for samples with both columnar and equiaxed grain structures as a function of radiation dose is shown in Table 6-1 and Table 6-2. A 600-second poling step at 10 V (approximately five times the coercive voltage, V_C) was performed directly before the piezoelectric measurements in both pre- and post-irradiation measurement sets in order to maximize polarization alignment in the out-of-plane direction. Low-field dielectric permittivity (ε_r) measurements were conducted at 100 mV and 1 kHz using an Agilent 4284A precision LCR meter. Polarization-electric field (P-E) hysteresis loops were performed up to fields of 250 kV/cm at 100 Hz, using a Radiant P-PM2 ferroelectric test system. Nonlinear AC dielectric permittivity (ε_r-E_{AC}) was measured up to approximately 150 kV/cm AC at 1 kHz. DC-dependent dielectric permittivity (ε_r-E_{DC}) measurements were performed up to 250 kV/cm DC bias with an overlapping small-signal 100 mV AC bias at 1 kHz. Measurements of the converse, effective longitudinal piezoelectric response ($d_{33,f}$) were performed on an aixACCT double beam laser interferometer (DBLI) measurement system up to 250 kV/cm DC bias with an overlapping AC signal $V_{AC} \approx 0.5 V_C$. All measurements reported are subject to experimental error up to 3-5% due to sample variability.

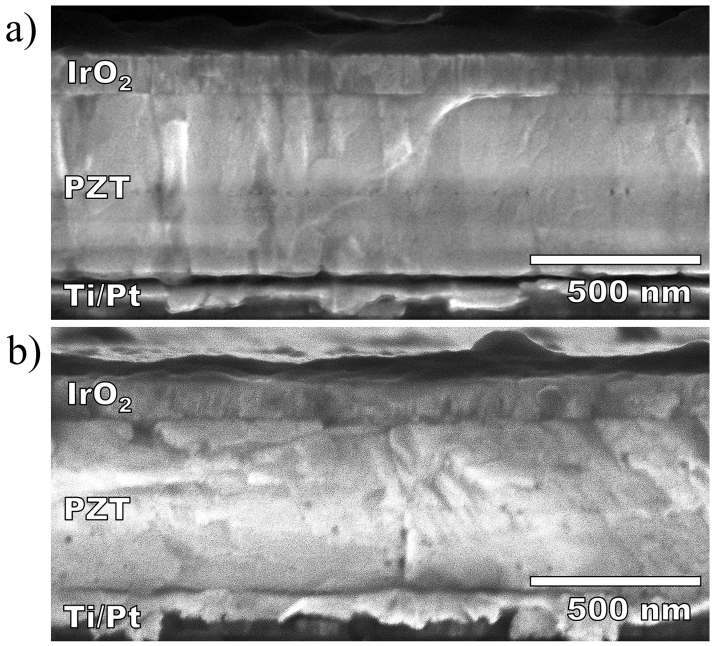

Figure 6-2 Scanning electron microscopy (SEM) images of samples with columnar and equiaxed grain structures. Notable is the greater degree of porosity in the samples with equiaxed grains (b) (see also Table 6-3).

The nonlinear dielectric response was analyzed through the Rayleigh approach to quantify changes in intrinsic and extrinsic dielectric response.[24,29,236] This analysis yields the reversible Rayleigh parameter, ε_{init}, which is the intercept of the linear AC field-dependent relative dielectric permittivity; and the irreversible Rayleigh parameter, α, which is the slope of the AC field-dependent relative permittivity. ε_{init} describes intrinsic contributions to the dielectric response such as lattice vibration as well as low field, reversible extrinsic contributions, while α designates extrinsic contributions to the dielectric response, *e.g.,* from irreversible domain wall and phase boundary motion. Accordingly, the ratio $\alpha/\varepsilon_{init}$ is commonly employed as a measure of extrinsic contributions to the functional dielectric response.[33]

Cross-sectional scanning electron microscopy (SEM) was used to visually observe grain microstructure through the thickness of the films and measure porosity. Samples were sputter-coated with a 20 nm-thick Au layer to increase sample conductivity during SEM imaging. Cross sectional characterization was performed using an FEI Verios field-emission scanning electron microscope in secondary lens mode. Thickness measurements of distinct layers in the samples and porosity calculations were performed using ImageJ (Table 6-3).

In order to quantify the microstructure and grain orientations in the film, transmission Kikuchi diffraction (TKD) was performed on the samples (Figure 6-3). Focused ion beam (FIB) milling was used to prepare thin specimens for TKD, after which they were sputter-coated with a 20 nm-thick Au layer to increase sample conductivity and to mitigate drift during the data acquisition. A 3 μm-thick Pt layer was also deposited on the sample surface before FIB milling under FEI Quanta 3D FEG to protect the sample surface from potential electron and ion damage. Cross-sectional TKD samples were prepared using FEI Quanta 3D FEG which employs both electron and ion beam guns (SEM/FIB). TKD imaging was performed on the FIB samples using an Oxford Instruments NordlysNano Electron Backscatter Diffraction (EBSD) detector. Kikuchi diffraction patterns were acquired at 30 kV with the Oxford Instruments Aztec software. TKD data was processed using the HKL CHANNEL5 program Tango. Kikuchi images for the PZT were indexed to the cubic phase of the perovskite structure, which results in a description of the grain orientations in the PZT film. The PZT composition is in close proximity to a morphotropic phase boundary (MPB) and the small structural distortions from cubic cannot be reliably indexed.

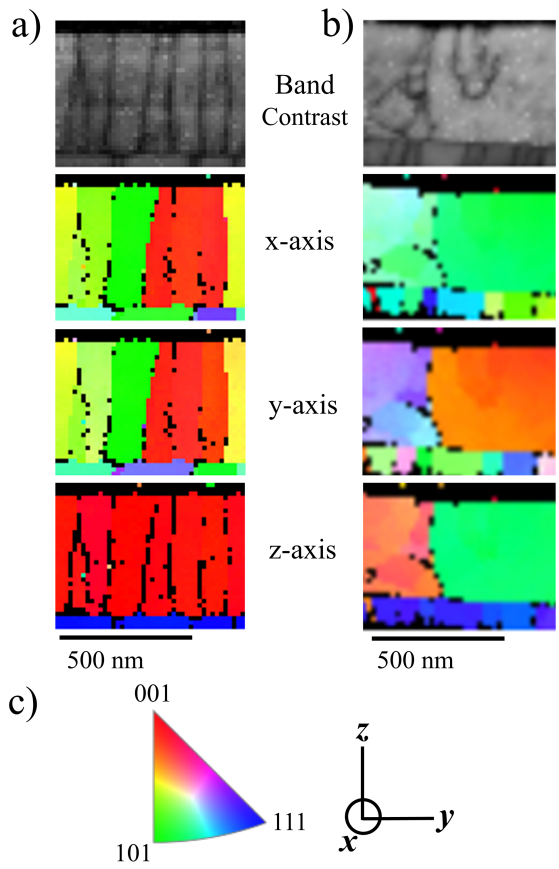

Figure 6-3 Representative transmission Kikuchi diffraction (TKD) orientation maps and Kikuchi band contrast images for samples with (a) columnar and (b) equiaxed grain structures images from the *x*-, *y*-, and *z*-axes. (c) shows the inverse pole figures for the cubic indexing of both PZT and Pt, and the coordinate system used for this figure. Note that in the highly 100-textured columnar samples, the *x*- and *y*-axis TKD images are very similar, due to the 4-fold rotational symmetry of the cubic lattice used for indexing. In the samples with equiaxed grains and weak texture, the corresponding images from *x*- and *y*-axes do not show similar symmetry, confirming their more randomly-oriented nature.

Table 6-1 Measured dielectric permittivity, loss tangent, polarization, and effective longitudinal piezoelectric responses at increasing radiation doses for PZT thin films with columnar grain structures. Percent change (where applicable in the text) is calculated from measurements before and after the given radiation dose for the set of samples and electrodes exposed to that dose. Uncertainties expressed represent standard error to one significant figure. Measurement values are reported to the same decimal place as the uncertainties.[172]

Columnar		0 Mrad	0.2	0.5	1.0	2.0	5.0	10.0
Low-field Dielectric								
ε_r	Virgin	1229 ± 1	1247 ± 3	1230 ± 1	1227 ± 2	1237 ± 1	1233 ± 1	1248 ± 1
	Irradiated	1222 ± 6	1297 ± 10	1229 ± 4	1208 ± 4	1188 ± 3	1127 ± 4	1083 ± 2
tan(δ) (%)	Virgin	1.3 ± 0.1	1.3 ± 0.1	1.3 ± 0.1	1.3 ± 0.1	1.5 ± 0.1	1.4 ± 0.1	1.2 ± 0.1
	Irradiated	1.6 ± 0.1	2.4 ± 0.2	1.5 ± 0.1	1.6 ± 0.1	1.3 ± 0.1	1.2 ± 0.1	1.0 ± 0.1
Rayleigh Analysis								
ε_{init}	Virgin	1219 ± 4	1263 ± 8	1230 ± 10	1253 ± 8	1223 ± 4	1221 ± 8	1237 ± 8
	Irradiated	1146 ± 3	1137 ± 6	1136 ± 9	1157 ± 6	1169 ± 10	1142 ± 10	1156 ± 27
α (cm/kV)	Virgin	26.9 ± 0.4	27.2 ± 0.4	36.8 ± 0.9	30.1 ± 0.4	34.7 ± 0.2	29 ± 2	29.1 ± 0.4
	Irradiated	29 ± 4	25.2 ± 0.3	23.6 ± 0.2	19 ± 1	20.1 ± 0.4	21 ± 4	15 ± 1
$\alpha/\varepsilon_{init} x10^3$ *(cm/kV)*	Virgin	22.1 ± 0.3	21.5 ± 0.4	30 ± 1	24.1 ± 0.5	28.3 ± 0.1	24 ± 1	23.5 ± 0.5
	Irradiated	26 ± 4	22.2 ± 0.3	20.8 ± 0.3	16 ± 1	17 ± 1	18 ± 4	13 ± 1
Polarization								
$P_{saturation}$ *(μC/cm²)*	Virgin	35.4 ± 0.1	35.6 ± 0.1	35.7 ± 0.1	35.4 ± 0.1	35.3 ± 0.1	35.4 ± 0.1	35.5 ± 0.1
	Irradiated	35 ± 0.1	35 ± 0.2	35 ± 0.2	35 ± 0.1	35 ± 0.1	35 ± 0.1	35 ± 0.1
$P_{remanent}$ *(μC/cm²)*	Virgin	12.2 ± 0.1	10.4 ± 0.2	10.7 ± 0.1	11.1 ± 0.2	11.1 ± 0.1	10.4 ± 0.1	11.1 ± 0.6
	Irradiated	11.2 ± 0.4	10.1 ± 0.3	9.8 ± 0.1	9.2 ± 0.1	9.6 ± 0.3	7.9 ± 0.1	8.3 ± 0.4
ε_r-E_{DC}								
% Diel. Tunability	Virgin	74.3 ± 0.2	74.7 ± 0.2	74.3 ± 0.1	74.5 ± 0.1	74.6 ± 0.2	74.2 ± 0.1	74.8 ± 0.1
	Irradiated	74.0 ± 0.4	74.2 ± 0.2	74.0 ± 0.3	73.1 ± 0.1	73.0 ± 0.2	71.8 ± 0.3	71.3 ± 0.3
$\varepsilon_{DC,low\text{-}field}$	Virgin	1402 ± 7	1354 ± 2	1400 ± 5	1359 ± 5	1390 ± 20	1400 ± 20	1382 ± 8
	Irradiated	1350 ± 20	1324 ± 2	1348 ± 2	1307 ± 1	1320 ± 20	1320 ± 20	1247 ± 1
Piezoelectric								
$d_{33,f,saturation}$ *(pm/V)*	Virgin	79 ± 3	76.2 ± 0.5	77 ± 5	78 ± 3	79 ± 1	79 ± 3	80.8 ± 0.6
	Irradiated	79 ± 2	76 ± 1	72 ± 2	77 ± 2	78 ± 1	76 ± 1	77 ± 2
$d_{33,f,remanent}$ *(pm/V)*	Virgin	49 ± 6	38 ± 2	43 ± 1	10 ± 1	43 ± 1	47 ± 5	41.5 ± 0.7
	Irradiated	34 ± 4	28 ± 1	25 ± 1	22 ± 1	23 ± 2	24 ± 6	7 ± 2

Table 6-2 Measured dielectric permittivity, loss tangent, polarization, and effective longitudinal piezoelectric responses at increasing radiation doses for PZT thin films with equiaxed grain structures. Percent change (where applicable in the text) is calculated from measurements before and after the given radiation dose for the set of samples and electrodes exposed to that dose. Uncertainties expressed represent standard error to one significant figure. Measurement values are reported to the same decimal place as the uncertainties.[172]

Equiaxed		0 Mrad	0.2	0.5	1.0	2.0	5.0	10.0
Low-field Dielectric								
ε_r	Virgin	1405 ± 1	1481 ± 1	1366 ± 6	1512 ± 2	1445 ± 3	1454 ± 1	1496 ± 2
	Irradiated	1357 ± 4	1323 ± 2	1215 ± 6	1284 ± 4	1284 ± 5	1262 ± 6	1175 ± 2
tan(δ) (%)	Virgin	3.5 ± 0.1	3.3 ± 0.1	4.0 ± 0.1	3.8 ± 0.1	2.8 ± 0.1	2.5 ± 0.1	3.7 ± 0.1
	Irradiated	2.7 ± 0.1	1.7 ± 0.1	1.9 ± 0.1	1.5 ± 0.1	1.4 ± 0.1	1.3 ± 0.1	1.3 ± 0.1
Rayleigh Analysis								
ε_{init}	Virgin	1290 ± 40	1251 ± 3	1251 ± 5	1330 ± 10	1300 ± 3	1224 ± 3	1280 ± 10
	Irradiated	1200 ± 30	1161 ± 6	1100 ± 10	1138 ± 5	1263 ± 7	1227 ± 4	1112 ± 7
α (cm/kV)	Virgin	40 ± 2	57.7 ± 0.2	35.0 ± 0.5	51 ± 2	38.9 ± 0.1	52.2 ± 0.3	39 ± 1
	Irradiated	33 ± 1	37 ± 1	29 ± 1	34.5 ± 0.2	26.4 ± 0.2	23.2 ± 0.3	20.4 ± 0.4
$\alpha/\varepsilon_{init} x10^3$ *(cm/kV)*	Virgin	30.9 ± 0.9	46.1 ± 0.3	27.9 ± 0.5	39 ± 2	29.9 ± 0.2	42.6 ± 0.3	30 ± 1
	Irradiated	28 ± 1	32 ± 1	26.1 ± 0.2	30.3 ± 0.3	20.9 ± 0.1	18.9 ± 0.2	18.4 ± 0.5
Polarization								
$P_{saturation}$ *(μC/cm²)*	Virgin	43.8 ± 0.1	43.3 ± 0.5	42.4 ± 0.1	41.9 ± 0.2	42.6 ± 0.3	41.7 ± 0.1	41.9 ± 0.1
	Irradiated	43 ± 1	42.5 ± 0.1	41.8 ± 0.2	41 ± 1	41 ± 1	40.9 ± 0.1	42.0 ± 0.1
$P_{remanent}$ *(μC/cm²)*	Virgin	14.8 ± 0.2	17 ± 1	19.2 ± 0.1	16 ± 1	15.3 ± 0.1	16.6 ± 0.4	14.7 ± 0.3
	Irradiated	15.4 ± 0.4	16 ± 1	17.2 ± 0.3	15 ± 1	13.9 ± 0.3	13.5 ± 0.3	12.8 ± 0.5
ε_r-E_{DC}								
% Diel. Tunability	Virgin	77.9 ± 0.1	77.6 ± 0.1	77.4 ± 0.2	79.2 ± 0.1	78.1 ± 0.1	78.0 ± 0.1	79.5 ± 0.2
	Irradiated	77.9 ± 0.2	79.1 ± 0.1	76.7 ± 0.1	78.2 ± 0.3	77.4 ± 0.1	77.0 ± 0.2	76.4 ± 0.2
$\varepsilon_{DC,low\text{-}field}$	Virgin	1520 ± 9	1657 ± 8	1480 ± 20	1675 ± 6	1644 ± 5	1631 ± 4	1712 ± 1
	Irradiated	1443 ± 7	1489 ± 4	1360 ± 10	1440 ± 2	1455 ± 3	1410 ± 2	1297 ± 5
Piezoelectric								
$d_{33,f,saturation}$ *(pm/V)*	Virgin	66.8 ± 0.6	68.2 ± 0.7	67.7 ± 0.5	64 ± 4	60 ± 2	62.5 ± 0.4	64 ± 1
	Irradiated	68 ± 3	61 ± 3	63 ± 1	64 ± 1	59 ± 2	64 ± 1	64 ± 6
$d_{33,f,remanent}$ *(pm/V)*	Virgin	39 ± 2	76 ± 8	48 ± 3	57 ± 1	47 ± 2	54 ± 5	69 ± 6
	Irradiated	43 ± 3	48 ± 6	25 ± 3	33 ± 3	30 ± 4	30 ± 2	19 ± 5

6.4 Experimental Results

Fabrication of PZT thin films using 2-MOE- and IMO-CSD methods resulted in films with large differences in grain orientation and microstructure. XRD crystallographic orientation analysis (Figure 6-1) shows highly 100-textured films processed with 2-MOE-based CSD, while the IMO CSD-processed samples demonstrate a relatively strong 110-peak. Minor tetragonal peak splitting is observable in the samples processed with 2-MOE-based solutions, due to proximity of the precursor solutions to the morphotropic phase boundary and accompanying changes to the Curie temperature (T_C). Differences in microstructure, porosity, and crystallographic texture are further elucidated via SEM imaging (Figure 6-2) and TKD analysis (Figure 6-3). SEM images show highly-columnar grain structures with low porosity concentrated at the crystallization interfaces in the samples processed via 2-MOE-based solutions. The films processed with IMO solutions show randomly-oriented grains with a greater degree of porosity (1.35% for equiaxed, 1.10% for columnar) distributed through the thickness of the film (Table 6-3). TKD analysis further confirms the grain orientation and texture, showing large regions of 100-oriented columnar grains for the samples processed with 2-MOE-based CSD (Figure 6-3a) compared with a more random distribution of crystallographic orientations for those processed via IMO CSD (Figure 6-3b). For simplicity throughout the results and discussion, the films processed via 2-MOE-based and IMO CSD methods will be referred to as “columnar” and “equiaxed,” respectively.

Shown in Figure 6-4 are statistical measurements of the distribution of in-plane grain sizes, out-of-plane grain heights, and size of multi-grain regions of similar orientation, as calculated using ASTM E112-12 average grain intercept methods from

multiple TKD band contrast images.[237] Samples with columnar grains show smaller mean in-plane grain size (Figure 6-4b) and a larger mean grain height (Figure 6-4c), with a greater frequency of multi-grain regions (Figure 6-4d). Equiaxed samples have greater mean grain surface area, but due to their much greater mean volume, a smaller surface-area-to-volume ratio. Quantified statistical results are available in Table 6-3.

Table 6-3 Statistical data for measurements of in-plane grain size, grain height, and various geometry-related values for samples with columnar and equiaxed grain structures. Also calculated are the number of electron-hole pairs (ehp) per grain.

Grain structure	% Porosity	Mean grain height (nm)	Mean in-plane grain size (nm)	Mean grain surface area (cm^2)	Mean grain volume (cm^3)	Surface area per volume	Number of electron-hole pairs (ehp) per grain· Mrad
Columnar (cylindrical)	1.10	391 ± 220	66 ± 27	8.8×10^{-10}	1.3×10^{-15}	6.8×10^{5}	1.2×10^{5}
Equiaxed (ellipsoidal)	1.35	215 ± 109	177 ± 160	11.3×10^{-10}	3.6×10^{-15}	3.1×10^{5}	3.4×10^{5}

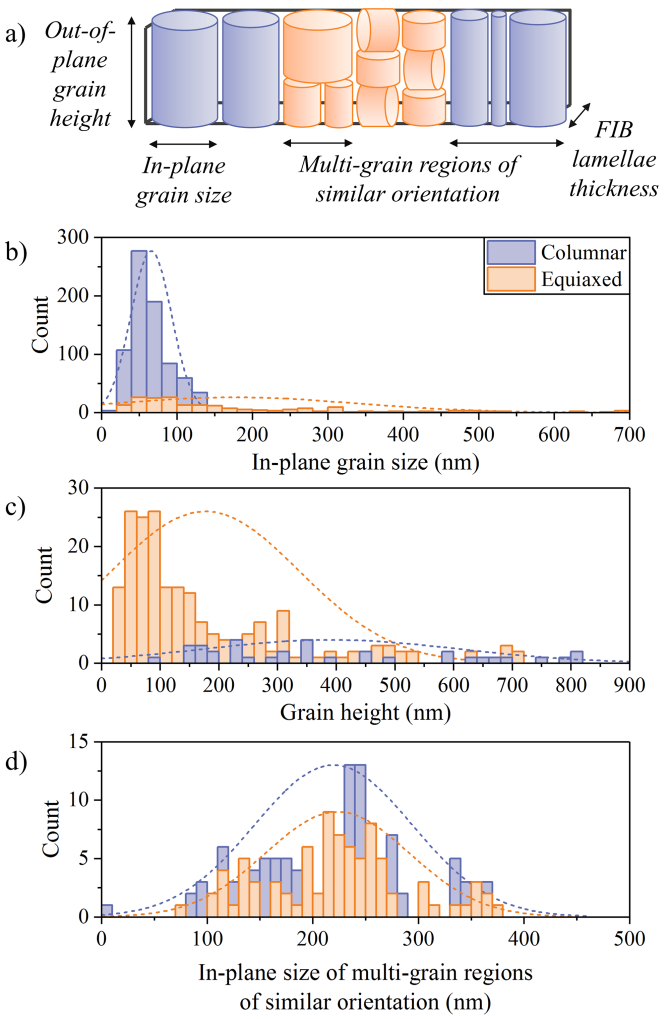

Figure 6-4 Statistical analysis of grain characteristics for PZT thin films with columnar (blue) and equiaxed (orange) grains. Schematic for statistical measurements shown in (a). Measurements include (b) in-plane grain size, (c) out-of-plane grain height, and (d) size of multi-grain regions of similar orientation. Normal distribution curve is shown as a dotted line to suggest trends in data.

Figure 6-5 shows trends in the characterization of dielectric response at low AC electric field (ε_r) and intermediate AC electric field (α). Samples with equiaxed grains show greater degradation of relative dielectric permittivity, ε_r, as a function of radiation dose, as well as greater reductions in dielectric losses, *tan(δ)* (Table 6-1 and Table 6-2). Similarly, at increasing AC field, degradation of the extrinsic contributions to the dielectric response,

α, is slightly greater for samples with equiaxed grains (Table 6-1and Table 6-2, Figure 6-5), potentially indicating that contributions from irreversible motion of internal interfaces are greater in those samples than in samples with columnar grains.

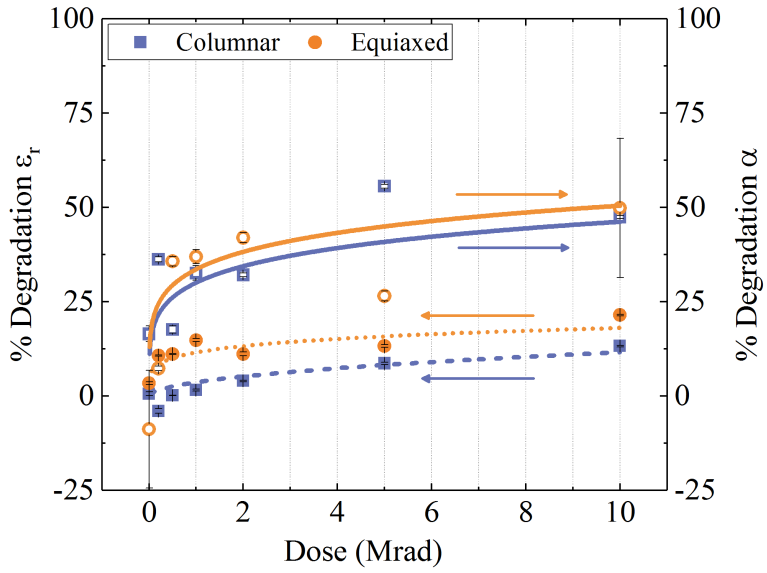

Figure 6-5 Degradation trends for dielectric responses at low (a, b) and increasing (c) AC electric field. Notable are the large differences in degradation trends at low field when comparing samples with different grain structures, but similar trends of degradation of the Rayleigh extrinsic to intrinsic ratio are observed for both sets of samples.

The degradation data for remanent polarization response and coercive field (negative potential) are plotted in Figure 6-6 (with sample loops shown in Figure 6-7a and Figure 6-7b). Samples with columnar grains show more severe degradation for both remanent and saturated polarization (P_{rem} and P_{sat}, respectively) compared to samples with equiaxed grains. Decrease in the negative coercive field (E_{C-}) is closely matched for both sets of samples (Table 6-1 and Table 6-2).

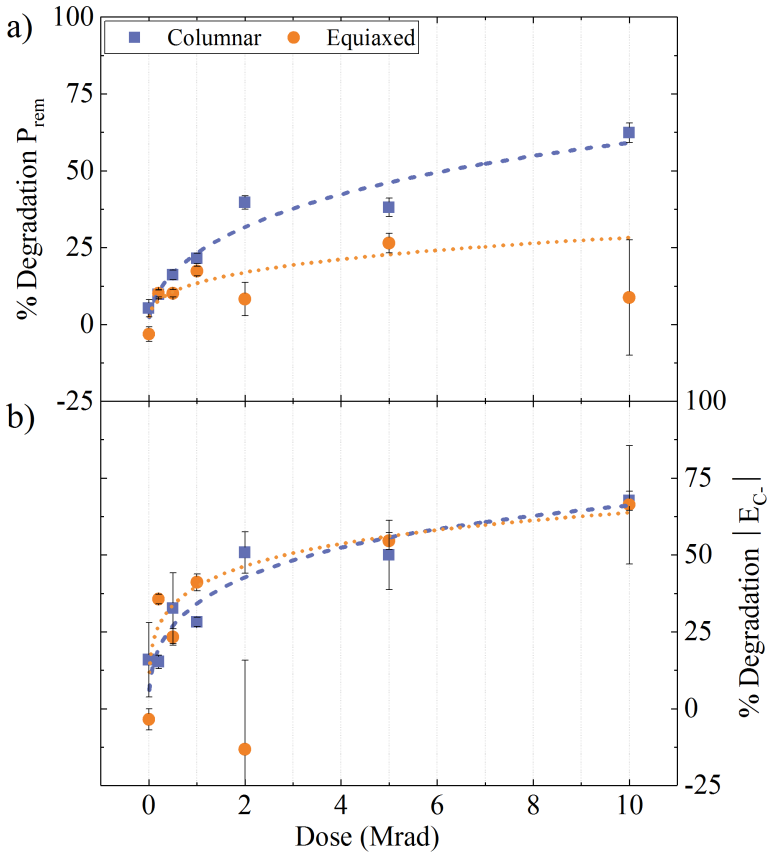

Figure 6-6 Degradation trends for polarization and coercive field. Note the severe degradation of remanent polarization, compared to the mild degradation of saturation polarization.

The summary of functional response characterization shown in Table 6-1 and Table 6-2 allow for a variety of observations regarding the behavior of samples with both columnar and equiaxed grains as a function of radiation dose, particularly from a high-dose perspective. For example, focusing on dielectric response, PZT thin films with columnar and equiaxed grain structures show relatively low levels of degradation of low-field dielectric permittivity (ε_r) at 10 Mrad dose (13% and 22% respectively), compared to much greater degradation of remanent effective piezoelectric coefficient ($d_{33,f,rem}$) – up to 83% for samples with columnar grains, and 70% for samples with equiaxed grains (see Figure 6-8). Additionally, large degradation (up to 50%) of α is noted for all samples at 10 Mrad.

This suggests that gamma radiation negatively interacts with sources of extrinsic contributions to the dielectric response, such as the irreversible motion of domain walls. This result is consistent with prior studies at discrete gamma radiation doses.[32] In order to more comprehensively quantify radiation-induced defect interactions and the resulting effects on the functional response in PZT thin films of different grain morphologies, we apply a phenomenological model developed in prior work to analyze trends as a function of radiation dose.[189] The implementation thereof will be addressed in the following Discussion.

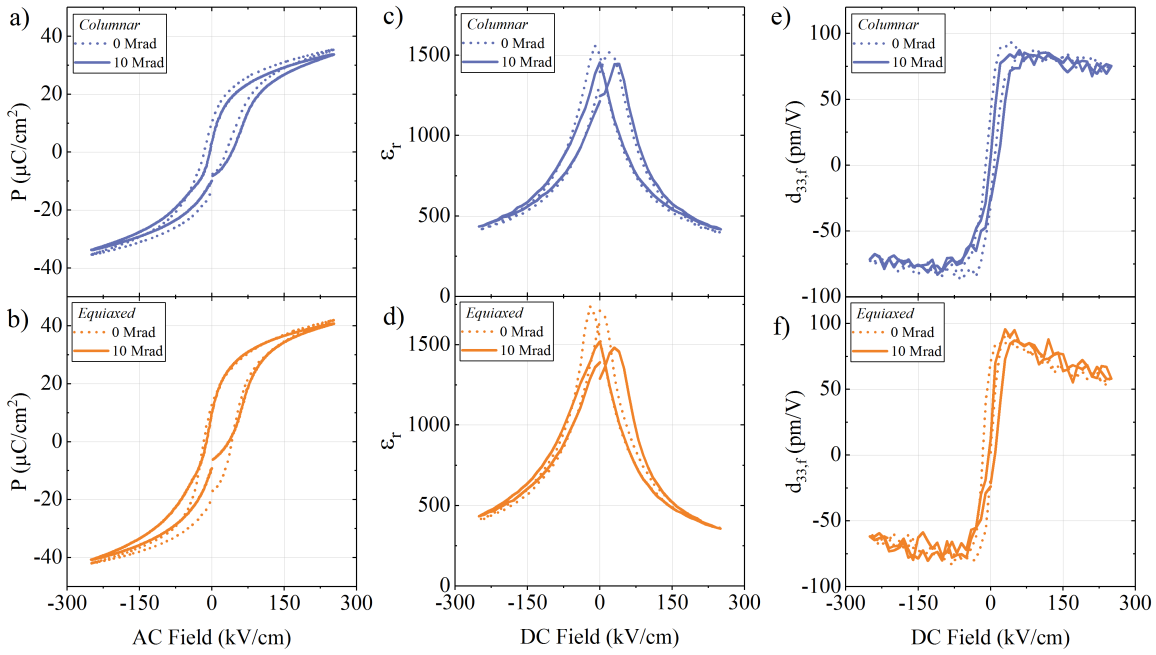

Figure 6-7 Comparison of (a, b) polarization-field (*P-E*) hysteresis loops; (c, d) permittivity-DC field (ε_r-E_{DC}); and (e, f) piezoelectric-field loops ($d_{33,f}$-E_{DC}) for samples with (a, c, e) columnar grains and (b, d, f) equiaxed grains in virgin (0 Mrad) samples and after exposure to 10 Mrad gamma irradiation. Notable is the larger shift in the positive direction of the *P-E* loop at 10 Mrad for the sample with columnar grains (a), as well as slight pinching of the *P-E* loops for both samples (a, b), indicating changes to the defect energy landscape of the material. The internal bias is also visible

in piezoelectric plots (e, f). The formation of new peaks in the ε_r-E_{DC} loops (c, d) potentially indicates changes to the defect energy landscape.

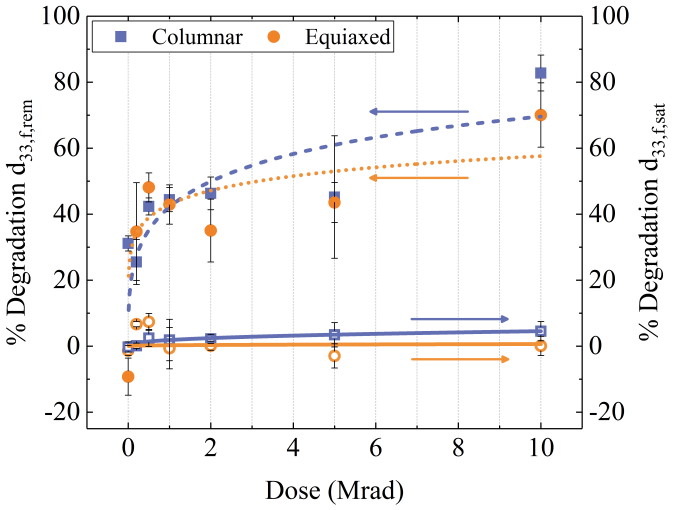

Figure 6-8 Degradation trends and fitted model for DC field-dependent piezoelectric responses ($d_{33,f}$-E_{DC}) and percent dielectric tunability. Notably, samples with columnar grains appear to be slightly more susceptible to radiation-induced degradation of DC field-dependent responses. However, the magnitude of degradation of $d_{33,f,sat}$ and *% tunability* (high DC field) are somewhat negligible, compared to $d_{33,f,rem}$ (low DC field).

6.5 Discussion

The employed phenomenological model relies on the assumption that exposure of ferroelectric materials to gamma radiation creates or activates defects in the material.[32] We note that radiation-induced defects (RID) may refer to both ionic/electronic defects, such as electron-hole pairs and trapped charges, or atomic displacements, *e.g.*, vacancy/interstitial pairs, with the former being the more likely result of ionizing gamma irradiation. The newly-created/activated defects interact with a given volume of

ferroelectric material and, potentially, with existing defects therein, such as domain walls, grain boundaries, existing point defects, defect dipoles, *etc.*, thereby modifying the defect-energy landscape of the material. The result is an effective "pinning" of ferroelectric volume (normalized to total probed volume)[189] due to defect interactions, V_d, which can be directly correlated to degradation of functional response parameters. The volume of pinned ferroelectric material is related to the number of radiation-induced defects, N, (assumed proportional to radiation dose) by the expression

$$V_d = 1 - e^{-\varphi_N\left(\frac{N^{1-k}}{1-k}\right)} \qquad 6\text{-}1$$

where two parameters determine the response to radiation: (1) φ_N, the normalized effective change in material volume pinned per new defect introduced; and (2) k, the effective rate of defect saturation. φ_N can be considered as the global susceptibility of the material to radiation-induced change, while k is useful for describing the nonlinear physical phenomena governing the effective rate of change and the more nuanced effects of defect concentration on degradation of response. Full details of the model are available elsewhere, including derivation and detailed discussion of the assumptions and parameters.[189] It should be noted that the values of φ_N are normalized to an arbitrary total volume, thus comparisons between values of φ_N represent fractional comparisons, rather than absolute value. Results of fitting the model to the functional characterization data (Table 6-1) are given in Table 6-4.

Table 6-4 Extracted parameters from applying the phenomenological model developed in prior work to TID study data of dielectric, polarization, and piezoelectric responses of the irradiated samples with columnar and equiaxed grains. Note that values of φ_N are multiplied by three orders of magnitude to make interpretation more manageable.

	Columnar		Equiaxed	
	$\varphi_N \times 10^3$	k	$\varphi_N \times 10^3$	k
Low-field Dielectric				
ε_r	19	0.48	26	0.79
$tan(\delta)$	25	0.77	57	0.92
Rayleigh Analysis				
α	85	0.76	96	0.77
ε_{init}	11	0.76	19	0.79
$\alpha/\varepsilon_{init}$	86	0.68	97	0.68
Polarization				
P_{rem}	140	0.47	52	0.64
P_{sat}	6	0.65	2	0.85
E_{C-}	173	0.59	153	0.70
ε_r-E_{DC} Response				
% Tunability	7	0.43	6	0.44
$\varepsilon_{DC,low\text{-}field}$	15	0.63	34	0.72
Piezoelectric				
$d_{33,f,rem}$	185	0.66	104	0.82
$d_{33,f,sat}$	7	0.61	1	0.62

By comparing the fitting parameters in Table 6-4, we can now perform a more quantitative analysis of both the global and local response of PZT thin films and the effect of grain morphology on gamma radiation-induced defect interactions. Generally, gamma irradiation of PZT thin films with both columnar and equiaxed grains resulted in degradation of dielectric, polarization, and piezoelectric functional properties. However,

several notable trends are observed regarding the dependence of radiation-induced degradation on grain structure, magnitude/type of electric field, and the type of functional response measured.

First and foremost, samples with equiaxed grains exhibit consistently greater values of k throughout all measurements in Table 6-4. The distinct trend of larger k across all functional response parameters in equiaxed-grained samples suggests a strong correlation between grain morphology and defect saturation rates in gamma irradiated PZT thin films. The coefficient k accounts for the effects of material anisotropies, *e.g.*, grain boundaries, pre-existing defects, chemical heterogeneity, *etc.* Elevated values of k potentially signal either enhanced rates of defect creation/activation, increased damage by newly-introduced defects, or a combination of both. A variety of reports have suggested that the harmful effects of radiation-induced defects are potentially alleviated by decreasing grain size in functional materials, and thus increasing the density of grain boundary sinks for defect accumulation.[220,221,238-241] Defects either created or accumulated at grain boundaries potentially result in less severe and shorter-range degradation, due to the relative absence of functional material volume at grain boundaries. The columnar grains studied in this work are both smaller than the equiaxed grains studied and have a surface-area-to-volume ratio that is more than twice as large (Table 6-4). The result is a slower rate of defect saturation and resulting degradation of response in samples with columnar grains, signaled by consistently smaller values of k compared to samples with equiaxed grains.

Trends of global susceptibility (φ_N) to radiation-induced degradation for both columnar- and equiaxed-grained samples are observed through measurements of dielectric properties. Focusing on the Rayleigh analysis of nonlinear AC dielectric response, values

of φ_N are similar for measurements of ε_{init} ($\varphi_N = 11\times10^{-3}$ for columnar samples, $\varphi_N = 19\times10^{-3}$ for equiaxed samples) and α ($\varphi_N = 85\times10^{-3}$ for columnar samples, $\varphi_N = 97\times10^{-3}$) for samples with both grain orientations. Two important observations can be gleaned from this data. First, the relative values of φ_N for α are four to five times greater than corresponding values for ε_{init} (see also the ratio, $\alpha/\varepsilon_{init}$). This result indicates that the impact of radiation on irreversible motion of domain walls is larger than the effects on intrinsic response and reversible motion of domain walls, consistent with multiple reports on gamma, X-ray, proton, and neutron irradiation of PZT thin films.[32,40,97] Prior work has suggested that ionizing radiation can excite electrons and holes, leading to potential trapped charges in the material.[32,97,101] Such trapped charges can modify the charge state of existing defects and lead to pinning of domain wall motion, similar to mechanisms driving ferroelectric fatigue.[32,61,70,75,101,242] Proie *et al.* and Brewer *et al.* have previously reported the nature of charge accumulation due to gamma irradiation and the subsequent creation of charged defects through TID and bias studies in PZT thin films.[32,100]

Second, the values of φ_N for both α and ε_{init} are slightly greater for samples with equiaxed grains. It is noteworthy that the grain volume in samples with equiaxed structure is larger than columnar grains, as noted in Table 6-3, as well by visual inspection of the TKD band contrast maps in Figure 6-3. Numerous reports have shown that domain size (and thus, wall mobility) in ferroelectric materials scales with grain size.[243,244] In grains with larger domains, domain walls are expected to be more mobile, due to lower chances of interaction with other domain walls, potentially resulting in greater extrinsic contributions to the dielectric response. Indeed, comparing the actual values of α, in Table 6-1 and Table 6-2, the samples with equiaxed grains consistently show greater magnitude

of extrinsic contributions to dielectric response across the entire range of radiation doses. In other words, samples with larger, equiaxed grains have higher extrinsic contributions in virgin samples. On the other hand, in samples with smaller columnar grains, the smaller domains and proximity to grain boundaries may result in to lower extrinsic contributions, even prior to irradiation.[245] A higher value of α in the equiaxed samples might also be attributable to greater chemical homogeneity in those samples. Prior research compared cation distributions through the thickness of films prepared with 2-MOE-based and IMO PZT solutions, showing greater chemical homogeneity for IMO-based solutions prepared under conditions typically used for PZT thin film preparation.[136] Additionally, it was demonstrated that films with increased chemical homogeneity can produce enhanced dielectric properties due to their consistent proximity to the morphotropic phase boundary (MPB), which is associated with enhanced extrinsic contributions to the dielectric response, *e.g.*, greater domain wall mobility.[246] The consequence is greater observed radiation-induced degradation of response in equiaxed grains as the larger, more mobile domains are pinned and result in greater *percent degradation* of response, while maintaining larger measured values of extrinsic response. This phenomenon is potentially supported by the previously-mentioned greater values of k in samples with equiaxed grains, as defects are created/activated at an increased rate relative to columnar-grained samples.

It is also useful to compare the values of φ_N for polarization response at low and high field, *i.e.*, remanent and saturated polarization response (P_{rem} and P_{sat}). At low electric field, the effects of gamma radiation are quite severe for P_{rem}, with φ_N values of 140×10^{-3} and 52×10^{-3} for columnar- and equiaxed-grained samples, respectively. However, at the higher fields (250 kV/cm) required to reach polarization saturation, the effects of radiation-

induced defect interactions are substantially reduced (values of φ_N for saturated polarization of columnar and equiaxed samples are 6×10^{-3} and 2×10^{-3}, respectively). These results suggest that the defects generated or activated with gamma irradiation are of relatively low energy, and the effects of their presence are almost fully overcome at higher electric fields.

As shown in Figure 6-7a and Figure 6-7b, internal bias and the associated horizontal shift of the polarization-field (*P-E*) loops in the positive electric field direction are potentially responsible for some degree of degradation of remanent polarization response. However, reductions in the magnitude of negative coercive field, E_{C-}, are very similar for both sets of samples (Figure 6-6b), indicating that internal bias for samples with columnar grains may not be the sole contributor to the greater observed rates of degradation. Indeed, pinching of the hysteresis loops for both sets of samples is visible (Figure 6-7a and Figure 6-7b), consistent with work on single-dose radiation studies, and indicating the presence of charged defects and/or defect dipoles, and potential pinning of internal interfaces.[32,40] Such pinching, coupled with the observed asymmetric internal bias, makes exact interpretation of the P_{rem} and E_C trends difficult, as deconvolution of these effects is not trivial.

Meanwhile, piezoelectric and dielectric measurements as a function of DC electric field show severe degradation at low-fields ($d_{33,f,rem}$, $\varphi_N = 185\times10^{-3}$ for columnar, $\varphi_N = 103\times10^{-3}$ for equiaxed) and the relative abatement thereof at high-field measurements ($d_{33,f,sat}$, $\varphi_N = 7\times10^{-3}$ for columnar, $\varphi_N = -1\times10^{-3}$ for equiaxed; and % dielectric tunability) (Table 6-4 and Figure 6-8). Li *et al.*[25] and Bassiri-Gharb *et al.*[24] have previously reported that increasing applied DC electric field significantly raises the threshold at which

nonlinear domain wall motion is initiated. At the low DC electric field used for $d_{33,f,rem}$ measurements, domain walls are largely mobile, and the previously-discussed radiation-induced reduction of domain wall motion dominates the large degradation observed for both sets of samples. At substantially higher DC electric field (such as those used to measure $d_{33,f,sat}$ and percent dielectric tunability), domain wall motion is essentially restricted, and intrinsic factors, such as lattice strain and crystal anisotropy dominate the piezoelectric response. Prior work has shown that radiation-induced damage to the crystal lattice in gamma-irradiated PZT is virtually nonexistent, even at gamma radiation doses up to 10 Mrad.[32] Accordingly, extremely mild trends of degradation are observed for measurements at high DC electric field, reflected in the essentially negligible values of φ_N, and flat degradation trends as shown in Figure 6-8.

Additionally, we note that the values of φ_N for remanent and saturated piezoelectric responses ($d_{33,f,rem}$ and $d_{33,f,sat}$) are somewhat similar to those observed for P_{rem} and P_{sat}, respectively, for both set of samples. This similarity is consistent with the fact the piezoelectric response often scales with the degree of coherent alignment of the polarization direction in the sample. In fact, piezoelectric response is often closely correlated to the polarization in ferroelectric materials, especially with decreasing film thickness below 1.5 μm.[35] Consequently, the internal electrical bias and changes in the defect energy landscape causing pinching of the *P-E* loops are expected to also be present in the piezoelectric and DC field-dependent dielectric responses. Indeed, the presence of internal bias is noted in the piezoelectric response plots (Figure 6-7e and Figure 6-7f), as well as notable reductions in the irradiated positive remanent piezoelectric response

($d_{33,f,rem+}$), indicating that defects created/activated prevent the alignment of dipoles to some degree.

A final factor to consider is the effect of defect creation at locations where gamma rays interact with grain boundaries. Work by Claeys and Simoen suggested that in ferroelectric materials exposed to ionizing radiation, rates of trapped charge creation and activation are highly dependent on the surface area of grain boundaries with which the radiation interacts.[218] They further noted that such trapped charges at grain surfaces can screen local polarization.[218] Leray *et al.* also suggested that potential trapped charges in gamma-irradiated PZT are activated proportionally to exposed grain boundary area.[101] Grain boundary density is greater in samples with columnar grains (Table 6-3), and thus, incident gamma rays may create more trapped charges at grain boundary locations. While the previously-discussed effects of grain boundaries acting as defect sinks likely neutralizes these trapped charges and any extensive domain wall-pinning at those locations, the local charges potentially contribute further to the observed internal bias and previously-discussed convolution of polarization/piezoelectric response trends. These phenomena are observed by slightly greater RID of P_{rem} and $d_{33,f,rem}$ in columnar-grained samples (Figure 6-6a, Figure 6-7e, Figure 6-7f, Figure 6-8).

6.6 Conclusions

PZT thin films processed with 2-MOE-based and methanol-based IMO solutions were fabricated resulting in films with columnar and equiaxed grain structures, respectively, and irradiated with ^{60}Co gamma radiation from 0.2 to 10 Mrad(Si).

Degradation trend data was fitted using a modified sigmoid function to quantify defect interactions in irradiated ferroelectrics, and the resulting values describing (1) the ferroelectric volume pinned per new defect, and (2) the effective rate of defect saturation, were compared. For films with both types of grain structures, significant amounts of degradation were observed for dielectric, ferroelectric, and piezoelectric properties. Compared to samples with columnar grains, those with equiaxed grains consistently showed greater rates of defect saturation and nonlinear degradation of response as a function of radiation dose, due to their larger grains and relatively lower density of grain boundaries acting as defect sinks, the presence of which can reduce nonlinear rates of defect saturation.

Trends in the Rayleigh analysis indicate that pinning of domain walls is the dominant mode of dielectric response degradation. This effect is marginally greater in samples with equiaxed grains than those with columnar grains, potentially due to the larger grain size and correspondingly larger domains and more labile domain walls in the former. Greater initial dielectric response is quickly degraded in such samples, and greater percent degradation of extrinsic contributions to the dielectric response is thus observed. On the other hand, samples with columnar grains show slightly increased degradation of both polarization and piezoelectric responses at the high radiation doses studied here. The pinning energy of the domain walls as a result of irradiation is, however, somewhat limited to lower energies: in fact, low-field measurements of the dielectric, ferroelectric and piezoelectric response show substantial degradation, while high-field responses remain essentially unaffected by irradiation even at 10 Mrad.

The results presented in this study can be leveraged for the design of radiation-tolerant devices that rely on ferroelectric thin films, such as for use in satellite or nuclear energy applications. The distinct trends in functional response degradation are strongly correlated to the microstructure of the PZT thin films, and can be used to tailor eventual device properties to meet the needs of a variety of radiation-tolerant applications. Furthermore, the quantification of the effects of radiation *dose* allows for a nuanced assessment of material performance across device exposure and lifetime.

6.7 Acknowledgements

This work was supported by the Defense Threat Reduction Agency, Basic Research Award No. HDTRA1-15-1-0035 to Georgia Institute of Technology. The contents do not necessarily reflect the position or the policy of the federal government, and no official endorsement should be inferred. IMO film synthesis was supported by the Laboratory Directed Research and Development program at Sandia National Laboratories, a multi-mission laboratory managed and operated by Sandia Corporation, a wholly owned subsidiary of Lockheed Martin Corporation, for the U.S. Department of Energy's National Nuclear Security Administration under contract DE-AC04-94AL85000. The authors acknowledge the contributions of Joel Martin and Brian Power of the Army Research Laboratory and Steven Isaacson of General Technical Services for their roles in the fabrication of the PZT thin films. This work was performed in part at the Analytical Instrumentation Facility (AIF) at North Carolina State University, which is supported by the State of North Carolina and the National Science Foundation (award number ECCS-

1542015). The AIF is a member of the North Carolina Research Triangle Nanotechnology Network (RTNN), a site in the National Nanotechnology Coordinated Infrastructure (NNCI).

CHAPTER 7. FUNCTIONAL AND STRUCTURAL EFFECTS OF INTERNAL LAYER INTERFACES AND CHEMICAL HETEROGENEITY

The content in this chapter has been published in the *Journal of the American Ceramic Society*.[247] The text has been slightly modified from the original manuscript to accommodate the Supplemental Materials.

Functional and Structural Effects of Layer Periodicity in Chemical Solution-Deposited $Pb(Zr,Ti)O_3$ Thin Films

Steven J. Brewer, Samuel C. Williams, Carmen Z. Deng, Aaron B. Naden, Sabine M. Neumayer, Brian J. Rodriguez, Amit Kumar, Nazanin Bassiri-Gharb

Journal of the American Ceramic Society, (2017), doi: 10.1111/jace.15057

7.1 Summary

This work investigates the role of crystallization layers' periodicity and thickness on functional response in chemical solution-deposited lead zirconate titanate thin films, with periodic, alternating Zr and Ti gradients normal to the surface of the film. The films were processed with a range of layer periodicities and similar total film thickness, in order to relate the number of layers and compositional oscillations to structural and functional response changes. Trends of increased extrinsic contributions to the dielectric and ferroelectric responses are observed with increasing layer periodicity, but are counterpointed by simultaneous reduction of intrinsic contributions to the same. Transmission electron microscopy reveals in-plane crystallographic discontinuity at individual crystallization interfaces. Samples with smaller periodicity, and thus thinner layers, potentially suffer from grain size refinement and subsequent reduction in domain size, thereby limiting extrinsic contributions to the response. The strong compositional oscillations in samples with larger periodicity result in deep fluctuations to the tetragonal side of the phase diagram, potentially reducing intrinsic contributions to the response. Conversely, piezoresponse force microscopy results suggest that large chemical oscillations in samples with larger periodicity also result in closer proximity to the morphotropic phase boundary, as evidenced by local acoustic softening at switching, signaling potential field-induced phase transitions.

7.2 Introduction

Ferroelectric thin films find use in ferroelectric random access memories (FeRAM), thin film capacitors, infrared (IR) detectors, acoustic and ultrasound devices, and microelectromechanical systems (MEMS) sensors and actuators.[1,229,230,232] Traditional processing of such films has often stressed chemical homogeneity in order to maximize dielectric, ferroelectric, and electromechanical responses.[44,108,111] In lead zirconate titanate (PZT), the presence of a morphotropic phase boundary (MPB), which separates the rhombohedral and tetragonal (R/T) phases, has further increased interest in compositions with minimal chemical variation: enhanced polarizability arising from the coupling of phases in the vicinity of the MPB results in large increases to dielectric and piezoelectric responses, making compositions in its proximity extremely attractive.[49,50] While attempts to obtain homogeneous PZT compositions near the MPB have become ubiquitous both in research and industrial applications, recent work on heterogeneous compositions and film structures that traverse the MPB have shown promising enhancements to ferroelectric and piezoelectric responses in increasingly thin films.[248-250]

A variety of approaches have been implemented to elucidate the effects of chemical heterogeneity in ferroelectric thin films. Theoretical methods have predicted large dielectric and piezoelectric anomalies in heterolayered epitaxial films.[251,252] Experimental approaches, including discrete heterolayers, graded compositions, bi- and tri-layer superlattices, and other fabrication approaches have been employed to study interactions between dissimilar phases and layers in ferroelectric thin films.[249,250,252-261] The majority of these have demonstrated some degree of enhancement to ferroelectric response, in addition to interesting polarization interactions and thermodynamic properties, such as unusual

phase change sequences and nonergodicity.[261] Specifically, ferroelectric hetero-, bi-, and gradient-layers can show large enhancements of the overall dielectric, ferroelectric, and electromechanical responses of ferroelectric thin films.[249,250,257,261] However, while functional response enhancements are often reported, the mechanisms by which such enhancements are derived are somewhat debated. Anbusathaiah *et al.,* concluded that labile ferroelastic nanodomains in R/T bilayered PZT thin films contribute to giant electromechanical couplings in the films.[250] Work by Mangalam *et al.,* demonstrated nearly coherent strain in PZT R/T bi-layered and graded thin films, contributing to asymmetric bias profiles in the films, thereby resulting in increased tolerance to strain relaxation and enhanced ferroelectric properties.[249] Others have suggested that electrostatic coupling, internal bias fields, interfacial asymmetry, and flexoelectricity contribute to increased polarizability and resulting enhancements of functional properties in ferroelectric superlattices.[248,249,251,252,255,258,262,263] While the origins of response enhancement are perhaps multifaceted and not unequivocally elucidated, the fact remains that the overwhelming majority of these reports has concentrated on single-layer films with unique B-site cation (Zr/Ti) gradients, or unique bi-layers of rhombohedral and tetragonal compositions.

In this work, we investigate chemical solution deposition (CSD) of periodic PZT thin films deposited with alternating R/T layers across a range of layer periodicities. Attractive response enhancement has clearly been demonstrated for films spanning the MPB and leveraging the resulting phase boundary; by studying films of similar thickness but varying layer periodicity, we can elucidate the contributions of the *periodicity* of fluctuations in chemical heterogeneity to changes in functional response. Furthermore, we

can study potential contributions to the functional properties from the mobility of internal interfaces, *e.g.*, phase boundary and domain wall motion, by correlating structural and chemical variations in the films to trends in their dielectric and ferroelectric responses. The study of periodically-layered, chemically-heterogeneous CSD thin films is expected to shed light on the interactions and mechanisms for response enhancement of PZT compositions in proximity to and traversing the MPB.

7.3 Experimental Procedures

Periodic R/T (pR/T) $PbZr_{0.53}Ti_{0.47}O_3$ (PZT) thin films were fabricated via CSD from precursor solutions with concentrations varying from 0.10M to 0.40M. The films were spin-coated on platinized 100-oriented, *p*-type Si wafers (675 μm Si // 500 nm thermal SiO_2 // 35 nm sputtered TiO_2 // 100 nm Pt), pyrolyzed at 400° C for 60 seconds to remove solvent and residual organic material, and annealed at 700° C for 60 seconds in a rapid thermal annealer after each deposited layer. A seed layer of 0.15M PZT, approximately 15 nm thick, was deposited first to induce 100-texture in the subsequent PZT layers. The overall target thickness for all samples was ~200 nm. Thermodynamic and kinetic nucleation and growth factors, as described by Brooks *et al.*,[264] and Calame and Muralt,[265] result in films with steep Ti/Zr cation gradients (and expected R/T phases, discussed later) normal to the thickness of the film across each individually-crystallized layer. Measured layer periodicity, Λ_{meas}, was calculated using contact profilometry (KLA-Tencor P15 (Milpitas, California, USA), subject to 3-5% experimental error), using the formula

$$\Lambda_{meas} = \frac{d}{n} \qquad 7\text{-}1$$

where d is the film thickness (subtracting the seed layer thickness from the total measured thickness) and n is the number of crystallized layers.

For comparison of crystallographic orientation, chemical composition, and film microstructure, multiple films were also fabricated using a traditional "multi-layer anneal" (MLA) method, where multiple layers are pyrolyzed together before a final crystallization anneal (see Figure 7-1).[111] This method yields highly-homogenous CSD PZT thin films with good dielectric and electromechanical properties, as described elsewhere.[111]

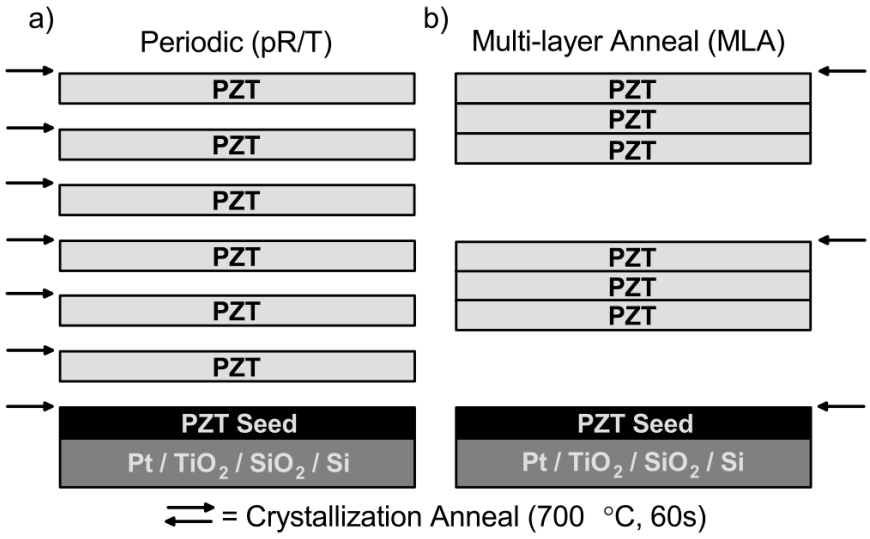

Figure 7-1 Illustration of the deposition and crystallization scheme for the (a) periodic (pR/T) and (b) multi-layer anneal (MLA) films. Note that the MLA films are studied for comparisons of microstructure and orientation; functional properties of similarly-processed films have been reported elsewhere.[111]

Baseline X-ray diffraction (XRD) analysis of both the pR/T thin films as well as the MLA films for comparison was performed on PANalytical Alpha-1 using Cu Kα X-

rays (Figure 7-2b). The periodicity of the pR/T films is investigated by the presence of satellite peaks centered around the 100- and 200-peaks of PZT (Figure 7-2a, Figure 7-2c), as described by Schuller.[266] In addition to the previously-described method of determining each individual layer thickness, the stacking periodicity of the pR/T films were also determined using the Schuller formula:[267]

$$\Lambda_{Schuller} = \frac{\lambda}{2[\sin(\theta_i - \theta_{i-1})]} \qquad 7\text{-}2$$

where λ is the wavelength of the X-ray beam and $\sin(\theta_i - \theta_{i-1})$ represents the incident angle between two subsequent satellite peaks in the XRD trace. Comparisons of the Schuller periodicities, $\Lambda_{Schuller}$, and measured periodicities, Λ_{meas}, are shown in Table 7-1. Chemical fluctuations across the thickness of the films were studied through use of X-ray photoelectron spectroscopy (XPS) depth profiling (Figure 7-3) on a ThermoFisher K-Alpha (Waltham, Massachusetts, USA) using Ar bombardment to etch the sample between measurements.

Table 7-1 Properties of CSD pR/T films. Comparison of layer periodicities, Λ, as measured via contact profilometry (taking into account the seed layer thickness), Λ_{meas}, and by using the Schuller formula, $\Lambda_{Schuller}$.[266] The results show good agreement between Λ_{meas} and $\Lambda_{Schuller}$, with a maximum of 8% variation. Average grain sizes were measured via atomic force microscopy (AFM) on the surface.

Solution Molarity (M)	Layers	Thickness (nm)	Lotgering Factor (100-texture) (%)	Λ_{meas} (nm)	$\Lambda_{Schuller}$ (nm)	Variation between Λ_{meas} and $\Lambda_{Schuller}$	Grain Size (nm)
0.10	16	199 ± 6	93	11.5 ± 0.3	10.9 ± 0.1	6%	56 ± 3
0.15	9	201 ± 6	96	20.7 ± 0.6	20.4 ± 1.6	1%	
0.20	7	211 ± 6	99	28.0 ± 0.8	26.4 ± 1.2	6%	
0.25	6	216 ± 6	98	33.5 ± 1.0	32.3 ± 0.6	4%	
0.30	5	205 ± 6	99	38.0 ± 1.1	41.5 ± 1.9	8%	67 ± 4
0.35	4	208 ± 6	99	48.3 ± 1.4	49.1 ± 2.2	2%	
0.40	4	241 ± 7	98	56.5 ± 1.7	57.6 ± 1.7	2%	
0.40	3	190 ± 6	99	58.3 ± 1.7	58.8 ± 0.1	1%	89 ± 4
MLA (0.40)	4	232 ± 7	99	--	--	--	113 ± 6

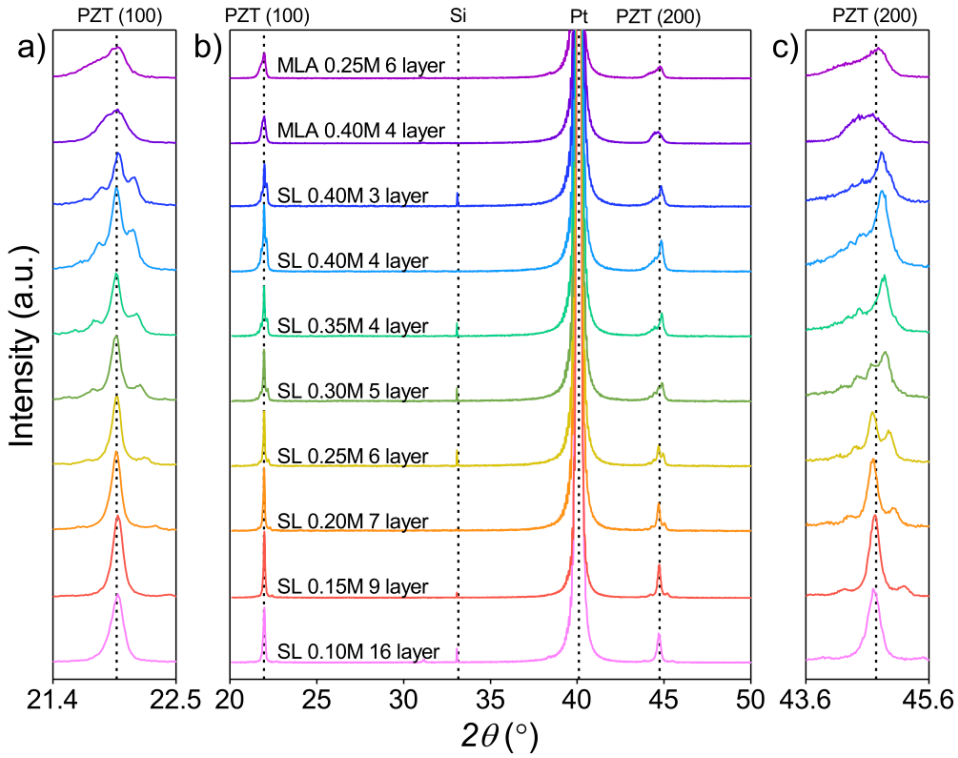

Figure 7-2 X-ray diffraction (XRD) crystallographic phase analysis of periodic (pR/T) films and multi-layer anneal (MLA) films for comparison. (a) and (c) highlight details of the 100- and 200-PZT peaks, respectively. Films are labeled with the molarity of the precursor solution used and the number of layers deposited. Film thicknesses, layer periodicities, and Lotgering factor are available in Table 7-1.

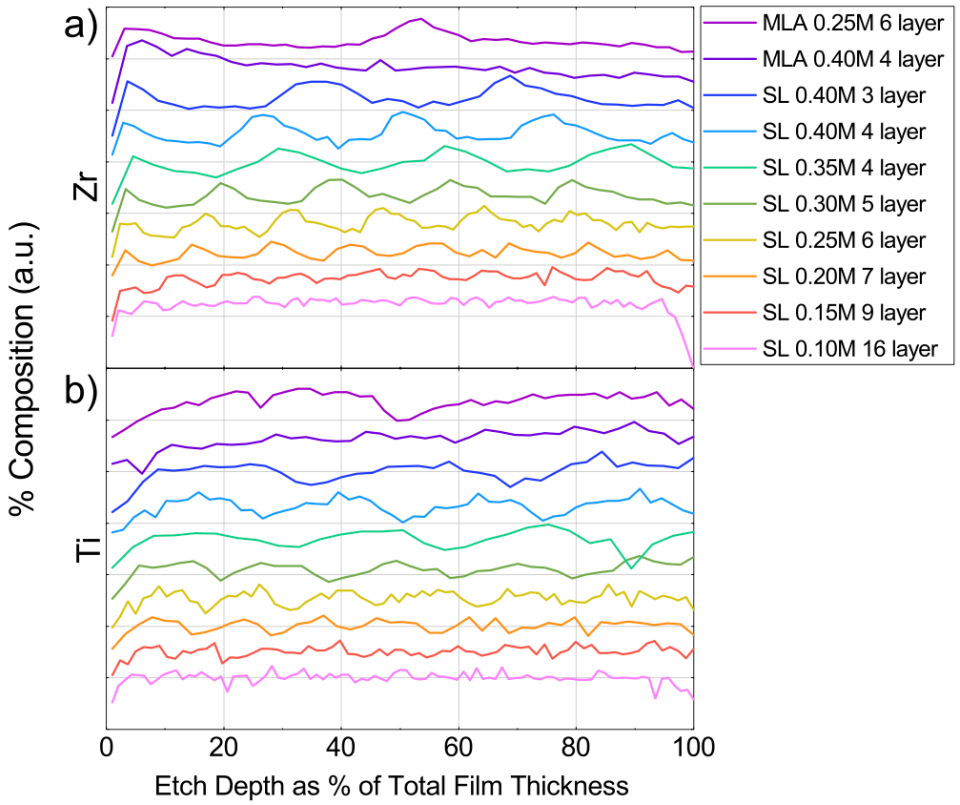

Figure 7-3 X-ray photoelectron spectroscopy (XPS) depth profiling shows composition profiles of (a) Zr and (b) Ti through the thickness of the PZT film. Each tick on the y-axis represents 5% composition of the respective cation.

To further investigate internal interfaces in the films, transmission electron microscopy (TEM) was performed on selected samples. Cross-sections were prepared on an FEI Nova 600 (Hilsboro, Oregon, USA) dual-beam instrument using standard protocols. (S)TEM and energy dispersive X-ray spectroscopy (EDX) analyses were performed on a Philips TF20 (Amsterdam, Netherlands) at 200 kV and equipped with an EDAX Phoenix EDX (Philips, Amsterdam, Netherlands) system. EDX spectrum images were acquired with low dwell times and summed to improve the signal-to-noise ratio and minimize damage/contamination. The intensity of the Zr and Ti Kα lines was determined by background subtraction/integration (HyperSpy).[268] The Zr composition was estimated

using the Cliff-Lorimer analysis of the Zr/Ti ratio.[269] The *k*-factor was estimated from the MLA sample assuming a Zr content of $x \approx 0.53$ for the median ratio of intensities from the Zr and Ti profiles and applied to both samples.[269] This estimate provides good agreement with the XPS data, revealing Zr enrichment in the narrow uppermost portion of each deposited layer, possibly leading to slightly more rhombohedral structure. Results of bright-field TEM (BF-TEM) imaging, integrated EDX profiles, and high-angle annular dark field (HAADF) imaging are shown in Figure 7-4. Due to the relatively fine spatial fluctuations of composition, balancing the signal-to-noise ratio and sample damage under the electron beam, EDX analysis was not practical on the 0.10M (16-layer) film.

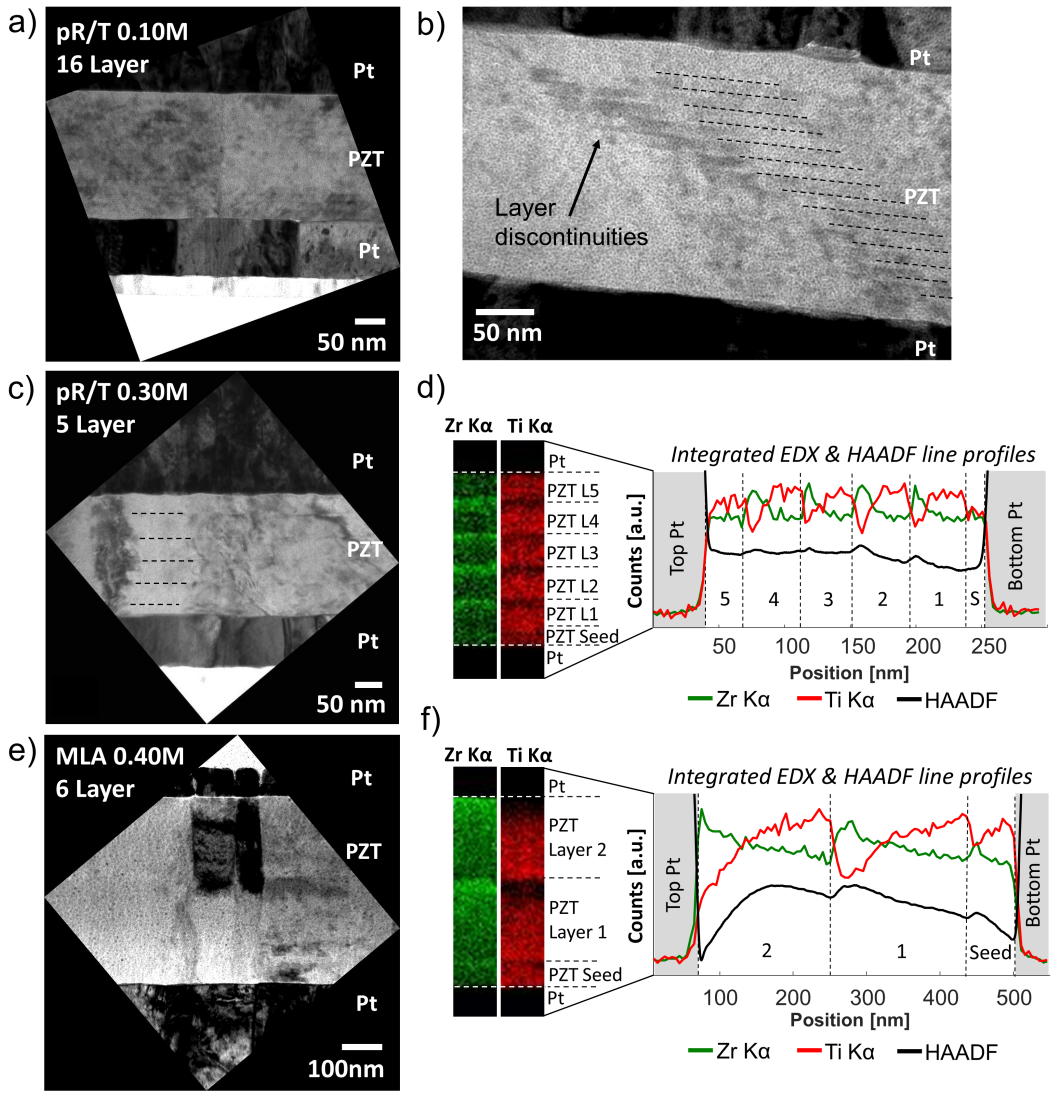

Figure 7-4 Transmission electron microscopy (TEM) of (a, b, c, d) selected periodic R/T (pR/T) and (e, f) multi-layer anneal (MLA) samples. The bright-field (BF-TEM) images (a, b, c, e) show regions of mottled contrast, and some degree of discontinuity at layer interfaces, especially for the 0.30M, 5-layer pR/T film in (c), and a stark change in orientation at the central layer interface in the MLA film (e), suggesting that the crystallization interfaces play a critical role in the films' structure. Lines have been added to guide the eye on (b) and (c) according to layer interfaces. Energy dispersive X-ray spectroscopy (EDX) and high-angle annular dark field (HAADF) imaging (d, f) were undertaken for the 5-layer SL film and the MLA film, confirming the compositional gradients shown in the XPS data (Figure 7-3). Notably, the depth of Ti fluctuations are more dramatic than the corresponding Zr fluctuations in the same layer, due to asymmetric nucleation and growth behavior (see also Figure 7-8). Due to the fine spatial fluctuations of composition within the 16-layer film along with

the necessity of balancing the signal-to-noise ratio and damage under the electron beam, it was not practical to perform the same EDX analysis on that film.

Dielectric, ferroelectric, and piezoelectric characterization were performed on all samples following fabrication. The measurements included, in order, low-field permittivity (ε_r), polarization-electric field hysteresis (*P*-*E*), dielectric permittivity as a function of AC electric field amplitude (ε_r-E_{AC}), dielectric permittivity-DC field tunability characterization (ε_r-E_{DC}), and macroscopic piezoelectric response as a function of DC electric field ($d_{33,f}$-E_{DC}). Specific measurement parameters are found in the Supplemental Materials. Samples were poled with an applied DC bias at ambient temperature for 600 s at approximately five times the coercive voltage, V_C, directly before macroscopic electromechanical measurements, in order to maximize out-of-plane polarization contributions to the piezoelectric response. A summary of these measurements is available in Table 7-2. The Rayleigh approach was used to study intrinsic and extrinsic contributions to the dielectric response by analysis of the AC field-dependent permittivity.[24] The analysis quantifies reversible contributions (ε_{init}) due to reversible domain wall motion and lattice vibration via the intercept of the AC field-dependent dielectric response; as well as irreversible contributions (α), including from domain wall and phase boundary motion, via the slope of the response.

Low-field dielectric permittivity (ε_r) measurements were conducted at 100 mV and 1 kHz using an Agilent 4284A precision LCR meter. Polarization-electric field (*P*-*E*) hysteresis loops were performed up to fields of 300 kV/cm at 100 Hz, using a Radiant P-PM2 ferroelectric test system. Nonlinear AC dielectric permittivity (ε_r-E_{AC}) was analyzed up to approximately 60 kV/cm at 1 kHz. DC electric field-dependent dielectric permittivity

(ε_r-E_{DC}) measurements were performed up to 300 kV/cm DC bias with an overlapping small-signal 100 mV at 1 kHz. Measurements of the converse, effective longitudinal piezoelectric response ($d_{33,f}$) as a function of DC field ($d_{33,f}$-E_{DC}) were performed on an aixACCT double beam laser interferometer (DBLI) up to 300 kV/cm DC bias with an overlapping AC signal $V_{AC} \approx 0.5V_c$. All measurements reported are subject to experimental error up to 3-5%, due to sample variability. The vertical shift in the polarization-field (*P-E*), *ΔP/2* (Table 7-2), is calculated using the formula

$$\Delta P/2 = \frac{P_{rem+} + P_{rem-}}{2} \tag{7-3}$$

where P_{rem+} and P_{rem}- are the values of the positive and negative remanent polarization, respectively. Similarly, the horizontal shift of the electric field in both the *P-E* and $d_{33,f}$-E_{DC} hysteresis loops is determined by

$$E_{internal\ bias} = \frac{E_{C+} + E_{C-}}{2} \tag{7-4}$$

where E_{C+} and E_{C-} are the positive and negative coercive fields, respectively. The dielectric tunability is calculated using the expression

$$dielectric\ tunability = \frac{\varepsilon_{DC,max} - \varepsilon_{DC,min}}{\varepsilon_{DC,max}} \tag{7-5}$$

where $\varepsilon_{DC,max}$ and $\varepsilon_{DC,min}$ are the maximum and minimum values of the dielectric permittivity under DC field measurements, respectively.

Table 7-2 Measured dielectric permittivity, loss tangent, polarization, and effective longitudinal piezoelectric responses for periodic R/T PZT thin films. Uncertainties expressed represent standard deviation to one significant figure. Measurement values are reported to the same decimal place as uncertainty for said measurement.[172]

Precursor Solution Molarity (M)	0.10	0.15	0.20	0.25	0.30	0.35	0.40	0.40
Number of Layers	16	9	7	6	5	4	4	3
Low-field Dielectric								
ε_r	760 ± 40	800 ± 30	720 ± 20	680 ± 20	690 ± 40	740 ± 20	790 ± 40	690 ± 30
tan(δ) (%)	1.5 ± 0.1	1.5 ± 0.1	1.4 ± 0.2	1.6 ± 0.2	1.6 ± 0.1	1.6 ± 0.2	2.1 ± 0.1	1.6 ± 0.1
Rayleigh Analysis								
ε_{init}	780 ± 40	760 ± 10	730 ± 40	682 ± 7	675 ± 7	740 ± 30	780 ± 60	730 ± 50
α (cm/kV)	2.3 ± 0.3	2.1 ± 0.1	2.4 ± 0.2	2.4 ± 0.1	2.3 ± 0.1	2.8 ± 0.2	3.7 ± 0.6	2.7 ± 0.2
$\alpha/\varepsilon_{init}\ x10^3$ ***(cm/kV)***	3.0 ± 0.3	2.8 ± 0.1	3.2 ± 0.2	3.5 ± 0.2	3.4 ± 0.1	3.8 ± 0.2	4.8 ± 0.5	3.7 ± 0.2
Polarization								
$P_{saturation}$ $(\mu C/cm^2)$	33.5 ± 0.9	34 ± 1	35 ± 2	34.1 ± 0.6	35.4 ± 0.8	36.0 ± 0.5	36 ± 1	35.3 ± 0.8
$P_{remanent}$ $(\mu C/cm^2)$	12.7 ± 0.6	12.9 ± 0.4	14 ± 1	13.9 ± 0.2	15.4 ± 0.4	15.6 ± 0.1	15.7 ± 0.6	16.1 ± 0.8
E_{C+} ***(kV/cm)***	56 ± 3	56 ± 5	52 ± 9	64 ± 2	62 ± 2	57 ± 3	53 ± 4	53 ± 1
E_{C-} ***(kV/cm)***	-91 ± 2	-92 ± 5	-95 ± 7	-101 ± 7	-102 ± 4	-100.5 ± 7	-95 ± 7	110 ± 2
$E_{internal,P}$ ***(kV/cm)***	-17 ± 2	-18 ± 3	-21 ± 2	-18 ± 4	-20 ± 1	-22 ± 4	-21 ± 3	-29 ± 2
$\Delta P/2$ $(\mu C/cm^2)$	1.9 ± 0.2	2.0 ± 0.4	2.5 ± 0.3	2.0 ± 0.3	2.5 ± 0.1	2.8 ± 0.4	3.0 ± 0.3	3.4 ± 0.2
ε_r-E_{DC}								
% Diel. Tunability	69.1 ± 0.5	68.5 ± 0.6	68.2 ± 0.1	66.8 ± 0.7	67.4 ± 0.8	67.4 ± 0.2	70 ± 1	68.4 ± 0.1
$\varepsilon_{DC,low\text{-}field}$	900 ± 10	890 ± 10	842 ± 4	788 ± 9	790 ± 20	815 ± 3	880 ± 40	790 ± 40
Piezoelectric (poled)								
$d_{33,f,saturation}$ ***(pm/V)***	51 ± 2	52 ± 2	51 ± 5	50 ± 3	52 ± 2	49 ± 1	49 ± 3	49 ± 3
$d_{33,f,remanent}$ ***(pm/V)***	24 ± 1	26 ± 2	29 ± 1	29 ± 2	30 ± 1	29 ± 1	31 ± 2	31 ± 2
$E_{internal,piezo,poled}$ ***(kV/cm)***	-20 ± 1	-20 ± 1	-22 ± 3	-24 ± 5	-25 ± 1	-24 ± 2	-22 ± 2	-28 ± 1
Piezoelectric (unpoled)								
$d_{33,f,saturation}$ ***(pm/V)***	48 ± 2	51 ± 1	52 ± 4	50 ± 1	52 ± 3	50 ± 2	50 ± 1	49 ± 3
$d_{33,f,remanent}$ ***(pm/V)***	19 ± 5	22 ± 3	25 ± 3	23 ± 3	24 ± 2	24 ± 2	27 ± 2	27 ± 2
$E_{internal,piezo,unpoled}$ ***(kV/cm)***	-15 ± 2	-15 ± 2	-18 ± 5	-17 ± 3	-18 ± 2	-19 ± 1	-17 ± 2	-22 ± 1

In order to sample the local piezoelectric response and probe for structural phase transitions, band excitation piezoresponse force microscopy (BE-PFM) was performed using an Asylum Research Cypher (Santa Barbara, California, USA) atomic force microscope (AFM). BE-PFM switching spectroscopy (BE-SSPFM) was employed to monitor changes in the local hysteresis loops and resonant frequency of the films (Figure 7-5). BE-SSPFM was performed on a 50 × 50 grid over a 2 µm × 2 µm area. A composite map of the piezoresponse amplitude for each point of the grid at the first step of the waveform before applying DC voltage pulses is shown in Figure 7-5c (bottom).

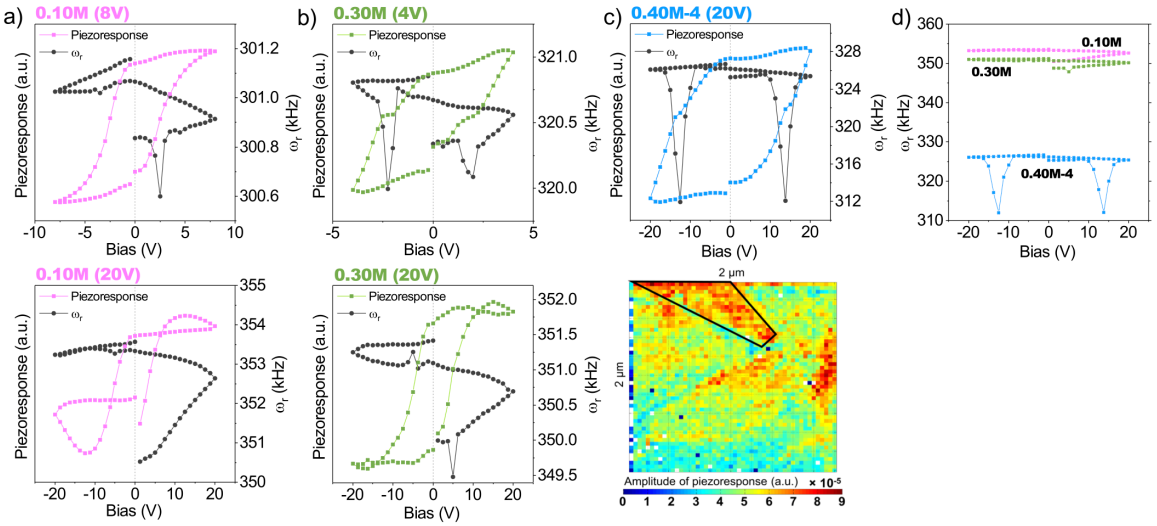

Figure 7-5 (a, b, c) Plots of piezoresponse and resonant frequency responses gathered via band-excitation piezoresponse force microscopy (BE-SSPFM) and averaged over multiple points from a 2 µm × 2 µm area. Notable is the acoustic softening of the resonant frequency in (c, top). Similar acoustic softening was not observed in other samples (a, b) (noted that piezoresponse is represented in arbitrary unites (a.u.), but the range is the same for each measurement). Also notable are small bumps or spikes in the piezoresponse at corresponding locations to the acoustic softening in (c, top). (c, bottom) shows a composite map of the piezoresponse amplitude for each point of the 50 × 50 grid at the first step of the waveform before applying DC voltage pulses (20 V), and outlines the area averaged for (c, top). (d) shows the relative magnitude of the resonant frequency responses from measurements up to 20 V, demonstrating

the comparatively large change in the 0.40M film due to acoustic softening relative to the other two films with lower periodicity.

AFM measurements of the surface topography of selected samples was performed prior to BE-SSPFM (Figure 7-6) to compare lateral surface grain sizes in selected pR/T and MLA films (see Table 7-1). Grain sizes were determined via the average grain intercept (AGI) method. AFM measurements on selected pR/T samples was performed with an Asylum Research Cypher; measurements on the MLA film was performed with a Veeco 3100. Deflection measurements were not taken on the MLA sample. Images were flattened with a first order fitting to account for variations in the images due to sample mounting.

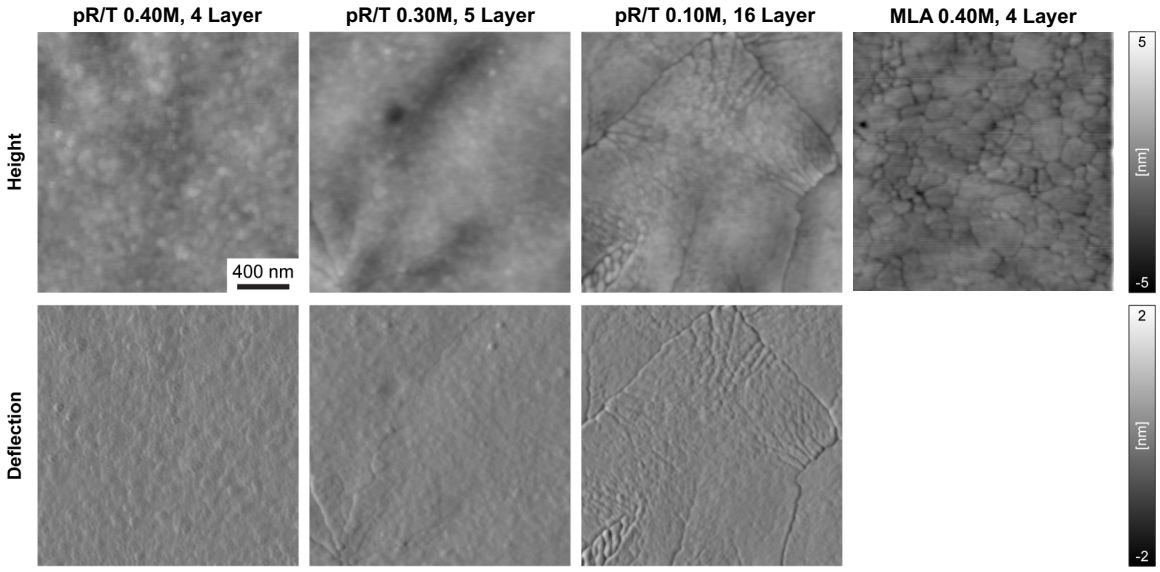

Figure 7-6 Atomic force microscopy (AFM) scans of selected pR/T and MLA, showing differences in surface microstructure. Calculated grain sizes are reported in Table 7-1.

7.4 Results

Fabrication of CSD PZT thin films annealed after deposition and pyrolysis of each layer showed strong evidence of periodic changes in chemical composition (Figure 7-3, Figure 7-4d, Figure 7-4f) and structural changes (Figure 7-2, satellite peaks) through the thickness of the films. Thermodynamic and kinetic factors drive heterogeneous Ti-rich nucleation at the substrate-film interface during crystallization, followed by growth of a Zr-rich phase, thus forming the compositional gradient and accompanying R/T phases in the crystallized PZT film.[265,270] XPS measurements (Figure 7-3a, b) confirmed strong Zr/Ti chemical gradients for the films processed in the range of 0.20M to 0.40M precursor solutions. However, the films processed with 0.10M and 0.15M solutions showed flatter, less distinct gradients, potentially due to cation interdiffusion between the relatively thin layers, or insufficient instrumental resolution of chemical fluctuations (individual crystallized layers are 10 to 20 nm in this range). The compositional gradients normal to the surface of the films are further confirmed via EDX as shown in Figure 7-4d and Figure 7-4f for selected samples (see also Figure 7-8b, discussed later), showing up to 4% compositional variation in either direction from the initial composition of x = 0.53. These chemical variations, especially in the samples with thicker layers, are expected to demonstrate local extremes in composition up to $PbZr_{0.57}Ti_{0.43}O_3$ and $PbZr_{0.49}Ti_{0.51}O_3$, corresponding to purely rhombohedral and tetragonal phases in bulk PZT, respectively. Thus, we expect that the alternating Zr/Ti gradients exhibited by the samples in this work yield some degree of periodic R/T phases.

XRD crystallographic orientation analysis of the films showed distinct satellite peaks for films fabricated in the range of 0.15M to 0.40M precursor solutions (Figure 7-2),

indicating that the interfaces between Zr/Ti regions of each layer and parallel to the substrate exhibit a large degree of coherency.[266] Calculations of the Schuller periodicities, $\Lambda_{Schuller,}$ showed excellent agreement (≤ 8% variation) with calculations of the measured periodicity, Λ_{meas} (Table 7-1), consistent with the periodic nature of the fabricated films.[266] Both sets of films showed only perovskite peaks with a large degree of 100-texture (> 93% Lotgering factor for all films, reference powder diffraction file (PDF) 04-016-2735, Table 7-1).

Figure 7-7 shows trends in measured dielectric, ferroelectric, and macroscopic piezoelectric responses as a function of layer periodicity in the films. At low AC electric field, dielectric permittivity (ε_r) showed a moderate decreasing trend and the dielectric loss tangent, *tan(δ)*, exhibited a slight increasing trend (Figure 7-7a) with increasing periodicity. At intermediate AC electric fields, the results of the Rayleigh analysis show an increase of α with increasing layer periodicity (Figure 7-7b). On the other hand, ε_{init} (Figure 7-7b), shows a minor decreasing trend with increasing periodicity. Accordingly, trends in the ratio $\alpha/\varepsilon_{init}$, generally follow those observed for α, *i.e.*, overall increasing extrinsic contributions in films with larger layer periodicities (Figure 7-7c).

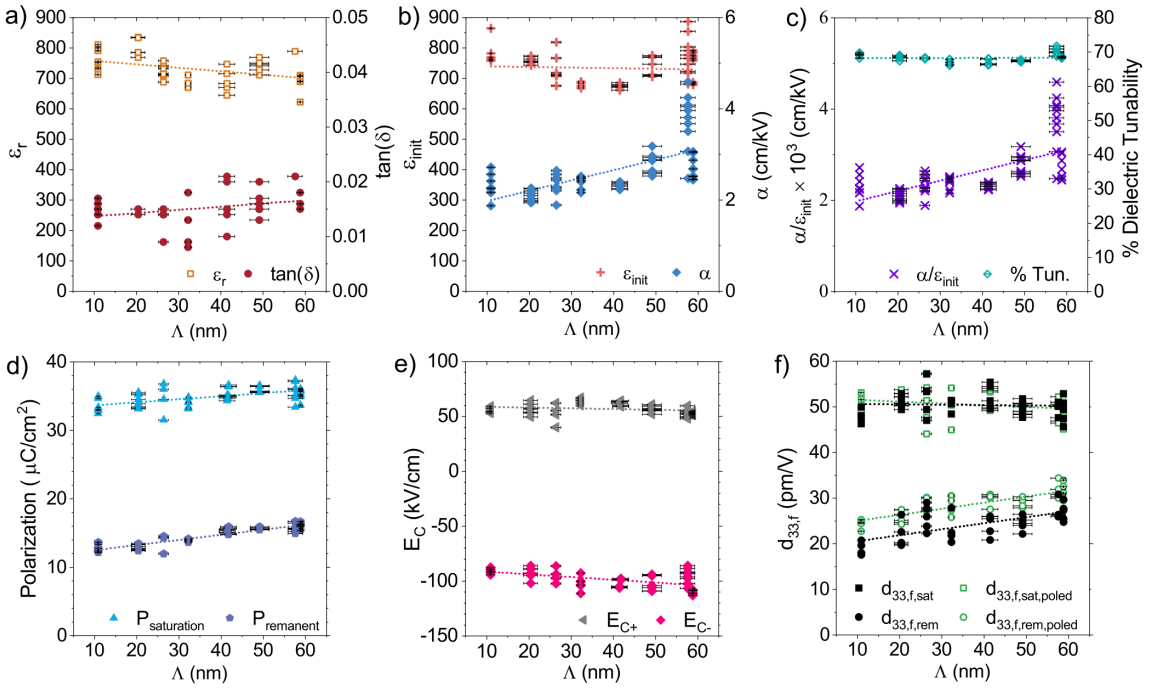

Figure 7-7 Functional response characterization for (a) low-field dielectric, (b) AC nonlinear dielectric, (c) Rayleigh ratio and % dielectric tunability, (d) polarization, (e) coercive field, and (f) piezoelectric responses as a function of layer periodicity. Lines have been added to guide the eye. Note the increasing trends for dielectric loss tangent, polarization, extrinsic contributions to dielectric response, and remanent piezoelectric response, suggesting domain wall motion is increased in films with larger layer periodicity. Conversely, slight decreasing trends in the low-field permittivity and intrinsic contributions to response with increasing layer periodicity are observed. Error in the periodicity is calculated from $\Lambda_{Schuller}$.

Trends in the coercive field, both positive and negative (E_{C+} and E_{C-}, Figure 7-7e), suggest that a relatively large internal bias is developed with greater layer periodicity (see also Figure 7-9c). A similar shift towards the positive direction of asymmetry in remanent polarization, $\Delta P/2$, is noted (Figure 7-9b). This shift indicates increasing self-polarization with increased periodicity.[58]

Figure 7-4a to Figure 7-4c, and Figure 7-4e show representative bright field (BF-)TEM images of selected pR/T films and a multi-layer anneal (MLA) film for comparison of microstructure. Figure 7-4d and Figure 7-4f show Zr and Ti elemental maps and

corresponding integrated line profiles from the 5-layer 0.30M pR/T and 6-layer 0.40M MLA films, respectively. HAADF intensity line profiles (Figure 7-4d and Figure 7-4f) along the PZT films show maxima in intensity in the Zr-rich regions due to the high sensitivity of HAADF contrast to atomic number, *Z*. Due to the polycrystalline nature of the films, the BF-TEM images of both the pR/T and MLA films show extensive regions of mottled contrast, which are attributed to variations in grain and/or domain structure (see also Figure 7-10). The (16-layer) 0.10M pR/T film in Figure 7-4a and Figure 7-4b exhibits a relatively continuous contrast throughout the film thickness whereas the (5-layer) 0.30M pR/T and MLA films (in Figure 7-4c and Figure 7-4e, respectively) demonstrate somewhat columnar crystallites. However, a stark change in contrast of crystallites at the central crystallization interface in the MLA film (Figure 7-4e) is observed and likely arises from slight changes in the in-plane crystallographic orientation, resulting in a discontinuity between the layers. This is a representative example and similar variations in contrast are observed throughout the cross-section which is several μm long, suggesting that this is a common feature to the MLA sample and not simply confined to one location. Similarly, regions of relative discontinuity at film-layer interfaces are observed in the pR/T films (Figure 7-4b and Figure 7-4c), further suggesting that the crystallization interfaces play a critical role in determining the properties of these films. In the (5-layer) 0.30M pR/T film, these changes in contrast in the BF-TEM image coincide with large increases in the Zr concentration, with x up to ~0.60. Therefore, they likely arise from a combination of both changes in density of the material and slight changes in crystallography since this composition lies towards the rhombohedral portion of the phase diagram.

BE-SSPFM results show characteristic piezoresponse hysteresis loops, with switching voltages in the range of 2 to 15 V, and generally increasing with film layer periodicity. The effects of charging in the 0.10M and 0.30M samples are noted in the piezoresponse hysteresis loops at high electric field through the noses at the end of the loops (Figure 7-5a right, Figure 7-5b right). The contact resonant frequency extracted from simple harmonic oscillator (SHO) fitting of the measured piezoresponse *vs.* excitation frequency was monitored, as it is sensitive to changes in lattice stiffness.[271] Namely, "acoustic softening" (*i.e.*, large reductions in the stiffness of the locally-interrogated material) can indicate potential phase transitions, especially if accompanied by local enhancements of the piezoelectric response, as demonstrated by Vasudevan *et al.*[271] It has been reported that some degree of acoustic softening is typically observed at ferroelectric switching, but that such softening is expected to increase dramatically when it is the result of field-induced phase transitions.[271] Substantial acoustic softening (~4% reduction to contact resonant frequency) was observed in local regions in the pR/T film processed with 0.40M (4 layer) precursor solution (Figure 7-5c and Figure 7-5d). Similar effects were not observed in other samples at both low and high applied tip voltages (Figure 7-5a, Figure 7-5b, Figure 7-5d).

7.5 Discussion

The observed trends of greater dielectric irreversible Rayleigh coefficient (α) with increasing layer periodicity signal potentially increased extrinsic contributions – *e.g.*, from domain walls or phase boundary motion – in samples with thicker crystallized layers.

However, these results are counterpointed by the slight tendency of decreasing ε_{init} contributions to the dielectric response with increasing film periodicity, suggesting a complex interaction of the compositional interfaces in the films, or alternatively, due to the chemical excursions away from the MPB. Grain and domain size effects, pinning of hysteretically and nonlinearly mobile internal interfaces, chemical heterogeneity, and residual stresses inevitably play critical roles in determining the effects of crystallized layer thickness in the periodic-layered pR/T PZT films studied here. In the following discussion, we consider several of the possible contributions to the observed trends in functional response.

Discontinuity at the crystallization interfaces, both in the grain/domain structure and crystallite orientation are readily visible in the TEM analyses (Figure 7-4b, Figure 7-4c, and Figure 7-4e). Despite the strongly-columnar texture of the films (Figure 7-4c and Figure 7-4e), the crystallites extending through the thickness of the film do not necessarily maintain consistent in-plane orientation, as evidenced by the contrast changes across the crystallization interface (Figure 7-4e). This observation is important since these discontinuities in the MLA film suggest that the density of such interfaces and the number of anneals can have a substantial impact on the crystallography throughout the film thickness, and hence the overall functional properties of the film. Based on the observations here, the most abrupt discontinuities arise for films with thicker as-deposited layers and hence, fewer anneals. When annealing the samples more frequently (*i.e.*, lower periodicity and thinner crystallized layers), exposure to higher crystallization temperatures allows for increased diffusion and therefore less abrupt crystallization interfaces, thus reducing the presence of satellite peaks in the corresponding XRD data (Figure 7-2). Such changes in

crystallography through the film thickness may result in grain size reduction for samples with smaller layer periodicity, through limitation of the maximum out-of-plane grain size to the individual layer thickness (Table 7-1). Such reduction is consistent with AFM measurements of lateral grain size, as performed on the films' surface (Table 7-1). Numerous reports have shown that domain size (and thus wall mobility) in ferroelectric materials scales with grain size.[243,244] In smaller grains where smaller domains are expected, domain walls are bound to exhibit reduced mobility, due to greater chances of interaction with other defects, including grain boundaries and domain walls – potentially resulting in diminished extrinsic contributions to the dielectric response. These scaling effects are consistent with reduced α and lower polarization and remanent piezoelectric response ($d_{33,f,rem}$) in samples with thinner crystallized layers. However, while grain size reductions can explain trends in extrinsic contributions to the dielectric and ferroelectric responses, it cannot fully account for the trends in intrinsic contributions shown in Figure 7-7. Below, we consider other factors impacting observed trends in the intrinsic and extrinsic contributions to the response.

While the proximity of the PZT composition to the morphotropic phase boundary generally results in favorable enhancements of dielectric and electromechanical responses, there are differences in intrinsic and extrinsic contributions for compositions on either side of the MPB. Rhombohedral compositions (Zr > 0.53) generally demonstrate greater values of α than tetragonal compositions at an equal distance from the phase boundary.[48,51] Coupled with the magnitude of chemical oscillations through the thickness of the film, such asymmetry can lead to additional dependence of functional response on periodicity. Chemical fluctuations from the mean composition will inevitably traverse regions of the

phase diagram that offer varying levels of both extrinsic and intrinsic dielectric response. For samples with higher periodicity (thicker layers), these deviations from the mean composition are of greater magnitude than for samples with smaller periodicity, as illustrated in Figure 7-8a. Hence, the latter show, on average, a more homogeneous composition. On the other hand, as noted in the EDX data, the spatial extent of Ti chemical fluctuations are greater than those of Zr, which is especially apparent in the films processed with larger layer periodicity. Results of higher spatial resolution EDX analysis for a single layer of the (5 layer) 0.30M pR/T film in Figure 7-8b show that through the thickness of the film, the Ti-rich zones are significantly thicker (> 60 % of the layer thickness) than the corresponding Zr-rich regions with a notable compositional gradient stretching over several nm. These significant chemical oscillations in the direction of the Ti-rich composition (*i.e.*, greater compositional heterogeneity) correlate with the substantial reductions to the intrinsic response, ε_{init}, with increased layer periodicity discussed above.[272,273] For the samples with small periodicity, their more homogeneous composition prevents compositional oscillations of similar magnitude, and corresponding reductions to the intrinsic response are relatively absent.

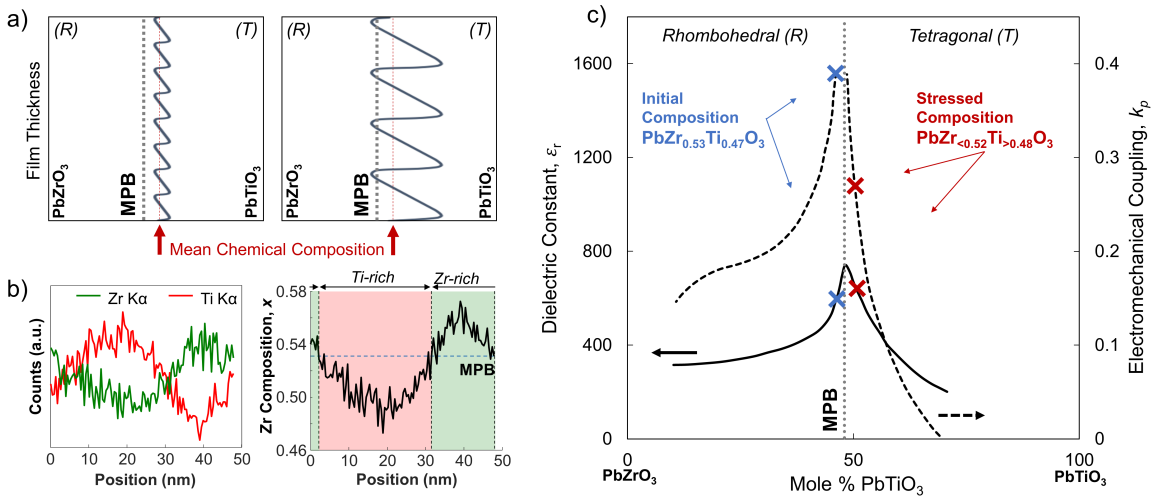

Figure 7-8 (a) Chemical fluctuations across the thickness of the film vary in magnitude dependent on layer periodicity. Films with lower periodicity show less-intense fluctuations (a, left), while those with greater periodicity are able to approach the MPB (a, right), thus enhancing extrinsic contributions to response. However, chemical gradients begin with strong nucleation of Ti, simultaneously driving lower intrinsic response on the tetragonal side of the diagram for films with greater magnitude of cation fluctuations. (b) EDX profiles of the Zr and Ti content in an individual layer of the 0.30M (5-layer) pR/T film. The Zr profile is shown in (b, right) oscillating over the initial composition of 53% Zr, showing the greater Ti content in each individual layer (red). (c) Diagram showing dielectric and electromechanical response as a function of mole percent $PbTiO_3$. The morphotropic phase boundary (MPB) is shown as the vertical dotted line. The initial $PbZr_{0.53}Ti_{0.47}O_3$ composition used in this work is shown as a blue "X" on the diagram. With tensile stress induced in the PZT thin film during crystallization anneals via the SiO_2 layer and Si substrate, the PZT composition can effectively shift to the tetragonal side of the MPB (shown as red "X" on the diagram).

Thermal loading during crystallization can potentially result in large variations in residual stress in ferroelectric thin film material stacks. Numerous studies have shown that residual stresses can effectively shift the MPB, thus modifying the transition temperature, T_C.[52-55] In PZT thin films, biaxial compressive stresses can result in a T to R phase transition, while tensile stresses have been shown to shift MPB compositions towards the tetragonal phase.[52,53] Given the initial proximity of the PZT precursor solutions to the MPB, the expected tensile stresses in 200 nm-thick films (reported up to 180 MPa)[274] can

potentially push the effective average composition into the tetragonal region of the phase diagram. This concept is demonstrated in Figure 7-8c, showing initial composition $PbZr_{0.53}Ti_{0.47}O_3$, and an effective "stressed composition" after crossing the MPB. From the stressed composition on the tetragonal side of the MPB, the previously-discussed effects of large chemical excursions towards the tetragonal side of the phase diagram further exacerbate the potential reductions to intrinsic dielectric response.

The results of BE-SSPFM experiments show evidence of localized potential phase transitions that further support the hypothesis of deeper chemical excursions, and thus, closer proximity to the MPB in the sample with the highest periodicity. A relatively dramatic reversible acoustic softening occurs specifically in the 0.40M, 4-layer sample (Figure 7-5c), where Zr/Ti cation gradients are enhanced over a wide region. However, while evidence of possible phase transitions is available in the acoustic softening of the 0.40M sample, the corresponding changes to piezoresponse observed are somewhat limited (Figure 7-5c top, notable as small steps corresponding to ferroelectric switching). Meanwhile, similar effects are not observed in the other films; we discuss multiple size- and chemical heterogeneity-related potential causes for this. First, in the samples with thinner layers, deficient chemical fluctuations do not result in sufficient proximity to the MPB to yield an R/T phase transition. The individual crystallization layers of the 0.40M samples are nearly 20% thicker than the 0.35M sample (Table 7-1), allowing for a greater level of chemical fluctuation in the 0.40M samples. Second, the 0.40M, 4-layer film is the sample with the greatest total thickness, and 10 to 20% thicker than all other films studied here, including the 0.40M, 3-layer and 0.35M, 4-layer films whose Zr/Ti fluctuations are also relatively dramatic (Figure 7-3). Thinner films are likely more susceptible to the

previously-mentioned effects of residual stress. The effective composition of PZT in thinner films conceivably shifts even further from the MPB composition compared to the thicker 0.4M, 4-layer sample, to the point that even large chemical oscillations are not close enough to the MPB to observe R/T phase transitions and accompanying acoustic softening. While film thickness may affect susceptibility to residual stress effects, we note that the functional response trends in Figure 7-7 do not correlate with trends related to total film thickness (see Figure 7-11). Additional contributions from flexoelectric effects and Vegard strains are also possible, but are expected to be limited, as discussed in Supplemental Materials.

7.6 Conclusions

Successful processing of polycrystalline PZT thin films with periodic heterogeneous Zr/Ti oscillations has been demonstrated across a range of layer periodicities, with compositional gradients normal to the surface. XRD and the Schuller formula show good agreement of satellite peak locations with measured layer periodicities, suggesting some degree of superlattice-like coherency between phases in the material; rhombohedral/tetragonal phases are expected to correspond to the Zr-/Ti-rich zones of individual layers, respectively. Trends in the measured functional response show strong dependencies of dielectric, ferroelectric, and electromechanical response on layer periodicity. Notably, remanent and saturation polarizations, remanent piezoelectric response, and extrinsic contributions to the dielectric response show strong increasing trends with increasing layer periodicity, suggesting increased mobility of internal

interfaces, *e.g.*, domain walls and phase boundaries. On the other hand, minor decreasing tendencies are noted for the low-field permittivity and intrinsic contributions to dielectric response with increasing layer periodicity, suggesting a complex interaction in the samples that exceeds simple variations in domain wall mobility.

Crystallization interfaces are thought to strongly influence grain size and structure, resulting in grain and domain size refinement in samples with thinner layers, and corresponding reductions to domain wall motion. On the other hand, the magnitude of chemical fluctuations greatly affects functional response: asymmetric chemical oscillations towards the tetragonal side of the MPB result in decreased intrinsic contributions to the dielectric response in samples with larger chemical gradients, *i.e.*, larger periodicity. Residual stress effects potentially push the effective composition of the films further to the tetragonal side of the MPB, additionally exacerbating the effects of compositional oscillations. These results suggest that crystallization interface number density and compositional gradients are strong contributors to functional responses trends of CSD-processed ferroelectric thin films through modification of film structure (*e.g.*, grain size) with respect to their epitaxial, single-crystalline counterparts. These findings can be employed to tailor the functional response of ferroelectric thin films for microelectronics applications, by engineering the chemical heterogeneity and number of crystallization interfaces within the film.

7.7 Supplemental Materials

7.7.1 Additional Piezoresponse Force Microscopy Considerations

We consider the effects of Vegard strains as a result of applied pressure from the PFM probe. Defect motion as a result of applied pressure from PFM probe tips has been strongly correlated to grain size and chemical composition, and can result in changes to the ferroelectric transition temperature.[275,276] It is possible that the grain size differences as a function of layer periodicity (as discussed in the main section) result in local fluctuations of the transition temperature with the pressure of the applied probe during BE-SSPFM measurements, potentially masking evidence of phase transitions in those experiments. We also note that the observed softening of the resonant frequency (Figure 7-5) is unlikely to be the effects of local charge injection, the effects of which are typically associated with thinner films. Comparison of the two samples processed with 0.40M solutions showed that substantially greater softening occurs in the *thicker* of the two samples: 241 nm with 4 crystallized layers *vs.* 190 nm thick from 3 deposited layers, and is thus not likely to result from simple charge injection.

7.7.2 Flexoelectric Contributions

Possible contributions of the flexoelectric effect – *i.e.*, polarization generated in a solid through application of a strain gradient – to the observed trends in functional response as a function of periodicity should also be considered.[262] While flexoelectric contributions are typically small and difficult to fully separate from piezoelectric properties in

ferroelectric-phase materials, their presence has been proposed in (heterostructured) epitaxial PZT thin films.[248,249] Specifically, large strain gradients in thin films potentially arise from misfit lattice strain and due to the presence of internal interfaces, leading to flexoelectric couplings in the material. The strain-induced flexoelectricity can subsequently create large internal bias fields, breaking internal field symmetry and resulting in changes to the functional properties of such films.[248] In the pR/T PZT thin films studied here, large Zr/Ti chemical gradients (and the expected R/T phase transitions) inevitably lead to some amount of lattice mismatch, exacerbated in samples with greater layer periodicity. In fact, in the pR/T samples, the greater magnitude of chemical fluctuations is correlated with increasing levels of internal bias, both in the *P-E* and d_{33}-E_{DC} hysteresis loops (Figure 7-9b and Figure 7-9c). This large internal electrical bias in samples with larger layer periodicity suggest that flexoelectric effects potentially affect functional response in samples with enhanced chemical oscillations and corresponding strain gradients.

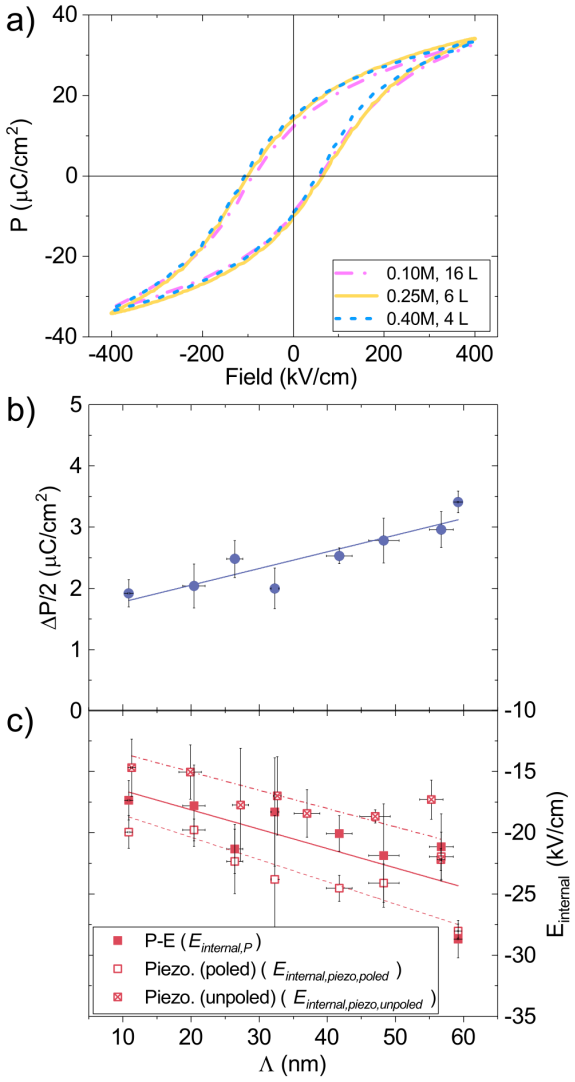

Figure 7-9 (a) Sample *P-E* hysteresis loops showing potential shifting in the negative horizontal electric field direction. (b) shows the vertical shift in polarization, *ΔP/2*, calculated from the *P-E* loops. (c) shows the horizontal shift in electric field, $E_{internal}$, extracted from both the *P-E* loops and d_{33}-E_{DC} hysteresis loops. Trends in (c) suggest strong internal biases developed with increasing layer periodicity. Error in the periodicity is calculated from $\Lambda_{Schuller}$.

7.7.3 Transmission Electron Microscopy Imaging of Ferroelectric Domains

Transmission electron microscopy (TEM) showed potential striped domain structures in the 0.30M, 5-layer PZT thin film pR/T sample (Figure 7-10). Due to resolution limitations, similar images in the 0.10M, 16-layer film were not possible. No significant variations in domain structure is observed corresponding to Zr/Ti fluctuations through individual layers, though general discontinuities in domain structure are observed at individual layer interfaces.

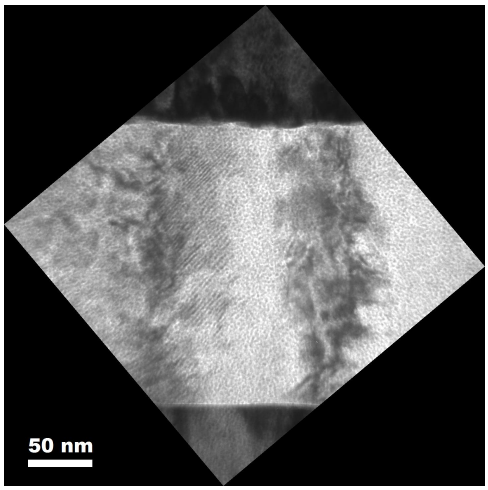

Figure 7-10 Cross-sectional transmission electron microscopy (TEM) of a 0.30M, 5-layer PZT thin film pR/T sample, showing potential striped domain structures.

7.7.4 Film Thickness Effects

Variations in processing conditions and indivisible layer thicknesses (*e.g.*, a 0.40M precursor solution results in individual layer thickness of ~60 nm, hence the total film thickness is either ~180 nm or ~240 nm (discounting the seed layer)) resulted in deviations from the 200-nm target film thickness by up to ~20% (see Table 7-1). Numerous previous

reports have studied scaling effects in perovskite-phase ferroelectrics, showing strongly-decreasing trends of functional properties with reduced film thickness.[37,244] Figure 7-11 shows literature data from a variety of studies on polycrystalline thin-film ferroelectrics, compared to the present work.[35,244,277-284] Logarithmic trendlines are fit to the data from this work to guide the eye in the inset plots. Neither ε_r or $d_{33,f,sat}$ showed a strong trend correlated to scaling effects, comparable to those observed in the literature. These results suggest that scaling effects are limited in the pR/T films studied in this work, and are not the root cause for the observed trends in functional response as a function of layer periodicity.

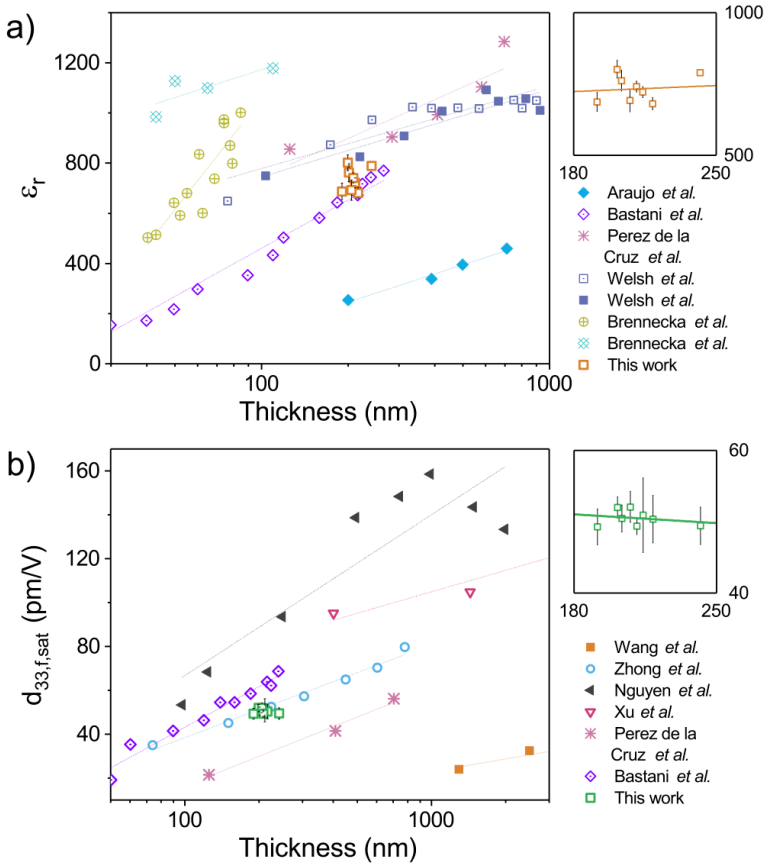

Figure 7-11 Comparison of data from this work to trends of functional response from the literature on polycrystalline ferroelectric thin films.[35,244,277-284] Functional property trends are plotted against film thickness. Note the reduction in dependence on thickness, especially for measurements of piezoelectric properties. Secondary plots are shown to illustrate goodness of a fitted line to guide the eye. The lack of an apparent trend is noted for both (a) dielectric permittivity, and (b) saturated piezoelectric response. Apparent trends of thickness dependence in the films studied here are arguably absent.

7.8 Acknowledgements

S.B., S.W., C.D., and N.B.G. acknowledge funding from the U.S. National Science Foundation (NSF) under grant numbers DMR-1255379 and CMMI-153726.2 S.B. and N.B.G acknowledge. support by the Defense Threat Reduction Agency, Basic Research

Award No. HDTRA1-15-1-0035 to Georgia Institute of Technology. The contents do not necessarily reflect the position or the policy of the federal government, and no official endorsement should be inferred. A.B.N. and A.K. acknowledge support by Department of Education and Learning, Northern Ireland through the US-Ireland R&D partnership grant no. USI-082 and funding support from the Engineering and Physical Sciences Research Council (EPSRC) through contract EP/N018389/01. S.N. and B.J.R. acknowledge support from Science Foundation Ireland (14/US/I3113). A portion of this research was conducted at the Center for Nanophase Materials Science which is a DOE Office of Science User Facility, under proposal number CNMS2014-282. The authors gratefully acknowledge Ronald G. Polcawich and Joel Martin of the U.S. Army Research Laboratory for providing the platinized Si substrates for this work.

CHAPTER 8. LAYER CRYSTALLIZATION INTERFACES: INTERACTION WITH RADIATION

At the time of this publication, the content in this chapter is under review at *Applied Physics Letters*.

Effects of Crystallization Interfaces on Irradiated Ferroelectric Thin Films

Steven J. Brewer, Samuel C. Williams, Cory D. Cress, Nazanin Bassiri-Gharb

Applied Physics Letters, (*in review*), (2017)

8.1 Summary

This work investigates the role of crystallization interfaces and chemical heterogeneity on the radiation tolerance of chemical solution-deposited lead zirconate titanate (PZT) thin films. Two sets of PZT thin films were fabricated with crystallization performed at (i) every deposited layer or (ii) every three layers, resulting in distinct variations in chemical heterogeneity through the films' thickness. The films were exposed to a range of ^{60}Co gamma radiation doses, between 0.2 and 20 Mrad, and their functional response was compared before and after irradiation. The observed trends indicate enhancements of dielectric, ferroelectric, and piezoelectric responses at low radiation doses, and degradation of the same at higher doses. Response enhancements are expected to result from low-dose, ionizing radiation-induced charging of internal interfaces – an effect that results in neutralization of pre-existing internal bias in the samples. At higher radiation doses, accumulation and self-ordering of mobile defects contribute to degradation of dielectric, ferroelectric, and piezoelectric properties, exacerbated in the samples with more crystallization layers, potentially due to increased defect accumulation at these internal interfaces. These results suggest that the interaction between radiation and crystallization interfaces is multifaceted – the effects of ionization, domain wall motion, point defect mobility, and microstructure are considered.

8.2 Introduction

Ferroelectric thin films, such as lead zirconate titanate (PZT), find widespread use in a multitude of microelectronics applications, including microelectromechanical system (MEMS) sensors and actuators, multilayer ceramic capacitors, logic and memory elements, and environmental energy harvesters, due to their large dielectric, ferroelectric, and piezoelectric responses.[1,285] Growth in the area of connected devices (*Internet of Things*) has been accompanied by increasingly rigorous functional requirements with small footprints, leveraging multiple functionalities in continuously thinner films. Among the many areas of interest, sustained operation in radiation-hostile environments, *i.e.*, for satellite and nuclear power applications, is of particular interest.[40] A variety of work has studied the fundamental mechanisms underpinning radiation interaction with ferroelectric materials and their functional response, generally demonstrating degradation thereof by X-ray, gamma, proton, and neutron irradiation.[40,97,100] In polycrystalline ferroelectric thin films, such degradation is largely due to reduced motion of nonlinearly-mobile internal interfaces (*e.g.*, domain walls) pinned by defects induced by ionization (by X-rays and gamma radiation) and atomic displacement events (*e.g.*, when exposed to protons and neutrons).[32,40,101] However, the processing conditions used to fabricate ferroelectric thin films can dramatically modify a material's pre-existing defects, including ferroelectric domains and internal interfaces, their eventual contributions to the functional response, and the nature of their interaction with radiation.

In this work, we report the effects of ^{60}Co gamma irradiation on PZT thin films with different thermal processing histories and numbers of crystallization steps. Ample previous work has focused on *functional response enhancement* in ferroelectric thin films

by modifying the layer crystallization arrangements and chemical heterogeneity through the films' thickness, including studies of bi-layered, graded, and superlattice films.[247-252,255,258,262,263] While many of these approaches have demonstrated attractive enhancements to ferroelectric and piezoelectric properties, the degree to which layer crystallization periodicity, thermal processing history, and compositional heterogeneity affect *radiation tolerance* is relatively unknown. We report local enhancements and subsequent degradation of functional responses in gamma-irradiated PZT thin films, as correlated to interface periodicity and chemical heterogeneity throughout the thickness of the films.

8.3 Experimental Procedures

$PbZr_{0.53}Ti_{0.47}O_3$ (PZT) thin films, 200 (± 6) nm-thick, were fabricated via chemical solution deposition (CSD) with 0.25M precursor solutions on 100-Si wafers with 500 nm thermal oxide and a continuous bottom electrode of 35 nm sputtered TiO_2 and 100 nm sputtered Pt. A 15 nm thick, $PbZr_{0.53}Ti_{0.47}O_3$ seed layer was deposited using a 0.15 M precursor solution, to induce 100-texture in subsequent layers.[100,111,132] Film and seed precursor solutions were batched for 20% and 30% molar excess Pb, respectively, to compensate for Pb loss at high crystallization temperatures. Specific details of film processing are outlined elsewhere.[111,247,286]

The resulting "multi-layer anneal" (MLA) films have six layers, grouped in two crystallization steps of three layers each, while the "single-layer anneal" (SLA) films are annealed at each of the six layers. For both sets of films, pyrolysis was performed after

each deposition at 400 °C for 60 s, and crystallization was achieved at 700 °C for 60 s in a rapid thermal annealer. MLA films have typically shown compositional homogeneity throughout the thickness of the film, while similarly-processed SLA films exhibit dramatic compositional Zr/Ti gradients due to asymmetric nucleation and growth behaviors in films with relatively short layer-stacking periodicities.[111,265,286] X-ray diffraction (XRD) was performed to study crystallographic phase (PANalytical Alpha-1); scanning electron microscopy (SEM) (Zeiss Ultra60 FE-SEM) and atomic force microscopy (AFM) (Asylum Research MFP-3D) were used to image film microstructure. Film thicknesses were measured via contact profilometry (KLA Tencor P15), after chemical etch (buffered oxide etch (BOE), 6:1 NH_4F:HF) removal of part of the film to access the bottom electrode.

The films were exposed to various gamma radiation doses between 0.2 and 20 Mrad(Si) at a rate of ~600 rad(Si)/s from a ^{60}Co source, with a geometry that yields an isotropic exposure. Electrodes were left floating during exposure. Functional response of the samples was characterized before and after irradiation (on the same electrodes and samples), including (in order): low-field dielectric permittivity (ε_r) at 100 mV and 1 kHz (Agilent 4284A LCR meter); polarization-electric field (P-E) loops to 500 kV/cm at 100 Hz (Radiant P-PM2); nonlinear AC dielectric permittivity (ε_r-E_{AC}) for up to ~120 kV/cm AC electric field at 1 kHz; DC electric field-dependent permittivity response (ε_r-E_{DC}) up to 400 kV/cm DC bias with an overlapping 100 mV AC signal at 1 kHz; and the converse, effective longitudinal piezoelectric response ($d_{33,f}$) performed on an aixACCT double beam laser interferometer (DBLI), up to 400 kV/cm DC bias with an overlapping AC signal, E_{AC} ~ 0.5E_C, where E_C is the coercive field. Table 8-1 shows percent changes in functional response measurements at each radiation dose. At intermediate-low AC electric fields, the

Rayleigh approach was used to quantify changes in intrinsic (ε_{init}) and extrinsic (α) contributions to the dielectric response, *i.e.,* contributions from the lattice and domain vibration, and irreversible domain wall motion, respectively.[24,29,33,236] All measurements were performed on at least five electrodes and are subject to experimental error of up to 3-5% due to sample/measurement variability.

Table 8-1 Maximum percent enhancement (+) and degradation (-) for various dielectric, polarization, and piezoelectric responses at each gamma radiation dose. "0%" indicates measurable enhancement/degradation, albeit negligible with respect to the error. Uncertainties expressed represent one standard deviation to one significant figure. Measurement values are reported to the same decimal place as the uncertainties.[172]

	Mrad(Si)	0	0.2	0.5	1.0	2.0	5.0	10.0	20.0
ε_r	SLA	6.8 ± 0.7	10.0 ± 0.6	10.2 ± 0.7	8.7 ± 0.3	6.8 ± 0.2	2 ± 1	-1.5 ± 0.8	-5.8 ± 0.7
	MLA	6 ± 4	11 ± 2	10 ± 2	8 ± 1	11 ± 2	7 ± 2	2 ± 1	-6 ± 3
ε_{init}	SLA	0 ± 1	1.0 ± 0.8	3 ± 3	0.8 ± 0.4	-0.2 ± 0.4	-1.8 ± 0.7	-2.3 ± 0.5	-3.9 ± 0.6
	MLA	3 ± 2	4.0 ± 0.7	3.7 ± 0.6	2.2 ± 0.5	1.9 ± 0.7	0 ± 1	-1.1 ± 0.4	-2.1 ± 0.3
α (cm/kV)	SLA	19 ± 3	-6 ± 1	-8 ± 2	-5 ± 2	-10 ± 2	-12 ± 1	-15 ± 1	-17 ± 2
	MLA	-2 ± 6	3 ± 4	0 ± 3	-2 ± 3	-3 ± 3	-1 ± 4	-5 ± 1	-4 ± 3
P_{sat} (μC/cm^2)	SLA	-2.2 ± 0.2	-1.5 ± 0.3	-1.1 ± 0.2	0.3 ± 0.2	-0.1 ± 0.2	-1.0 ± 0.2	-1.8 ± 0.3	-2.7 ± 0.4
	MLA	-3.3 ± 0.3	-2.3 ± 0.3	-0.7 ± 0.4	-0.3 ± 0.4	0.6 ± 0.5	-0.6 ± 0.9	-2.3 ± 0.3	-3.7 ± 0.6
P_{rem} (μC/cm^2)	SLA	-3.0 ± 0.9	-1.3 ± 0.3	0.6 ± 0.8	5.7 ± 0.5	5.5 ± 0.7	3 ± 1	-1 ± 1	-7 ± 2
	MLA	-8 ± 2	-5.3 ± 0.6	0.2 ± 0.4	1.2 ± 0.5	3 ± 1	1 ± 1	-2.8 ± 0.8	-8.5 ± 0.6
$d_{33,f,sat}$ (pm/V)	SLA	-4 ± 4	-6 ± 2	1 ± 3	-8 ± 5	2 ± 7	-1 ± 8	-1 ± 6	-12 ± 6
	MLA	-4 ± 2	-1.3 ± 0.5	-8 ± 6	-4 ± 4	-5 ± 4	-1 ± 4	-8 ± 7	-11 ± 7
$d_{33,f,rem}$ (pm/V)	SLA	3 ± 6	-12 ± 5	7 ± 3	-15 ± 6	9 ± 7	-8 ± 7	-2 ± 5	-17 ± 6
	MLA	-1 ± 1	0 ± 2	-14 ± 6	-5 ± 4	-5 ± 3	-10 ± 5	-14 ± 8	-20 ± 8

8.4 Results and Discussion

The distinct differences in crystallization interfaces and chemical composition across the film thickness are consistent with the presence of satellite peaks in the XRD analysis of the SLA films (Figure 8-1a, insets). Comparison of the Schuller periodicities, $\Lambda_{Schuller}$,[266] calculated using the diffraction data, and measured crystallized layer thickness, Λ_{meas}, for the SLA films shows excellent agreement: $\Lambda_{Schuller} = 30.2$ nm and $\Lambda_{meas} = 30.7$ nm, with minimal error (1.3%). Λ_{meas}, was calculated with $\Lambda_{meas} = d/n$, where d is the film thickness and n is the number of deposited layers (subtracting the seed layer's thickness from the total measured thickness). On the other hand, no satellite peaks are seen in the XRD patterns for the more chemically-homogeneous MLA films.[286] Both SLA and MLA sets of films are highly 100-textured (97% and 90% Lotgering factor, respectively).[45]

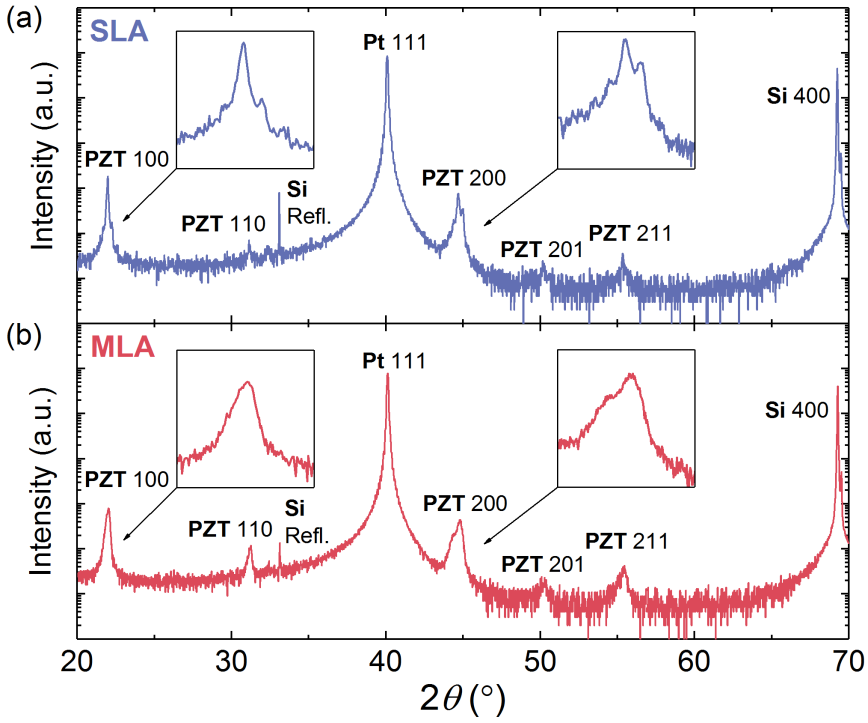

Figure 8-1 X-ray diffraction data for (a) single-layer anneal (SLA) and (b) multi-layer anneal (MLA) PZT thin films. Insets show PZT 100- and 200-peaks, with distinct satellite peaks shown for SLA samples, indicating a large degree of strain coherency between alternating Zr- and Ti-rich regions

Cross-sectional SEM shows smooth, dense structure, with continuous columnar grains (Figure 8-2). Minor porosity is observed locally in SLA films, seemingly at layer crystallization interfaces. AFM on the sample surface shows slightly smaller mean grain size for SLA samples (103 ± 5 nm) compared to MLA samples (118 ± 6 nm), calculated by the average grain intercept method.

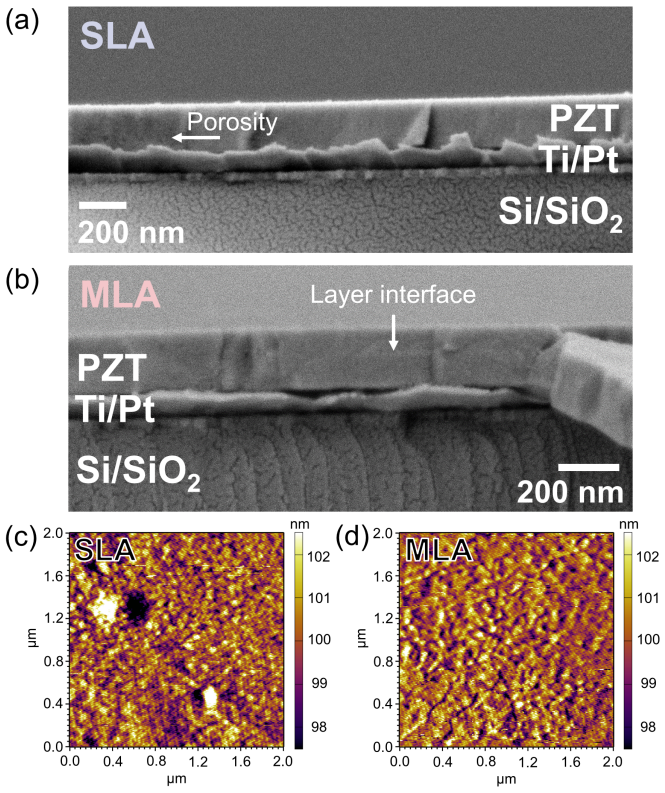

Figure 8-2 Scanning electron microscope (SEM) imaging of the (a) single-layer anneal (SLA) and (b) multi-layer anneal (MLA) PZT thin films. Both films show smooth, dense microstructure with continuous columnar grains through the thickness of the film. Notable are small pockets of potential porosity in the SLA films at layer crystallization interfaces and the observable crystallization interface in the MLA film. Atomic force microscopy (AFM) was performed on the surface of (c) SLA and (d) MLA films, indicating marginally smaller mean grain size for pR/T samples.

Functional response measurements as a function of total ionization dose (TID) for both SLA and MLA films show highly-nonlinear trends, with property enhancements observed at lower radiation doses and degradation at higher (Table 8-1). Figure 8-3a and Figure 8-3b show variations in dielectric responses ε_r and α as a function of TID. Enhancements to ε_r of over 10% are observed for both SLA and MLA samples, with stronger overall enhancement trends in the MLA films across the TID range. Trends in ε_{init} are similar to those for ε_r, *i.e.*, small enhancements (3-4 %) at low doses, and degradation at larger doses. SLA samples show increased degradation of α at both low and high doses,

in excess of 15%, compared to only 5% reduction observed in MLA samples. These trends suggest that the impact of radiation on extrinsic contributions, such as the irreversible motion of domain walls, is more pronounced in the SLA samples. Interestingly, large enhancement of α is noted for the SLA control sample, potentially due to the effects of aging.[62] Nevertheless, the large degradation of α in the SLA films across the entire dose range suggests that these samples are substantially more prone to radiation-induced degradation of domain wall motion than MLA samples. However, reversible domain wall motion (vibration) and lattice effects are comparable in both sets of samples. This result is consistent with prior work showing that gamma radiation-induced damage to the PZT crystal lattice is extremely limited, even at doses up to 10 Mrad.[32] Hence, the effects of layer crystallization and chemical heterogeneity in the films are more strongly associated with radiation-induced degradation of extrinsic contributions to the dielectric response, consistent with previous work.[32]

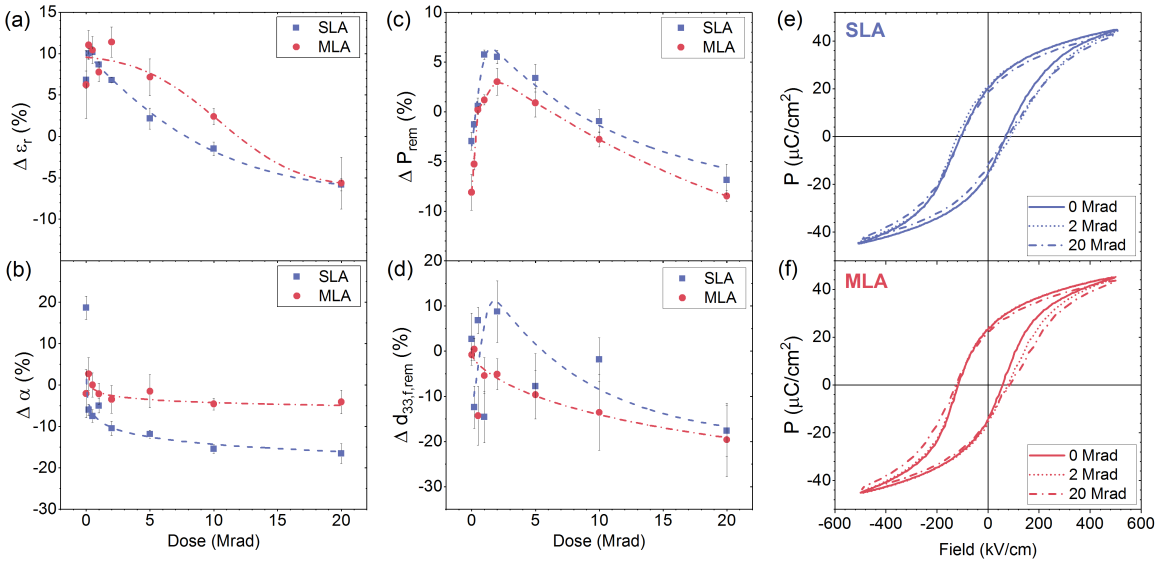

Figure 8-3 Plots of (a) dielectric permittivity (ε_r), (b) extrinsic contributions to AC electric field dielectric response (α), (c) remanent polarization (P_{rem}) and (d) remanent effective, converse piezoelectric response ($d_{33,f,rem}$) for SLA and MLA films as a

function of radiation dose. Lines have been added to guide the eye and demonstrate the relative magnitudes of enhancement/degradation for each measurement trend. Dielectric response is generally less degraded in MLA samples. Note the substantially greater enhancement of polarization and piezoelectric responses for SLA films, especially at lower radiation doses. (e) and (f) show representative *P-E* hysteresis loops at 0 and 2 Mrad radiation dose, where the enhancement in measured ferroelectric properties is largest.

Radiation-induced charges trapped at $V_O^{\cdot\cdot}$ sites have been shown to create more mobile $V_O^{\cdot}$ species in PZT samples exposed to ionizing radiation.[24,75,155,177] At low radiation doses, the concentration of mobile $V_O^{\cdot}$ may result in reduced pinning of domain wall motion and minor enhancements of domain wall vibration;[32] at higher radiation doses, increased density of trapped charges in the material leads to augmented populations of mobile $V_O^{\cdot}$. Larger populations of mobile defects can accumulate, self-order at interfaces, pin domain wall motion, increase internal bias, and create ferroelectric dead layers, similar to mechanisms driving ferroelectric fatigue.[32,60,61,70,72,75,97,100,101,242] In SLA samples, this effect is exacerbated due to an increased number of (crystallization) interfaces, and greater reductions to α are observed relative to MLA films.

The number of crystallization interfaces in the films also contributes to structural and compositional variations that potentially give rise to competing defect interactions in the samples. The thinner crystallized layers in the SLA films likely reduce grain sizes (and thus increase grain boundary density) relative to the MLA samples (Figure 8-2).[247] Greater grain boundary density has been shown to increase the degree of radiation interaction in a sample, due to interactions with defects at those locations.[101,218] Increased interaction of radiation with the SLA film (at grain boundaries *and* crystallization interfaces) potentially leads to accentuation of the TID trends compared to the MLA samples, *i.e.*, increased degradation of domain wall motion. Additionally, the large compositional gradients in the

SLA films may result in local radiation dose enhancements at denser Ti-rich regions of each individual layer, exacerbating charging effects in proximity to each crystallization interface.[32]

In contrast to the measured degradation of domain wall mobility, functional response enhancements are notably observed in the low-field dielectric response and remanent piezoelectric response, at intermediate-low TID. Trends in remanent polarization (P_{rem}), and remanent and saturation piezoelectric response ($d_{33,f,rem}$, and $d_{33,f,sat}$, respectively) generally show greater radiation-induced enhancement of response for SLA films compared to MLA films. Indeed, the maximum enhancements of P_{rem}, $d_{33,f,rem}$, and $d_{33,f,sat}$ (Table 8-1) are non-trivial for SLA samples – 6%, 3%, and 9%, respectively – while equivalent enhancements of the MLA films' response are markedly reduced (P_{rem}) or notably absent ($d_{33,f,rem}$, $d_{33,f,sat}$). Plots of P_{rem} and $d_{33,f,rem}$ show greater enhancements (at low TID) and reduced degradation (at high TID) of ferroelectric and piezoelectric responses for irradiated SLA samples compared to MLA samples (Figure 8-3a to Figure 8-3d). These differences between SLA and MLA functional responses may result from convolution of the internal bias and the polarization response. Piezoelectric response often scales with the degree of coherent dipole alignment and thus is closely correlated to the polarization in ferroelectric materials, especially in films of decreasing thickness below 1.5 μm.[35] Consequently, the effects of radiation-induced degradation on the piezoelectric response are expected to closely follow the trends observed for the polarization response (Figure 8-3d).

Trapping of radiation-generated electron-hole pairs at grain boundaries and crystallization interfaces in ferroelectric thin films can contribute to local charging of the

material, develop internal bias, and change resistivity behavior.[96,101,189,198,218,287] The SLA films studied here exhibit a smaller internal bias at 0 Mrad (-37 ± 6 kV/cm) compared to MLA samples (-55 ± 5 kV/cm), potentially due to the more uniform distribution of crystallization interfaces through the thickness of the SLA films (Figure 8-3e and Figure 8-3f). At 2 Mrad, internal bias in the SLA samples is marginally diminished (36 ± 1 kV/cm), while that of the MLA samples is reduced by ~16% (-46 ± 4 kV/cm), indicating a stronger radiation-induced shift towards greater symmetry in polarization switching of the MLA films. An even greater trend towards symmetric internal bias is observed in the MLA films at 20 Mrad in Figure 8-3f. This effective trend towards neutralization of pre-radiation negative internal bias suggests positive charge (hole) trapping, potentially at $V_O^{\cdot\cdot}$ sites as discussed earlier, and can result in measured enhancements of low-field dielectric, polarization, and piezoelectric responses at low TID (Figure 8-3).[4] Similar effects of local charge-related property enhancement have been noted in prior studies on irradiated ferroelectrics.[198,288] For example, Scott *et al.* have previously demonstrated increased symmetry of the coercive fields in *P-E* hysteresis loops of gamma-irradiated PZT thin films due to these trapped charges, effectively reducing inherent internal sample bias by exposure to irradiation.[96]

Finally, we consider response enhancements via ionic conductivity in PZT ceramics and the existence of stable $[V_{Pb}'' - V_O^{\cdot\cdot}]$ defect dipoles, potentially modified by charge trapping at V_{Pb}'' sites, leading to V_{Pb}' species of increased mobility.[289] At low radiation doses, radiation-induced electron-hole pairs may become trapped at existing $[V_{Pb}'' - V_O^{\cdot\cdot}]$ defect dipole sites, leading to simultaneous generation of singly-charged $[V_{Pb}'$-$V_O^{\cdot}]$ dipoles. The binding energy between singly-charged V_{Pb}' and $V_O^{\cdot}$ is significantly

reduced relative to their doubly-charged counterparts,[289] and increased mobility of the defect dipoles, or even complete dissociation thereof, may occur. However, greater populations of A-site vacancies in PZT are known to increase domain wall mobility; here, only marginal enhancement (3%) of α in the MLA samples at 0.2 Mrad dose is observed, suggesting that the potential effects of $[V''_{Pb} - V^{\cdot\cdot}_{O}]$ defect dipole charging/dissociation are limited or obscured by other factors.

8.5 Conclusions

In conclusion, we report on local functional response trends in gamma-irradiated ferroelectric PZT thin films with different layer crystallization schemes. At low radiation doses, notable enhancements of functional responses are observed in both SLA and MLA films, with overall degradation at high doses. Generally, SLA films show greater radiation-susceptibility of extrinsic dielectric contributions, but increased radiation tolerance of polarization and piezoelectric response. The effects of low-dose neutralization of internal bias are likely responsible for the radiation-dependent functional response enhancements: oxygen vacancy mobility accounts for degradation thereof. These results suggest promising avenues for tailoring materials' response via irradiation and processing approaches, based on functional requirements of specific applications.

8.6 Acknowledgments

A portion of this work was supported by the Defense Threat Reduction Agency, Basic Research Award No. HDTRA1-15-1-0035 to Georgia Institute of Technology. The contents do not necessarily reflect the position or the policy of the federal government, and no official endorsement should be inferred. S.J.B, S.C.W., and N.B.G. also acknowledge funding from the U.S. National Science Foundation (NSF) under grant numbers DMR-1255379 and CMMI-1537262. C.D.C. acknowledges funding from the Office of Naval Research and the Defense Threat Reduction Agency. The authors gratefully acknowledge Ronald G. Polcawich and Joel Martin of the U.S. Army Research Laboratory for providing the platinized Si substrates for this work.

CHAPTER 9. INTERNAL DOPANT DEFECT INTERACTIONS

The content in this chapter has been published in *Applied Physics Letters*.[290]

Enhanced Radiation Tolerance in Mn-doped Ferroelectric Thin Films

Steven J. Brewer, Samuel C. Williams, Lee A. Griffin, Cory D. Cress, Manuel Rivas, Ryan Q. Rudy, Ronald G. Polcawich, Evan R. Glaser, Elizabeth A. Paisley, Jon F. Ihlefeld, Jacob L. Jones, Nazanin Bassiri-Gharb

Applied Physics Letters, vol. 111, no. 2, (2017), doi: 10.1063/1.4992791

9.1 Summary

This work investigates the role of Mn-doping of ferroelectric lead zirconate titanate (PZT) thin films exposed to a range of ionizing radiation doses. PZT thin films were fabricated with both undoped and 4% Mn-doped compositions, and the functional response was compared both before and after exposure to gamma radiation doses up to 10 Mrad. A phenomenological model was applied to quantify defect interactions and compare trends in the degradation of functional response. Mn-doped PZT samples demonstrate reduced magnitude of functional response in non-irradiated samples, but exhibit vastly superior radiation tolerance of dielectric and ferroelectric properties across the range of gamma doses studied here. Strong $Mn''_{Zr/Ti} - V_O^{\cdot\cdot}$ defect dipoles pin domain walls, resulting in lower initial functional response, and mitigating the deleterious effects of irradiation on extrinsic contributions to said response. Piezoelectric response trends as a function of radiation dose are highly nonlinear. The results of this work can be leveraged to engineer next-generation radiation-tolerant ferroelectric materials for applications where high levels of functional response stability are required, especially at elevated ionizing radiation dose.

9.2 Introduction

The large dielectric, pyroelectric, and piezoelectric responses exhibited by ferroelectric thin films make them ideal candidates for use in many microelectronics applications, such as multi-layer ceramic capacitors (MLCC), ferroelectric logics and memories, and microelectromechanical systems (MEMS) sensors and actuators.[1,291] The rapid evolution of such devices has necessitated functional materials capable of operating in increasingly demanding environments, such as use in facilities processing radioisotopes or space-related applications. Prior studies on the effects of radiation on ferroelectric thin films has, in many cases, shown substantial radiation-induced degradation of functional response, thus altering critical device functionality.[40,97,100,287] The radiation-induced effects caused by newly-created vacancies (for proton, neutron studies) are secondary to those induced by ionizing energy transferred to the material from these particles and by X-rays and gamma-rays, suggesting that the primary radiation-induced effects stem from activation or charging of existing defect sites rather than new vacancy-interstitial pair formation.[32,40,97,100] These observations are consistent with the fact that PZT contains a large fraction of lead and oxygen vacancies, especially in undoped materials.[289] Work to mitigate the effects of radiation-induced degradation on ferroelectric materials has primarily focused on retention properties of ferroelectric memories, often through modifications to the material stack.[32,292,293] Other approaches have sought to maximize functional response in order to retain critical device functionality even after substantial radiation-induced degradation.[294] While these approaches have contributed to radiation-tolerant ferroelectric films/stacks, more robust approaches to inherently radiation-tolerant ferroelectric materials with greater operational stability are relatively nonexistent.

In this work, we investigate the effects of gamma radiation on the functional response of PZT thin films with and without Mn-doping. Dopants have long been employed for increasing radiation-hardness in semiconductors and functional materials, for applications ranging from photovoltaic (PV) cells to Si-based sensors, to detectors for the Large Hadron Collider (LHC).[295-297] It is well-known that acceptor doping of PZT, *e.g.*, with Mn ions, increases the oxygen vacancy concentration with respect to undoped PZT, creating $Mn''_{Zr/Ti} - V_O^{\cdot\cdot}$ defect dipoles that stabilize domain wall motion and result in a "hard" PZT composition.[298-302] Mn-doped PZT thin films have demonstrated increased polarization retention properties as a result of reduced oxygen vacancy mobility, which is strongly associated with ferroelectric fatigue.[4,32,72,300-302] Oxygen vacancy mobility and eventual accumulation at ferroelectric-electrode interfaces has also been shown to result in radiation-induced degradation of dielectric and piezoelectric response in ferroelectric thin films and MEMS devices.[32,100] Here, we probe the effects of Mn-doping on gamma-irradiated ferroelectric thin films, correlating changes in defect interactions (both inherent and radiation-induced) to radiation tolerance and eventual device performance. Such studies elucidate the fundamental interactions of radiation with ferroelectric materials and defect concentrations therein.

9.3 Experimental Procedures

$PbZr_{0.52}Ti_{0.48}O_3$ (PZT) thin films were fabricated via chemical solution deposition (CSD) with 0.4 M precursor solutions, prepared via a 2-methoxyethanol (2-MOE) route,[109,120,235] described by Sanchez *et al.*[131] Manganese (II) acetate tetrahydrate purum,

p.a., ≥ 99.0% (KT) (Sigma Aldrich) was substituted for 4 wt.% of the B-site cations (2 wt.% each Zr, Ti) in the Mn-doped precursor solutions before initial preparation. Previous literature reports suggest that 1% Mn concentration results into dominant B-site substitutions, consistent with reductions in extrinsic contributions (*e.g.,* domain wall motion) to the dielectric response.[298,303] Films were spin-coated onto 150 mm-diameter, 100-silicon wafers consisting of 100 nm Pt, 35 nm TiO_2, 2000 nm SiO_2, Si, and resulting in PZT films with thicknesses of 523 ± 5 nm.[120,131,132] A ~17-nm thick $PbTiO_3$ seed layer was deposited before all PZT layers to induce 100-texture.[131] Films were pyrolyzed at 365 ºC for 60 s for each spin-coated layer and crystallized at 700 ºC for 60 s every 2 layers in flowing O_2 at 7 sccm.[131] 100 nm-thick IrO_2 electrodes were sputter-deposited at 500 ºC and processed with a post-deposition anneal at 650 ºC in flowing O_2 for 30 min, as outlined elsewhere.[100] Baseline X-ray diffraction (XRD) was performed using a PANalytical Alpha-1. Scanning electron microscopy (SEM) (Zeiss Ultra60 FE-SEM) and atomic force microscopy (AFM) (Asylum Research MFP-3D) were used to image film microstructure.

The films were exposed to a range of gamma radiation doses from 0.2 to 10 Mrad (Si) at a rate of ~600 rad(Si)/s from a ^{60}Co source in an isotropic exposure, during which electrodes were left floating. Functional responses of the samples were characterized before and after irradiation (on the same electrodes/sample), including (in order) measurements of low-field dielectric permittivity (ε_r) (100 mV, 1 kHz, Agilent 4284A LCR meter); polarization-electric field (*P*-*E*) hysteresis loops (400 kV/cm, 100 Hz sine wave, Radiant P-PM2), nonlinear dielectric permittivity response (ε_r-E_{AC}) (40 kV/cm AC, 1 kHz); DC electric field-dependent permittivity response (ε_r-E_{DC}) (200 kV/cm with overlapping AC signal $V_{AC} \approx 0.5V_c$); and electric field-dependent converse, effective longitudinal

piezoelectric response ($d_{33,f}$) (200 kV/cm DC with an overlapping AC signal of 1 V, aixACCT double beam laser interferometer (DBLI)). Table 9-1shows percent changes in functional response at each radiation dose. All measurements were performed on a minimum of five electrodes and are subject to 3-5% experimental error due to sample variability and measurement error. The Rayleigh approach was used to analyze the nonlinear dielectric response and quantify changes in intrinsic (ε_{init}) and extrinsic (α) dielectric response, *i.e.,* contributions from the lattice and domain walls' vibration, and irreversible domain wall motion, respectively.[24,29,33,236]

Table 9-1 Percent degradation at each gamma dose of measured functional responses, including dielectric, polarization, and piezoelectric data. Degradation is positive and enhancement negative, for continuity with plots in Figure 9-4, and for fitting with the phenomenological model. Values of "0%" are within the uncertainty. Uncertainties expressed represent one standard deviation to one significant figure. Measurement values are reported to the same decimal place as the given uncertainty.[172] Fitting parameters φ_N and k are shown for all measurements, with the exception of the piezoelectric response, due to the strongly non-monotonic nature of those trends (see Figure 9-4d).

	Mrad(Si)	0	0.2	0.5	1.0	2.0	5.0	10.0	$\varphi_N \times 10^3$	k
ε_r	Undoped	-0.1 ± 0.3	-0.1 ± 0.1	0.1 ± 0.2	1.6 ± 0.1	3.0 ± 0.1	6.6 ± 0.3	9.3 ± 0.1	13	0.22
	4% Mn	3.0 ± 0.2	3.4 ± 0.5	3.1 ± 0.1	2.9 ± 0.2	3.3 ± 0.1	2.8 ± 0.1	3.5 ± 0.1	0	0.99
ε_{init}	Undoped	12 ± 2	4.9 ± 0.9	4.2 ± 0.6	4.0 ± 0.4	3.4 ± 0.4	3.50 ± 0.4	-5.5 ± 0.5	-1	1.33
	4% Mn	0.4 ± 0.4	0.7 ± 0.4	0.9 ± 0.1	0.3 ± 0.6	1.0 ± 0.1	0.7 ± 0.4	1.3 ± 0.6	1	0.84
α (cm/kV)	Undoped	2 ± 9	2 ± 2	8.3 ± 0.6	11 ± 2	16 ± 2	31.5 ± 0.6	31 ± 3	7	0.48
	4% Mn	1 ± 2	2 ± 2	1.7 ± 0.5	4 ± 2	2.7 ± 0.7	1.5 ± 0.7	3 ± 4	3	0.88
$P_{saturation}$ ($\mu C/cm^2$)	Undoped	1.2 ± 0.6	1.5 ± 0.1	1.3 ± 0.1	1.6 ± 0.3	1.8 ± 0.1	1.8 ± 0.2	2.5 ± 0.1	2	0.89
	4% Mn	-0.7 ± 0.6	-1.2 ± 0.3	-1.1 ± 0.5	-1.2 ± 0.7	-1.1 ± 0.3	0.2 ± 0.1	-1.0 ± 0.2	0	0.97
$P_{remanent}$ ($\mu C/cm^2$)	Undoped	7 ± 3	10 ± 2	6.2 ± 0.9	12 ± 2	11 ± 1	15.7 ± 0.8	22.6 ± 0.7	3	0.74
	4% Mn	10 ± 2	9 ± 1	9 ± 1	9 ± 2	9.8 ± 0.7	5.8 ± 0.3	11 ± 2	1	0.99
Dielectric Tunability	Undoped	0.7 ± 0.4	0.6 ± 0.4	1.3 ± 0.1	1.5 ± 0.1	1.5 ± 0.3	2.7 ± 0.2	2.7 ± 0.3	4	0.70
	4% Mn	-0.2 ± 0.4	0.0 ± 0.3	0.2 ± 0.1	0.2 ± 0.2	0.2 ± 0.2	0.0 ± 0.1	0.2 ± 0.1	0	0.74
$d_{33,f,saturation}$ (pm/V)	Undoped	0 ± 10	3 ± 5	7 ± 9	14 ± 5	7 ± 8	9 ± 1	-11 ± 9	--	--
	4% Mn	11 ± 5	15 ± 6	7 ± 5	10 ± 8	-11 ± 9	-3 ± 6	7 ± 8	--	--
$d_{33,f,remanent}$ (pm/V)	Undoped	10 ± 20	30 ± 20	30 ± 10	30 ± 20	20 ± 20	20 ± 30	10 ± 20	--	--
	4% Mn	0 ± 20	0 ± 30	10 ± 30	0 ± 20	0 ± 30	20 ± 20	20 ± 20	--	--

9.4 Results and Discussion

XRD analysis reveals that both undoped and Mn-doped PZT samples are highly 100-textured (Figure 9-1), with Lotgering factors of 89 and 90%, respectively (PDF 01-070-4060).[143] Some peak splitting of the 001- and 002-peaks is observed in the Mn-doped samples (Figure 9-1) – B-site substitution of Mn in the PZT lattice has been shown to increase tetragonality of the unit cell and lead to small splitting of the 100- and 200-peaks

in highly-textured PZT thin films.[298,303] Microstructural comparisons via cross-sectional SEM show columnar grains in both samples, but greater apparent porosity and potential grain size reduction are observed in the Mn-doped samples (Figure 9-2c and Figure 9-2d). Work by Ng and Alexander (and later corroborated by Xin *et al.*)[298] suggested that such grain size and porosity effects are attributable to segregation of Mn dopant at grain boundaries.[303] AFM images (Figure 9-2c and Figure 9-2d) of the sample surface confirm the reduced grain size in Mn-doped PZT samples relative to undoped samples.

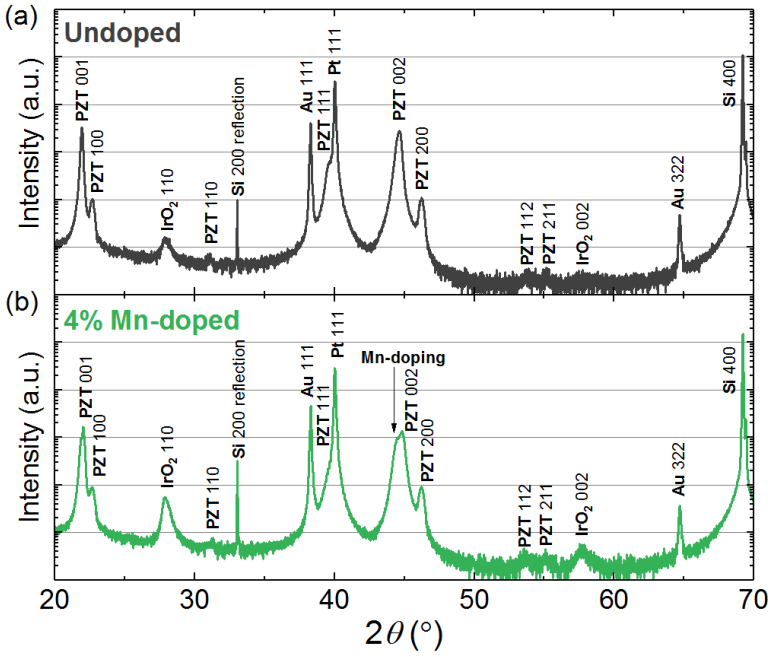

Figure 9-1 X-ray diffraction data for (a) undoped and (b) 4% Mn-doped PZT thin films used in this work. The results indicate strong 100-texture in both sets of samples. Notable is a small shoulder on the PZT 002-peak exhibited in the Mn-doped samples (also notable to a lesser degree on PZT 001-peak).

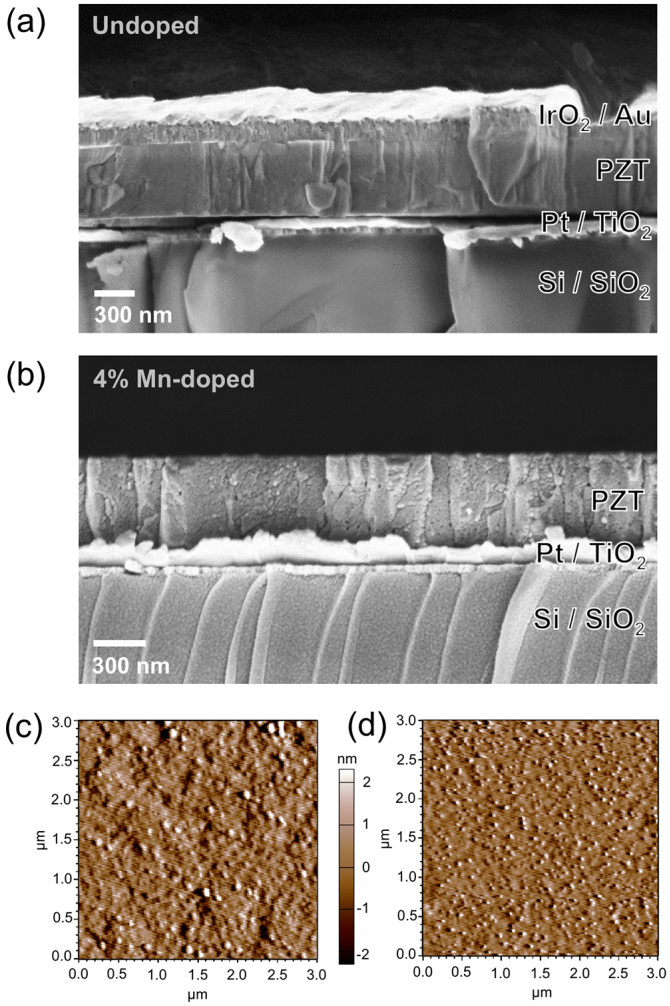

Figure 9-2 Cross-sectional scanning electron microscope (SEM) images of the (a) undoped and (b) 4% Mn-doped PZT samples. Large differences are noted in density and porosity. Both samples show highly columnar microstructure, but the Mn-doped samples exhibit greater porosity and some apparent grain size reduction. (c) and (d) show the deflection trace of atomic force microscopy (AFM) scans of the surface of the undoped and Mn-doped samples, respectively.

Measurements of the functional responses as a function of total ionization dose (TID) show distinct differences for the two sets of samples, especially prevalent in dielectric (Figure 9-3b and Figure 9-3c) and piezoelectric (Figure 9-3d) responses. Notably, Mn-doped samples show markedly reduced initial dielectric and piezoelectric response

compared to the undoped samples (Table 9-1). However, the Mn-doped samples demonstrate superior tolerance to radiation even up to 10 Mrad, as evidenced by minimal variation in the ferroelectric, dielectric, and piezoelectric responses over the studied TID range. In order to more comprehensively quantify trends in radiation-induced degradation of functional response and defect interactions, we apply a phenomenological model developed in prior work to analyze trends as a function of TID.[189]

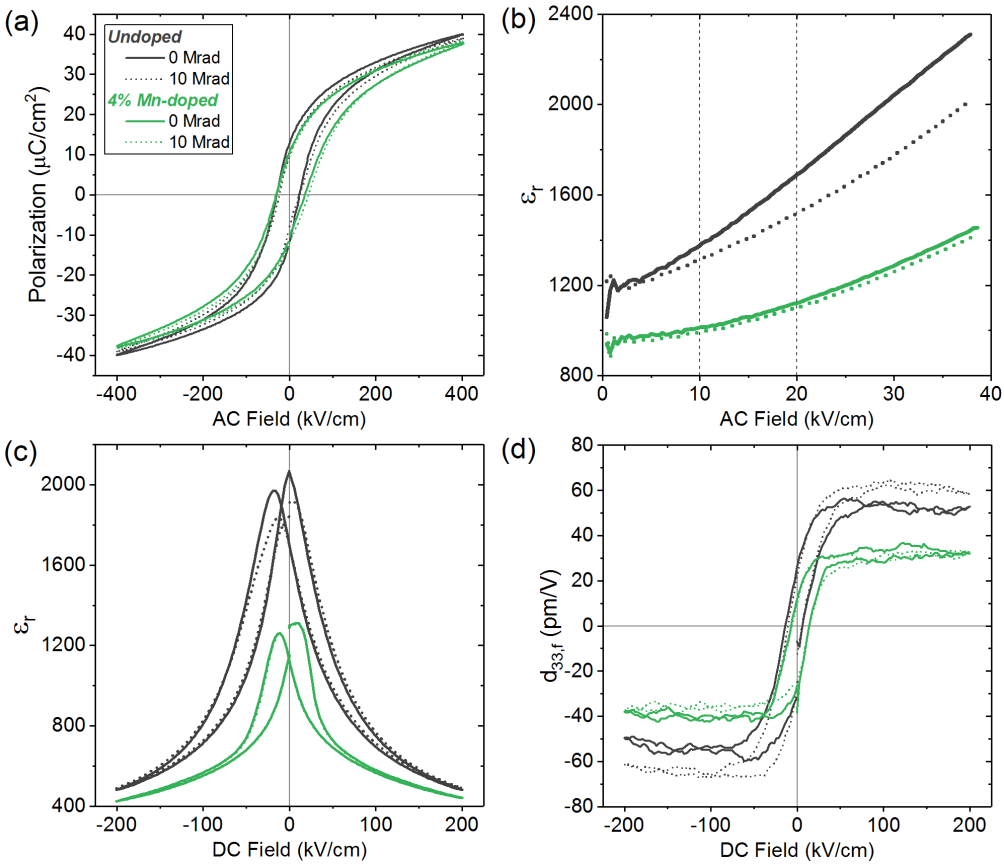

Figure 9-3 Representative (a) polarization, (b) AC dielectric, (c) DC dielectric, and (d) piezoelectric functional response loops for the undoped and 4% Mn-doped PZT thin films studied at 0 and 10 Mrad radiation exposure. Notably, the magnitude of dielectric and piezoelectric functional response is reduced in Mn-doped samples, but those samples demonstrate substantially greater radiation tolerance. Polarization properties are relatively similar, but larger rotation and pinching of the loop is noted for irradiated undoped samples. Limits for extraction of Rayleigh parameters are shown as vertical dotted lines in (b). Piezoelectric data has been smoothed using an

adjacent-averaging filter to reduce noise for this figure (piezoelectric response parameters were extracted from the raw data).

The employed model relies on the assumption that exposure of ferroelectric materials to radiation proportionally creates/activates defects in the material.[32,40,97,101] These new defects interact with a given volume of ferroelectric material, and, potentially with existing defects therein – *e.g.*, domain walls, grain boundaries, point defects, defect dipoles, *etc.* – thus modifying the defect-energy landscape of the material, and pinning/unpinning domain walls within the affected ferroelectric volume.[189] The normalized volume of pinned ferroelectric material, V_d, is correlated to the number of radiation-induced defects, N, (assumed proportional to radiation dose) by the expression

$$V_d = 1 - e^{-\varphi_N\left(\frac{N^{1-k}}{1-k}\right)} \qquad 9\text{-}1$$

where φ_N is the normalized effective change in material volume pinned per new defect introduced, and k is the effective rate of defect saturation. Generally, φ_N can be interpreted as the global susceptibility of the material to radiation-induced change, while k is a function of microstructural features that modify the rate of response degradation, such as the anisotropic interactions of defects. The model presented allows for quantification of defect interactions from a *phenomenological* perspective, *i.e.*, it provides a quantifiable relationship between radiation dose; the resulting radiation-induced defect interactions from a macroscopic, volume-averaged perspective; and the subsequent modifications to functional response behavior. Full derivation and detailed discussion of the phenomenological model are available elsewhere,[189] though we note here that Expression 9-1 is a modified sigmoid function which are often used to describe nucleation, growth,

and saturation behavior, such as the Johnson-Mehl-Avrami-Kolmogorov equation for phase transitions in solids, and justifiably relatable to radiation-induced defects, growth of a defect-saturated region, and the subsequent pinning of ferroelectric material volume.[213] Results of fitting the model to the functional characterization data as a function of TID are given in Table 9-1. Plots of degradation trends and the fitted model are shown in Figure 9-4.

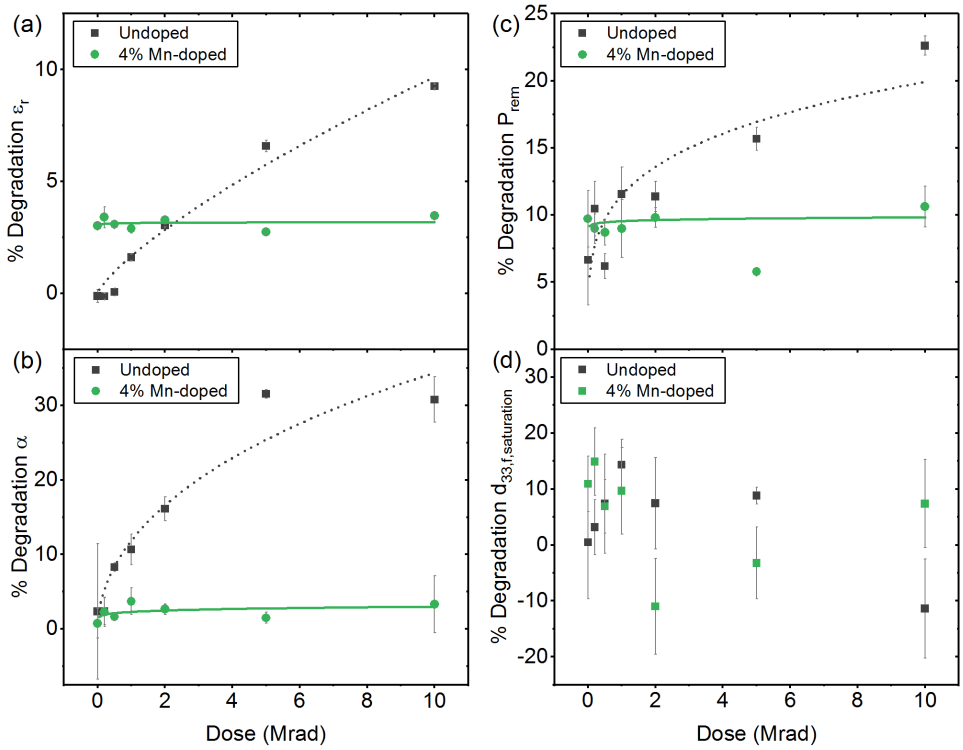

Figure 9-4 (a) Dielectric permittivity (ε_r) at low AC electric field, (b) extrinsic contributions to the AC electric field dielectric response (α), (c) remanent polarization (P_{rem}), and (d) saturated converse, effective piezoelectric response ($d_{33,f,saturation}$) as a function of radiation dose for the undoped and 4% Mn-doped PZT samples. A phenomenological model employing a modified sigmoid function has been fit to each set of data to quantify defect interactions and compare degradation-related

parameters, except for the $d_{33,f,sat}$ data – only the raw data is presented due to the strong non-monotonicity thereof.

By comparing the fitting parameters from Table 9-1, we observe that for all measurements, with the exception of ε_{init} (potentially due to sample/measurement error), Mn-doped samples demonstrate smaller values of φ_N and simultaneously larger values of k. Smaller φ_N values indicate that newly-created/activated defects have a limited impact on pinning of ferroelectric volume in Mn-doped samples. It is expected that the high levels of Mn-doping in PZT are compensated by oxygen vacancies, but subsequently form stable defect dipoles with the substituted Mn ions. The formation of such defect dipoles results in an effective reduction of *mobile* oxygen vacancy concentration.[298,301,304] In previous studies on undoped PZT, trapped charges generated by irradiation have been shown to modify the ionic state of mobile oxygen vacancies into singly-charged $V_O^{\cdot}$, leading to pinning of domain wall motion, accumulation and self-ordering of oxygen vacancies at internal interfaces, and radiation-induced fatigue-like effects on ferroelectric properties.[32,40] In the Mn-doped samples, the reduction of mobile oxygen vacancy population through the formation of stable defect dipoles with Mn ions mitigates, to some degree, the deleterious effects of radiation-modified mobile oxygen vacancies, leading to enhanced ferroelectric retention properties, even at elevated TID. On the other hand, the strong pinning of domain walls by $Mn''_{Zr/Ti} - V_O^{\cdot\cdot}$ defect dipoles is readily apparent in the heavily-reduced initial values of dielectric and piezoelectric responses for Mn-doped samples with respect to the undoped PZT films (Figure 9-3).

The greater values of k observed for functional response measurements of Mn-doped films suggest that these samples exhibit increased rates of defect saturation with

TID. Increased $Mn''_{Zr/Ti} - V_O^{\cdot\cdot}$ defect dipoles formed by substituted Mn ions and potential Mn-dopant segregation at grain boundaries leads to higher defect concentrations in Mn-doped films, thereby resulting in elevated concentrations of pinning centers, even prior to irradiation[301] – subsequent exposure does not substantially contribute to increased pinning of ferroelectric material volume, and mild degradation trends are generally observed as a function of TID (Table 9-1, Figure 9-4a, Figure 9-4b, Figure 9-4c). Lastly, we note that increased porosity and apparent grain size reduction in Mn-doped samples with respect to undoped samples can also result in increased radiation tolerance of the former. Greater grain boundary density and porosity are associated with an effective lack of functional material volume at these sites, causing them to serve as defect sinks and mitigate pinning caused by radiation-induced defects, yielding improved radiation-hardness.[220,221,238-241,305] We note that structural effects of gamma radiation on the PZT lattice are not likely, as evidenced by previous work demonstrating a lack of radiation-induced strain in PZT irradiated to 10 Mrad.[32]

We note that the degradation trends for the piezoelectric response could not be fit with the phenomenological model, due to the lack of monotonic trends as a function of TID (Figure 9-4d). However, radiation tolerance of Mn-doped samples does not appear to exceed that of undoped samples for $d_{33,f,saturation}$, and is only marginally better for $d_{33,f,remanent}$ (when comparing maximum degradation across the TID range, Table 9-1). The piezoelectric response is often determined by large contributions both from domain wall motion and the degree of coherent dipole alignment in the samples.[35] The observed trends in $d_{33,f}$ suggest that these two contributors are affected differently by irradiation, and the competing effects of defects on such contributions result in nonlinear, non-monotonic

degradation behavior of the piezoelectric response. Previous literature reports have shown that charging of ferroelastic domain walls can result in large changes to the electromechanical response.[306] Ionizing radiation has been shown substantially modify local charge states in ferroelectric materials by introducing electron-hole pairs and trapped charges, resulting in changes to domain walls and altering the electromechanical response.[32,101] The appearance of domain variants can be further activated by ferroelectric fatigue and defect agglomerates in ceramic PZT:[307] such domains are concentrated at regions near the electrodes, and form to accommodate mechanical stresses resulting from fatigue and/or defect accumulation. It is possible that formation of these domains results from defect concentrations in the material, both inherent (Mn-induced defect dipoles) and radiation-induced. Charging of domain walls would therefore result in complex defect-defect interactions in the material, thereby nonlinearly modifying the piezoelectric response at varying levels of TID.

9.5 Conclusions

In summary, we have investigated the role of Mn acceptor-doping of PZT thin films on radiation tolerance when exposed to varying levels of ionizing gamma radiation. Mn-doped samples show reduced magnitude of dielectric, ferroelectric, and piezoelectric responses at all levels of TID, but generally demonstrate a far greater resistance to radiation-induced degradation of the same properties when compared to undoped samples. It is expected that stable $Mn''_{Zr/Ti} - V_O^{\cdot\cdot}$ defect dipoles created by doping result in more substantial pinning of domain walls relative to undoped PZT and reduce dynamic, oxygen-

related fatigue mechanisms. When exposed to gamma radiation, the reduced population of *mobile* oxygen vacancies in Mn-doped samples leads to greater stability of functional response across the studied dose range. Acceptor doping of PZT is suggested as an excellent approach for designing radiation-hard devices where enhanced stability of functional response, even at high radiation doses, is a primary design criteria.

9.6 Acknowledgments

This work was supported by the Defense Threat Reduction Agency, Basic Research Award No. HDTRA1-15-1-0035 to Georgia Institute of Technology. The contents do not necessarily reflect the position or the policy of the federal government, and no official endorsement should be inferred. The authors acknowledge Joel Martin and Brian Power of the Army Research Laboratory and Steven Isaacson of General Technical Services for their contributions to the fabrication of the PZT thin films.

CHAPTER 10. ELASTIC LAYER BOUNDARY AND EFFECTS OF RESIDUAL STRESS

10.1 Summary

This chapter investigates the effects of modifying the level of residual strain in the ferroelectric material on the radiation tolerance of the material stack. Strain variations in the ferroelectric thin film are accomplished by varying the elastic layer thickness and material selection. Three sets of films were fabricated for comparison – one each with 750 nm SiO_2, 2035 nm SiO_2, and 760 nm AlN elastic layer thickness. The fabricated PZT thin films exhibited strong PZT 001-texture, but TKD analysis of the samples prepared with AlN elastic layers shows a limited amount of random grain misorientation, while those with SiO_2 elastic layers appear to have highly uniform in-plane texture. Estimations of relative strain suggest that the films with SiO_2 elastic layers are subject to a substantially greater degree of (in-plane) biaxial, tensile strain than similarly-processed samples with AlN elastic layers. Trends of radiation-induced functional response degradation generally demonstrate reduced radiation tolerance of samples prepared on AlN elastic layers compared to to SiO_2 elastic layers. Grain misorientation potentially leads to greater discontinuity at grain boundaries in the samples with AlN elastic layers, exacerbating the grain boundary-radiation interaction. Greater in-plane tensile stress in the samples with SiO_2 elastic layers likely increases defect mobility, and potentially leads to defect accumulation at grain boundary defect sinks, augmenting radiation tolerance in those samples compared to those with AlN elastic layers. On the other hand, more stable defect populations in the AlN samples with reduced tensile stress leads to greater pinning of domain wall motion and elevated rates of defect saturation.

10.2 Introduction

The typical thin film ferroelectric material stack consists of six discrete layers (substrate, elastic layer, adhesion layer, bottom electrode, ferroelectric film, and top electrode), leading to a variety of complex interfacial interactions. Many are addressed throughout this thesis, with a focus on direct interactions with the ferroelectric layer, such as the top electrode-ferroelectric interface; as well as internal interactions, *i.e.*, grain morphology, dopant interactions, layer crystallization interfaces, *etc.* However, the lower portion of the material stack, including the substrate and elastic layer, plays a large role in determining functional properties of the stack, foremost through residual stress development and clamping of the ferroelectric material (CHAPTER 11). Stress and clamping can inhibit the functional response of the ferroelectric material by restricting domain wall motion and eventual rhombohedral/tetragonal (R/T) phase transitions.[228] The study of misfit strain between the substrate and lower material stack and the resulting effects on structural and functional properties has been the subject of extensive research.[228,308] These effects become increasingly more apparent with decreasing film thickness, due to the proximity of the domains to the clamped interface where residual stresses are higher, often depriving the film of precious functional response, specifically for films grown on Si substrates.[1,36,309] Furthermore, tensile stress in multiple functional material systems has resulted in increased defect mobility by reducing the defect-migration energy barrier.[310,311] Changes of the elastic layer are expected to change the stress state and this energy barrier, potentially affecting the mobility of defects (both inherent and/or radiation-induced) and their effects on the functional and structural properties of the ferroelectric material.

Additionally, variations in microstructure, roughness, and texture of the substrate/elastic layer can propagate through the material stack, eventually affecting the structural and functional properties of the ferroelectric. Prior work on substrate/elastic layer variation in CSD ferroelectric thin films has demonstrated distinct changes in microstructure, texture, and functional response of the films. Kim *et al.* showed substantial changes in the preferred crystallographic orientation of sol-gel CSD PZT thin films fabricated with glass substrates substituted for the traditional Si/SiO_2 lower material stack – the films on glass exhibited a much greater 111-orientation compared to the mixed 100- and 111-orientation of the PZT grown on Si/SiO_2 substrates.[312] A variety of similar studies on the effects of fabricating PZT thin films on substrates/buffer layers consisting of Ti, diamond, ZnO, Al_2O_3, GaAs, MgO, $(La_{0.7}Sr_{0.3})MnO_3$ (LSMO), *etc.*, have also shown strong dependence of ferroelectric response, fatigue properties, and crystallographic orientation on the substrate and elastic layer material used.[133,135,228,313,314 315 316]

In this work, two different thicknesses of thermal SiO_2 elastic layer, as well as a sputtered AlN elastic layer are used in order to study the resulting structural and functional effects on gamma-irradiated PZT thin films. Two different thicknesses of thermal SiO_2 elastic layer are studied, as well as a sputtered AlN elastic layer. Si/SiO_2 substrates have traditionally been employed for fabrication of ferroelectric thin films, due to their ubiquity in microelectronics processing, high resistivity, and the diffusion-barrier properties exhibited by SiO_2.[228] On the other hand, AlN is a highly resistive, wurtzite-structured, wide band gap semiconductor material, and is commonly used for applications in surface acoustic wave sensors (SAW), RF filters, and bulk acoustic resonator (BAR) MEMS devices due to its piezoelectric properties and CMOS compatibility.[1] Growth of thermal

SiO_2 on Si wafers is typically expected to result in up to several hundred MPa biaxial stress, but can be highly-dependent on ambient growth conditions and total thickness.[317] Sputtered AlN films similarly exhibit several hundred MPa up to GPa-range residual stress, depending on thickness and sputtering conditions.[318] While the stress states of as-grown/as-deposited SiO_2 and AlN films are well-studied, the repeated thermal cycling of subsequently-deposited electrodes and ferroelectric layers inevitably alters the global stress state of the material stack. The work in this chapter attempts to elucidate this critical interaction by applying general X-ray diffraction estimates of the residual stress in the PZT thin films. However, due to the difficulty of assessing strain in highly-textured crystalline solids and the unavailability of unstressed PZT thin films with which to compare, the estimates in this chapter are primarily relative and serve as basic comparisons of materials and thicknesses.

10.3 Experimental Methods

Substrates for film deposition were prepared by growing dry thermal SiO_2 on 100-Si substrates to final thicknesses of 760 nm and 2035 nm. A third set of samples was prepared on Si substrates sputtered with 750 nm AlN. The bottom electrode contact consisted of 35 nm sputtered TiO_2 and 100 nm sputtered Pt on all three substrate/elastic layer stacks.[132,235] $PbZr_{0.52}Ti_{0.48}O_3$ (PZT) thin films were synthesized via chemical solution deposition (CSD) on each of the three substrates with 2-methoxyethanol (2-MOE)-based precursor solutions.[111] A $PbTiO_3$ seed layer was deposited for the 2-MOE films to induce 001-texture.[131] The films were deposited with a target thickness of 500 nm using 0.4M

solutions and pyrolysis temperatures of 365 °C for 60 s for each spin layer, and a crystallization anneal at 700 °C for 60 s after every 2 layers in a rapid thermal anneal furnace. IrO_2 top electrodes, selected for continuity with prior work,[32] were sputter-deposited onto films at 500 °C and processed annealed at 650 °C after deposition in flowing O_2 for 30 min. The top electrode and PZT layer were patterned using argon ion milling to create interconnects (of Au) to the electrode structures. This process is outlined elsewhere.[100]

The fabricated samples were exposed to gamma radiation from a ^{60}Co source at discrete doses ranging from 0.2 to 10 Mrad (equivalent Si dose) and a dose rate of ~600 rad(Si)/s at the US Naval Research Laboratory (NRL). The geometry of the ^{60}Co gamma source surrounds the sample, exposing it isotropically and eliminating potential effects resulting from the directionality of incident gamma rays. Electrodes were left floating during exposure. Dielectric, ferroelectric, and piezoelectric responses of the samples were fully characterized both before and after irradiation, including (in order) measurements of the low AC electric field dielectric permittivity, polarization measurements, nonlinear AC electric field dielectric response, DC electric field dielectric permittivity response, and DC electric field piezoelectric response. All measurements were performed on the same electrode/sample pre- and post-irradiation in order to accurately track changes in the response as function of radiation dose. The results of these measurements are shown in Table 10-1, Table 10-2, and Table 10-3. A 600-second poling step at 10 V (approximately five times the coercive voltage, V_C) DC bias was performed at room temperature directly before the measurements of piezoelectric response for both pre- and post-irradiation sets of measurements in order to maximize dipole alignment in the out-of-plane measurement

direction. Low-field dielectric permittivity (ε_r) measurements were conducted at 100 mV and 1 kHz using an Agilent 4284A precision LCR meter. Polarization-electric field (*P-E*) hysteresis loops were performed up to fields of 250 kV/cm at 100 Hz, using a Radiant P-PM2 ferroelectric test system. Nonlinear AC dielectric permittivity (ε_r-E_{AC}) was measured up to approximately 150 kV/cm AC at 1 kHz. DC field-dependent dielectric permittivity (ε_r-E_{DC}) measurements were performed up to 250 kV/cm DC bias with an overlapping small-signal 100 mV AC bias at 1 kHz. Measurements of the converse, effective longitudinal piezoelectric response ($d_{33,f}$) were performed on an aixACCT double beam laser interferometer (DBLI) system up to 250 kV/cm DC bias with an overlapping AC signal $V_{AC} \approx 0.5V_C$. Reported measurements are subject to experimental error up to 3-5% due to sample variability and measurement error. The vertical shift in the *P-E* loops, *ΔP/2* (Table 2), the horizontal shift in the *P-E* and $d_{33,f}$ - E_{DC} hysteresis loops, and the dielectric tunability were calculated from according to formulas available in CHAPTER 3, Section 3.3. The nonlinear dielectric response at low and intermediate AC electric field was analyzed using the Rayleigh approach to quantify changes in intrinsic and extrinsic dielectric response and is discussed in CHAPTER 2.[24,29,236]

Baseline X-ray diffraction (XRD) analysis was performed on samples prior to irradiation using a PANalytical Alpha-1. Atomic force microscopy (AFM) was performed to image film surface microstructure using an Asylum Research MFP-3D in contact mode. Cross-sectional scanning electron microscopy (SEM) was employed to visually observe grain microstructure and porosity through the thickness of the films. Samples were sputter coated with 20 nm of Au before SEM imaging to increase sample conductivity. Cross

sectional imaging was performed using an FEI Verios field-emission scanning electron microscope in secondary lens mode.

Transmission Kikuchi diffraction (TKD) was performed on the samples to quantify microstructure and local grain orientations. Samples were prepared with focused ion beam (FIB) milling after depositing a 3 μm-thick Pt layer on the sample surface for protection from electron and ion damage (FEI Quanta 3D FEG). A 20 nm Au layer was subsequently sputtered on the FIB liftout to increase sample conductivity and mitigate sample drift. Cross-sectional TKD samples were prepared using both electron and ion beam guns (SEM/FIB) (FEI Quanta 3D FEG). TKD images were acquired using an Oxford Instruments NordlysNano electron backscatter diffraction (EBSD) detector; Kikuchi diffraction patterns were taken at 30 kV (Oxford Instruments Aztec software). TKD data was processed using the HKL CHANNEL5 program Tango. Kikuchi images for the PZT were indexed to the cubic phase of the perovskite structure to describe grain orientations in the PZT film. The PZT composition is in close proximity to a morphotropic phase boundary (MPB) and the small structural distortions from cubic to tetragonal cannot be reliably indexed.

In order to observe local piezoelectric response in the PZT thin films, dual amplitude resonance tracking (DART) piezoresponse force microscopy (PFM) was performed on one sample from each set of films with different elastic layers with an Asylum Research MFP-3D. PFM scans were performed on 3 μm × 3 μm areas to observe local domain structures. Local switching spectroscopy (SS-PFM) was performed to obtain the amplitude and phase of the piezoresponse at that location. Measurements were

performed with a probe set point of 1 V (~ $0.5V_C$), and SS-PFM loops were performed up to 8 V tip bias. Piezoresponse is calculated using the expression

$$Piezoresponse = Amp * \cos\phi \quad (10\text{-}1)$$

where Amp and ϕ are the amplitude and phase of the measured SS-PFM response, respectively. Raw SS-PFM response data was smoothed with an adjacent-point averaging algorithm for better visualization.

Table 10-1 Measured dielectric permittivity and loss tangent, polarization, and effective longitudinal piezoelectric response at increasing radiation doses for PZT thin films 760 nm SiO_2 elastic layer. Percent change is calculated from measurements before and after the given radiation dose. Uncertainties expressed represent one standard deviation from the mean to one significant figure. Measurement values are reported to the same decimal place as the uncertainties.[172]

760 nm SiO_2		0 Mrad	0.2	0.5	1.0	2.0	5.0	10.0
Low-field Dielectric								
ε_r	Virgin	1254 ± 5	1241 ± 4	1290 ± 20	1243 ± 3	1270 ± 8	1250 ± 10	1270 ± 10
	Irradiated	1230 ± 10	1250 ± 10	1260 ± 20	1215 ± 3	1206 ± 8	1130 ± 30	1090 ± 20
	% Change	-2 ± 1	0.6 ± 0.9	-2.3 ± 0.4	-2.3 ± 0.1	-5.0 ± 0.8	-2 ± 2	-15 ± 1
tan(δ) (%)	Virgin	2.4 ± 0.3	1.6 ± 0.3	4.4 ± 0.8	2.2 ± 0.3	2.6 ± 0.7	1.6 ± 0.2	3.2 ± 0.7
	Irradiated	2.6 ± 0.2	1.7 ± 0.2	4.1 ± 0.9	2.3 ± 0.4	3 ± 1	1.5 ± 0.1	2.0 ± 0.5
	% Change	10 ± 20	8 ± 9	-7 ± 7	3 ± 2	-0 ± 20	-10 ± 10	-40 ± 6
Rayleigh Analysis								
ε_{init}	Virgin	1280 ±030	1050 ± 20	1200 ± 200	1090 ± 20	1100 ± 100	1100 ± 100	1200 ± 200
	Irradiated	1190 ± 80	1053 ± 8	1180 ± 90	1200 ± 200	1200 ± 20	1070 ± 40	1090 ± 50
	% Change	-7 ± 4	0 ± 1	-2 ± 7	10 ± 20	10 ± 10	0 ± 5	0 ± 10
α (cm/kV)	Virgin	41 ± 1	40.2 ± 0.2	42 ± 3	50.1 ± 0.6	36 ± 2	41 ± 3	46 ± 5
	Irradiated	33 ± 5	31 ± 1	32 ± 2	29 ± 3	27 ± 2	23 ± 2	25 ± 7
	% Change	-20 ± 20	-23 ± 3	-22 ± 10	-43 ± 6	-25 ± 3	-43 ± 9	-70 ± 30
$\alpha/\varepsilon_{init}$ $x10^3$ (cm/kV)	Virgin	32 ± 2	38 ± 1	35 ± 8	45.7 ± 0.9	31 ± 4	39 ± 6	50 ± 10
	Irradiated	28 ± 3	29.2 ± 0.7	27 ± 1	25 ± 6	22 ± 1	21.6 ± 0.9	24 ± 5

	% Change	-10 ± 10	-24 ± 4	-20 ± 10	-50 ± 13	-29 ± 5	-40 ± 10	-50 ± 20
Polarization								
$P_{saturation}$ ($\mu C/cm^2$)	Virgin	37.8 ± 0.6	36.8 ± 0.2	42 ± 2	38.0 ± 0.6	38 ± 1	40.1 ± 0.6	39.1 ± 0.9
	Irradiated	36.9 ± 0.7	36.2 ± 0.4	41 ± 2	37.4 ± 0.8	38 ± 2	35.0 ± 0.3	35.1 ± 0.6
	% Change	-2.5 ± 0.5	-1.6 ± 0.8	-2.4 ± 0.8	-1.5 ± 0.6	-2 ± 2	-13 ± 2	-10 ± 1
$P_{remanent}$ ($\mu C/cm^2$)	Virgin	14.1 ± 0.9	11.2 ± 0.5	16 ± 2	13.4 ± 0.6	14 ± 1	15.1 ± 0.6	16 ± 1
	Irradiated	14 ± 1	10.4 ± 0.8	15 ± 2	12 ± 1	12 ± 1	8.0 ± 0.9	8.2 ± 0.7
	% Change	-1 ± 9	-6 ± 4	-10 ± 4	-13 ± 3	-12 ± 2	-47 ± 4	-47 ± 3
$\Delta P/2$ ($\mu C/cm^2$)	Virgin	-0.6 ± 0.1	-2.0 ± 0.3	-2.0 ± 0.1	-1.1 ± 0.1	-1.4 ± 0.4	-1.7 ± 0.1	-0.4 ± 0.1
	Irradiated	-0.1 ± 0.6	-3 ± 2	-2.1 ± 0.2	-1.4 ± 0.2	-1.5 ± 0.6	-1.7 ± 0.6	-1.0 ± 0.3
	% Change	-90 ± 100	100 ± 100	5 ± 5	30 ± 20	0 ± 20	0 ± 40	200 ± 100
E_{C+} (kV/cm)	Virgin	23.6 ± 0.8	32 ± 2	29 ± 2	22 ± 1	29 ± 1	26 ± 1	21.6 ± 0.6
	Irradiated	34 ± 2	39 ± 1	36 ± 5	33 ± 4	34 ± 3	38 ± 4	31 ± 5
	% Change	43 ± 9	21 ± 7	20 ± 20	50 ± 20	20 ± 10	40 ± 20	40 ± 20
E_{C-} (kV/cm)	Virgin	-34 ± 1	-17 ± 2	-30 ± 2	-33 ± 2	-21 ± 2	-35 ± 4	-37 ± 2
	Irradiated	-28 ± 3	-15 ± 1	-22 ± 1	-20 ± 3	-18 ± 1	-12 ± 2	-14 ± 2
	% Change	-20 ± 10	-13 ± 4	-28 ± 4	-41 ± 7	-12 ± 6	-67 ± 5	-63 ± 6
$E_{internal,P}$ (kV/cm)	Virgin	-5.0 ± 0.3	7 ± 2	0 ± 1	-6 ± 2	4 ± 1	-8 ± 1	-8 ± 1
	Irradiated	3 ± 1	11.9 ± 0.8	7 ± 2	7 ± 3	8 ± 1	13 ± 2	9 ± 3
	% Change	-160 ± 30	70 ± 30	-800 ± 90	-230 ± 50	120 ± 80	-500 ± 300	-210 ± 50
ε_r-E_{DC}								
% Diel. Tunability	Virgin	72.9 ± 0.1	74.1 ± 0.2	72.6 ± 0.1	73.2 ± 0.3	74.6 ± 0.2	74.1 ± 0.8	72.8 ± 0.1
	Irradiated	72.7 ± 0.3	73.6 ± 0.1	71.8 ± 0.4	72.3 ± 0.3	73.3 ± 0.5	71.7 ± 0.6	70.1 ± 0.1
	% Change	-0.4 ± 0.5	-0.7 ± 0.3	-1.0 ± 0.6	-1.3 ± 0.9	-1.7 ± 0.5	-3.3 ± 0.4	-3.6 ± 0.1
$\varepsilon_{DC,low\text{-}field}$	Virgin	1420 ± 20	1354 ± 5	1430 ± 10	1450 ± 10	1395 ± 3	1380 ± 20	1433 ± 10
	Irradiated	1350 ± 20	1323 ± 8	1390 ± 10	1360 ± 5	1377 ± 7	1290 ± 30	1260 ± 10
	% Change	-5 ± 2	-2.3 ± 0.7	-2.9 ± 0.1	-6.3 ± 0.8	-1.3 ± 0.4	-6 ± 2	-12.1 ± 0.5
Piezoelectric								
$d_{33,f,saturation}$ (pm/V)	Virgin	72 ± 3	67 ± 3	70 ± 3	76 ± 2	80 ± 10	73 ± 4	75 ± 4
	Irradiated	69 ± 4	61 ± 3	74 ± 5	73 ± 9	75 ± 9	70 ± 6	73 ± 3
	% Change	-5 ± 2	-8 ± 8	5 ± 6	0 ± 10	-7 ± 9	0 ± 10	-3 ± 9
$d_{33,f,remanent}$ (pm/V)	Virgin	51 ± 6	27 ± 5	36 ± 8	43 ± 5	45 ± 7	34 ± 5	52 ± 3
	Irradiated	37 ± 7	21 ± 4	30 ± 10	32 ± 8	27 ± 3	20 ± 10	23 ± 6
	% Change	-29 ± 9	-20 ± 20	-20 ± 50	-30 ± 10	-40 ± 10	-40 ± 40	-60 ± 10

Table 10-2 Measured dielectric permittivity and loss tangent, polarization, and effective longitudinal piezoelectric response at increasing radiation doses for PZT thin films 2035 nm SiO_2 elastic layer. Percent change is calculated from measurements before and after the given radiation dose. Uncertainties expressed represent one standard deviation from the mean to one significant figure. Measurement values are reported to the same decimal place as the uncertainties.[172]

2035 nm SiO_2		0 Mrad	0.2	0.5	1.0	2.0	5.0	10.0
Low-field Dielectric								
ε_r	Virgin	1231 ± 3	1250 ± 6	1232 ± 2	1228 ± 6	1238 ± 6	1233 ± 2	1252 ± 5
	Irradiated	1230 ± 10	1290 ± 20	1224 ± 7	1200 ± 20	1180 ± 20	1120 ± 10	1083 ± 2
	% Change	0 ± 1	3 ± 1	-1 ± 1	-2 ± 1	-5 ± 1	-9.1 ± 0.8	-13.5 ± 0.5
tan(δ) (%)	Virgin	1.4 ± 0.1	1.5 ± 0.2	1.3 ± 0.1	1.3 ± 0.1	1.5 ± 0.1	1.5 ± 0.3	1.2 ± 0.1
	Irradiated	1.5 ± 0.1	2.2 ± 0.3	1.5 ± 0.1	1.5 ± 0.2	1.3 ± 0.1	1.1 ± 0.1	1.0 ± 0.1
	% Change	13 ± 7	60 ± 40	12 ± 9	10 ± 10	-12 ± 3	-20 ± 10	-16 ± 5
Rayleigh Analysis								
ε_{init}	Virgin	930 ± 50	1103 ± 4	1070 ± 30	1148 ± 5	1164 ± 3	940 ± 40	1079 ± 3
	Irradiated	900 ± 100	991 ± 2	879 ± 5	1013 ± 3	1070 ± 20	1060 ± 30	1110 ± 70
	% Change	-10 ± 10	-10.2 ± 0.4	-18 ± 2	-11.7 ± 0.3	-8 ± 1	13 ± 6	3 ± 7
α (cm/kV)	Virgin	50 ± 5	39.7 ± 0.7	52 ± 1	38.5 ± 0.3	40.9 ± 0.9	52 ± 2	41.1 ± 0.3
	Irradiated	44 ± 5	34.8 ± 0.7	37.7 ± 0.5	28.5 ± 0.2	26.6 ± 0.6	27 ± 7	18 ± 3
	% Change	-10 ± 10	-12.5 ± 0.4	-26.8 ± 0.7	-26.2 ± 0.2	-35 ± 3	-50 ± 20	-57 ± 7
$\alpha/\varepsilon_{init}$ $x10^3$ *(cm/kV)*	Virgin	54 ± 8	36.0 ± 0.6	48 ± 2	33.6 ± 0.4	35.1 ± 0.7	56 ± 2	38.1 ± 0.4
	Irradiated	51 ± 7	35.1 ± 0.8	42.9 ± 0.3	28.1 ± 0.3	24.9 ± 0.9	25 ± 6	16 ± 3
	% Change	-6 ± 1	-3 ± 1	-11 ± 3	-16.5 ± 0.5	-29 ± 4	-60 ± 10	-58 ± 9
Polarization								
$P_{saturation}$ $(\mu C/cm^2)$	Virgin	35.5 ± 0.1	35.6 ± 0.1	35.3 ± 0.1	35.5 ± 0.1	35.7 ± 0.1	35.6 ± 0.1	35.4 ± 0.1
	Irradiated	35.0 ± 0.3	35.1 ± 0.3	34.9 ± 0.2	34.8 ± 0.2	35.0 ± 0.2	34.6 ± 0.2	34.0 ± 0.3
	% Change	-1 ± 1	-1.0 ± 0.9	-1.0 ± 0.6	-1.8 ± 0.6	-1.9 ± 0.7	-2.7 ± 0.5	-4.0 ± 0.7
$P_{remanent}$ $(\mu C/cm^2)$	Virgin	12 ± 1	10.6 ± 0.2	11.2 ± 0.2	10.4 ± 0.2	12.9 ± 0.4	11 ± 1	10.6 ± 0.2
	Irradiated	10.9 ± 0.7	9.6 ± 0.2	9.4 ± 0.4	8.2 ± 0.5	7.8 ± 0.6	6.9 ± 0.9	4.0 ± 0.8
	% Change	-5 ± 6	-10 ± 3	-16 ± 4	-21 ± 4	-40 ± 5	-38 ± 7	-62 ± 7
$\Delta P/2$ $(\mu C/cm^2)$	Virgin	-0.8 ± 0.8	-1.6 ± 0.1	-1.1 ± 0.1	-1.1 ± 0.1	-1.0 ± 0.6	-1.0 ± 0.6	-1.4 ± 0.1
	Irradiated	-0.9 ± 0.4	-1.9 ± 0.2	-1.6 ± 0.3	-2.2 ± 0.2	-2.2 ± 0.3	-1.9 ± 0.5	-3.1 ± 0.4
	% Change	200 ± 300	15 ± 6	50 ± 20	30 ± 10	400 ± 100	100 ± 100	130 ± 30
E_{C+} *(kV/cm)*	Virgin	23 ± 3	29.8 ± 0.6	24 ± 1	29.6 ± 0.3	15.6 ± 0.8	23 ± 3	28.3 ± 0.9

	Irradiated	32 ± 6	37 ± 1	34 ± 7	39 ± 1	33 ± 9	35 ± 9	41 ± 1
	% Change	40 ± 30	24 ± 5	40 ± 30	33 ± 3	110 ± 50	50 ± 50	44 ± 7
E_{C-} (kV/cm)	Virgin	-26 ± 6	-16.2 ± 0.7	-23.9 ± 0.6	-15.8 ± 0.4	-26 ± 1	-25 ± 5	-17 ± 3
	Irradiated	-20 ± 3	-13.7 ± 0.2	-16 ± 6	-11.4 ± 0.6	-13 ± 4	-12 ± 5	-6 ± 1
	% Change	-20 ± 30	-15 ± 5	-30 ± 30	-28 ± 3	-50 ± 20	-50 ± 30	-68 ±
$E_{internal,P}$ (kV/cm)	Virgin	-1 ± 5	6.8 ± 0.6	0 ± 0.9	6.9 ± 0.2	-5 ± 1	-1 ± 4	5 ± 2
	Irradiated	6 ± 5	11.6 ± 0.5	9 ± 6	14.0 ± 0.8	10 ± 7	12 ± 7	18 ± 1
	% Change	-200 ± 200	70 ± 20	-80 ± 40	103 ± 8	-300 ± 200	-300 ± 400	300 ± 200
ε_r-E_{DC}								
% Diel. Tunability	Virgin	74.3 ± 0.3	74.7 ± 0.4	74.3 ± 0.2	74.5 ± 0.2	74.6 ± 0.3	74.2 ± 0.1	74.8 ± 0.2
	Irradiated	74.0 ± 0.7	74.2 ± 0.3	74.0 ± 0.2	73.0 ± 0.1	73.0 ± 0.1	71.8 ± 0.3	71.3 ± 0.5
	% Change	-0.3 ± 0.6	-0.7 ± 0.1	-0.5 ± 0.6	-1.9 ± 0.2	-2.1 ± 0.3	-3.2 ± 0.5	-4.7 ± 0.6
$\varepsilon_{DC,low-field}$	Virgin	1400 ± 10	1355 ± 3	1400 ± 9	1359 ± 9	1400 ± 30	1400 ± 30	1380 ± 10
	Irradiated	1350 ± 30	1324 ± 4	1348 ± 3	1307 ± 1	1319 ± 9	1320 ± 40	1247 ± 2
	% Change	-4 ± 2	-2.3 ± 0.5	-3.7 ± 0.7	-3.8 ± 0.5	-5 ± 1	-5 ± 3	-10 ± 1
Piezoelectric								
$d_{33,f,saturation}$ (pm/V)	Virgin	78 ± 5	75.1 ± 0.8	76.4 ± 0.6	74 ± 6	78 ± 2	78 ± 5	80.0 ± 0.9
	Irradiated	78 ± 3	78 ± 2	72 ± 3	76 ± 3	76 ± 1	74 ± 1	77 ± 4
	% Change	0 ± 2	0 ± 2	-6 ± 4	0 ± 10	-3 ± 3	-3 ± 7	-4 ± 5
$d_{33,f,remanent}$ (pm/V)	Virgin	50 ± 10	40 ± 1	43 ± 2	40 ± 3	43 ± 3	51 ± 5	42 ± 1
	Irradiated	34 ± 8	27.1 ± 0.6	25 ± 2	22 ± 1	23 ± 4	19 ± 7	7 ± 4
	% Change	-31 ± 4	-32 ± 4	-42 ± 4	-44 ± 6	-46 ± 9	-60 ± 20	-83 ± 9

Table 10-3 Measured dielectric permittivity and loss tangent, polarization, and effective longitudinal piezoelectric response at increasing radiation doses for PZT thin films 750 nm AlN elastic layer. Percent change is calculated from measurements before and after the given radiation dose. Uncertainties expressed represent one standard deviation from the mean to one significant figure. Measurement values are reported to the same decimal place as the uncertainties.[172]

750 nm AlN		0 Mrad	0.2	0.5	1.0	2.0	5.0	10.0
Low-field Dielectric								
ε_r	Virgin	1170 ± 20	1180 ± 30	1190 ± 20	1210 ± 10	1200 ± 40	1193 ± 8	1200 ± 12
	Irradiated	1100 ± 30	1100 ± 20	1080 ± 40	1095 ± 5	1090 ± 50	1000 ± 20	990 ± 30
	% Change	-6 ± 1	-6.6 ± 0.8	-9 ± 2	-9.8 ± 0.5	-10 ± 1	-16 ± 1	-18 ± 2
	Virgin	1.7 ± 0.2	2.2 ± 0.2	4.0 ± 0.3	2.3 ± 0.2	2.8 ± 0.8	1.5 ± 0.1	2.0 ± 0.3

tan(δ) (%)	Irradiated	1.3 ± 0.1	1.7 ± 0.1	3.0 ± 0.3	1.4 ± 0.1	2.0 ± 0.7	1.0 ± 0.1	1.1 ± 0.2
	% Change	-22 ± 3	-23 ± 8	-26 ± 5	-37 ± 4	-32 ± 9	-34 ± 5	-45 ± 7
Rayleigh Analysis								
ε_{init}	Virgin	1000 ± 100	1000 ± 100	923 ± 6	1000 ± 100	1000 ± 100	991 ± 4	950 ± 30
	Irradiated	891 ± 7	900 ± 40	920 ± 30	951 ± 5	930 ± 30	889 ± 6	910 ± 30
	% Change	-10 ± 10	-14 ± 8	-1 ± 3	0 ± 10	0 ± 10	-10 ± 0.3	-4 ± 2
α (cm/kV)	Virgin	34 ± 5	36.1 ± 0.6	33.7 ± 0.3	41 ± 3	40 ± 6	27 ± 1	32 ± 2
	Irradiated	27 ± 3	23 ± 1	19 ± 2	22.4 ± 0.34	20 ± 3	12.1 ± 0.6	12 ± 2
	% Change	-20 ± 20	-36 ± 5	-44 ± 6	-45 ± 4	-50.8 ± 0.9	-54.9 ± 0.5	-61 ± 5
$\alpha/\varepsilon_{init}$ $x10^3$ ***(cm/kV)***	Virgin	37 ± 3	35 ± 4	36.5 ± 0.5	43 ± 3	43 ± 9	27 ± 1	34 ± 2
	Irradiated	28.5 ± 0.1	26 ± 3	21 ± 3	23.5 ± 0.4	21 ± 4	13.6 ± 0.8	14 ± 2
	% Change	-22 ± 6	-25 ± 5	-43 ± 8	-45 ± 4	-50 ± 6	-49.7 ± 0.7	-60 ± 5
Polarization								
$P_{saturation}$ $(\mu C/cm^2)$	Virgin	41.2 ± 0.1	41.5 ± 0.2	39.7 ± 0.2	41.5 ± 0.2	40. ± 0.4	40.7 ± 0.1	41.0 ± 0.1
	Irradiated	40.7 ± 0.7	41 ± 1	38.8 ± 0.8	40.5 ± 0.6	39.5 ± 0.6	39.5 ± 0.2	39.3 ± 0.4
	% Change	-1 ± 2	-2 ± 2	-2 ± 1	-2 ± 1	-2 ± 1	-2.9 ± 0.3	-4 ± 1
$P_{remanent}$ $(\mu C/cm^2)$	Virgin	15.6 ± 0.4	15.4 ± 0.6	17.7 ± 0.2	16.1 ± 0.3	16.5 ± 0.4	12.2 ± 0.8	15.9 ± 0.8
	Irradiated	15.2 ± 0.2	15 ± 1	15 ± 1	14.0 ±0.2	13.6 ± 0.9	6 ± 2	7 ± 2
	% Change	-2 ± 1	-3 ± 5	-16 ± 6	-13.1 ± 0.8	-18 ± 4	-50 ± 20	-50 ± 10
$\Delta P/2$ $(\mu C/cm^2)$	Virgin	-1.3 ± 0.4	-1.6 ± 0.3	1.0 ± 0.4	-1.3 ± 0.2	0.5 ± 0.6	-1.3 ± 0.3	-0.6 ± 0.6
	Irradiated	-0.9 ± 0.3	-1.1 ± 0.3	0.3 ± 0.2	-1.1 ± 0.3	0.3 ± 0.8	-4 ± 2	-3 ± 2
	% Change	-30 ± 20	-30 ± 30	-70 ± 30	-10 ± 20	-100 ± 200	200 ± 100	900 ± 500
E_{C+} ***(kV/cm)***	Virgin	33 ± 1	29 ± 1	26 ± 1	30 ± 3	20 ± 6	27 ± 1	32 ± 2
	Irradiated	44 ± 3	40 ± 6	44 ± 3	48 ± 1	40 ± 20	47 ± 4	51 ±7
	% Change	30 ± 10	40 ± 20	70 ± 20	60 ± 10	70 ± 80	80 ± 20	60 ± 30
E_{C-} ***(kV/cm)***	Virgin	-20 ± 1	-24 ± 4	-40 ± 1	-25 ± 3	-38 ± 3	-15.2 ± 0.9	-19 ± 1
	Irradiated	-16.7 ± 0.5	-18 ± 2	-21.4 ± 0.8	-16 ± 2	-18 ± 4	-3 ± 4	-6 ± 4
	% Change	-13 ± 6	-20 ± 10	-47 ± 3	-37 ± 8	-50 ± 10	-80 ± 30	-70 ± 20
$E_{internal,P}$ ***(kV/cm)***	Virgin	6.8 ± 0.8	3 ± 2	-7 ± 1	3 ± 3	-9 ± 2	5.9 ± 0.7	6 ± 1
	Irradiated	14 ± 1	11 ± 4	11 ± 2	16.0 ± 0.7	10 ± 10	22 ± 4	23 ± 5
	% Change	100 ± 30	600 ± 500	-250 ± 20	0 ± 2000	-200 ± 100	300 ± 100	300 ± 100
ε_r-E_{DC}								
% Diel. Tunability	Virgin	74.8 ± 0.1	74.0 ± 0.1	74.5 ± 0.3	74.6 ± 0.3	74.3 ± 0.6	74.0 ± 0.2	74.6 ± 0.3
	Irradiated	74.8 ± 0.1	73.7 ± 0.4	72.8 ± 0.3	74.3 ± 0.1	73 ± 1	72.6 ± 0.3	72.1 ± 0.4
	% Change	0.1 ± 0.3	-0.4 ± 0.4	-2.3 ± 0.5	-0.5 ± 0.3	-1 ± 1	-1.8 ± 0.2	-3.3 ± 0.3
	Virgin	1300 ± 20	1315 ± 9	1278 ± 2	1320 ± 10	1330 ± 30	1339 ± 3	1320 ± 20

$\varepsilon_{DC,low\text{-}field}$	Irradiated	1230 ± 40	1195 ± 7	1163 ± 3	1229 ± 3	1190 ± 40	1125 ± 3	1130 ± 70
	% Change	-6 ± 2	-9.1 ± 0.3	-9.1 ± 0.1	-7.2 ± 0.5	-10.5 ± 0.9	-16.0 ± 0.4	-14 ± 4
Piezoelectric								
$d_{33,f,saturation}$ ***(pm/V)***	Virgin	74 ± 6	74 ± 4	72 ± 2	74 ± 5	68 ± 2	76 ± 3	75 ± 2
	Irradiated	75 ± 2	77.7 ± 0.4	74 ± 4	74 ± 3	73 ± 1	73 ± 2	73 ± 2
	% Change	1 ± 8	5 ± 6	3 ± 8	0 ± 4	7 ± 5	3 ± 5	3.2 ± 0.4
$d_{33,f,remanent}$ ***(pm/V)***	Virgin	66 ± 5	58 ± 4	68 ± 8	56 ± 3	70 ± 10	44 ± 4	70 ± 20
	Irradiated	63 ± 9	52 ± 4	44 ± 5	41 ± 7	50 ± 10	5 ± 4	10 ± 10
	% Change	5 ± 9	10 ± 10	30 ± 10	33 ± 3	31 ± 8	90 ± 10	80 ± 20

10.4 Results and Discussion

10.4.1 Crystallographic Phase and Strain Analysis

Baseline XRD shows distinct differences in crystallographic texture arising from elastic layer material selection (Figure 10-1). While all three samples demonstrate a strong 001-texture (93%, 94%, and 93% Lotgering factor for 760 nm SiO_2, 2035 nm SiO_2, and 750 nm AlN, respectively), the samples with SiO_2 elastic layers demonstrate notable peak splitting of the PZT 001 peak. On the other hand, the samples fabricated with AlN elastic layers show no evidence of such splitting, but also exhibit notable PZT 110-orientation, suggesting a nominally more varied orientation than the SiO_2 samples.

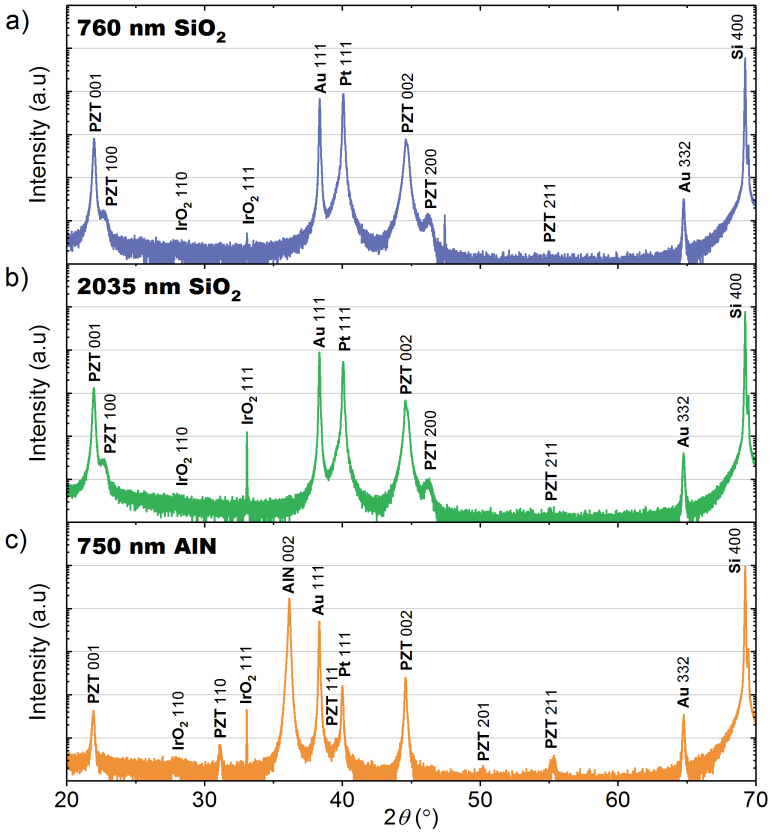

Figure 10-1 XRD analysis of un-irradiated films with (a) 750 nm SiO_2, (b) 2035 nm SiO_2, and (c) 760 nm AlN elastic layers. Notably, the two films with SiO_2 elastic layers are highly 001-textured and show splitting of the same, while the film with AlN show slightly weaker 001-texture and some presence of PZT 110- and 111-peaks.

As discussed previously, modification of the elastic layer thickness and material can result in changes to the residual stress state of the entire material stack during thermal loading for fabrication and crystallization of the ferroelectric material. However, measurement of this residual stress proved to be quite difficult. Wafer curvature measurements were not taken before fabrication of the PZT thin films, and thus, strain estimation using the Stoney formula for thin film residual stress was not possible.[319-322] X-ray diffraction is often used to measure stress/strain in crystalline materials, using the Williamson-Hall method, in which crystallographic texture is tracked while rotating the stage about three axes, and compiled after measurements to extract the lattice strain. [323]

Williamson-Hall measurements were performed (PANalytical Empyrean), but in highly-textured samples such as those studied here, insufficient data points in directions not aligned with the crystallographic texture of the samples does not allow for accurate estimation of the strain. Further attempts to characterize the strain via estimations of the lattice ellipsoid parameter were also unsuccessful, due to the relative obscurity of the method and need for verification thereof via simulations.[324]

Though accurate characterization of the stress was not feasible, an estimation of relative strain in each sample is possible using high-resolution XRD scans and Bragg's law. Bragg's law describes the angles for scattering of incident X-rays from contact with a crystal lattice, given by the expression

$$n\lambda = 2d_{space} \sin\theta \qquad 10\text{-}2$$

where n is the diffraction order, λ is the X-ray wavelength, d_{space} is the out-of-plane lattice spacing of the interrogated material, and θ is the diffraction angle. Using the locations of the peaks in the XRD trace, the d_{space} for each sample can be roughly estimated and relatively compared.

Figure 10-2 shows profiles for the PZT 001- and 002-peaks of the XRD measurements, having been aligned to the Si 400 peak (see Figure 10-1) and adjusted along the y-axis for easier comparison. A Voigt profile was fit to the PZT 001-peak (OriginLab Pro nonlinear peak fit) to extract the peak center and full width at half maximum (FWHM) (Table 10-1). The d_{space} values were extracted using $\lambda = 0.1540598$ nm (PANalytical Alpha-1 Cu Kα radiation), and compared to the lattice parameter from a PZT powder sample with

d_{space} = 4.055 Å (PDF 01-07-4060).[325] Calculations of stress were performed using Young's modulus E_y = 84 GPa as estimated by Yagnamurthy *et al.*[326] The results of the comparison show reduced lattice parameters and corresponding estimates of up to several hundred MPa out-of-plane compressive stress in the PZT lattice. This out-of-plane compressive stress translates to in-plane, biaxial, tensile *film* stress in the PZT thin films of reasonable (if not slightly high) values comparable to those found in the literature (Figure 10-1).[274,319,327] However, these results should be taken cautiously, and the more noteworthy result is demonstrating the *relative* values of in-plane film strain in the three samples – *i.e.*, the two samples with SiO_2 elastic layers show comparatively much greater magnitude of tensile film stress/strain than the film with an AlN elastic layer, and the disparity between the two samples with SiO_2 elastic layers is small relative to their difference from the AlN. These relative comparisons are important for elucidating potential contributions of stress and defect motion in irradiated films.

Table 10-4 Rough estimates for lattice parameter d_{space}, strain, and stress in the PZT samples used in this work, based on position of the PZT 001-peak. Peak fitting for maximum and FWHM was performed with a Voigt profile. Negative values of strain and stress denote compressive.

Sample	760 nm SiO_2	2035 nm SiO_2	750 nm AlN
$2\theta_{center}$ (°)	$21.9695 \pm 2\times10^{-4}$	$21.9529 \pm 1\times10^{-4}$	$21.9111 \pm 6\times10^{-4}$
FWHM	$0.1351 \pm 7\times10^{-4}$	$0.1431 \pm 5\times10^{-4}$	0.167 ± 0.002
d_{space} (Å)	4.043	4.046	4.053
Out-of-Plane Strain (%)	-0.307	-0.233	-0.044
Out-of-Plane Stress (MPa)	-258	-195	-37

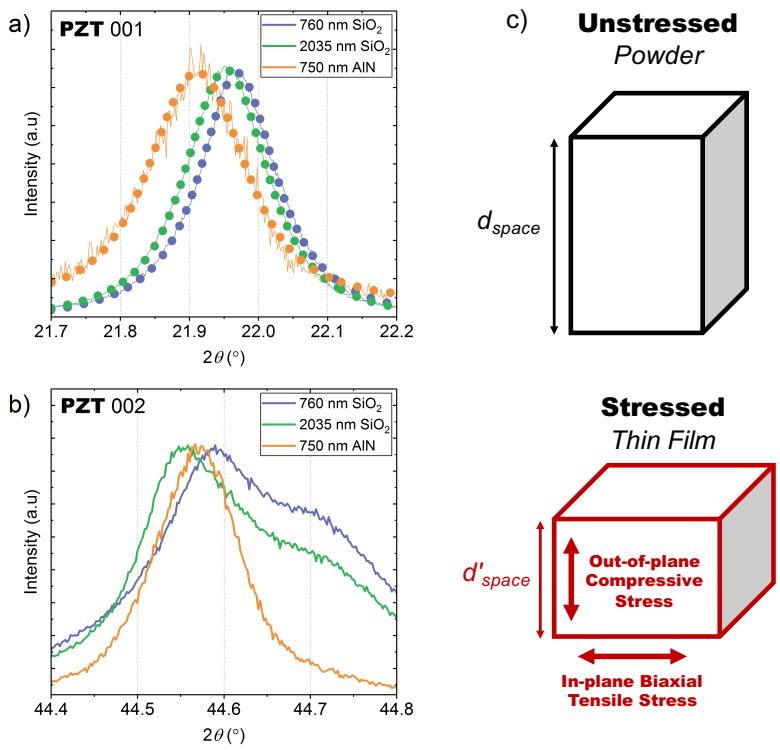

Figure 10-2 High-resolution profiles of the XRD data for the PZT (a) 001- and (b) 002-peaks. The 001-peaks in (a) have been fit with a Voigt profile for estimation of lattice strain. (c) shows a schematic illustration of a powder and thin film tetragonal PZT lattice, with a reduction to the lattice parameter d_{space} , and the resulting out-of-plane compressive stress and corresponding in-plane tensile stress in the thin film.

10.4.2 Microstructural and Morphological Analysis

Results of SEM, AFM, and TKD experiments elucidate microstructural factors potentially contributing to eventual radiation tolerance and functional response modification. Figure 10-3 shows cross-sectional SEM images of the three samples, demonstrating dense, columnar microstructure in all three films. All three sets of samples show some degree of discontinuity at a central interface in the thickness of the film, possibly interpreted as the first crystallization step. AFM images of the surface of each of

the three films shows very smooth structure and generally indistinguishable grains (Figure 10-4). The TKD data shown in Figure 10-5 demonstrates interesting differences in grain orientation characteristics for three samples: those with SiO_2 show a large degree of grain orientation uniformity in both the cubic and tetragonal out-of-plane indexing, while the sample with the AlN elastic layer shows large variations in grain orientation in the out-of-plane direction (Figure 10-1).

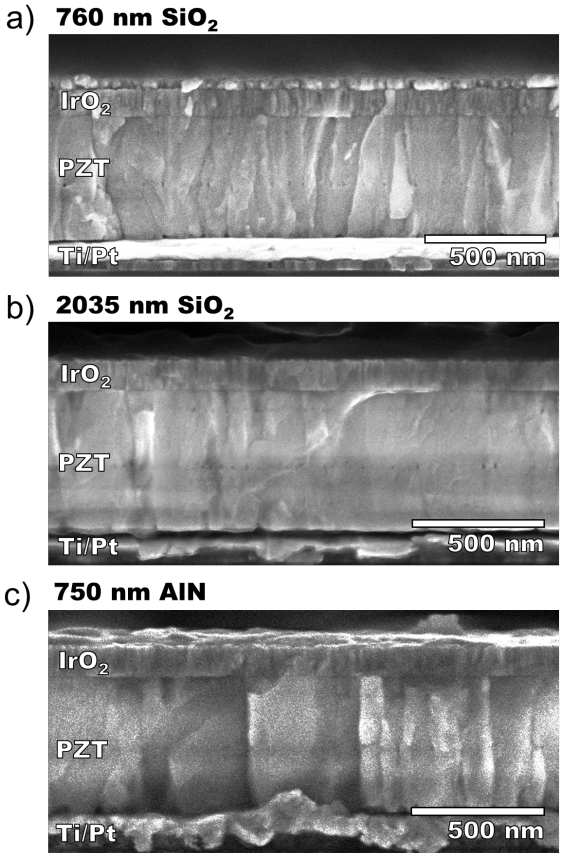

Figure 10-3 Cross-sectional scanning electron microscopy (SEM) images PZT thin films with elastic layers consisting of (a) 760 nm SiO_2, (b) 2035 nm SiO_2, and (c) 750 nm AlN.

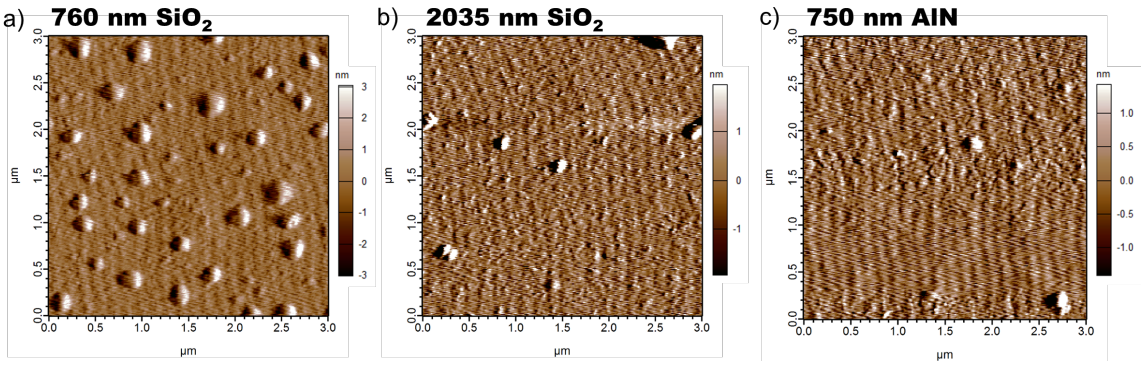

Figure 10-4 Atomic force microscopy (AFM) scans of the surface of samples from each of the three types of films studied here. All samples show generally smooth surface structure. Note that the raised bumps in (a) are likely residue from processing. Images have been flattened with a first order algorithm to eliminate sample tilt.

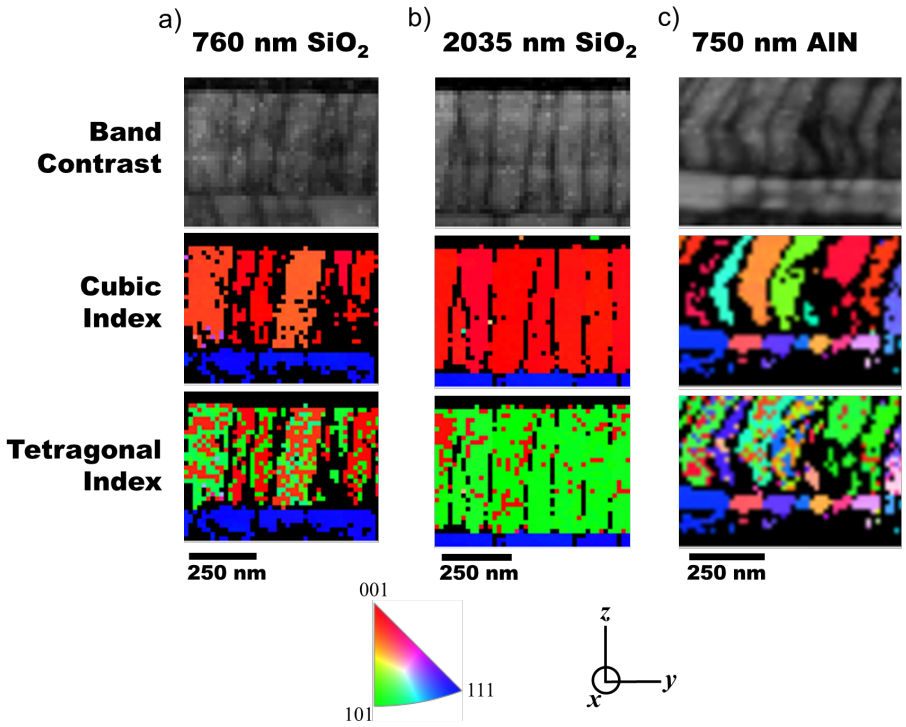

Figure 10-5 Trasmission Kikuchi diffraction of the films with (a) 760 nm SiO_2, (b) 2035 nm SiO_2, and (c) 750 AlN elastic layers. Band contrast, cubic index, and tetragonal index images are shown. Notably, the two samples with SiO_2 elastic layers show very uniform grain orientations, while the film with an AlN elastic layer shows a large degree of randomness.

10.4.3 Trends in Functional Response with Radiation Dose

The results of the dielectric, ferroelectric, and piezoelectric functional response characterization generally demonstrate (with exception of the nonlinear AC dielectric response) that samples with 760 nm SiO_2 and 750 nm AlN elastic layers appear to suffer from qualitatively greater radiation-induced degradation. Selected hysteresis loops and responses have been plotted from the ferroelectric, dielectric, and piezoelectric responses as a function of both AC and DC electric field in Figure 10-6. Greater pinching of the *P-E* hysteresis loops (Figure 10-6a and Figure 10-6c) and the formation of a new peak is observed in the DC field-dielectric permittivity (ε_r-E_{DC}) response (Figure 10-6l) for samples with AlN elastic layers. On the other hand, samples with 2035 nm SiO_2 elastic layer do not demonstrate such notable changes to the *P-E* hysteresis loop and show slightly less degradation of the piezoelectric and ε_r-E_{DC} response loops. The AC dielectric response for 750 nm AlN samples also shows notably greater degradation for than both samples with SiO_2 (Figure 10-6d).

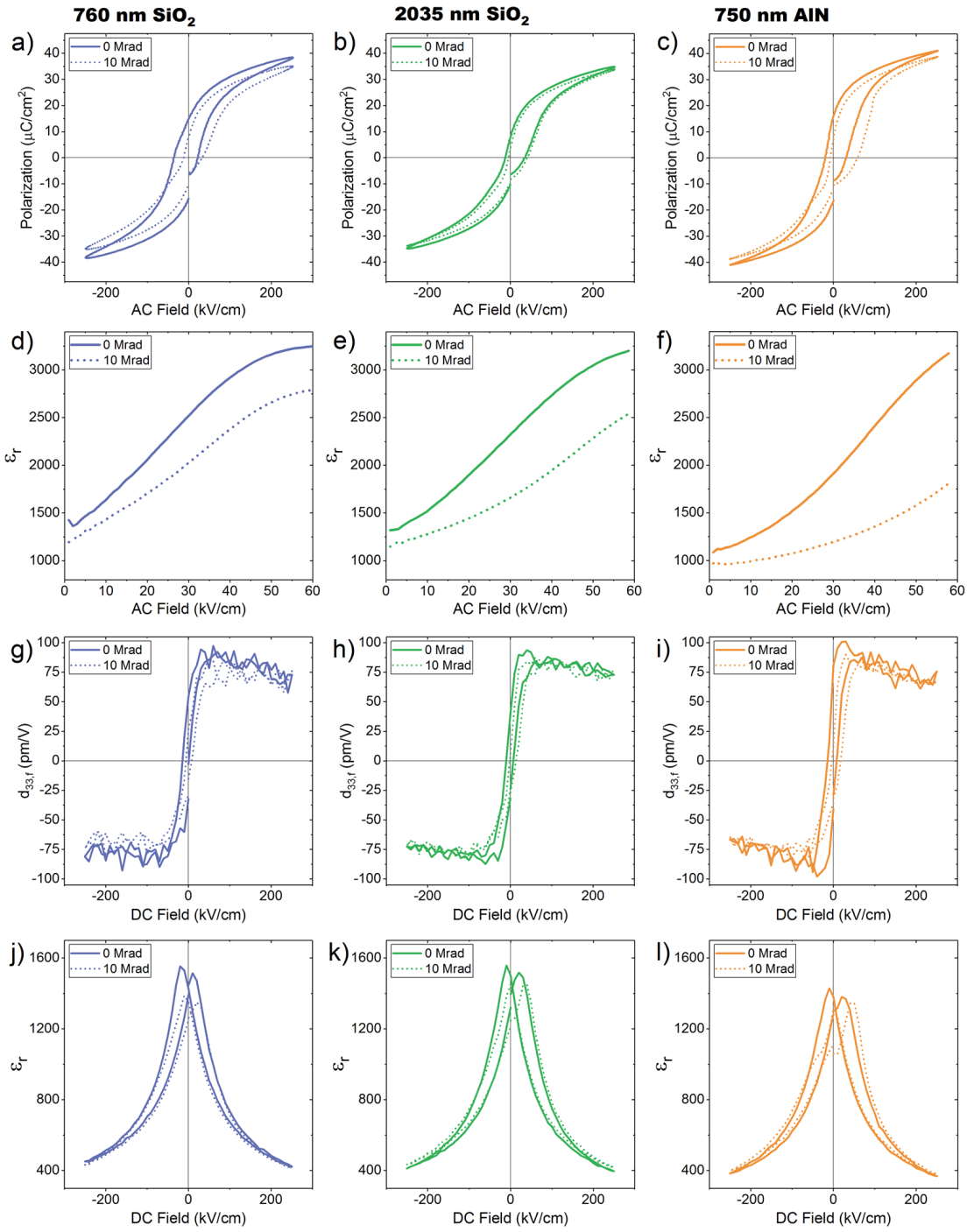

Figure 10-6 Selected plots and hysteresis loops from the ferroelectric (a, b, c), AC dielectric (d, e, f), DC piezoelectric (g, h, i) and DC dielectric (j, k, l) functional responses for samples with (a, d, g, j) 760 nm SiO_2, (b, e, h, k) 2035 nm SiO_2, and (c, f, i, l) 750 nm AlN elastic layers.

The phenomenological model developed in CHAPTER 5 is applied to selected response parameters in order to offer a more quantitative approach to evaluating the TID trends.[189] Full details of the model derivation and detailed discussion are available in CHAPTER 5 and elsewhere.[189] Results of fitting the model to the functional characterization data as a function of TID are given in Table 10-5. Plots of degradation trends and the fitted model are shown in Figure 10-7, Figure 10-8, and Figure 10-9.

Table 10-5 Extracted φ_N and k parameters using the phenomenological model developed in CHAPTER 5 for selected functional response parameters from the degradation trends for the samples with each type of elastic layer studied here.

	760 nm SiO_2		2035 nm SiO_2		750 nm AlN	
	$\varphi_N \times 10^3$	k	$\varphi_N \times 10^3$	k	$\varphi_N \times 10^3$	k
ε_r	21	0.24	19	0.17	26	0.76
ε_{init}	1	0.36	-9	1.17	-12	1.23
α	120	0.70	133	0.61	126	0.79
$\alpha/\varepsilon_{init} \times 10^3$	87	0.77	127	0.34	110	0.80
$P_{saturation}$	19	0.40	6	0.69	3	0.86
$P_{remanent}$	101	0.30	139	0.48	117	0.34
Diel. Tunability	6	0.57	7	0.49	5	0.58
$d_{33,f,saturation}$	-3	1.08	7	0.50	2	1.30
$d_{33,f,remanent}$	78	0.80	171	0.75	280	0.32

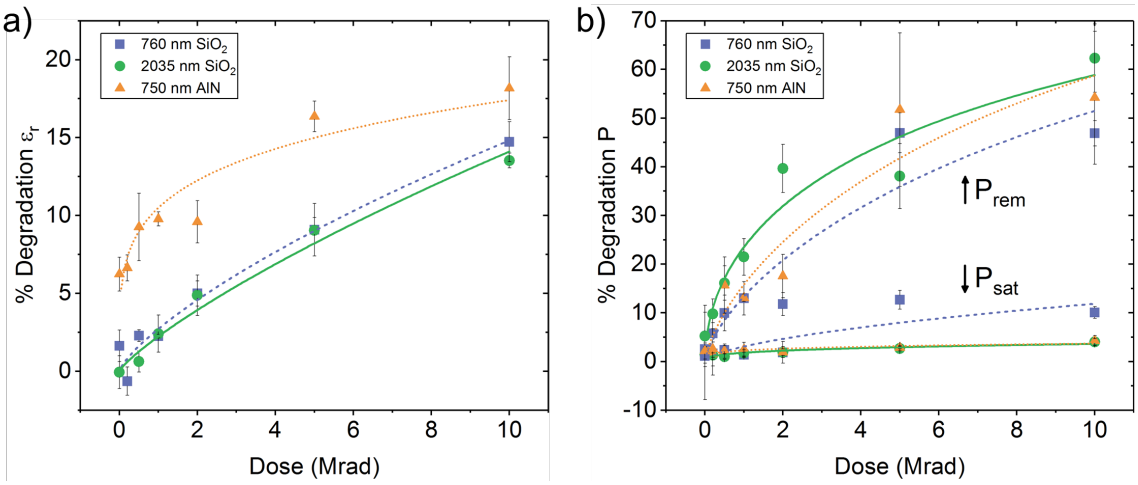

Figure 10-7 Degradation trends and fitted phenomenological model for (a) low-field dielectric permittivity and (b) *P-E* hysteresis as a function of gamma radiation dose.

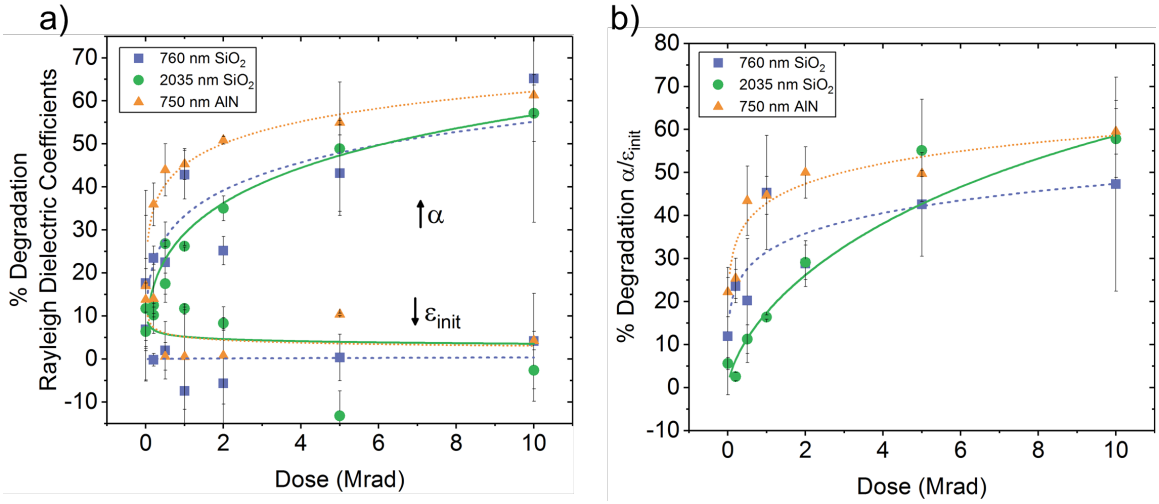

Figure 10-8 Degradation trends and fitted phenomenological model for (a) Rayleigh dielectric coefficients and (b) their ratio as a function of gamma radiation dose.

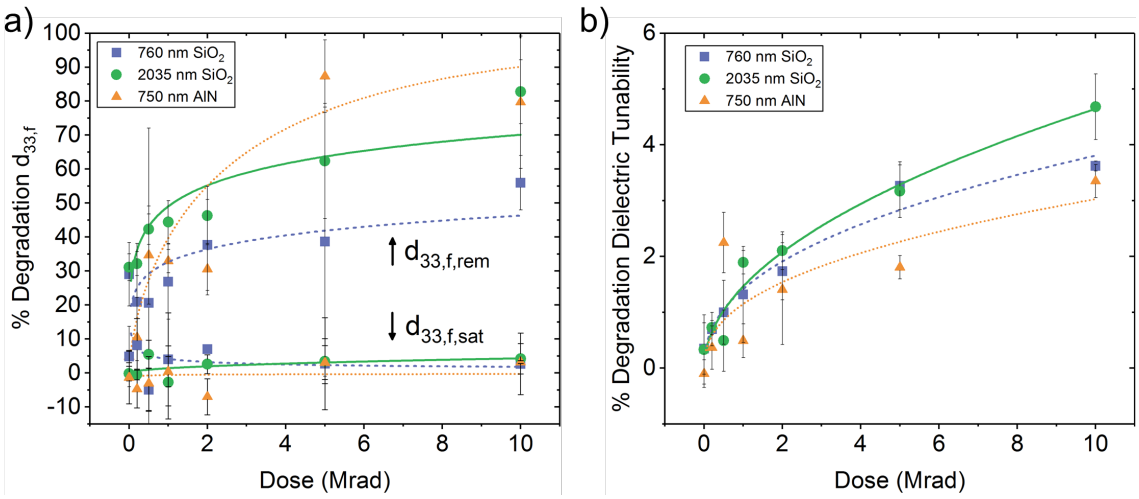

Figure 10-9 Degradation trends and fitted phenomenological model for (a) remanent and saturation piezoelectric response and (b) DC electric field-depeendent dielectric response as a function of gamma radiation dose.

Comparison of the fitting parameters in Table 10-5 helps to make more robust conclusions regarding the effects of modifying the elastic layer on irradiated functional response. Most notably, the k parameter is greatest for the samples with the AlN elastic layer for all measurements with the exception of remanent polarization (P_{rem}) and remanent piezoelectric response ($d_{33,f,rem}$). However, it is notable that the value of φ_N is much greater for samples with AlN elastic layer for $d_{33,f,rem}$, and observation of the plotted trend shows a larger degradation of the response across the dose range, especially at higher doses (Figure 10-9). Furthermore, the trends for P_{rem} appear to suggest that behavior for samples with AlN would demonstrate greater global degradation (higher φ_N) at doses exceeding 10 Mrad. On the other hand, comparison of the two sets of samples with different thicknesses of SiO_2 elastic layers does not appear to show any conclusive trend – in many cases the degradation tend is substantially different (P_{rem}, P_{sat}, $d_{33,f,rem}$) and in other cases, the trends are very similar (ε_r, α). These and the previous results seem to suggest that PZT thin films

fabricated with AlN elastic layers results in reduced radiation tolerance when compared to those fabricated on SiO_2 elastic layers, but SiO_2 layer thickness trends are inconclusive.

10.4.4 Piezoresponse Force Microscopy

Results of the DART PFM surface scans shed light on the local, microscopic piezoelectric response inherent to each of the samples (Figure 10-10). Specifically, the samples with SiO_2 elastic layers of both thicknesses show similar amplitude and phase of the piezoresponse, with domain structures of roughly 100 nm size (Figure 10-10a and Figure 10-10b). On the other hand samples with AlN elastic layers showed reduced piezoresponse, apparent by the less distinct domain structure and lower amplitude of the response (Figure 10-10c and Figure 10-10f).

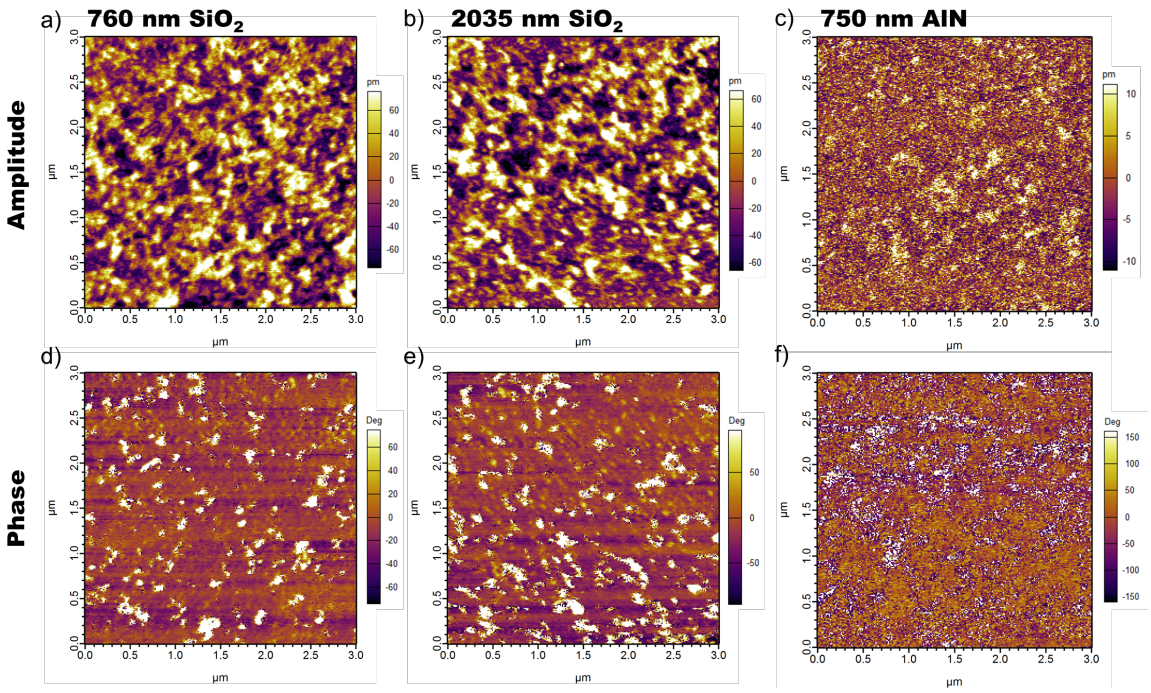

Figure 10-10 Dual amplitude resonance tracking (DART) piezoresponse force microscopy (PFM) scans of each of the three types of films studied in this chapter with (a, d) 760 nm SiO_2, (b, e) 2035 nm SiO_2, and (c, f) 750 nm AlN elastic layers. (a, b, c) Amplitude and (d, e, f) phase of the piezoresponse are shown. Images have been flattened with a first order flattening algorithm to remove effects of sample tilt.

The results of the DART PFM scans are further accentuated by local switching spectroscopy measurements (SS-PFM) of the piezoresponse hysteresis (Figure 10-11). Samples with SiO_2 elastic layers show well-developed butterfly strain loops with distinct phase and switching behavior (Figure 10-11a and Figure 10-11b). The samples with the AlN elastic layer, on the other hand, show poor loops with questionable switching, noisy phase, and much lower amplitude response with respect to the samples with SiO_2 layers. These results suggest that microscopic piezoelectric response and hysteresis is limited in samples with AlN. Amplitude loops on samples with SiO_2 elastic layers show internal bias (Figure 10-11), similar to the macroscopic *P-E* hysteresis loops shown in Figure 10-6,

while the nature of the response for the sample with the AlN elastic layer make such an assessment extremely difficult.

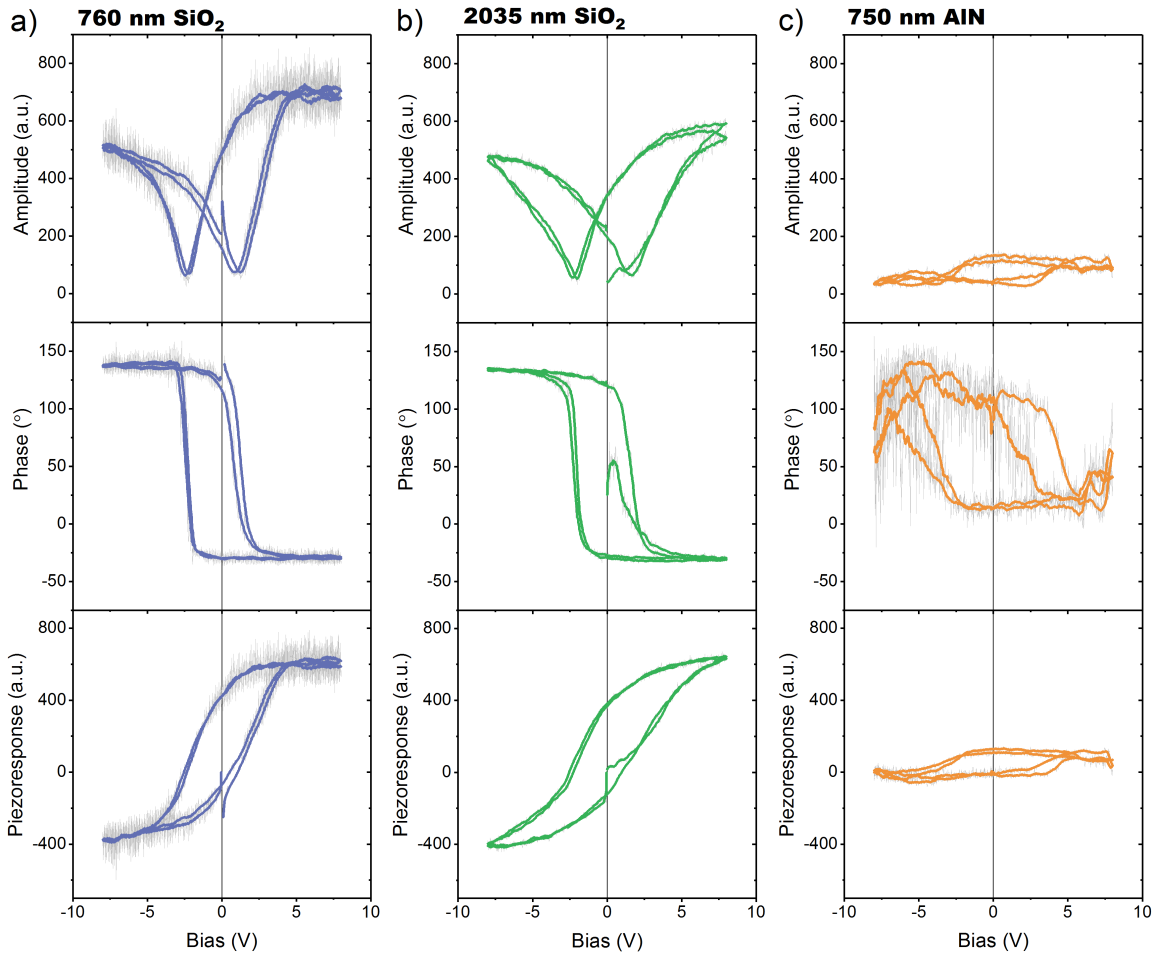

Figure 10-11 Switching spectroscopy piezoresponse force microscopy (SS-PFM) measurements of local piezoresponse hysteresis. Shown are the amplitude, phase, and calculated piezoresponse for samples with (a) 760 nm SiO_2, (b) 2035 nm SiO_2, and (c) 750 AlN elastic layers. Raw data is shown in light gray, and the bold curve shows the data after smoothing with an adjacent-point averaging algorithm. Scales are equal for comparisons of magnitude of response.

10.4.5 Discussion

General trends and observations of microstructure, stress/strain, and material properties suggest that samples fabricated with AlN elastic layers are more susceptible to radiation-induced degradation, but also likely exhibit reduced inherent, pre-irradiation piezoelectric and ferroelectric response. First, grain size and morphology are generally very similar, as shown in cross-sectional SEM images (Figure 10-3) – all samples show columnar grains with dense microstructure and very little porosity. However, the results of the TKD analysis demonstrate distinct grain orientations for the film with an underlying AlN elastic layer, suggesting that there exists a greater degree of misorientation at grain boundary interfaces in those samples. The work in CHAPTER 6 showed that grain morphology and microstructure plays a large role in determining the eventual radiation hardness and functional response as a function of gamma radiation dose.[217] Prior work on irradiation of ferroelectric materials has shown that rates of trapped charge creation/activation are highly-dependent on characteristics of the grain boundaries with which the radiation interacts, especially the density of grain boundaries in the sample.[101,218] For the samples with AlN elastic layers, it is possible that the greater grain discontinuity and misorientation leads to an augmented interaction of radiation with the grain boundaries, greater effects of radiation on functional response, and accentuated nonlinearity of defect saturation (k). Indeed, the effects of greater defect population and saturation in the AlN samples are supported by greater extracted values of k in nearly all functional response measurements studied here as a function of TID.

Additionally, the effects of residual stress may play a role in determining the level of radiation tolerance of PZT thin films. Based on the estimation of strain in from the XRD

data, the samples with SiO_2 elastic layers show significantly higher in-plane residual tensile stresses in the PZT layer than those with AlN elastic layers. While accurate calculations of the stress were not possible, these relative comparisons are useful for making general correlations between relative stress states in the three sets of films. Generally, compressive stress in PZT has been shown to lead to enhanced polarizability and increased piezoelectric response, while tensile results can degrade such properties.[274,319,327] The strain estimates indicate that the samples with AlN elastic layers are subject to lower tensile stress than the films with SiO_2 elastic layers. Comparison of the virgin polarization measurements indicates greater response for samples with AlN elastic layers (Table 10-3), and virgin piezoelectric response is among the largest measured in this study, suggesting that the lower values of tensile stress indeed contribute to greater initial response compared to films with SiO_2 and greater tensile stress. However, it is unclear how such residual stress effects contribute to RID effects in ferroelectric thin films. Several reports on functional metal oxides have shown that tensile strain reduces the defect migration energy barrier, allowing for enhanced defect (especially oxygen vacancies) mobility in such samples.[310,311] In the samples with SiO_2 elastic layers and greater tensile strain in the ferroelectric layer, increased defect mobility potentially transports defects away from the grain bulk (and corresponding ferroelectric volume) toward grain boundaries or other internal interfaces, such as layer crystallization interfaces or electrode-ferroelectric hetero-interfaces. Grain boundaries are expected to behave as effective defect sinks, reducing the deleterious effects of defects on functional response behavior when accumulated at these locations. In samples with AlN elastic layers, lower tensile stress may reduce defect mobility (relative to films

with SiO_2), thus pinning domain wall motion to a larger degree and degrading the radiation-dependent functional response.

10.4.6 Conclusions

The results from this work demonstrate that modification of residual film stress via engineering of the elastic layer for fabrication of PZT thin films results in significant effects on eventual material properties and radiation tolerance of the material stack. While modifying the thickness of traditionally-employed SiO_2 elastic layers did not result in large microstructural variations or conclusive radiation tolerance benefits, the selection of an alternative material, AlN, demonstrated notable differences. Namely, interesting crystallographic changes, grain orientations, and residual stress/strain effects in samples with AlN elastic layers likely contribute to reductions in radiation tolerance with respect to samples with SiO_2 elastic layers. Worth noting is the fact that the effects of microstructure, residual stress, and crystallographic phase do not exist independently – their interaction with radiation and the material stacks studied in this chapter presents a complex interaction and tradeoff between these effects. These results offer potential insights into the strong influence and interconnected nature of the various components of the material stack on eventual material properties, functional response, and radiation tolerance of the ferroelectric thin film.

CHAPTER 11. SUBSTRATE MECHANICAL INTERFACE AND RESIDUAL FILM CLAMPING EFFECTS

11.1 Summary

This chapter studies the effects of the substrate on residual clamping of the ferroelectric thin film, by selectively etching the backside of the Si substrate in a PZT thin film material stack to release the ferroelectric. Previous reports from related studies have shown notable enhancements to functional response in ferroelectric thin films on thinned substrates or when completely released from the substrate, attributed to long-range motion of unclamped extrinsic contributions to the response. These long-range contributions to the dielectric and electromechanical responses were expected after progressively thinning the backside Si via deep reactive ion etching. Multiple sets of films with various film, stack, and substrate etching parameters were fabricated and their functional response characterized. The results of demonstrated a highly-complex interaction between the multiple components of the material stack, residual stress effects, and the release of substrate clamping. Enormous enhancements to the electromechanical response were observed with decreasing Si substrate, due to increased substrate bending. However, only minor local enhancements of dielectric properties were observed, and were not universally present. Large deflection of both the substrate and individual top electrode contacts results in competing strain effects, likely overcoming any enhancements resulting from the substrate release. Local probing of the ferroelectric response on released regions of the film via piezoresponse force microscopy (PFM) showed substantial reductions in switching voltages and enhancements of the piezoresponse with respect to clamped regions. These results suggest that both the substrate and the top electrode contacts play a significant role in clamping the ferroelectric thin film, and are important considerations for eventual application of ferroelectric thin films in various MEMS devices.

11.2 Introduction

As discussed throughout this thesis, traditionally-processed PZT thin films require a substrate, elastic layer, and bottom electrode stack for mechanical and experimental procedures. While the substrate provides a structural foundation for thin film deposition, it can also produce deleterious effects by clamping the ferroelectric material, thus restricting domain wall motion and potential rhombohedral/tetragonal (R/T) phase transitions. These effects become noticeably more apparent with decreasing film thickness, due to proximity of the film to the clamped interface,[1,36] and are especially prevalent for application in MEMS devices, where substrate conditions are modified and thinner films and substrates are preferred.

Clamping to the substrate largely originates from thermal loading during the fabrication process of ferroelectric PZT thin films; the crystallization anneal produces large residual stresses not only in the ferroelectric layer, but throughout all components of the material stack.[24,274,319,321,328-335] In the ferroelectric film, shrinkage and densification, lattice mismatch, thermal expansion mismatch with the substrate, and even B-site cation gradient formation can induce significant biaxial residual stresses, reportedly up to 180 MPa.[274,321,326,328,336] For applications in microelectronics devices and structures that rely on the ferroelectric thin film for sensing, actuation, data storage, or energy harvesting, these residual stresses can be detrimental to device reliability and performance, or in some cases, be advantageously leveraged to induce strain and polarization.

Prior reports have investigated the effects of substrate clamping and the resulting residual stresses, including application of external stress and the use of thinner substrates

for thin film fabrication. Residual tensile stress has typically been shown to degrade dielectric and electromechanical response of ferroelectric thin films, while compressive stress can potentially enhance functional properties.[321,327,329,330,332,337-339] In-plane tensile strains in the as low as 0.08% result in reductions of up to 14% of the remanent polarization.[339] Additionally, numerous studies have shown that residual stresses can effectively shift the compositional location of the morphotropic phase boundary (MPB), thus modifying the transition temperature, T_C, and potentially degrading functional response or fully suppressing ferroelectricity [52-55,331]. Experiments to probe the effects of various substrates and/or film thicknesses have also resulted in substantial changes to their dielectric, ferroelectric, and piezoelectric responses.[278,340,341] Suzuki *et al.* showed 400% increase to piezoelectric response and 18% increase to dielectric response of PZT thin films deposited on Si substrates of decreasing thickness from 500 to 50 μm.[342]

Recent work by Griggio *et al.* focused on releasing a portion of a deposited and crystallized PZT thin film from the substrate following fabrication, reporting the presence of long-range nonlinear strain fields due to interactions of individual domains.[343] These long-range motion and interactions can substantially enhance dielectric and piezoelectric responses in the films – enormous increases (up to 114%) to both reversible and irreversible Rayleigh coefficients of the AC electric field-dielectric response were observed in thin film PZT capacitors released from the Si substrate, but also likely attributable in part to changes in local stresses and mechanical effects of a less-rigid material stack.[309] Work by Bintachitt *et al.* has suggested that cooperative, avalanche-like interactions of domain wall motion and/or potential phase boundaries are enhanced proportional to decreasing material thickness and correlated to reduced degrees of substrate clamping.[344]

In this chapter, the effects releasing the ferroelectric thin film from substrate clamping are investigated, by progressively thinning the Si substrate from the backside via deep reactive ion etching (DRIE), and continuously monitoring changes in the functional material response. Giant enhancements to the macroscopic electromechanical response (up to 80x) result from mechanical interactions between the PZT thin film and the thinned substrate. However, trends in the macroscopic polarization and dielectric response do not show significant changes with decreasing substrate thickness. PFM experiments suggest local piezoresponse is enhanced in released films, suggesting that the top electrode contact plays a role in clamping a film that is released from the substrate.

11.3 Experimental Methods

11.3.1 PZT Thin Film Preparation and DRIE Etching

Multiple sets of $Pb_{0.53}Ti_{0.47}O_3$ (PZT) thin films were synthesized via chemical solution deposition (CSD) on platinized 100-Si substrates with 2-methoxyethanol (2-MOE)-based 0.4M precursor solutions.[111] The details of each of these sets of samples is outlined in Table 11-1. The sets will be designated as M1, M4.1, *etc.*, throughout this chapter, as indicated in Table 11-1, where "M" is derived from the "membrane"-like nature of the samples. The SiO_2 elastic layer was grown thermally (wet/dry designated in Table 11-1), and the Ti/Pt or TiO_2/Pt bottom electrode contacts were sputter-deposited.[132,235] The deposited films were pyrolyzed after each deposition at 400 °C for 60 s, and annealed in groups of either 3 or 4 pyrolyzed layers at 700 °C for 60 s (Table 11-1), with a target

thickness of ~750-1000 nm. A seed layer of 0.15M PZT and approximately 15 nm thickness was first deposited to induce 100-texture in the subsequent PZT layers.[131]

Backside etching of the double-side polished (DSP) Si substrate was performed using an STS Multiplex inductively coupled plasma (ICP) deep reactive ion etch (DRIE) with SF_6 etching and C_4F_8 passivation layer, achieving an etch rate between 2 and 5 μm/min depending on the use of the passivation layer and variations in tool performance (Figure 3-20). A multi-mask photolithography process was employed to selectively etch a 1 cm^2 area to various etch depths. A schematic of the material stack and the etching process is shown in Figure 11-1. Full details of the photolithography process are available in CHAPTER 3, Section 3.5.

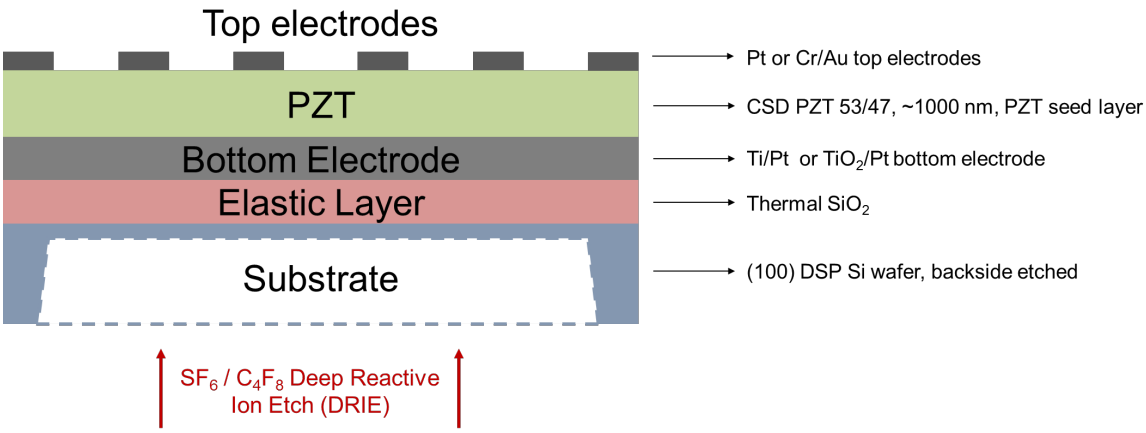

Figure 11-1 Schematic respresentation of the material stack used to investigate the effects of thinning the Si substrate by deep reactive ion etching on the backside of the chip upon which the PZT thin film was fabricated.

Table 11-1 Outline of the processing parameters used for the 6 sets of experiments used in this chapter to study the effects of substrate clamping on the functional response of the membrane-like PZT thin films.

Sample set	Substrate	Bottom Electrode	PZT Deposition (Layers)	PZT Thickness	Top electrode	Electrode layout	Lotgering Factor
M1	300 µm Si, 1300 nm wet SiO_2 (GT)	20 nm Ti, 80 nm Pt	Seed+16 L, 4 L/anneal	1050 nm	80 nm Pt	Remote traces	85%
M2	500 µm Si, 500 nm dry SiO_2 (ARL)	35 nm TiO_2, 100 nm Pt	Seed+15 L, 3 L/anneal	750 nm	80 nm Pt	Remote traces	95%
M3	500 µm Si, 500 nm dry SiO_2 (ARL)	35 nm TiO_2, 100 nm Pt	Seed+15 L, 3 L/anneal	800 nm	80 nm Pt	Remote traces	93%
M4.1	500 µm Si, 500 nm dry SiO_2 (ARL)	35 nm TiO_2, 100 nm Pt	Seed+18 L, 3 L/anneal	1000 nm	100 nm Pt	On membrane	96%
M4.2 Pt	500 µm Si 500 nm dry SiO_2 (ARL)	35 nm TiO_2, 100 nm Pt	Seed+18 L, 3 L/anneal	1000 nm	100 nm Pt, heat treated	On membrane	94%
M4.3 Cr/Au	500 µm Si 500 nm dry SiO_2 (ARL)	35 nm TiO_2, 100 nm Pt	Seed+18 L, 3 L/anneal	1000 nm	70 nm Cr, 140 nm Au, heat treated	On membrane	94%

11.3.2 Functional Response Characterization

Dielectric, polarization, and piezoelectric response characterization was performed on all samples following fabrication, at various backside-DRIE etching intervals. The measurements included low-field dielectric permittivity (ε_r), polarization-electric (P-E) field hysteresis, dielectric permittivity as a function of AC electric field amplitude (ε_r–E_{AC}), dielectric permittivity-DC field (ε_r–E_{DC}) tunability characterization, and converse, effective longitudinal piezoelectric response as a function of DC electric field ($d_{33,f}$–E_{DC}).

Samples in set M1 were poled for 600 seconds at approximately five times the coercive voltage, V_C, directly before electromechanical measurements in order to maximize out-of-plane polarization contributions to the piezoelectric response. However, poling and high DC biases was discovered to substantially reduce the integrity of the thin Pt top electrode traces in the remote electrode layout (Figure 11-4), and was thus discontinued for subsequent sets of samples.

Measurements of ε_r were conducted at 100 mV and 1 kHz using an Agilent 4284A precision LCR meter. *P-E* hysteresis loops were taken up to fields of 200 kV/cm at 100-1000 Hz, using an aixACCT TFA FE module ferroelectric test system. Nonlinear ε_r–E_{AC} measurements were performed up to a maximum of 100 kV/cm at 1 kHz. ε_r–E_{DC} measurements were performed up to 150 kV/cm DC bias with an overlapping small-signal 100 mV at 1 kHz. $d_{33,f}$–E_{DC} response was measured as a function of DC field ($d_{33,f}$-E_{DC}) on an aixACCT double beam laser interferometer (DBLI) measurement system up to 300 kV/cm DC bias with an overlapping AC signal $V_{AC} \approx 0.5V_c$. All measurements are subject to experimental error up to 3-5%. The vertical shift in the *P-E* loops, $\Delta P/2$ (Table 2), the horizontal shift in the *P-E* and $d_{33,f}$-E_{DC} hysteresis loops, and the dielectric tunability were calculated according to formulas available in CHAPTER 3, Section 3.3. The nonlinear dielectric response at low and intermediate AC electric field was analyzed using the Rayleigh approach to quantify changes in intrinsic and extrinsic dielectric response and is discussed in CHAPTER 2.[24,29,236]

11.3.3 Non-contact Interferometry

Non-contact, white light interferometry was performed using a Wyko NT2000 in VSI mode on the etched side of the membranes to estimate the maximum deflection due to the residual stresses caused by the electrodes. At very thin levels of Si (< 2 μm), depressions in the backside of the film are visible due to the residual stresses caused by the top electrode and its effect on the underlying material stack (see Figure 11-2). The depressions are also visible on the top side of the sample, but due to the different refractive indices of PZT and Pt top electrodes, a large amount of error is introduced in the interferometric method. The deflection results of the interferometry measurements are used later as the baseline for analytical estimations the stress/strain in the PZT layer.

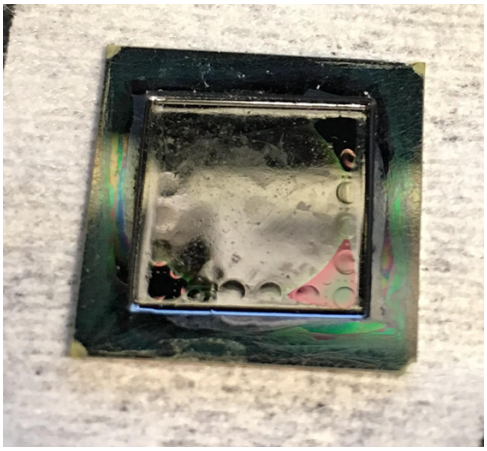

Figure 11-2 Image of the backside etch of sample M4.1. In the corners of the etched region, bare SiO_2 is visible (pink/green). Distinct depressions caused by residual stress interactions between the released $SiO_2/TiO_2/Pt/PZT/Pt$ material stack.

11.3.4 Scanning Transmission Electron Microscopy

Local grain, domain, and interface microstructure were probed via scanning transmission electron microscopy (STEM). Samples were prepared according to the multilayer cross-sectional sandwich method presented by Sridhara *et al.* and dimpled to thin the sample.[345] Samples were imaged with a spherical aberration (Cs) corrected, cold field-emission source, high-resolution Hitachi HD-2700 STEM operated at 200 kV. Initial preparation of sample M2 for STEM via focused ion beam (FIB) lift out was unsuccessful, and a backup sample from set M1 was used.

11.3.5 Piezoresponse Force Microscopy

Piezoresponse force microscopy (PFM) was performed to measure local ferroelectric response and avoid the potential stress effects imparted by the top electrode contacts. Dual amplitude resonance tracking (DART) mode PFM was employed. Switching spectroscopy PFM (SS-PFM) was performed on local regions of the material to extract strain hysteresis loops with applied bias. All measurements were performed with an Asylum Research MFP-3D in DART PFM mode, using a contact set point of 1 V, excitation voltages of 1 to 1.5 V, scan size of 1 μm, and scan rate of 0.75 Hz with a Pt-coated conductive probe tip.

11.4 Results and Discussion

Figure 11-3 shows baseline X-ray diffraction (XRD) analysis of each of the sets of samples used in this work, indicating a large degree of 100-texture in all of the films (see Table 11-1 for Lotgering factors). All sets except M1 show some degree of tetragonal peak splitting at the PZT 200-peak, likely due to the proximity of the precursor solutions to the morphotropic phase boundary and subsequent coexistence of R and T phases. The following sections detail the specifics of each set of samples in order to distinguish principal modifications to the fabrication process for each.

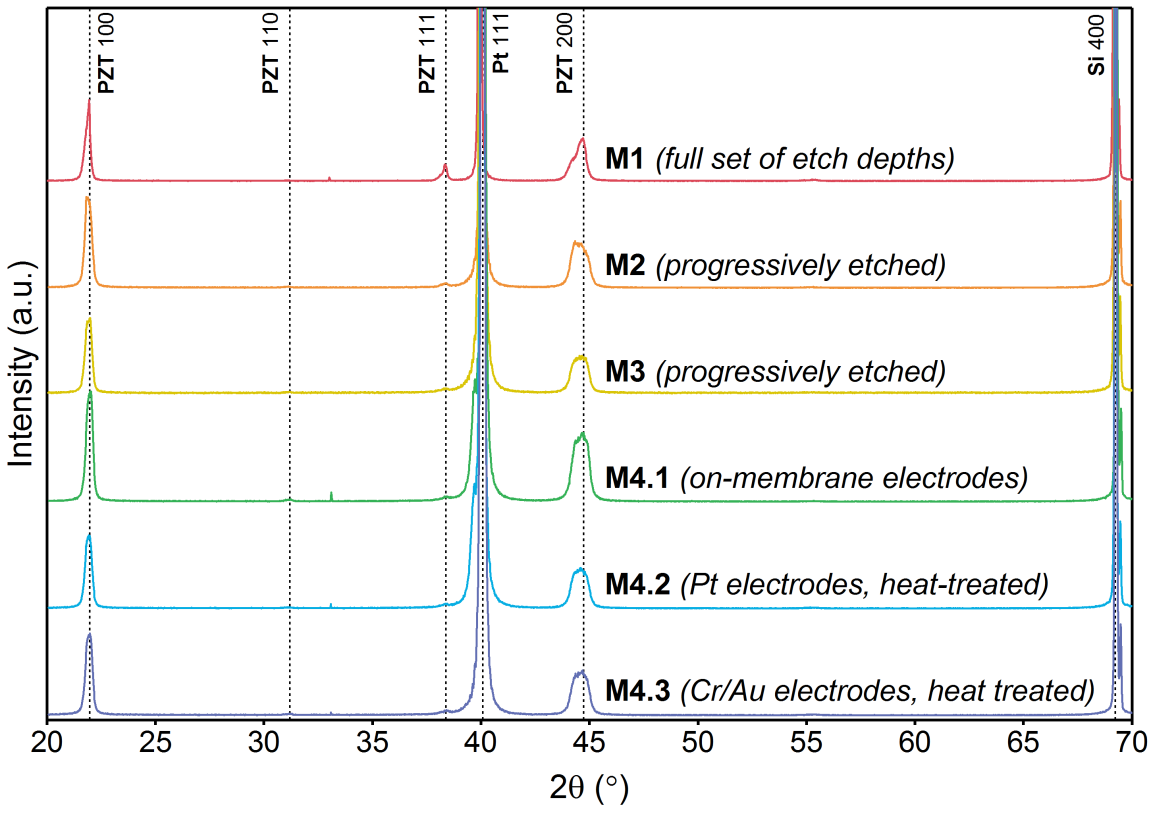

Figure 11-3 X-ray diffraction (XRD) showing the large degree of 100-texture in the samples used for this study.

11.4.1 Membranes M1 – Full Set of Etch Depths

300 μm initial Si thickness and 1.5 μm of wet thermal oxide were used for the samples in set M1. The PZT thin films from this set were deposited and pyrolyzed according the procedure outlined in the Experimental Methods chapter, with crystallization anneals after every 4 deposited layers. 16 total layers resulted in a final film thickness of 1.05 μm. Set M1 was also the only set that was deposited on a whole 4-inch Si wafer and later diced into chips of approximately 2 cm × 2 cm.

The top electrode layout employed is unique, with off-membrane electrode contacts connected via thin Pt traces to large circular, on-membrane electrodes, in order to probe the on-membrane capacitors remotely without damaging or influencing the fragile membrane at deep etch levels. Figure 11-4 shows the electrode layout overlaid on the area etched from the backside of the chip, which was used for sets M1, M2, and M3.

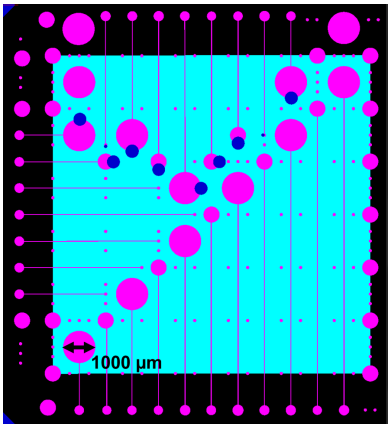

Figure 11-4 Remote electrode layout used for M1, M2, and M3. Black area is un-etched Si, the cyan region represents the area of material that is etched from the backside, and the magenta regions are the top electrode contacts.

In this initial study, a series of 10 chips was fabricated from a single 4-inch wafer of spin-coated PZT. All measurements of functional response were performed after

etching, and compared to an un-etched sample (300 μm Si thickness). However, the nature of large-area processing of CSD PZT thin films on entire Si wafers makes attaining material uniformity challenging. The shortcomings of this method became apparent as large variations in functional response were observed, likely due to variations in material thickness and quality across the diameter of the wafer. Furthermore, the added cost of DSP Si wafers makes processing mistakes on entire wafers costly. For these reasons, the whole-wafer fabrication process was abandoned in later sets of samples in favor of depositing films individually on 2 cm × 2 cm chips.

Additionally, as observed in Table 11-1 and Figure 11-3, the degree of crystallographic 100-texture in sample set M1 is substantially lower than that of subsequent sets of samples. The sputtered bottom Ti/Pt electrode typically serves as a crystallographic growth template for deposited PZT layers, eventually determining their texture.[132,235] However, due to inconsistencies in Ti/Pt film quality deposited using Unifilm Sputterer at Georgia Tech, subsequently-deposited PZT layers show large 111-texture in the samples in set M1. For future sets of samples, new substrates and growth templates were obtained from the US Army Research Laboratory, including a thicker substrate, thinner SiO_2 elastic layer, and slightly modified bottom electrode parameters (see Table 11-1).

11.4.2 Membranes M2 – Abbreviated Functional Characterization for FIB Liftout

A focused ion beam (FIB)-processed transmission electron microscopy (TEM) sample was intended to observe the interaction between the thinned Si substrate, elastic layer, bottom electrode stack, and PZT thin film. An abbreviated set of experiments at 4

discrete Si substrate thicknesses (300, 90, 10, 1 μm) was performed prior to TEM imaging, in order to correlate any observed phenomena in the imaging to trends in material response trends. However, preparing a FIB liftout from sample M2 proved challenging, and no TEM data was retrieved from that sample (see Experimental Methods).

To address the inconsistencies noted in set M1 when comparing measurements from different samples at different etch depths, a single sample was progressively etched, taking measurements before and after each DRIE process step. This approach was used throughout the remaining sets of membrane samples. New substrates were acquired from ARL (500 μm Si, 500 nm dry thermal SiO_2, 35 nm TiO_2, 100 nm Pt); previous experience with similar substrates showed near-perfect 100-texture of PZT thin films processed on them. The PZT films deposited on these substrates in this chapter show excellent PZT 100-texture, with minimal 111- and 110-peaks (Figure 11-3).

11.4.3 Membranes M3 – Progressively Etched

The sample preparation and testing for set M3 was largely identical to set M2, but with an expanded range of etch depths (500, 305, 229, 205, 50, 2 μm), and prepared with new PZT precursor solutions, resulting in slightly thicker films (800 nm *vs.* 750 nm).

11.4.4 Membranes M4.1 – On-Membrane Electrodes

A fourth set of samples was fabricated using the same substrate, elastic layer, bottom electrode stack, and PZT solutions (Table 11-1), resulting in films with similar XRD traces and thickness (Figure 11-3). This set of samples was, however, divided into M4.1, M4.2, and M4.3 based on the top electrode deposition parameters.

During functional response characterization of set M3, it was noticed that the long electrode traces (Figure 11-4) were resulting in visible strain on the PZT and underlying substrate when etched to very thin residual Si. Such strain was thought to result in deleterious stresses in the PZT layer, thereby suppressing potential enhancements from the release of the Si substrate. A second electrode layout, consisting of a grid of circular electrodes of 500 μm diameter was deposited on set M4.1, allowing for direct macroscopic probing of the material situated on the thinned Si substrate.

11.4.5 Membranes 4.2 – Pt Top Electrodes, Heat Treated

Heat treatment of sputtered electrodes deposited via photolithography is often performed following the final photoresist liftoff step in order to improve adhesion and continuity between the top electrode and ferroelectric material. Set M4.2 was fabricated identically to set M4.1, with the addition of a 20 min heat treatment at 350 °C following top electrode deposition. While continuity of top electrodes in set M4.1 (and previous sets) did not pose any notable problems, it was expected that the heat treatment may effect residual stress effects in the material stack when the Si substrate is substantially thinned.

11.4.6 Membranes 4.3 – Cr/Au Top Electrodes, Heat Treated

While Pt top electrodes are typically selected for work with ferroelectric thin films and especially PZT, Cr/Au top electrodes are occasionally employed for compatibility with other materials in the intended application.[346,347] Cr/Au electrodes were expected to alter the residual stress state of the released PZT capacitors compared to Pt top electrodes after deep etching of the Si substrate. The samples in set M4.3 are identical to those deposited in M4.2, with the exception of 70 nm Cr and 140 Au sputtered top electrodes. Set M4.3 was also heat treated at 350 °C for 20 min following top electrode patterning and liftoff.

11.4.7 Functional Response Characterization Results

The results of dielectric, ferroelectric, and piezoelectric functional response characterization generally suggest complex interactions between the ferroelectric material, substrate clamping, and stress/strain relief resulting from the backside Si substrate release. Extreme enhancements to the electromechanical response are universally observed through all sets of samples with decreasing substrate thickness. On the other hand, dielectric and ferroelectric properties exhibit both mild enhancement and degradation trends as a function of substrate thickness, depending on the sample set. The results of AC dielectric, polarization, and DC piezoelectric/dielectric response characterization is shown in Table 11-2, Table 11-3, and Table 11-4, respectively. Lines have been fitted to the guide the eye regarding any respective trends in the data, as shown in Figure 11-5 (low-field dielectric), Figure 11-6 (dielectric Rayleigh coefficients), Figure 11-7 (extracted ferroelectric

responses, coercive field), and Figure 11-8 (DC electric field piezoelectric and dielectric responses).

Table 11-2 AC dielectric response at low field and Rayleigh parameters from the dielectric response at intermediate AC electric fields of the various sets of backside-etched PZT thin films. One standard deviation to one significant digit is reported for the error, and measurement values are reported to the same digit as the error.[172]

AC Dielectric		Low field ε_r	tan(δ)	ε_{init}	α (cm/kV)	$\alpha/\varepsilon_{init}$ (cm/kV)
M1	**300 µm**	1360 ± 40	0.017 ± 0.002	1480 ± 30	61 ± 4	0.042 ± 0.002
	254 µm	1380 ± 40	0.017 ± 0.002	1500 ± 50	67 ± 2	0.045 ± 0.002
	208 µm	1340 ± 53	0.017 ± 0.002	1420 ± 20	59 ± 1	0.0413 ± 0.0004
	155 µm	1280 ± 40	0.016 ± 0.002	1400 ± 50	60 ± 3	0.044 ± 0.003
	117 µm	1290 ± 60	0.018 ± 0.008	1440 ± 60	64 ± 2	0.0445 ± 0.0004
	71 µm	1350 ± 80	0.018 ± 0.005	1550 ± 20	59 ± 3	0.038 ± 0.002
	41 µm	1360 ± 40	0.018 ± 0.005	1490 ± 50	67 ± 3	0.045 ± 0.001
	25 µm	1290 ± 70	0.016 ± 0.002	1460 ± 50	64 ± 4	0.043 ± 0.004
	15 µm	1350 ± 40	0.016 ± 0.002	1470 ± 50	62 ± 3	0.042 ± 0.002
	3 µm	1560 ± 50	0.036 ± 0.004	1400 ± 100	62 ± 3	0.044 ± 0.005
	2 µm	1480 ± 60	0.035 ± 0.003	1180 ± 40	60 ± 10	0.053 ± 0.008
	2 µm	1500 ± 40	0.033 ± 0.004	1170 ± 80	70 ± 10	0.06 ± 0.01
	1 µm	1490 ± 90	0.035 ± 0.008	1400 ± 100	66 ± 8	0.047 ± 0.007
M2	**300 µm**	940 ± 50	0.04 ± 0.02	890 ± 40	14.6 ± 0.8	0.016 ± 0.001
	90 µm	900 ± 30	0.029 ± 0.005	870 ± 40	14.3 ± 0.6	0.016 ± 0.001
	10 µm	920 ± 30	0.030 ± 0 .004	880 ± 40	13 ± 2	0.015 ± 0.001
	1 µm	930 ± 40	0.03 ± 0 .01	910 ± 50	15 ± 2	0.017 ± 0.003
M3	**500 µm**	1070 ± 40	0.025 ± 0.002	1030 ± 40	16.8 ± 0.6	0.0164 ± 0.0006
	305 µm	1160 ± 42	0.032 ± 0.002	1060 ± 40	19.2 ± 0.7	0.0182 ± 0.0005
	229 µm	1160 ± 40	0.0030 ± 0.002	1080 ± 40	18.3 ± 0.9	0.017 ± 0.0005
	205 µm	1130 ± 40	0.031 ± 0.002	1060 ± 40	17.9 ± 0.8	0.0169 ± 0.0005
	50 µm	1140 ± 40	0.029 ± 0.002	1080 ± 40	16.9 ± 0.8	0.0157 ± 0.0004
	2 µm	1110 ± 30	0.026 ± 0.003	1070 ± 40	16 ± 1	0.015 ± 0.0008
M4.1	**500 µm**	1050 ± 10	0.023 ±0.001	1050 ± 30	19.9 ± 0.9	0.019 ± 0.001
	200 µm	1080 ± 30	0.027 ± 0.003	1080 ± 20	21.4 ± 0.8	0.020 ± 0.001
	90 µm	1090 ± 40	0.026 ± 0.003	1080 ± 20	20 ± 1	0.019 ± 0.001
	35 µm	1060 ± 30	0.025 ± 0.003	1070 ± 10	20 ± 1	0.019 ± 0.001
	10 µm	1060 ± 20	0.023 ± 0.001	1080 ± 20	19 ± 1	0.018 ± 0.001
	2 µm	1100 ± 50	0.027 ± 0.003	1100 ± 40	21 ± 1	0.019 ± 0.001
M4.2	**500 µm**	1270 ± 10	0.030 ± 0.001	1224 ± 2	31.9 ± 0.5	0.026 ± 0.001

	50 µm	1240 ± 20	0.035 ± 0.001	1250 ± 20	28 ± 3	0.023 ± 0.002
	5 µm	1190 ± 20	0.029 ± 0.002	1220 ± 40	30 ± 1	0.024 ± 0.002
M4.3	**500 µm**	760 ± 20	0.039 ± 0.003	764 ± 7	2.3 ± 0.1	0.0030 ± 0.0002
	50 µm	720 ± 20	0.034 ± 0.002	710 ± 30	2.2 ± 0.1	0.0031 ± 0.0001
	5 µm	710 ± 20	0.034 ± 0.004	724 ± 7	2.3 ± 0.2	0.0032 ± 0.0002

Table 11-3 Polarization response and extracted parameters from the backside-etched PZT thin films from the various sets of samples. One standard deviation to one significant digit is reported for the error, and measurement values are reported to the same digit as the error.[172]

Polarization		P_{sat} (µC/cm^2)	P_{rem} (µC/cm^2)	$\Delta P/2$ (µC/cm^2)	E_{C+} (kV/cm)	E_{C-} (kV/cm)	$E_{internal}$ (kV/cm)
M1	**300 µm**	33 ± 1	14.1 ± 0.8	0.2 ± 0.3	22 ± 2	-21 ± 2	0 ± 1
	254 µm	33 ± 1	13.9 ± 0.5	0.1 ± 0.1	20 ± 2	-23 ± 4	-1 ± 3
	208 µm	32.2 ± 0.4	13.6 ± 0.4	-0.1 ± 0.1	22.1 ± 0.3	-20 ± 2	1 ± 1
	155 µm	39 ± 2	18.0 ± 0.9	-0.42 ± 0.07	24 ± 1	-21 ± 2	1.7 ± 0.4
	117 µm	41 ± 2	19 ± 1	-0.5 ± 1	25 ± 1	-22 ± 2	1.4 ± 8
	71 µm	28.7 ± 0.7	11.3 ± 0.9	0.9 ± 0.3	17 ± 1	-21 ± 2	-2 ± 1
	41 µm	33 ± 2	14 ± 1	0.2 ± 0.3	20 ± 3	-22 ± 4	-1 ± 3
	25 µm	40 ± 5	20 ± 4	-0.2 ± 0.5	28 ± 5	-24 ± 3	2 ± 4
	15 µm	33 ± 2	13.9 ± 0.9	0.1 ± 0.3	23 ± 3	-22 ± 3	1 ± 2
	3 µm	33 ± 2	14 ± 1	0.2 ± 0.1	19 ± 2	-24 ± 3	-3 ± 2
	2 µm	40 ± 3	18 ± 2	-0.1 ± 0.2	23 ± 4	-24 ± 4	-1 ± 4
	2 µm	33 ± 2	14 ± 1	-0.1 ± 0.2	22 ± 3	-23 ± 3	0 ± 3
	1 µm	38 ± 2	17 ± 1	0 ± 0.3	20 ± 4	-27 ± 5	-3 ± 4
M2	**300 µm**	33 ± 1	15 ± 1	4.1 ± 0.2	21 ± 2	-49 ± 2	-14 ± 1
	90 µm	33 ± 1	17 ± 1	3.9 ± 0.2	26 ± 1	-54 ± 1	-14 ± 1
	10 µm	33 ± 2	16 ± 1	3.9 ± 0.3	25 ± 3	-58 ± 4	-17 ± 3
	1 µm	33 ± 1	15 ± 1	3.7 ± 0.3	24 ± 3	-57 ± 2	-17 ± 2
M3	**500 µm**	34 ± 1	16.1 ± 0.9	3.2 ± 0.2	28 ± 3	-50 ± 4	-11 ± 2
	305 µm	34 ± 1	15.8 ± 0.9	2.7 ± 0.2	33 ± 2	-48 ± 3	-7 ± 2
	229 µm	33 ± 1	15.1 ± 0.7	2.5 ± 0.1	34 ± 2	-46 ± 2	-6 ± 1
	205 µm	32 ± 1	14.3 ± 0.7	2.3 ± 0.1	34 ± 1	-46 ± 2	-6 ± 1
	50 µm	32 ± 1	14.2 ± 0.7	2.4 ± 0.2	33 ± 2	-45 ± 2	-6 ± 2
	2 µm	31 ± 1	13.0 ± 0.9	2.2 ± 0.2	33 ± 2	-44 ± 1	-6 ± 1
M4.1	**500 µm**	33.3 ± 0.6	16.4 ± 0.4	3.0 ± 0.4	28 ± 3	-46 ± 5	-9 ± 2
	200 µm	33.1 ± 0.6	15.8 ± 0.3	2.4 ± 0.4	33 ± 5	-41 ± 4	-4 ± 3
	90 µm	32.3 ± 0.6	14.9 ± 0.3	2.2 ± 0.4	33 ± 4	-41 ± 6	-4 ± 4
	35 µm	31.8 ± 0.5	14.3 ± 0.4	2.1 ± 0.4	33 ± 4	-41 ± 6	-4 ± 4

	10 µm	32 ± 1	14 ± 1	2.3 ± 0.4	31 ± 4	-43 ± 6	-6 ± 3
	2 µm	34 ± 2	16 ± 2	3.4 ± 0.6	32 ± 3	-45 ± 7	-7 ± 4
M4.2	**500 µm**	32.2 ± 0.2	14.6 ± 0.1	0.81 ± 0.07	27.5 ± 0.5	-31.2 ± 0.3	-1.8 ± 0.3
	50 µm	31.9 ± 0.1	13.4 ± 0.6	0.6 ± 0.3	28 ± 2	-27 ± 2	0.3 ± 2
	5 µm	31.5 ± 0.9	13.0 ± 0.7	0.27 ± 0.07	35 ± 3	-25.5 ± 0.8	5 ± 2
M4.3	**500 µm**	13.5 ± 0.2	0.70 ± 0.03	-0.23 ± 0.01	13.9 ± 0.4	-7.8 ± 0.3	3.1 ± 0.1
	50 µm	13.3 ± 0.6	0.47 ± 0.03	-0.28 ± 0.02	11.9 ± 0.4	-5.4 ± 0.3	3.3 ± 0.3
	5 µm	13.3 ± 0.3	0.91 ± 0.03	-0.25 ± 0.02	12.0 ± 0.3	-5.8 ± 0.3	3.1 ± 0.2

Table 11-4 DC electric field-dependent piezoelectric and % dielectric tunability response. One standard deviation to one significant digit is reported for the error, and measurement values are reported to the same digit as the error.[172]

DC Piezoelectric/Dielectric		$d_{33,f,max}$ **(pm/V)**	*% dielectric tunability*
M1	**300 µm**	130 ± 20	74.2 ± 0.5
	254 µm	110 ± 20	76 ± 2
	208 µm	120 ± 3	73.8 ± 0.7
	155 µm	120 ± 40	74.1 ± 0.1
	117 µm	170 ± 80	74.9 ± 0.3
	71 µm	300 ± 100	73.8 ± 0.3
	41 µm	500 ± 200	75.2 ± 0.5
	25 µm	800 ± 400	77 ± 3
	15 µm	5000 ± 3000	74 ± 1
	3 µm	5000 ± 3000	79 ± 6
	2 µm	3000 ± 2000	75.8 ± 0.7
	2 µm	3000 ± 1000	73.7 ± 0.8
	1 µm	3000 ± 2000	80 ± 7
M2	**300 µm**	90 ± 10	69 ± 1
	90 µm	112 ± 8	
	10 µm	400 ± 200	69 ± 1
	1 µm	4000 ± 3000	
M3	**500 µm**	100 ± 20	63.2 ± 0.2
	305 µm	110 ± 20	62 ± 2
	229 µm	120 ± 10	60.6 ± 0.6
	205 µm	120 ± 20	60.2 ± 0.7
	50 µm	280 ± 140	58.9 ± 0.2
	2 µm	3000 ± 2000	58 ± 1
M4.1	**500 µm**	86 ± 4	64.0 ± 0.5

	200 µm	114 ± 4	63.6 ± 0.3
	90 µm	120 ± 50	62.4 ± 0.3
	35 µm	500 ± 200	61.3 ± 0.3
	10 µm	4000 ± 4000	61 ± 1
	2 µm	5000 ± 2000	62 ± 2
M4.2	**500 µm**	90 ± 10	66.4 ± 0.2
	50 µm	220 ± 20	65.1 ± 0.7
	5 µm	4000 ± 3000	64.5 ± 0.9
M4.3	**500 µm**	17.7 ± 0.3	40 ± 3
	50 µm	17.8 ± 0.4	50 ± 30
	5 µm	18.4 ± 0.5	400 ± 300

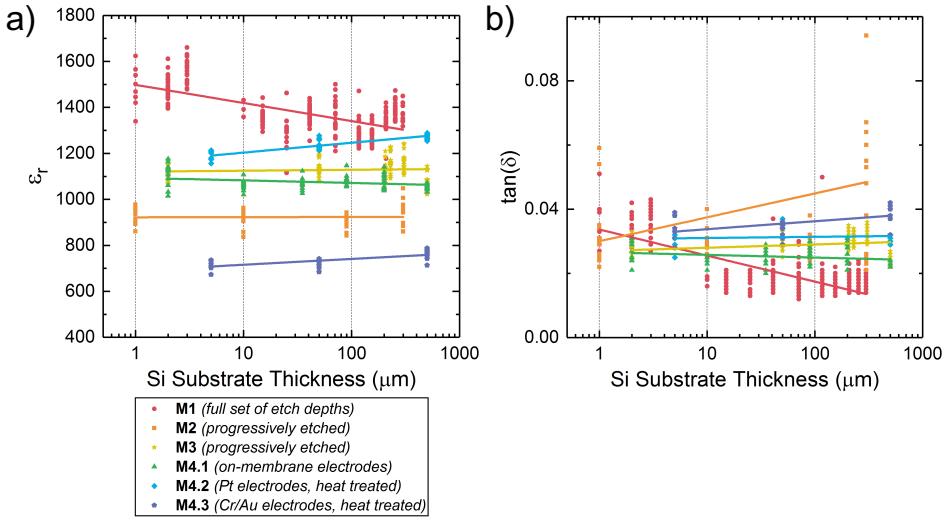

Figure 11-5 Trends in low field (a) dielectric permittivity (ε_r) and (b) dielectric loss tangent (*tan(δ)*) for all sets of membrane-line samples as a function of Si substrate thickness. Lines have been added to guide the eye.

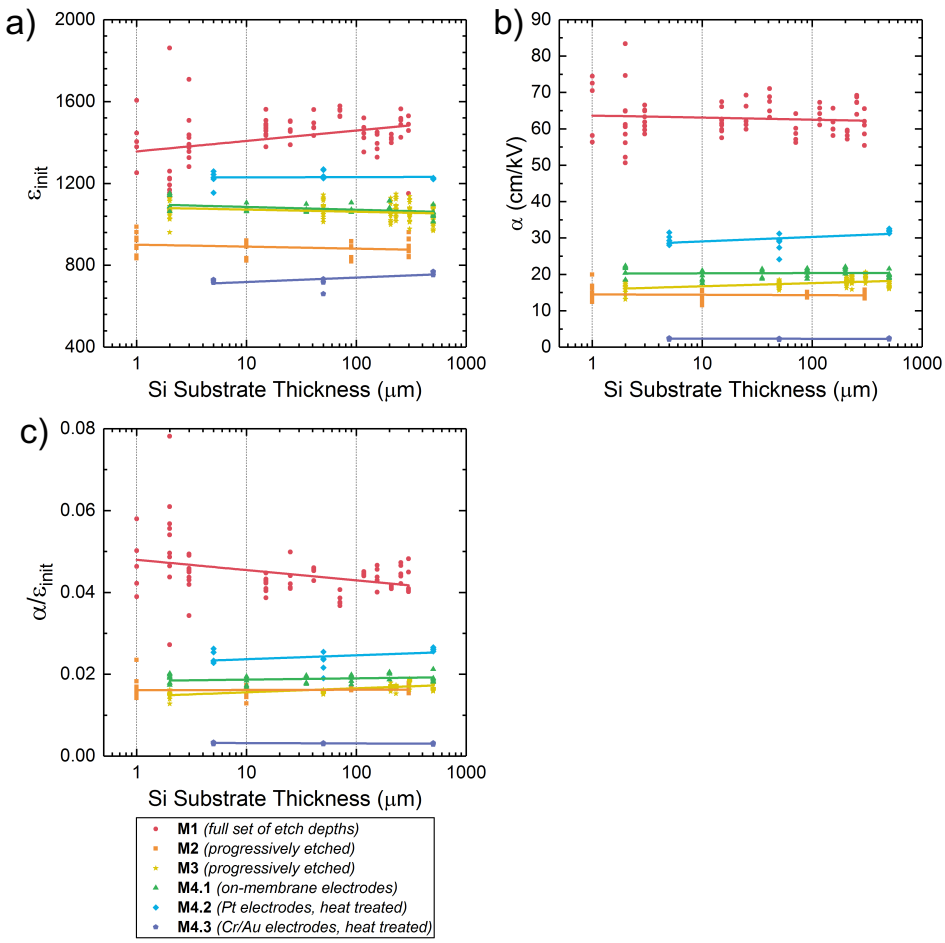

Figure 11-6 Trends in the extracted (a) reversible (ε_{init}), (b) irreversible (α), and (c) irreversible/reversible ratio ($\alpha/\varepsilon_{init}$) from the Rayleigh analysis of the AC electric field dielectric response.

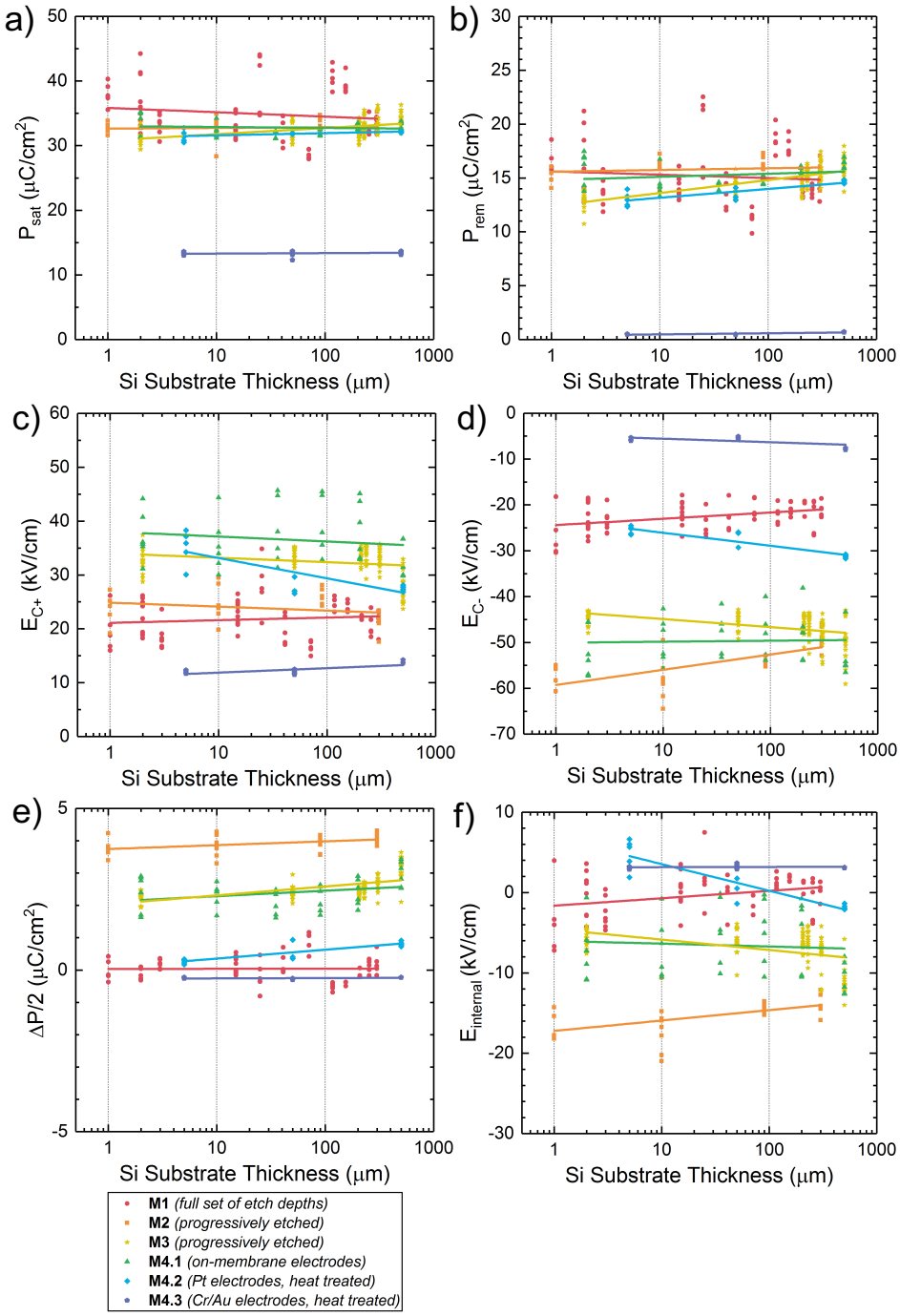

Figure 11-7 Plots of (a) saturated polarization (P_{sat}), (b) remanent polarization (P_{rem}), and (c) the vertical shift in polarization. Trends in the coercive field (d) E_{C+}, (e) E_{C-}, and (f) the internal bias in the horizontal electric field direction, $E_{internal}$, are shown.

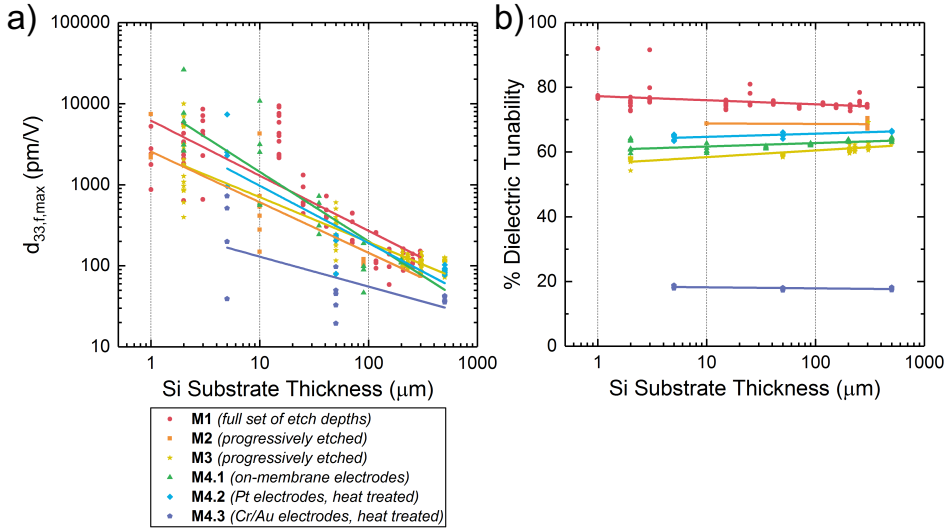

Figure 11-8 Plotted trends in the DC electric field piezoelectric and dielectric response. Shown is (a) the maximum measured value of the effective, converse, longitudinal piezoelectric coefficient, $d_{33,f,max}$, and (b) the % dielectric tunability. Note that $d_{33,f,max}$ is plotted on a log-log scale to show the large variation with Si substrate thickness. The maximum of the $d_{33,f}$ response is used due to the extreme nonlinearity in the piezoelectric-DC field curves, and resulting difficulting in extracting a reliable remanent or saturated value of the response (see Figure 11-10).

The plotted results of functional response characterization demonstrate mixed results of the dielectric and ferroelectric responses. The low-field dielectric permittivity (ε_r) and loss tangent ($tan(\delta)$) generally show flat or decreasing trends with decreasing thickness of the Si substrate, with the exception of set M1, which shows a potential correlation of reduced substrate thickness to an increase in both ε_r and $tan(\delta)$ (Figure 11-5). Such enhancements potentially indicate increases in domain wall mobility in those samples.[24] However, because of the method in which the etching/measurements of set M1 were carried out (*i.e.*, separate samples at discrete etch depths and accompanying variability from whole-wafer processing), the results are subject to some degree of error.

Trends in the extracted coefficients of the Rayleigh response are also inconclusive, with no significant changes in response with decreasing Si thickness (Figure 11-6). One

exception appears to be the measurements of ε_{init} for set M1, which shows a slight decreasing trend, but this result is, again, potentially affected by the error introduced by sample variability. This slight decrease in ε_{init}, coupled with the relatively flat trend for α results in a slightly increasing trend with decreasing Si thickness for the Rayleigh ratio, $\alpha/\varepsilon_{init}$. Increases to $\alpha/\varepsilon_{init}$ are often indicative of increased extrinsic contributions to the dielectric response, and potentially indicate increased domain wall motion.

Generally flat trends are noted for the polarization properties (P_{sat}, P_{rem}) as a function of Si substrate thickness, with a small shift in the vertical offset of P_{rem} noted in sample sets M3, M4.1, and M4.2 (Figure 11-7b, c). A vertical shift in the polarization potentially indicates strong preferential polarization directions in the samples.[58] Generally, this shift appears to relax with decreasing Si thickness, possibly due to the effects of evolving residual stresses that generate changes in the polarization behavior. Erratic trends in the coercive fields are observed, both positive (E_{C+}) and negative (E_{C-}), with substantial variations in the observed internal bias ($E_{internal}$), both within each individual set of samples and across multiple sets of samples (Figure 11-7d, e, f)

Notably, the electromechanical response universally increases with decreasing Si substrate thickness. Due to the nonlinearity in the piezoelectric-DC field curves, consistent extraction of the saturation and remanent values ($d_{33,f,sat}$ and $d_{33,f,rem}$, respectively) proved impractical, and the maximum value ($d_{33,f,max}$) of the response was plotted (Figure 11-8a). The results indicate extraordinary enhancements to the electromechanical response of the material stack, with up to two orders of magnitude increase in displacement per applied voltage. Due to the lack of observed enhancements to dielectric and ferroelectric responses corresponding to these changes in electromechanical response, these giant

electromechanical couplings are certainly due to substrate bending resulting from the design of the material stack.

The plotted and tabulated trends allow for a global view of the effects of progressively releasing the PZT thin film from the Si substrate, but does not allow for local analysis. The behavior of a biaxially-stressed Si membrane subjected to nonlinear residual stresses, variations in etch rate, electrode-induced stresses, *etc.* is a complex mechanical structure, and functional response measurements at different locations on the membrane inevitably demonstrate local deviations from the mean response. Figure 11-9, Figure 11-10, and Figure 11-11 demonstrate selected functional response curves and measurements to demonstrate these local variations.

Figure 11-9 illustrates the difficulty in interpreting the data from global trends with residual Si thickness and the complexity of the interaction between the ferroelectric, substrate, and resulting effects on individual functional responses. Remanent and saturation polarizations are reduced in the film with 2 μm Si, and switching occurs at lower voltage (E_{C+}). On the other hand, decreasing the thickness of the Si substrate from 25 to 2 μm results in minor enhancements of the AC electric field dielectric response for measurements taken on the same electrode in direct succession

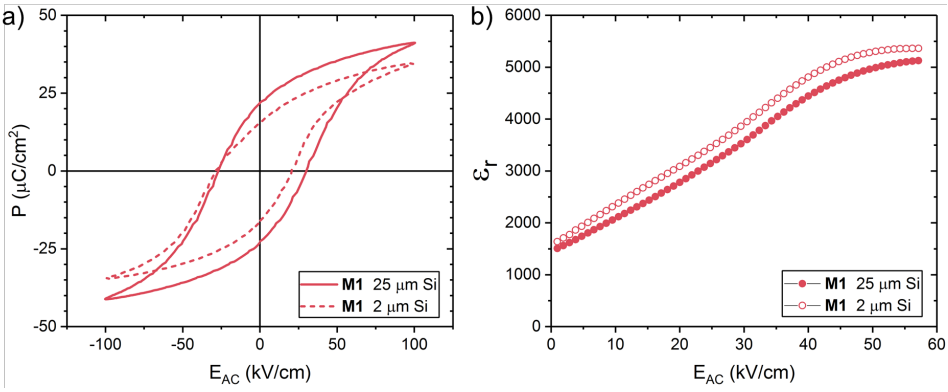

Figure 11-9 (a) *P-E* hysteresis loops and (b) AC electric field dielectric response from sample set M1 at approximately 25 μm and 2 μm Si substrate thickness. While the initial set of M1 samples were all prepared individually and measured separately, several of the samples that showed high functional response were re-etched to thinner Si. The loops shown here are on the same electrode and sample, etched to different depths.

Examination of the ferroelectric, dielectric, and piezoelectric response curves from sample M4.1 at selected etch depths further demonstrates the complexity of releasing the PZT film from the substrate (Figure 11-10). The ferroelectric and dielectric responses show non-trivial reductions when etching from 500 μm to 10 μm thickness, but subsequent enhancements when etching deeper to 2 μm Si thickness (Figure 11-10a, b, d). Distinct behavior is observed in the plots of $d_{33,f,max}$, where saturation of the curve does not result in a steady value for the sample etched to 2 μm Si thickness. This effect was quite common throughout all samples, making interpretation of any commonly-used piezoelectric response parameters (*e.g.*, $d_{33,f,sat}$ and $d_{33,f,rem}$) difficult.

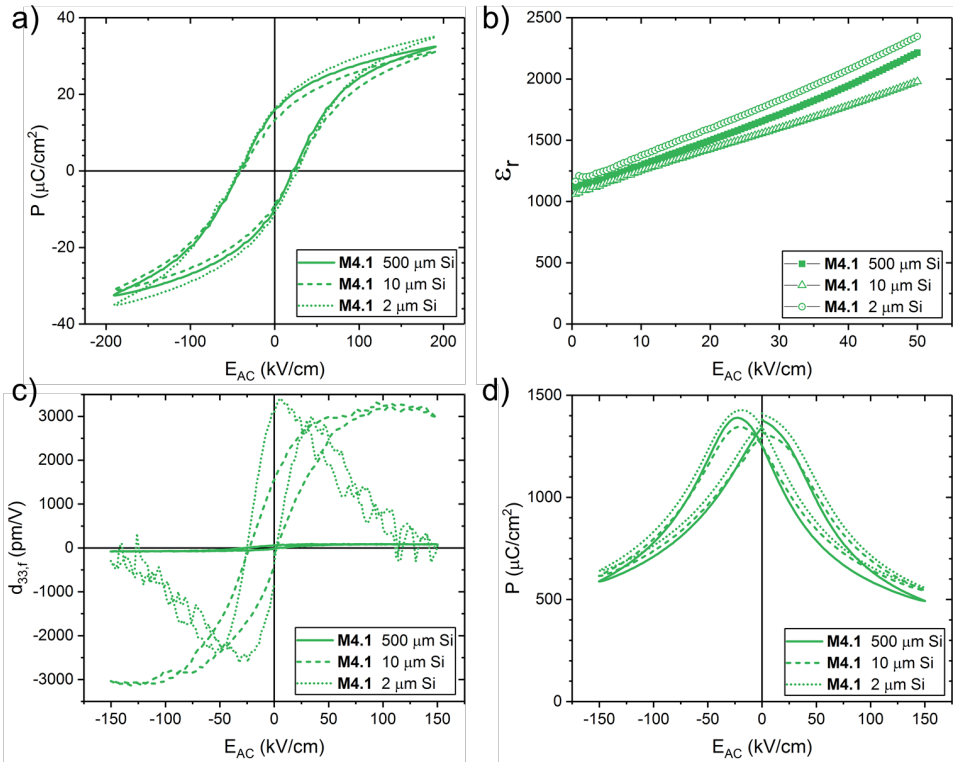

Figure 11-10 Selected (a) *P-E* hysteresis curves, (b) AC dielectric permittivity, (c) DC piezoelectric response, and (d) DC dielectric response from sample M4.1. Generally, the curves tend to show degradation when reduced from 500 to 10 μm Si substrate thickness, but subsequently demonstrate favorable inceases at 2 μm substrate thickness

Comparison of the *P-E* hysteresis loops at increasing AC electric field for an off-membrane (500 μm Si thickness) and on-membrane, completely released (0 μm Si thickness) shows an electric field-dependent interaction of the ferroelectric response. The released electrode shows superior values of saturated and remanent polarization up to 300 kV/cm, but polarization response is substantially lower at 400 kV/cm with respect to the off-membrane electrode, suggesting that applied electric field (and associated material deformation) may alter the degree of stress in the released PZT capacitors and subsequently modify the functional properties.

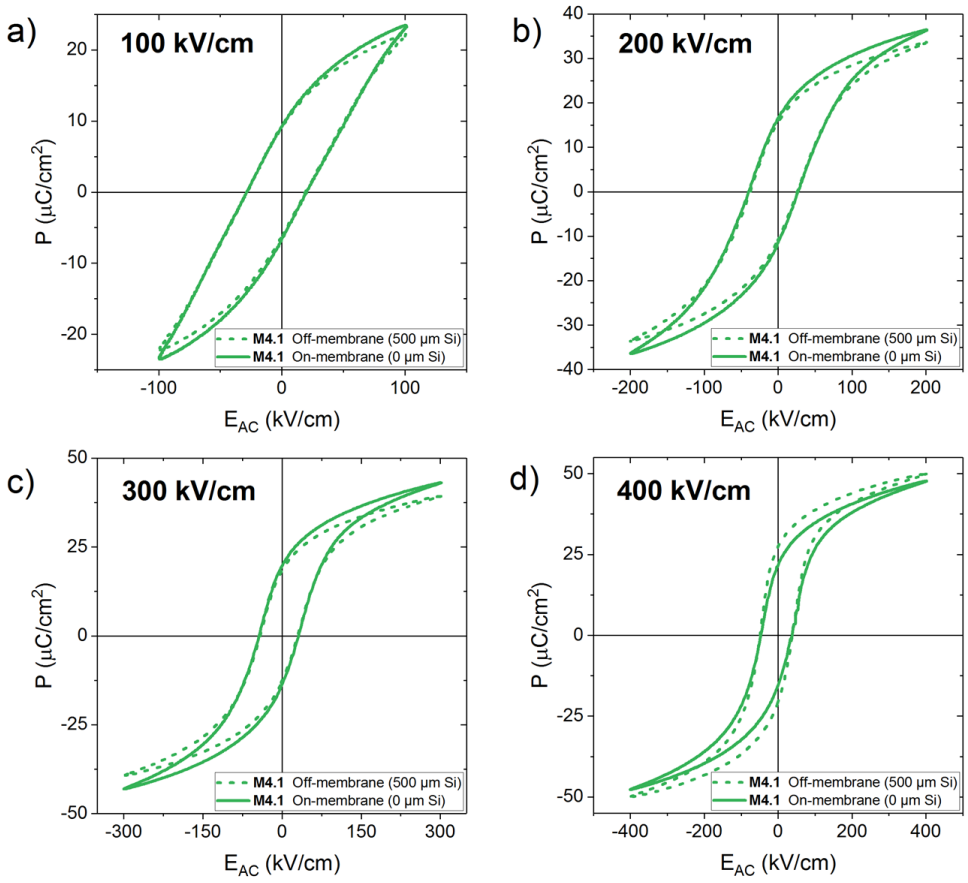

Figure 11-11 *P-E* loops at progressively higher applied AC electric field on and off a fully released (0 μm Si) PZT thin film from set M4.1. The fully released electrode shows superior polarization properties at all fields except 400 kV/cm, where it is eclipsed by the off-membrane electrode.

Finally, plots of the total displacement of the measured electrode as a function of applied AC electric field are shown in Figure 11-12. The plots demonstrate the highly nonlinear nature of the displacement of the membrane with applied electric field. Notably, at approximately 50 μm residual Si thickness, significant increases to the displacement begin to occur, and at very low levels of residual Si (< 5 μm), enormous nonlinearities are observed. The direction of displacement is highly reversible, likely due to residual stress interacting with induced displacement of what is essentially a bi-stable mechanism. The

displacement plots are beneficial for identifying the relative critical thickness of Si for onset of highly nonlinear displacement (see Figure 11-12b and Figure 11-12c).

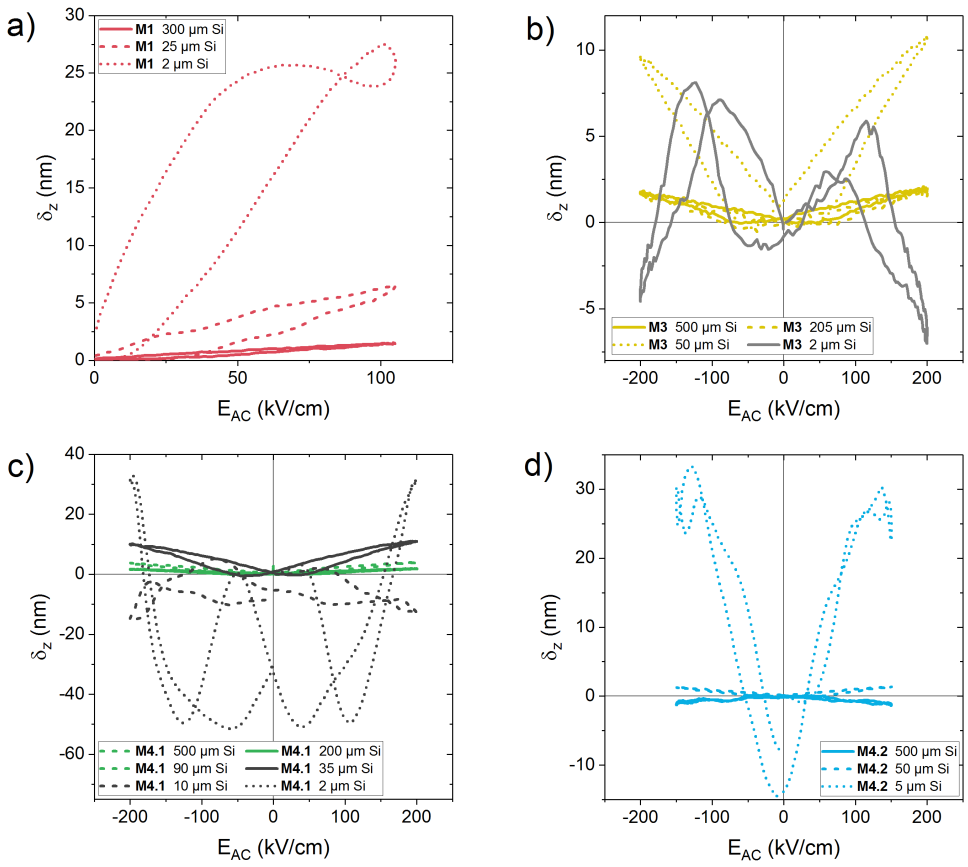

Figure 11-12 Plots of the measured displacement of the probed electrode as a function of applied AC electric field.

11.4.8 Non-contact Interferometric Strain Estimation

During fabrication and testing, two distinct stress/strain effects were noted: (i) the 1 cm^2 membrane experienced significant bowing and deflection in most samples, especially those with the remote electrode layout (Figure 11-4), and (ii) at very thin residual Si, the top electrodes also resulted in significant local deflection of the membrane (Figure

11-2). Precise determination of only one of these effects in isolation would be a non-trivial task, but the two compounded together results in a highly-complex interaction that changes with Si thickness, heating/fabrication conditions, electrode thickness, film thickness, uniformity of films, etching, *etc.* Non-contact, white-light interferometry and a simplified model can be used to estimate the maximum potential strain, assuming that the bowed film/membrane stack is strained (and not exhibiting relaxation thereof). Results of the non-contact interferometry on the backside of samples from sets M3 and M4.1 are shown in Figure 11-13. Large deflections due to the residual stresses are created by the patterned top electrode contact: up to 14 μm on sample M3 across a 1000 μm diameter electrode. These results can be used with various analytical formulations to estimate the stress in the thin film material structure.

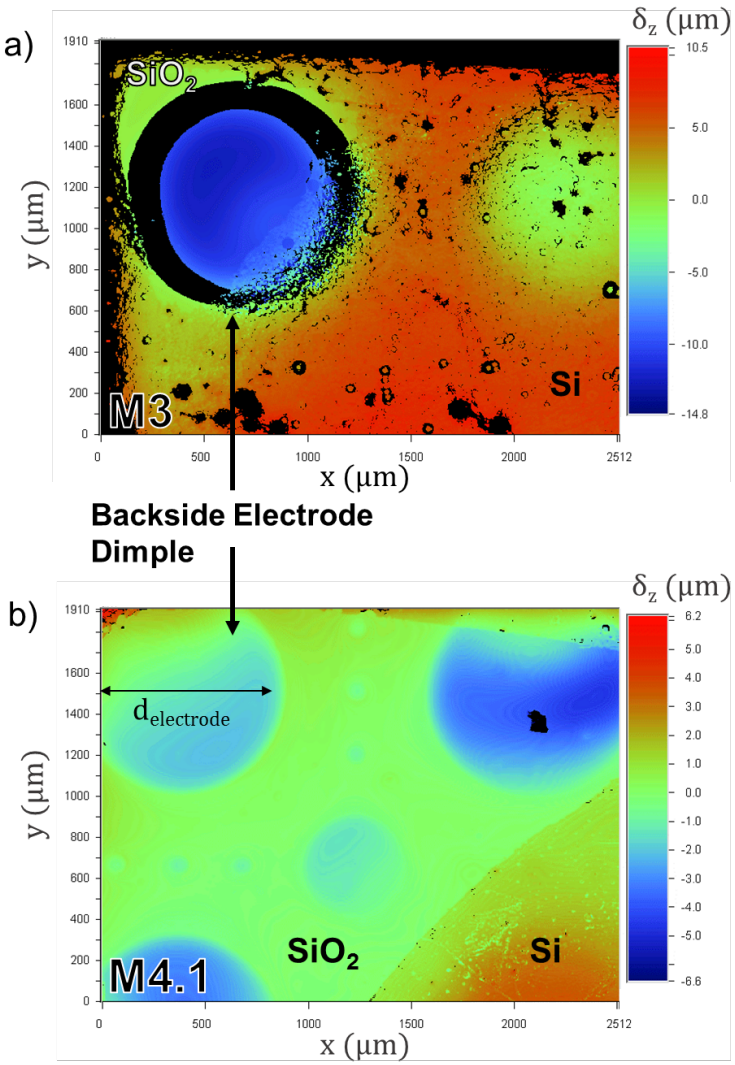

Figure 11-13 Relative height images from non-contact interferometry measurements on samples from set (a) M3 and (b) M4.1. Baseline displacement has been set to 0 at the SiO_2 layer. Notable is a maximum deflection of up to 14 µm for sample M3, across an electrode of 1000 µm diameter

11.4.9 Strain Estimation at Electrodes Using the Stoney Formula

The Stoney formula, initially published in the early 1900's to describe metallic films deposited via electrolysis, has been adopted for extensive use in thin film analysis for

microelectronics processes to describe residual stress developed in a thin film of uniform thickness on a relatively thick substrate of uniform thickness, both with the same radius of curvature.[319-322] Specific assumptions and criteria are discussed elsewhere.[320] The relatively similar thicknesses of the film layers present in the released PZT material stack here (Figure 11-14b) are not ideal for Stoney formula, but it serves as a first approximation.

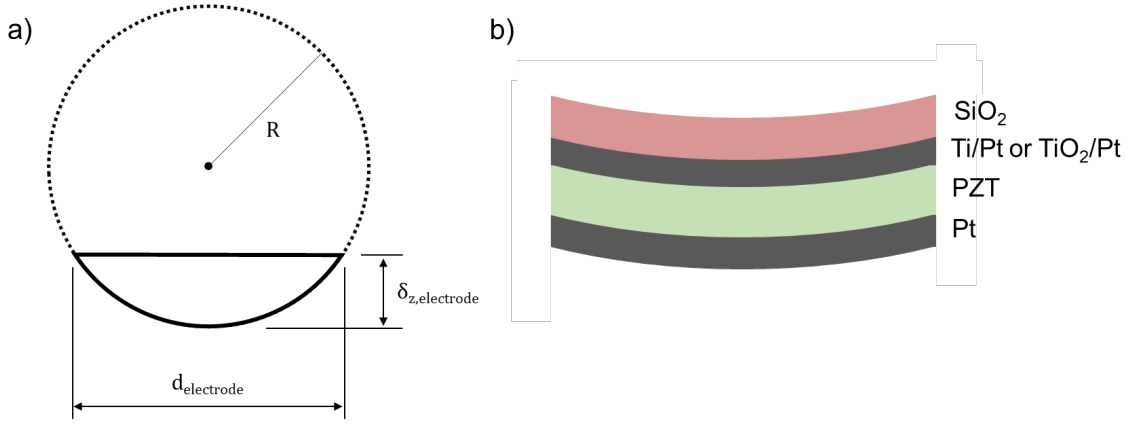

Figure 11-14 (a) Schematic of electrode deflection for estimating the radius of curvature for use in the Stoney formula. (b) Illustration of the released electrode and exaggerated curvature due to the local stress in the material stack.

We can employ the approximation shown in Figure 11-14a that shows the electrode diameter and maximum deflection, and assume that the resulting shape is approximately spherical in 3D, or circular in 2D across the diameter, and corresponds to the maximum deflection. We can estimate the radius of curvature, R, using the geometric expression

$$R = \frac{\delta_{z,electrode}}{2} + \frac{d_{electrode}^2}{8\delta_{z,electrode}} \qquad 11\text{-}1$$

where $\delta_{z,electrode}$ is the maximum deflection across the electrode and $d_{electrode}$ is the electrode diameter. The Stoney formula estimates the stress in the thin film, σ_{PZT}, given by

$$\sigma_{PZT} = \frac{E_{y,s} d_s^2}{6 d_{PZT} R (1 - \nu_s)} \qquad 11\text{-}2$$

where $E_{y,s}$ is Young's modulus of the substrate, d_s and d_{PZT} are the thicknesses of the substrate and the PZT layer, respectively, R is the radius of curvature, and ν_s is Poisson's ratio of the substrate. For this approximation, we will assume that the composite layer consisting of the SiO_2 elastic layer and the Ti/Pt (or TiO_2/Pt) bottom electrode serves as the substrate. The composite modulus of the SiO_2 and Ti/Pt (or TiO_2/Pt) bottom electrode is estimated using a formula derived from the rule of mixtures:[326]

$$E_{y,stack} d_{stack} = E_{y,SiO_2} d_{SiO_2} + E_{y,Ti} d_{Ti} + E_{y,Pt} d_{Pt} \qquad 11\text{-}3$$

where E_y is Young's modulus and d the thickness of each respective material in the stack. The composite Poisson's ratio is estimated using a volumetric mean of the constituent layers, which translates to thickness for the equal areas (top electrode area) used here. Table 11-5 shows the mechanical properties of each of the materials used in the stack for computation, taken from work by Yagnamurthy *et al.* on the mechanical properties of PZT thin film stacks. Data for ν is estimated using material properties from the literature.

Table 11-5 Mechanical properties of materials used in the ferroelectric thin film material stack.[326,348,349] An asterisk (*) next to the value of *v* indicates that the value has been estimated from extrapolation of the value using a weighted mean based on the thickness and *v* of each individual layer.

Material	E_y (GPa)	v
Si	169	0.064
SiO_2	72	0.2
SiO_2-TiPt	88	0.24*
SiO_2-TiPt-PZT	88	0.22*
SiO_2-TiPt-PZT-Pt	94	0.23*
Pt	182	0.41
PZT	84	0.3

Using the data from Table 11-5 in conjunction with Expression 11-2, the values for film thicknesses in Table 11-1, and interferometry measurements on sample M3, the maximum stress as estimated by the Stoney formula using a 14 μm deflection is approximately 1 MPa. Again, it is worth noting that the Stoney formula is primarily valid for thin films on thick substrates, at a large distance from the neutral axis of the membrane under bending. In the structure shown in Figure 11-13a, the neutral axis is located in the PZT layer (d_{PZT} = 800 nm, $d_{SiO2,Ti,Pt}$ = 635 nm), and likely results in small maximum potential stresses in the PZT layer for this reason. Also worth noting is the fact that the deflection of the structure when released does not necessarily indicate that all components in the stack are in a stressed state – relaxation of residual stresses may result in deflection of the structure in order to minimize local stresses. A detailed analysis using finite element analysis (FEA) or the Kirchoff-Love equations for clamped circular plates could be undertaken; solutions for the equations are non-trivial, and best left for future work.[350]

11.4.10 Estimation of Strain in Membrane with Linear Elastic Theory

The maximum static deflection measured in the membranes was 100-500 μm at the center for membranes with less than 5 μm of residual Si substrate, and typically bowed upwards out of the film surface, suggesting a tensile strain in the film. Simple linear elastic theory of a clamped membrane can be used to estimate the strain at the center and top surface of the PZT film on the membrane. The strain, $\epsilon_{xx} = \epsilon_{yy}$ is given by

$$\epsilon_{xx} = \epsilon_{yy} = -\frac{pdr^2}{32D}, W = -\frac{pr^4}{64D}, D = \frac{t^3 E_{Si}}{12(1-\nu_{Si}^2)} \qquad 11\text{-}4$$

where p, d, r and D are the applied differential pressure, thickness, radius, and flexural rigidity of the membrane structure, respectively. E_{Si} and ν_{Si} are Young's modulus and Poisson's ratio of the Si substrate. W is the maximum deflection at the membrane center. Due to the fact that the onset of membrane bowing and deflection began at roughly 20 μm of Si thickness, the flexural rigidity of the much thinner ~1 μm PZT film is neglected. Thus, the resulting biaxial stress at the PZT film can be calculated using the plane stress state:

$$\sigma_{xx} = \sigma_{yy} = \frac{E_{PZT}}{1-\nu_{PZT}^2}\left(\epsilon_{xx} + \nu\epsilon_{yy}\right) \qquad 11\text{-}5$$

An effective radius, r, can be estimated by equating the area of 1 cm^2 square membrane to a circular plate, and solving for r. Using r; the maximum displacement of the membrane, W; and the flexural rigidity of Si, we can solve for $\epsilon_{xx} = \epsilon_{yy}$, insert the result into expression 11-5, arriving at an estimate for the maximum stress in the membrane. For a residual Si thickness of 5 μm and maximum deflection of 500 μm, this yields an estimate of

approximately 80 MPa of tensile stress across the surface of the membrane (in the PZT layer). True stresses in the structure and PZT film are potentially lower, if the deflection occurs in order to relieve heat-related residual stress originating during fabrication.

11.4.11 Piezoresponse Force Microscopy Results

The complex stress/strain interaction between the thinned Si substrate, PZT thin film, and top electrode contacts makes macroscopic measurements of the functional response through the top electrode contacts difficult to interpret. Probing the local, microscopic ferroelectric response via piezoresponse force microscopy (PFM) allows for a more unadulterated view of material response by bypassing the top electrode and accompanying effects on local strain. The topographical height and amplitude/phase of the piezoresponse are shown in Figure 11-15. Domain structures are visible in the amplitude and phase plots. The on-membrane scan shows a qualitatively greater proportion of the material with a large piezoresponse phase, potentially indicating increased polarization alignment normal to the surface in on-membrane regions, due to the release from the substrate. Height scans appear to show some cracking in both regions of the film.

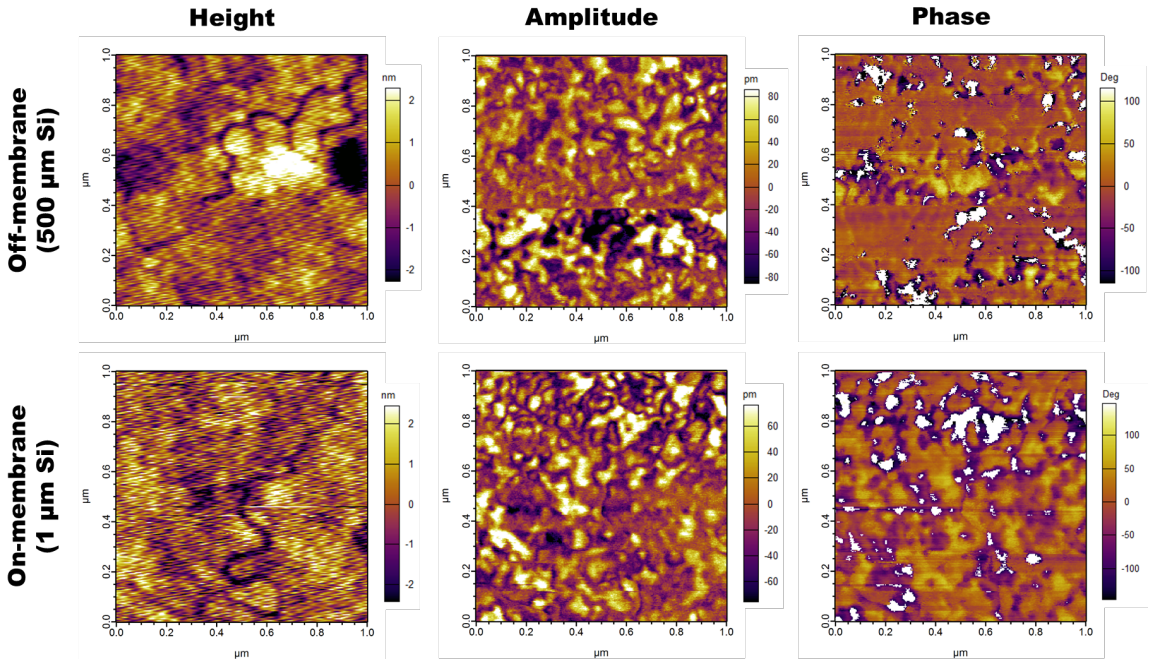

Figure 11-15 Height retrace and amplitude/phase of the piezoresponse for off- and on-membrane regions of the membrane from sample M4.1. Domain structures are visible in the amplitude/phase of the piezoresponse.

Switching spectroscopy measurements (SS-PFM) were performed on selected regions of the scans shown in Figure 11-15. SS-PFM probes the local hysteretic strain, using the conductive probe tip as the "top electrode" and continuous Pt bottom electrode. Nested hysteresis loops at 2 V increments from the SS-PFM measurements are shown in Figure 11-16. The on-membrane released loops show stronger development at lower applied voltages, reduced switching voltages, and greater amplitude of the piezoresponse. These results, especially the switching voltage, apparently contradict the results of the macroscopic measurements of the coercive fields, which are stable across the range of membrane thickness. The local PFM switching spectroscopy results suggest that the top electrodes strongly influence the stress state of the PZT thin film, counteracting the release of the ferroelectric from the substrate and negatively affecting the functional response.

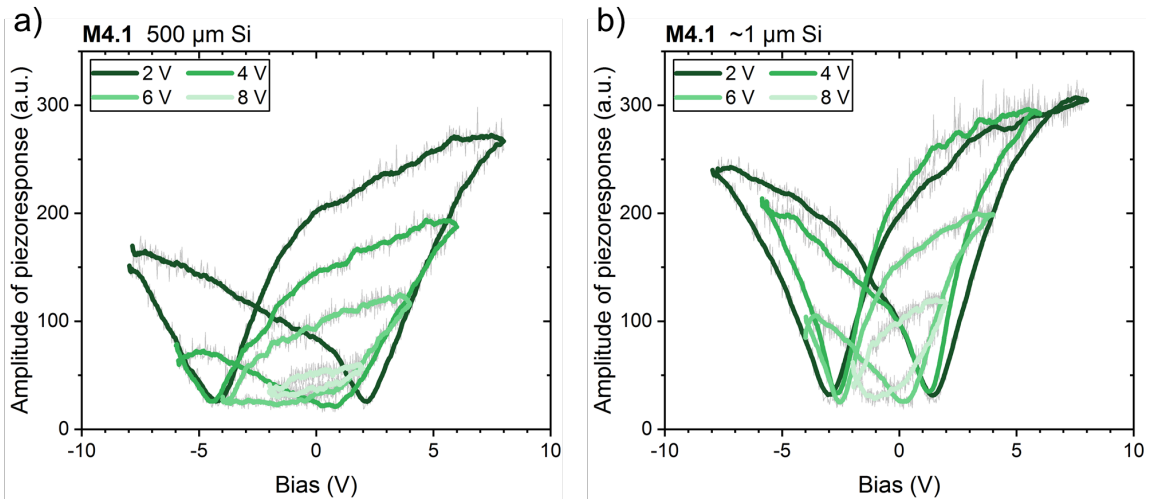

Figure 11-16 Switching spectroscopy piezoresponse force microscopy (SS-PFM) measurements on (a) off-membrane and (b) on-membrane locations. Nested butterfly loops are shown, at 2 V increments. Raw data is shown in light gray, and has been smoothed with an adjacent-point averaging filter for better visualization.

11.4.12 Scanning Transmission Electron Microscopy Results

The results of cross-sectional scanning transmission electron microscopy (STEM) show highly-columnar grains throughout the sample, and crystallization interfaces are visible as horizontal lines (Figure 11-17). The goal of performing STEM was to observe any potential changes in grain/domain microstructure in the films, especially near the interface with the bottom electrode, when released from the Si substrate. However, minimal variation in microstructure is observed. Future TEM work, such as nanobeam diffraction to effectively resolve the strain gradient across the films' cross section is ideal for ongoing studies, and is discussed in future work (CHAPTER 12).[351]

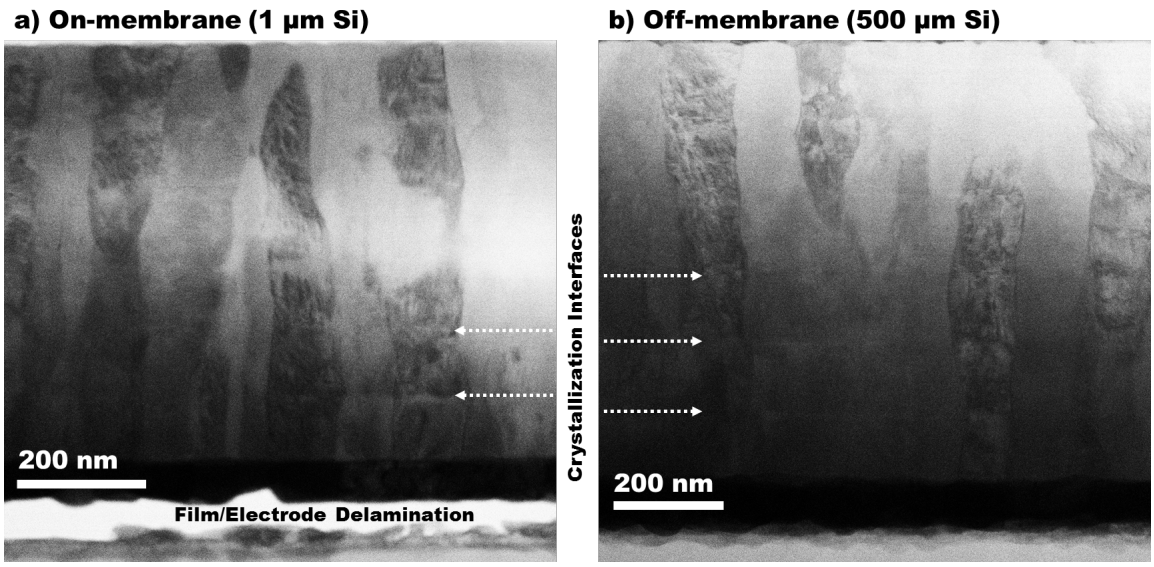

Figure 11-17 Scanning transmission electron microscopy (STEM) images of (a) on-membrane (~1 µm residual Si) and (b) off-membrane (500 µm Si substrate) from sample set M1. Dotted arrows indicate crystallization interfaces, consisting of three individual layers of 0.4M PZT. Delamination of the PZT and bottom electrode contact from the SiO_2 elastic layer occurred at some point during testing or STEM sample preparation for the on-membrane sample (a).

11.5 Discussion and Conclusion

Progressively releasing PZT thin films from the Si substrate via selective backside etching of the material stack demonstrates the complex interactions of residual stress through the material stack – results are difficult to decisively interpret. The enormous increases to the electromechanical response exhibited by the released PZT thin films represent a unique engineering approach to maximizing displacement for MEMS-related applications. Maximum electromechanical couplings on the order of 3 to 8 nm/V exceed the best thick film and bulk reports by at least one order of magnitude,[35,352] and could be leveraged as a relatively simple and effective means to enhance electromechanical response

for applications where thin films are already being implemented. The fragile nature of *fully-released* PZT thin films (0 μm Si) makes them impractical for many applications, but the electromechanical response is approximately doubled at 100 μm membrane thickness, and one order of magnitude increases are observed at approximately 10 μm Si thickness. Anecdotally, membranes from 10 to 100 μm were still quite robust during testing and transportation, and would likely be appropriate for implementation in low-stress/low-impact environments.

The multi-component material stack results in a more complex interaction of residual stresses than originally hypothesized. This point is clear from the plotted functional response curves. Apparent contradictions between ferroelectric and dielectric response enhancements (Figure 11-9), nonlinear enhancement/degradation trends with increasing etch depth (Figure 11-10), and electric field-dependent changes in ferroelectric behavior (Figure 11-11) all highlight the multifaceted interaction of stress, substrate clamping, and functional response. At various Si etch depths, especially approaching < 10 μm residual Si, the stress state is likely very nonlinear and varies with only minor additional etching. This interaction is demonstrated in Figure 11-10, where deleterious stresses at 10 μm Si result in property degradation, but are overcome by further releasing of the substrate to 2 μm Si. The apparent field dependence of ferroelectric properties in Figure 11-11 are most likely related to increased deflection and dynamic stress effects with increasing applied electric field in the on-membrane, fully-released capacitor – large deflections at elevated electric field yield additional stresses that supersede any previous enhancements derived from the lack of substrate clamping.

Finally, large bowing and warpage of the membrane structure with very thin residual Si were further complicated by the stresses created in the top electrode contacts. Yagnamurthy *et al.* showed that a significant portion of the residual stress in similarly-processed PZT material stacks originated in the Ti/Pt electrodes – over 500 MPa compared to 30 to 70 MPa for all other components.[326] When the upper film stack is released from the Si substrate, all remaining components (elastic layer, bottom electrode, PZT, top electrode) are within approximately one order of magnitude of thickness from one another, and the Ti/Pt bottom electrode likely dominates the clamping of PZT thin films. The curvature of the electrodes after release is consistent with the tensile stress indicated by Yagnamurthy *et al.*, but due to the location of the PZT layer near the neutral axis of the released structure, it is probable that it experiences only small fluctuations in stress, thus explaining the relatively small variation in functional properties. On the ther hand, clamping by the top electrode prevents complete release of the film for macroscopic functional response measurements – it is always constrained by at least one component of the material stack between which it is sandwiched. This hypothesis is supported by the PFM results of the local ferroelectric response, indicating reduced switching voltages, more highly-developed butterfly loops, and greater piezoresponse for regions of released PZT compared to clamped regions. Further investigation in future work of different substrates, elastic layers, heat treatments, film thicknesses, and electrode types must be undertaken in order to fully elucidate the nature of competing stresses and the interaction with substrate and top electrode clamping.

CHAPTER 12. CONCLUSIONS AND FUTURE WORK

In this chapter, the principal findings of this thesis are summarized and the major impacts are discussed. Potential directions for future undertakings and experiments that will expand the present studies are offered.

12.1 Summary and Conclusions

The continuous development and innovation of modern microelectronics devices have, in recent years, been met with increasingly rigorous functional and operational requirements for new applications and environments. The need for enhanced response, miniaturized devices, lower power, increased robustness, and full process integration have substantively driven the optimization of functional materials employed for sensing, actuation, transduction, energy harvesting, and a variety of other functionalities. Multifunctional ferroelectric oxides – boasting large dielectric, polarization, and piezoelectric responses – have assumed a crucial role in applications ranging from MEMS sensors and actuators to medical ultrasound devices, to ferroelectric memory devices and passive environmental energy harvesting.[1] However, with the increasing prevalence of satellites for telecommunications, alternative nuclear energy, and even space travel, the radiation tolerance of devices for such applications and the materials that drive them has become a critical concern.[40,353] The work in this thesis has taken a multifaceted approach to elucidating the fundamental interactions of ionizing radiation with ferroelectric materials and various interfaces in the material stack, identifying the principal causes for radiation-induced degradation of dielectric and ferroelectric functional responses. The augmented understanding of these fundamental mechanisms that govern ferroelectric thin films and their interaction with radiation is leveraged to develop practical knowledge for the design of higher-performance material stacks and devices. This is accomplished by implementing methods for mitigating radiation-induced damage, even at very high levels of ionizing gamma radiation. Such knowledge helps to address the performance of radiation-tolerant ferroelectric material stacks for use in microelectronics and MEMS devices.

Specifically, the investigations of radiation tolerance in thin film ferroelectric material stacks attempt to build on the scattered previous knowledge in the field. Multiple studies have demonstrated degradation of functional properties in both bulk and thin film ferroelectric materials with exposure to both low-energy photons (X-ray, gamma) and high-energy particles (protons, neutrons).[40,97,98,101] Such degradation is generally attributed to the creation and/or activation of defects in the ferroelectric material, eventually leading to the suppression of polarization and degradation of extrinsic contributions to the response (*e.g.*, domain wall motion).[32,40,101] While these previous investigations have uncovered, to some degree, the nature of radiation interactions with ferroelectric materials, few studies have attempted to compare the effects of modifying film properties and features of the material stack and measure the resulting effects on their radiation tolerance. The studies in this thesis have investigated the effects of critical interfaces and interactions in the irradiated ferroelectric material stack, including the ferroelectric-electrode interface, grain boundary interfaces, layer crystallization interfaces, dopant-ferroelectric-radiation interactions, and the mechanical boundaries in the lower material stack.

12.1.1 Electromechanical Interface at the Ferroelectric-Electrode Boundary

A study of a single 2.5-Mrad gamma radiation dose on the effects of Pt *vs.* IrO_2 top electrodes on PZT thin films demonstrated that the interface between the ferroelectric thin film and the electrode contacts plays a critical role in determining functional material response.[32] Samples with IrO_2 top electrodes exhibited greater tolerance to radiation-induced degradation of dielectric, polarization, and piezoelectric properties compared to

those with Pt top electrodes. The quantitative comparisons favoring samples with IrO_2 over Pt top electrodes were accentuated by visibly-exacerbated pinching of the *P-E* hysteresis loops and formation of new peaks in the ε_r-E_{DC} tunability curves for samples with Pt top electrodes. Interpretation of these results suggests that trapped charges generated by gamma irradiation modify pre-existing pinning centers in the material (especially oxygen vacancies), resulting in increased stabilization of domain walls. These oxygen vacancies are often mobile, especially with the application of electric field, and can migrate and accumulate to form planar structures at the film-electrode interface, in a process that resembles ferroelectric fatigue.[72] Metal-oxide IrO_2 top electrodes are likely conductive to some ionic motion, and annihilation or recombination of oxygen-related defects occurs at the PZT-electrode hetero-interface. On the other hand, the purely metallic Pt top electrodes do not allow for similar annihilation of defects, and formation of a ferroelectrically-inactive layer ensues. The results of this study not only demonstrate a practical approach to increasing radiation hardness in ferroelectric PZT thin films by simple variation of the top electrode material, but also shed light on the role of defects created/activated by irradiation, their interactions with interfaces in the material stack, and their eventual effects on functional material response.

12.1.2 Total Ionization Dose and Quantification of Defect Interactions in Irradiated Ferroelectric Materials

While studies of the functional response at a single radiation dose allow for an interesting comparison of radiation tolerance of the ferroelectric thin film and material

stack, total ionization dose (TID) studies offer a far more comprehensive picture of dynamic material-radiation interactions, as well as defect interactions that are initiated at different radiation dose/energy levels. In practical terms, TID studies more effectively expose a material to conditions representative of a radiation-hostile environment, allowing for the study across a range of time-dependent doses and subsequently related defect concentrations in the material. Multiple experiments were designed in this thesis that relied on a range of gamma radiation doses; however, the increased number of discrete doses for response characterization necessitated a method for quantifying performance and correlating to radiation dose.

A phenomenological model was thus developed that assumes the rate of defect creation/activation in a ferroelectric material (and thus defect population) is proportional to the radiation dose.[189] Newly created/activated defects in the material, including both ionization and displacement events, interact both with the material lattice and with other defects, *e.g.*, domain walls, point defects, defect dipoles, grain boundaries, *etc.* These defect interactions lead to modifications of the measured macroscopic functional response by impacting a given volume of functional ferroelectric material volume. A phenomenological model was thus developed that relates defect interactions (assumed proportional to radiation dose) to the degradation/enhancement of a given functional response parameter, yielding a modified sigmoid function for fitting such data.[189] Two parameters are quantified to describe defect interactions: the effective mean change in material volume impacted by defect interactions per each new defect created, and the effective rate of defect saturation. The *former* can be considered as the global susceptibility of the material to defect-induced change; the *latter* is useful for describing the nuanced

anisotropic physical phenomena governing the effective rate of change of the functional response with radiation dose.

In subsequent experiments on PZT thin films studying grain microstructure, Mn-doping, and elastic layer thickness/material, the phenomenological model was employed to quantify defect interactions and extract valuable comparisons of radiation-dependent trends. Additionally, the adaptability of the phenomenological model was demonstrated by expansion to multiple functional materials, including proton-conducting oxides for SOFCs/MIECs and high-temperature superconducting oxides, as well as variety of methods for stimulating defect interactions, *e.g.*, He^{2+} ion implantation, heavy-ion bombardment, and chemical doping.[198,199,204]

The developed model elegantly complements the attractive aspects of employing radiation as a tool for defect engineering in a host of functional materials. Creation of solid solutions and, in general, chemical modification (*i.e.*, doping) of materials has been the approach used since antiquity for the design of new materials and modification of preexisting ones. Irradiation of materials can be a strong alternative approach, due to the relative simplicity and favorable additive nature of radiation dose experiments. Correlation of materials' properties to radiation dose allows for careful, on-demand enhancement/reduction of properties and the ability to tailor functional response to the intended application. Examples include control of dielectric losses for ferroelectric energy harvesting applications, or modification of proton-conduction in metal oxides used for MIECs, among others. Quantification of material performance as a function of radiation dose has the potential to drive the design of next-generation materials and devices that increasingly rely on superlative control of defect concentrations to harness critical

functionality.

12.1.3 Internal Grain Boundary Interfaces

Application of the phenomenological model to historical data from the literature on bulk and thin film ferroelectrics exposed to gamma radiation showed generally greater degradation of bulk ceramics compared to thin films, suggesting that size effects and microstructural properties likely contribute to the severity of radiation interaction with ferroelectrics. To study the effects of microstructure and grain morphology, two sets of PZT thin films were fabricated: one set of samples with smaller, uniformly-textured columnar grains and another with larger, randomly-oriented equiaxed grains. Irradiation of the samples across a 0.2 to 10 Mrad dose range resulted in distinct degradation behavior correlated to ferroelectric material microstructure. Large degradation of domain wall motion was noted in both samples, and expected to be the principal contributor to degradation of functional responses in the films. However, the equiaxed samples had larger grains, and likely larger domains with more mobile domain walls with respect to the columnar-grained samples. When exposed to irradiation and the resulting defect interactions, these domain walls of elevated mobility are subject to greater magnitude of degradation compared to samples with columnar grains. Lower rates of defect saturation were observed in samples with columnar grains, likely due to the fact that increased grain boundary density serves as a more effective defect sink in such samples, allowing for defect accumulation at internal interfaces in the absence of functional material volume.

Not only do the results from this study allow for valuable insights regarding the

effects of microstructure on radiation-induced degradation of ferroelectric thin films, they also elucidate the fundamental interactions of radiation with these materials in general. Specifically, it was found that degradation of the remanent polarization and piezoelectric responses was far more severe than that of the saturation responses. Remanent response is measured at low electric field; saturation, at high field. This result suggests that the defects created by exposure to ionizing gamma radiation are of relatively low energy, and the effects of pinning on domain wall motion are abated at higher electric fields employed to measure saturation responses. These general considerations of radiation-induced defects in ferroelectrics, as well as the previous microstructural considerations, provide critical knowledge toward the design and tailoring of radiation-tolerant ferroelectric thin films and material stacks.

12.1.4 Functional and Structural Effects of Internal Layer Interfaces and Chemical Heterogeneity

The study of internal film interfaces was continued via deliberate fabrication of films with different numbers of layer crystallization interfaces. Recent reports on novel methods for processing hetero-layered, graded, and superlattice epitaxial ferroelectric films have shown attractive enhancements to dielectric, ferroelectric, and electromechanical properties.[249,250,252-261] However, the origin of these interesting properties is somewhat debated in the literature, having been attributed to mobile phase boundaries, chemical heterogeneity, misfit strain, flexoelectricity, *etc.* Furthermore, similar studies have not comprehensively studied related effects in CSD ferroelectric thin films. PZT thin films

were thus fabricated across a range of layer crystallization periodicities with similar total film thickness, resulting in dramatic, alternating Zr/Ti gradients, and corresponding to R/T phases in the films. These periodic rhombohedral-tetragonal (pR/T) films demonstrated increased extrinsic contributions to dielectric and ferroelectric responses with increasing layer periodicity, but were counterpointed by simultaneous reductions of intrinsic contributions to the response.

Notable crystallographic discontinuity contributed to grain size reductions in films with thinner layers, decreasing their domain size and related domain wall mobility. Residual stress and deep chemical oscillations in the samples initiated fluctuations to the tetragonal side of the phase diagram, yielding increased intrinsic contributions to the response. This effect was exacerbated in films with greater layer thickness and more dramatic Zr/Ti gradients, but such gradients simultaneously approached the MPB, and contributed to greater overall dielectric, ferroelectric, and piezoelectric responses. This work highlights the role of layer crystallization interfaces and chemical heterogeneity on determining functional response, and paves the way for work on radiation-tolerance of similarly-processed PZT thin films (CHAPTER 8) and the mechanisms that are susceptible to radiation-induced degradation of the functional response.

12.1.5 Layer Crystallization Interfaces: Interaction with Radiation

The work on the effects of hetero-interfaces (CHAPTER 4) and microstructure (CHAPTER 6) and in irradiated PZT thin films suggested that strong internal interactions govern, to a large degree, the eventual functional response that ferroelectric materials

exhibit. The effects of crystallization interfaces and chemical heterogeneity were shown to generate similar structural and grain size variations (CHAPTER 7). In order to study the interaction of layer crystallization interfaces and chemical heterogeneity *with radiation* in PZT thin films, two sets of films were fabricated, one with good compositional homogeneity and relatively thick crystallized layers (~100 nm) and a second with strong compositional Zr/Ti gradients and thin individual layers (~30 nm), and exposed to gamma radiation doses from 0.2 to 20 Mrad. At low doses (0.2 to 2 Mrad), noteworthy enhancements of dielectric, polarization, and piezoelectric responses were observed for both sets of samples, thought to originate from the radiation-induced reversal of inherent internal bias. At higher doses, these enhancements were overcome by greater numbers of trapped charges at oxygen vacancy sites, resulting in more mobile $V_O^{\cdot}$. These defects accumulate, order, and degrade functional properties. Samples with greater compositional heterogeneity and crystallization periodicity demonstrated greater degradation of extrinsic contributions to the dielectric response, likely due to more uniform distribution of defects throughout the sample thickness at internal interfaces, and potential radiation dose enhancements at denser regions of the compositional Zr/Ti oscillations in the films. These results suggest that the existence of fewer internal crystallization interfaces may reduce defect generation and accumulation in PZT thin films, and generally result in augmented radiation tolerance.

12.1.6 Internal Dopant Defect Interactions

Through the studies of electrode-ferroelectric interactions, microstructural effects, and layer crystallization schemes on irradiated ferroelectric thin films, it was found that defects – especially $V_O^{\cdot\cdot}$ and the radiation-modified, singly-charged, mobile $V_O^{\cdot}$ – play a critical role in determining these materials' functional response and degradation behavior (CHAPTER 7). Given this strong interaction of radiation with oxygen vacancies and their mobility, it was hypothesized that methods to reduce the population of such defects in the pre-irradiation PZT thin film would subsequently mitigate radiation-induced degradation of functional response with TID exposure. Acceptor doping of PZT is known to "consume" oxygen vacancies in PZT, resulting in a "hard" composition.[298] Hence, PZT thin films with 4 wt.% Mn substituted for the B-site (Zr/Ti) cation were fabricated and irradiated, comparing their response to similarly-processed undoped films. It was found that the substantial Mn-doping significantly reduced initial dielectric, polarization, and piezoelectric responses compared to undoped PZT samples. However, across the radiation dose range, the Mn-doped samples demonstrated a superior degree of radiation tolerance of dielectric and polarization properties, with minimal response fluctuations even at 10 Mrad.

Mn acceptor-doping of PZT is compensated by the creation of oxygen vacancies, which subsequently form $Mn''_{Zr/Ti} - V_O^{\cdot\cdot}$ defect dipoles, stabilizing domain walls and reducing the population of *mobile* oxygen vacancies relative to undoped PZT. The result is lower response in virgin Mn-doped films due to increased pinning of domain wall motion, but negligible change in dielectric and polarization responses across the dose range due to the lack of *mobile* oxygen vacancies relative to undoped PZT. Undoped samples, on the other hand, suffer from substantial degradation of functional response arising from

increased mobility of radiation-induced, singly-charged $V_O^{\cdot}$ and ordering thereof at internal interfaces, such as grain boundaries, layer crystallization interfaces, film-electrode interfaces, *etc.* These results suggest that doping, irradiation, and the resulting defect-defect interactions can be leveraged to create extremely radiation-tolerant ferroelectric thin films for use in applications where response stability across a range of doses is critically important.

12.1.7 Elastic Layer Boundary and Effects of Residual Stress

The effects of residual stress and substrate clamping on ferroelectric thin films have been shown to result in drastic effects on their functional response.[274,319,321,329-334] Residual stresses, developed during thermal cycling for film crystallization, potentially modify defect mobility in the samples, as has been demonstrated in other functional metal oxides. PZT thin films with different thicknesses of SiO_2 and AlN elastic (boundary) layers were fabricated and exposed to gamma radiation at doses from 0.2 to 10 Mrad to study the effects the residual stress/strain state in the ferroelectric material and the interaction with radiation. Generally, the results indicated that samples with SiO_2 elastic layers were more radiation-tolerant than those with the AlN layer, though the thickness of the SiO_2 layer did not seem to produce consistent trends. Samples with AlN suffer from greater degradation of low-field dielectric permittivity, extrinsic contributions to the dielectric response, saturation polarization, and saturation piezoelectric response compared to the samples studied with both thicknesses of SiO_2 elastic layers. Furthermore, the PFM results indicate substantially

lower amplitude of the piezoresponse in samples with AlN elastic layers. However, causes for these trends are difficult to discern, and may also depend on other film factors.

The samples fabricated on AlN exhibited more random in-plane grain orientation and lacked the 100-PZT peak splitting that both sets of samples with different thicknesses of SiO_2 elastic layers demonstrated. As shown in CHAPTER 6, grain microstructure can affect the radiation-ferroelectric interaction, potentially resulting in a distinct trend for the samples with AlN elastic layers. Estimations of the residual stress/strain show that the samples with 750 nm AlN elastic layer exhibit substantially lower levels of tensile stress than the samples with 2035 and 760 nm SiO_2 layers. Tensile stress is known to increase defect mobility in functional metal oxides,[310,311] potentially towards grain boundary sinks, thus increasing radiation tolerance in film with greater tensile stress. The interaction between radiation, defect interactions, and residual tensile stress is expected to substantially affect eventual radiation tolerance, and is a strong candidate for future work.

12.1.8 Substrate Mechanical Interface and Residual Film Clamping Effects

The functional role and influence of the substrate on which ferroelectric thin films are fabricated cannot be overstated – residual stress and substrate clamping have been shown to effectuate vast long-range effects on domain wall motion in such films, thus impacting dielectric, ferroelectric, and electromechanical properties.[1,24,36,274,319,321,328-335] Such effects are especially prevalent as ferroelectric thin films are implemented in MEMS devices, where substrate requirements fluctuate based on the application.[354] In order to study the effects of substrate clamping, PZT thin films were progressively released from

the Si substrate via backside etching to various depths, and functional response measured intermediately. The results indicated that the interaction between the film, residual stress, and substrate clamping is tremendously complex. Enormous enhancements to the electromechanical response were observed due to substantial bending of the relaxed elastic substrate boundary. However, no statistically relevant changes to the dielectric and polarization properties were observed via macroscopic characterization. Local PFM interrogation of released and clamped regions of the material, however, did show increased piezoresponse behavior for released PZT films. Coupled with estimates of strain in the region under top electrode contacts due to both membrane and electrode bowing, it is theorized that the release from the substrate creates a complex stress/strain state in the film-electrode interface, masking any enhancement of macroscopic response. Paired with the work in CHAPTER 10 on elastic layer, residual stress, and the effects on radiation tolerance, variations in substrate thickness and film clamping will likely modify defect motion and MEMS device radiation hardness, and is an important target for future work.

12.1.9 Radiation Interactions with Ferroelectric Thin Film Stack: Conclusions

While many reports on the general effects of radiation on ferroelectric materials and functional response exist in the literature, very little has been done prior to this work to study the strong microstructural, interfacial, chemical, and mechanical interactions that largely govern their functional response. The work in this thesis has attempted to shed light on these interactions, placing a strong emphasis on the types of defects created/activated by ionizing gamma radiation, and the subsequent interactions of said defects with external

hetero-interfaces, microstructure, internal crystallization interfaces, chemical heterogeneity, chemical dopants, and residual stress. The results have demonstrated that gamma radiation generally creates or activates mobile, oxygen-related vacancies in PZT thin films, resulting in reduced extrinsic contributions to the functional response, such as the nonlinear and hysteretic motion of domain walls. However, the degree to which these defects affect ferroelectrics' functional response is immensely impacted by factors within the control of fabrication processes. The enhanced understanding of the fundamental science underpinning radiation-ferroelectric interactions gained through this work can be leveraged to engineer, tailor, and tune the functional properties of PZT thin film material stacks and eventual device functionality.

12.2 Future Work

The following sections detail potential areas for future work and the advancement of both scientific understanding and engineering methods for increased radiation tolerance in ferroelectric thin films for MEMS and microelectronics devices. Ongoing and future work on the radiation tolerance of ferroelectric thin films is expected to span a variety of experiments and approaches, including multiple radiation sources, *in situ* measurements and bias conditions, diverse material systems, interfacial interactions, and post-irradiation methods for self-healing and acceleration of such recovery processes.

12.2.1 Further Phenomenological Model Development

Of the research presented in this thesis, perhaps the most impactful *and* most suitable for future development is the phenomenological model for defect interactions in irradiated functional materials. As discussed in CHAPTER 5, the model is not only appropriate for irradiated ferroelectrics, but also for diverse materials systems (*e.g.*, superconducting oxides, mixed-ionic electronic conductors (MIECs), and solid oxide fuel cells (SOFCs)) and methods for creating/activating defect interactions (ion implantation, chemical doping). The parameters extracted from application of the model to describe defects' impact and rate of saturation are useful for a host of analyses – several are described in this work, but the true power of the model is realized with extensive application throughout future work and the literature. Future studies should focus on extracting and comparing the φ_N and k parameters for various radiation sources, functional material systems, microstructures, material stack components, measurement and operating conditions, and virtually any experimental work where the quantification of defects can provide useful comparisons of design variables to compare materials. An extensive application of the model will serve to further illuminate the fundamental mechanisms of radiation interaction with ferroelectrics and a broader class of functional materials. Several areas of interest are suggested in the following discussion of future work.

12.2.2 Radiation Sources

As discussed previously, photonic irradiation, such as the gamma rays studied in this work, is generally not energetic enough (massless) to displace atoms in PZT; exposure

to such sources typically induces ionization events and results in the charging or activation of existing defects. On the other hand, irradiation with more energetic, massive particles – such as protons, neutrons, and heavy ions – can displace atoms in the lattice, leading to structural changes, loss of ferroelectric properties, domain modifications, and eventual amorphization of the material. Multiple experiments on fast neutron irradiation of PZT ceramics have demonstrated significant displacement of atoms in the PZT lattice to interstitial sites, leading to a structural phase transformation from tetragonal to cubic and substantial degradation of functional properties (Figure 12-1).[98,99] Henriques *et al.*, showed that Pb and O at lattice sites was significantly decreased (up to 6% decrease in Pb sites) in neutron-irradiated samples, leading to substantial accumulation of Pb and PbO at internal interfaces in the material, such as grain boundaries.[98] Other experiments have shown similar induced damage and phase transitions in ferroelectric metal oxides with swift heavy ion irradiation.[355,356]

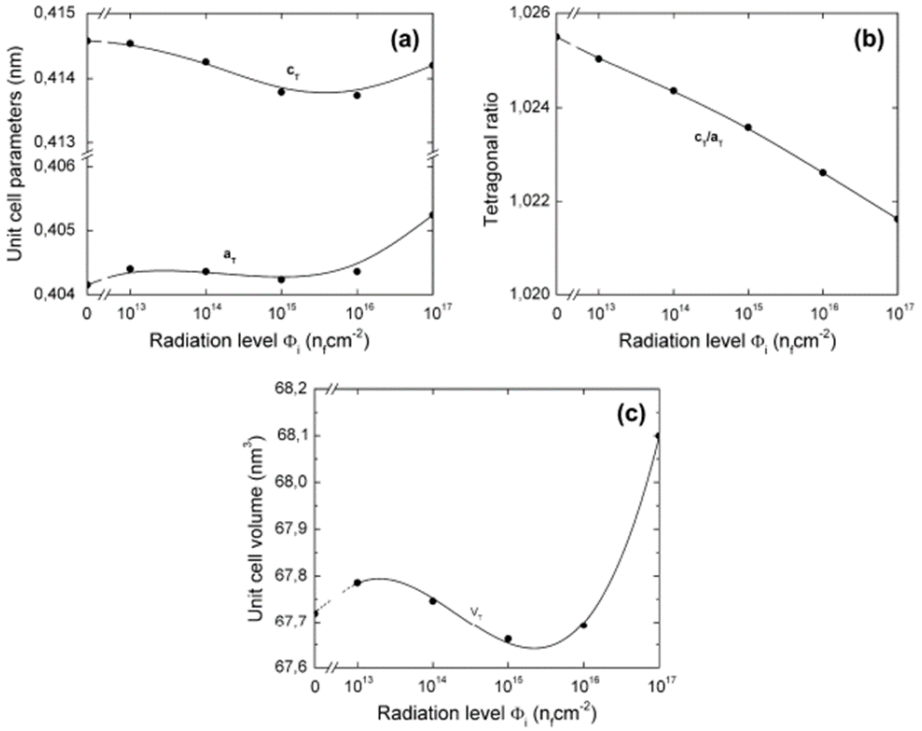

Figure 12-1 Changes to unit cell parameters in ceramic PZT exposed to a range of neutron doses, demonstrating the trend towards a phase transition from tetragonal to cubic structure.[99]

Previous studies from the literature on neutron, proton, and heavy ion irradiation of ferroelectric materials have provided valuable insights into the fundamental interactions of heavier particles with the ferroelectric. However, details of material stacks, comparisons of microstructure, interfacial interactions, and general work towards improving radiation tolerance are, for the most part, left uninvestigated. Similar to the motivation for the work contained in this thesis, further investigation of diverse radiation sources should be undertaken, not only with higher energy particles (*i.e.*, protons and neutrons), but also for X-ray and UV radiation. X-rays and UV rays have been shown to modify charge states and functional response in functional materials,[97,288] even resulting in potential enhancements thereof.[288] At the time of this writing, experiments on heavy Fe^{2+} irradiation of the 4% Mn-

doped and undoped PZT samples are being performed to investigate the effects of doping, defect-defect interactions, and more energetic particles on the functional properties. Further work with proton and neutron radiation is planned on similar sets of samples. Such work will allow for quantification of the φ_N and k parameters for various radiation sources and effects on microstructure, dopant concentration, *etc.*

12.2.3 In Situ Testing and Bias Conditions

Total ionization dose (TID) studies have been explored as a superior approach to single-dose studies, due to the greater range of radiation interaction studied, as well as offering a better approximation of the environment in which devices operate. However, many devices, such as those operating in space, are subject to operation during constant exposure to ionizing radiation. *In situ* measurements of material properties and functional response during radiation exposure allow for probing dynamic effects, and limit the possibility of relaxation or recovery that may occur after removal from the radiation source. However, *in situ* measurements are difficult and often limited by the irradiation experimental set up. Several areas of testing stand to benefit from *in situ* measurements.

First, preliminary measurements of the DC bias-dielectric response in PZT thin films directly after irradiation as well as after substantial relaxation time (4200 min) show significantly different results: the samples demonstrated a large degree of recovery over time (Figure 12-2). Second, the application of DC bias with opposite polarities during irradiation also drastically modifies the shape of the C-V curves and the formation of new peaks therein, suggesting that defects created/activated during irradiation are highly mobile

and accumulate at different regions in the sample and/or with distinct preferential orientations. This dynamic motion and accumulation of defects can vastly affect the functional properties of devices operating in radiation-hostile environments, and more rigorous *in situ* radiation testing of PZT thin films is necessary to fully uncover the effects of bias, measurements, and ultimately, device operation. These experiments should include a similar suite of functional characterization that was employed in this thesis, for proper comparison to TID studies. Notably, *in situ* electromechanical measurements are not possible with the same DBLI tool used throughout this thesis for probing the macroscopic piezoelectric response. To solve this problem, MEMS electromechanical resonators can be fabricated in the material stack and tested *in situ*.[357] The vibrating resonator device is excited across a band of frequencies, and resonance is monitored electrically.[358] The change in response as a function of radiation exposure can be monitored *in situ*, and a model can be used to estimate the $e_{31,f}$ electromechanical response.

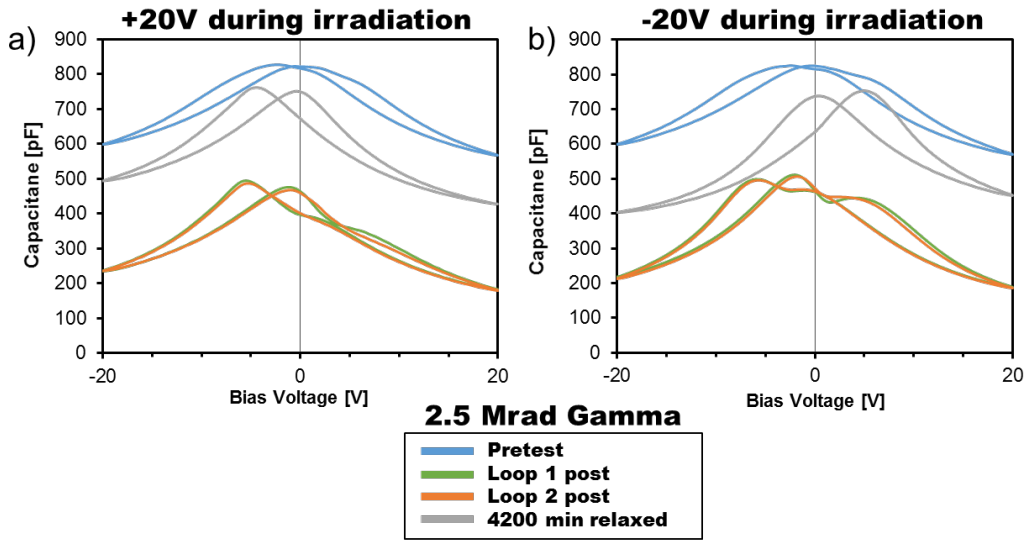

Figure 12-2 Capacitance-voltage (C-V) curves for PZT thin films irradated with 2.5 Mrad gamma dose, and measured before, directly after (Loop 1 and 2), and after 4200 min relaxation time. (a) shows measurements of samples on which +20 V was applied

during irradiation, and (b), -20 V. Data courtesy of Cory D. Cress (US Naval Research Laboratory), Ronald G. Polcawich (US Army Research Laboratory), and Ryan Q. Rudy (US Army Research Laboratory).

Additionally, *in situ* measurements of potential lattice strain in irradiated samples can elucidate any dynamic effects of radiation on the PZT lattice. In the single-dose study in CHAPTER 4 on the PZT-electrode interface, synchrotron XRD data on samples irradiated to 10 Mrad with gamma rays showed no evidence of lattice strain (Figure 12-3). These results suggest that no residual structural damage occurs *after* high levels of gamma radiation; on the other hand, in future work employing different radiation sources with heavier particles capable of causing atomic displacements, lattice strain is to be expected.[98,99] However, it is possible that ionizing radiation causes structural changes to the material that are elastically recoverable when removed from the exposure. These dynamic effects may lead to some amount of lattice strain, polarization suppression, and defect motion that is abated once the sample is removed from radiation exposure. While traditional X-ray diffraction (XRD) methods do not provide adequate resolution and high-energy synchrotron beams can obfuscate results with additional radiation exposure, micro-Raman spectroscopy is a compelling candidate for *in situ* monitoring of structural changes in ferroelectric thin films exposed to radiation. Prior work by Prof. Hiroshi Funakubo at Tokyo Institute of Technology has demonstrated *in situ* micro-Raman techniques for measuring structural changes in ferroelectric materials in a variety of conditions, including local stress as a function of cooling temperature,[359] field-dependent domain switching in MEMS cantilevers,[360] and oxygen vacancy concentration in $PbTiO_3$ thin films.[361] *In situ* micro-Raman can be used to dynamically probe the degree of lattice strain and potential changes to local oxygen vacancy concentration during exposure of ferroelectric thin films

to radiation. These *in situ* measurements would allow for the study of transient strain effects, and when coupled with the *in situ* functional characterization data, decipher whether they play a role in determining the functional response of irradiated ferroelectric materials operating in real-world environments.

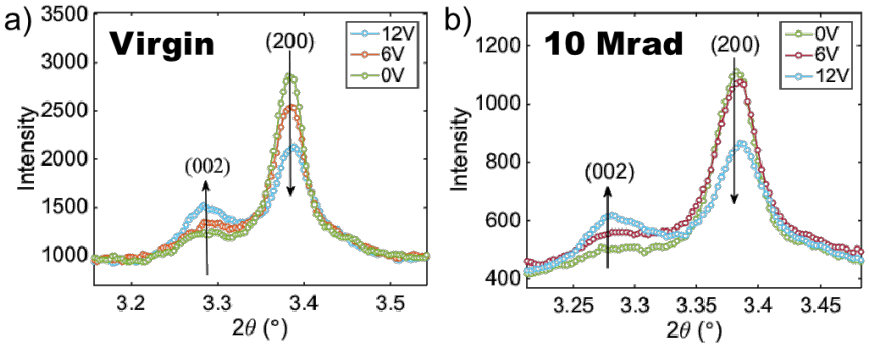

Figure 12-3 Synchrotron XRD data for (a) 0 Mrad and (b) 10 Mrad gamma radiation exposure of PZT thin films at different bias conditions, effectively demonstrating the lack of radiation-induced lattice distortion in the irradiated samples. Data courtesy of Jacob L. Jones, North Carolina State University.

12.2.4 Diverse Ferroelectric Materials

PZT has become one of the most technologically relevant ferroelectric materials for use in MEMS and microelectronics devices, due to its relative ease of fabrication, superlative control over material properties (even in CSD films), and highly attractive multifunctional response. However, in the past several decades, research on relaxor ferroelectric thin films, such as lead magnesium niobate-lead titanate, $Pb(Mg_{1/3}Nb_{2/3})O_3$-$PbTiO_3$ (PMN-PT), has demonstrated extremely attractive functional properties, especially the piezoelectric response, which eclipses that of PZT by a wide margin (Table 12-1).[362,363]

Table 12-1 Converse piezoelectric response of selected lead zirconate titanate (PZT) and relaxor ferroelectric binary systems, demonstrating the comparatively larger response in relaxor ferroelectrics, especially lead magnesium niobate-lead titanate (PMN-PT).[362,363]

Form	Material	d_{33} (pm/V)
Bulk ceramic	PZT (53/47) (lead zirconate titanate)	220
Polycrystalline	0.7PMN-0.3PT (lead magnesium niobate-lead titanate)	670
	0.58PSN-0.42PT (lead strontium niobate-lead titanate)	450
	0.5PNN-0.5PZT(35/65) (lead nickel niobate-lead zirconate titanate)	370
Single Crystal	70PMN-30PT (lead magnesium niobate, lead titanate)	~1500

Relaxor ferroelectrics are characterized by dispersion of the dielectric anomaly, dependent on frequency and temperature.[364] Some show a low-temperature phase that behaves as a traditional ferroelectric material.[364] In perovskite-structured relaxor ferroelectric solid solutions, mixed cations of different valences occupy the B sites in the ABO_3 structure with one end member a relaxor and the other often $PbTiO_3$. In PMN-PT, Mg, Nb, and Ti all occupy the B-site. These B-site substitutions and the unequal cationic ratios lead to a higher degree of chemical and structural disorder in PMN-PT relative to PZT (and other common ferroelectric compositions with single B-site cations, such as BTO and PTO), due to kinetic limitations in the material.[364] This disorder has been argued to result in a lack of stable domain states in PMN-PT, the presence of nanodomain structures, and reduced aging effects in the material.[364] The absence of such aging effects led NASA to implement PMN-based actuators to position the replacement Wide-Field and Planetary

Camera 2 (WFPC2) for the Hubble Space Telescope, which have performed admirably.[364] PMN-PT has also found ample use in underwater sonar for US Navy application and in the medical imaging field for ultrasonic transducers. However, processing of oriented PMN-PT ceramics and thin films is, to date, very challenging: large cracking of the material, Pb loss due to necessary high temperature crystallization, excessive porosity, and highly heterogeneous cation distribution can result in reduced functional properties (Figure 12-4).[362]

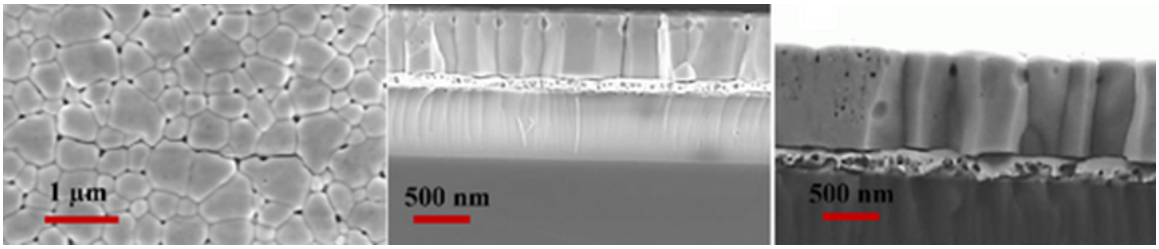

Figure 12-4 SEM micrographs of 600 nm thick PMN-PT thin films, demonstrating domed grains and high porosity in the material due to Pb loss at high crystallization temperatures.[362]

Very little work on the irradiation of relaxor ferroelectric PMN-PT exists in the literature. Angadi *et al.* reported modest increases to high-frequency dielectric permittivity and ~23% degradation of piezoelectric response in PMN-PT ceramics exposed to 1×10^4, 50 MeV Li^{3+} ions/cm^2, and observed no change in crystallinity.[365] However, in-depth investigations of radiation tolerance as a function of defect interactions, microstructure, *etc.* are notably absent in the literature. It is expected that the large degree of cationic disorder in PMN-PT films will result in an interaction with radiation that is distinct compared to that of PZT. On one hand, ionizing radiation has been demonstrated to modify existing defects in PZT, and may result in a more intense interaction with the greater disorder and cationic occupancies of PMN-PT.[32] On the other hand, it is also possible that

greater disorder will translate to the effect that radiation-created/activated defects are essentially "lost in the noise," minimally impacting functional response. Also worth considering are the effects of porosity and cracking in many PMN-PT thin films. Porosity can act as effective sites for accumulation of defects, and reduce deleterious effects on the functional response.[305] Finally, nanodomain structures in relaxor ferroelectric materials may reduce the long-range effects of domain-wall pinning by radiation-induced defects that critically affects irradiated PZT thin films. Work in CHAPTER 6 on grain microstructure showed that larger domains and subsequently more mobile domain walls experience greater proportional restriction of motion by radiation-induced defects. For PMN-PT thin films with smaller, more stable domain structures, the effects of defects on the pinning of domain wall motion can be potentially reduced relative to PZT thin films.

Recent work at Georgia Tech has demonstrated interesting functional properties in hetero-stacked PZT/PMN-PT films, suggesting that discrete heterolayering of these materials could be used to modify functional properties (Figure 12-5). This work could also be expanded to investigate the role of PZT/PMN-PT crystallization hetero-interfaces and resulting chemical heterogeneity on radiation-induced degradation, similar to work done in CHAPTER 7 and CHAPTER 8 of this thesis. Chemical heterogeneity and layer stacking arrangements have resulted in substantial changes to both intrinsic and extrinsic contributions to the dielectric and piezoelectric responses, and interaction with different radiation sources may result in diverse defect interactions with the material.

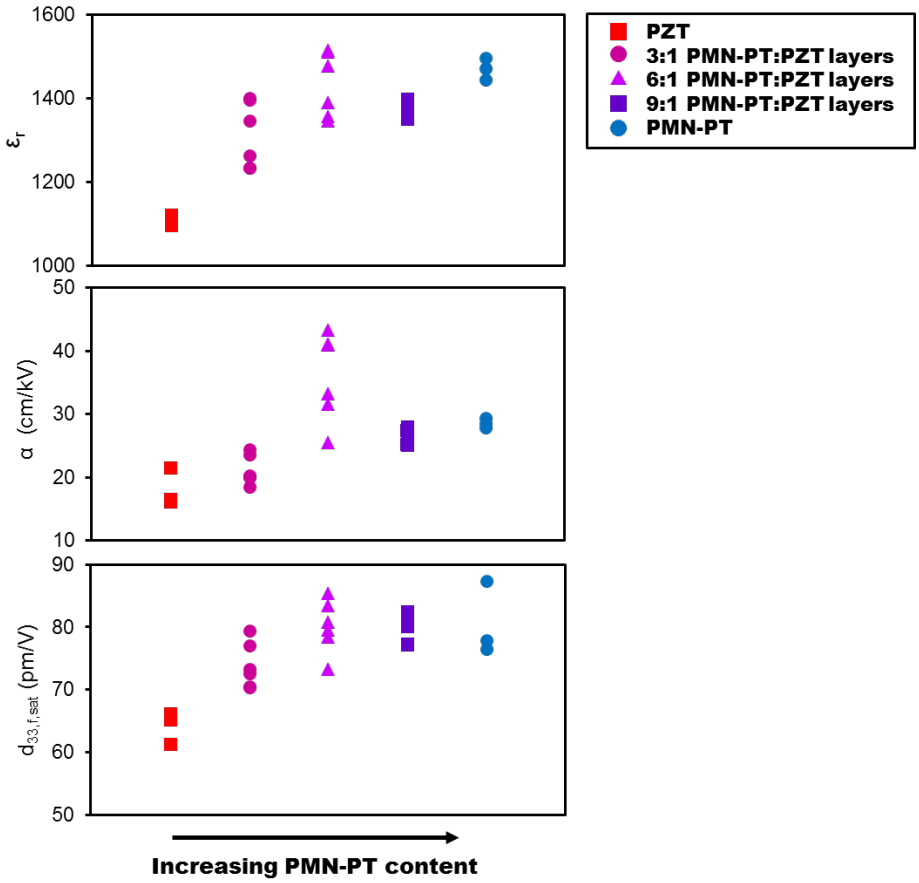

Figure 12-5 Functional properties in PZT/PMN-PT thin films fabricated at Georgia Tech, demonstrating interesting properties and potential enhancements of functional response as a function of hetero-layered film fraction. Data courtesy of Evelyn Chin, Georgia Institute of Technology.

12.2.5 Additional Critical Interfaces in the Material Stack

In this work, multiple critical interfaces and interactions in PZT thin films exposed to gamma radiation have been investigated, including the PZT-top electrode heterointerface, grain boundary interfaces and microstructural interactions, layer crystallization interfaces, chemical heterogeneity, dopant-ferroelectric interactions, and the mechanical boundary conditions of the lower material stack. However, other interfaces and interactions in the ferroelectric thin film material can affect radiation tolerance.

In CHAPTER 4, the hetero-interface between the PZT thin film and top electrode contact was studied, concluding that IrO_2 is generally superior to Pt, due to ionic motion and the effective annihilation of defects at the former. In the measurements performed for this study, bias conditions were applied in both the positive and negative directions, suggesting that defect motion would be bi-directional. However, only the top electrode material was modified – the bottom was consistently Pt. While the results of the study are compelling and represent a large step for increasing radiation tolerance in ferroelectric thin films, the effects of the bottom electrode contact material may differ from those on the top electrode. Defects may accumulate or be annihilated at different rates, dose enhancements might be asymmetric due to screening from the film and upper section of ferroelectric material, and crystallographic texture will likely vary for films grown on different substrates. Furthermore, the stack asymmetry may exacerbate film-surface defects and interaction with incident radiation, such as the photoelectric effect.[366,367] This effect can result in free electrons, and likely contributes to significant modifications of the local defect energy near the film surface.

Throughout the radiation work in this thesis, the Si substrate was identical for all films studied: *p*-type 100-Si wafers. Si is the standard for microelectronics devices, but newer semiconductor substrates, such as GaAs and InGaP, have demonstrated unique properties for exotic applications. While variations to the substrate most generally modify the crystallographic texture of ferroelectric thin films, they also control, to a large degree, the residual stress state in the film.[133,135,228,312-315] The work on elastic layers in CHAPTER 10 successfully demonstrated a correlation between residual stress state in irradiated PZT thin films and their functional response, but other factors, such as crystallographic texture, microstructure, and the inability to obtain reliable measurements of residual stress made proper isolation and direct conclusions regarding radiation tolerance unfeasible. Future work on this subject could include several studies: first, a thorough investigation of residual stress effects on radiation-induced degradation and subsequent defect motion. This can be accomplished by accurately quantifying film stress (using wafer curvature measurements during film fabrication) and subsequently correlating to TID degradation trends via the proposed phenomenological model. Various states of residual stress can be induced by bending the substrates during fabrication in a controlled manner,[336] or by careful manipulation of the lower material stack (substrate and elastic layer).

Second, variation of the substrate thickness has been shown to result in large modifications to the piezoelectric response in ferroelectric thin films – such experiments may provide interesting interactions of radiation with less severely-clamped films.[342] Films can be fabricated on Si substrates across a range of thicknesses and subsequently irradiated, characterized, compared via the phenomenological model, and the results correlated to substrate thickness and film clamping effects. Third, a proper study of the effects of SiO_2

elastic layer across a range of thicknesses, taking care to monitor stress, structural, and functional properties simultaneously. This study could potentially be combined with the previously-suggested investigation of residual stress, keeping in mind that modification of the elastic layer can potentially result in other structural changes in the films, which should be monitored and correlated to radiation tolerance simultaneously.

Approaches for carefully studying and quantifying the stress gradient through the thickness of the material stack may allow for additional insight regarding radiation tolerance in ferroelectric thin films. Recent work by Agar *et al.* has demonstrated nanobeam diffraction-based strain mapping of compositionally-graded PZT heterostructured films.[351] This transmission electron microscopy (TEM) technique effectively images both the in-plane and out-of-plane strains in crystalline samples, as well as the local rotation of the material lattice (Figure 12-6).[368] This approach can also be applied to more comprehensively study and quantify stress across the thickness of ferroelectric thin films whose elastic layer and/or substrate have been modified, and correlated to trends in the functional response as a function of TID.

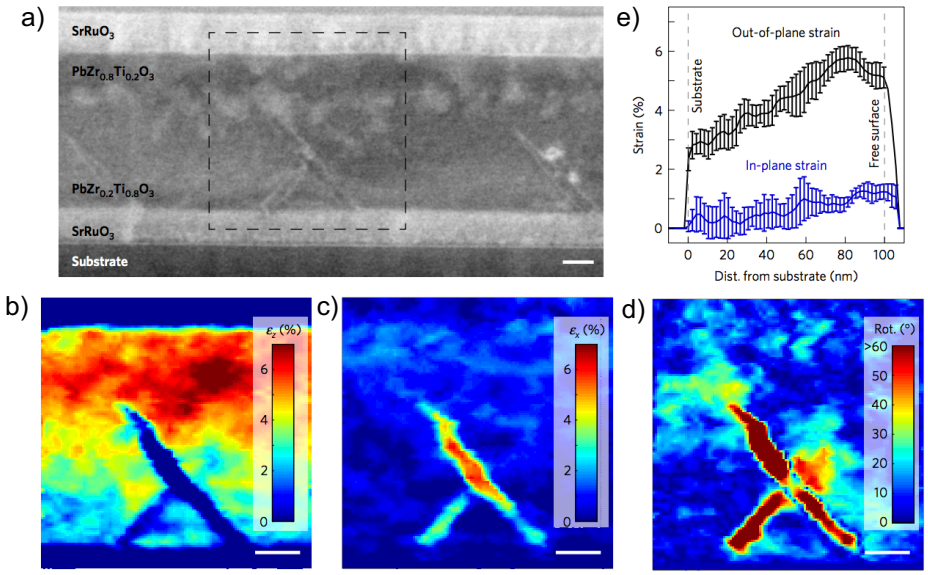

Figure 12-6. (a) High-angle, annular dark-field (HAADF) image of a compositionally graded PZT thin film.[351] (b) Out-of-plane, (c) in-plane strain, and (d) unit cell rotation imaged on the film's cross section with nanobeam diffraction techniques. (e) Plot of strain as a function of distance from the substrate.

Finally, a variety of reports have suggested that the harmful effects of radiation-induced defects are potentially alleviated by decreasing grain size in functional materials, and thus increasing the density of grain boundary sinks for defect accumulation.[220,221,238-241] Defects either created or accumulated at grain boundaries potentially result in less severe and shorter-range degradation, due to the relative absence of functional material volume at these locations. Nanocrystalline PZT ceramics have demonstrated reasonable ferroelectric properties;[369] PZT nanotube structures have shown increased extrinsic dielectric response and reduced susceptibility to damage due to their free-standing, discretely-packaged nature.[370] Nanostructured or nanocrystalline PZT has the potential to exhibit superior radiation tolerance compared to films with larger grain sizes, but is likely to suffer from reduced initial response, similar to the Mn-doped samples. Grain and domain size refinement and corresponding lower domain wall mobility reduces initial response,

but augments grain boundary density acting as effective defect sinks, and potentially increases radiation hardness. An investigation of the effects of TID on nanocrystalline and/or nanotube ferroelectric thin films would aptly complement the existing studies performed in this thesis on grain microstructure and dopants in PZT thin films.

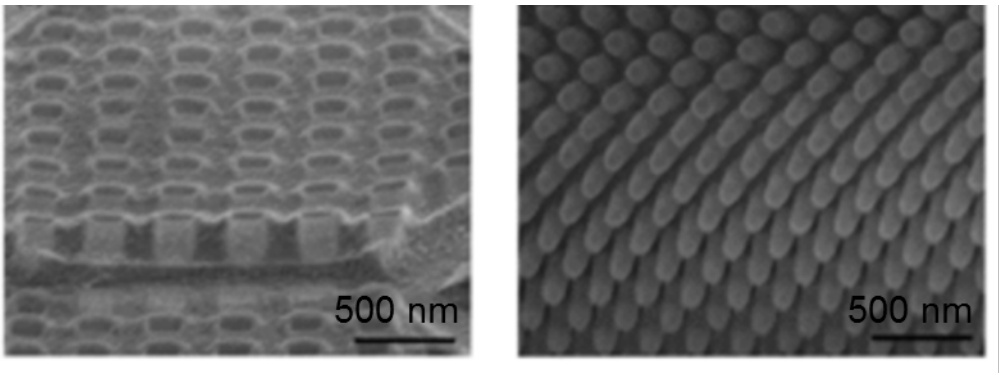

Figure 12-7 Image of free-standing PZT nanotubes, demonstrating the confined nature of the ferroelectric material, making it less susceptible to long-range effects on domain wall motion arising from radiation-induced defects.[370]

12.2.6 Post-Irradiation Recovery Methods

The effects of ferroelectric fatigue can be in part, if not entirely, reversed via application of a strong electric field and/or field cycling, elevated temperature, and exposure to UV light sources.[4] However, it has been found that in films for which the effects of fatigue have been reversed, subsequent onset of fatigue is more rapid, suggesting that fatigue results in permanent changes to the material. As discussed throughout this thesis, the effects of radiation-induced ionization and displacement events often mimic those of ferroelectric fatigue – notably present are increased oxygen vacancy mobility and ordering at interfaces, ferroelectric dead layers, polarization suppression, and

pinning/unpinning of domain walls on oxygen vacancy-related defects.[4] As shown in Figure 12-2, recovery of radiation-induced damage in the *C-V* curves occurs simply with time, in what appears to be a type of reverse ferroelectric aging. In devices relying on ferroelectric materials for sensing and actuation in radiation-hostile environments, these effects are of immense concern, as the stability of such devices over long periods of time, actuation voltages, temperature ranges, and with exposure to various types of radiation is paramount.

Future work on this topic should include studies of methods to mitigate these fatigue-like effects in irradiated thin films. Studies on aging, thermal loading, electrical cycling, and exposure to controlled doses of UV light are relatively straightforward to implement, both from an experimental perspective, as well as in eventual devices.

12.2.7 High Temperature Ferroelectric Compositions

As discussed in the previous section, thermal cycling of ferroelectric thin films has been shown to effectively reverse the effects of ferroelectric fatigue and aging.[4] Continuous operation of devices with integrated heating methods could potentially alleviate the effects of radiation-induced defects. When integrated with methods investigated in this thesis, such as an oxygen vacancy-amenable top electrode material, thermal treatment could significantly extend the usable lifetime of devices operating in radiation-hostile environments. However, PZT suffers from a relatively low transition temperature to the paraelectric cubic phase (< 400 °C), especially in the context of aerospace applications, which often require response stability above 500 °C (Figure 12-8).[371] Work on high

temperature ferroelectrics is abundant, with a focus on exotic materials, Pb-free compositions, and mechanical methods for increasing the transition temperature.[371-374] Among these, barium titanate (BTO) and bismuth ferrite (BFO) and their solid solutions have shown promising performance at higher temperatures than PZT is capable of enduring, but response is often lower with respect to PZT.[375] Recent work on Mn-doped BTO-BFO ceramics has demonstrated attractive piezoelectric and dielectric properties above 500 °C, making these types of materials attractive for use in aerospace applications, and for potential integration of heating sources to induce defect motion and annihilation, effectively reversing the effects of radiation-induced degradation in the ferroelectric material. Further work on high-temperature material systems and experiments to study the effects of applied temperature cycling on defect accumulation and fatigue-like properties in these films are both necessary.

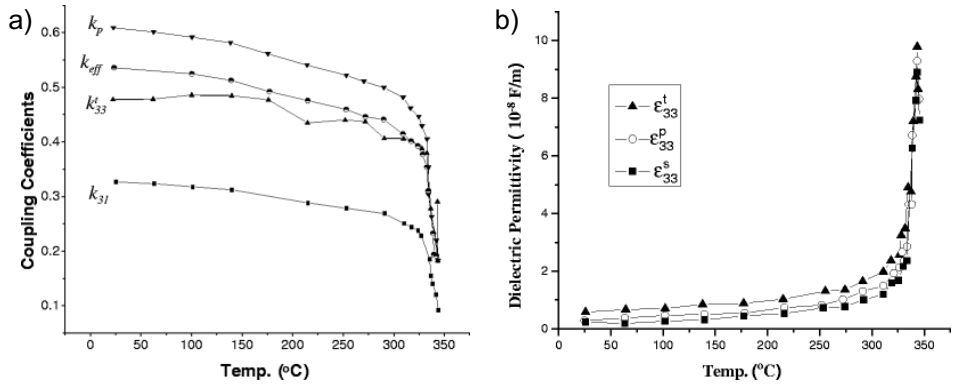

Figure 12-8 Temperature dependence of (a) electromechanical couplings and (b) dielectric permittivity in ceramic PZT Navy Type II, PKI-502 (soft composition).[371] Notably, large instability of response occurs as the Curie temperature is approached.

12.2.8 Single Crystal Ferroelectrics

Single-crystal ferroelectrics demonstrate reduced concentrations of defects relative to their polycrystalline counterparts, not only from limited inherent surface defects, but also due to overall lower defect concentrations resulting from processing conditions and employed fabrication methods. The accumulation of oxygen vacancies and other impurity ions at grain boundaries of polycrystalline ferroelectrics has been shown to contribute to ferroelectric fatigue, the effects of which are often very similar to those imparted by irradiation.[291] The absence of these effects in single-crystal ferroelectrics is potentially advantageous for reducing rates of defect creation, saturation, and accumulation in irradiated samples. Furthermore, poling of a single-crystal ferroelectric can (theoretically) result in a nearly single-domain state, potentially resulting in an interesting interaction of radiation and subsequently created/activated defects within that domain. Recent work on gamma-irradiated epitaxial PZT thin films has demonstrated significant degradation of their dielectric properties, proposed to be the result of radiation-induced modification and redistribution of mobile defects, potentially accumulating at ferroelectric-electrode interfaces.[376] However, the accumulation of defects at grain boundaries has been shown throughout the literature and this thesis to potentially increase radiation tolerance in ferroelectric thin films exposed to ionizing radiation. Future work comparing side-by-side TID experiments on ferroelectric PZT thin films in both single- and poly-crystalline thin film form should be performed to carefully study the effects of grain boundaries, internal interfaces, defect concentrations, and even domain size on the radiation-ferroelectric interaction. Such experiments could be further enhanced by use of epitaxial PZT films,

which will allow for precise control of residual stress through varying degrees of lattice mismatch with the substrate.

12.2.9 Electron Paramagnetic Resonance

Electron paramagnetic resonance (EPR) or electron spin resonance (ESR), is a technique that measures unpaired electrons in a sample by interrogating the sample with microwave-frequency electromagnetic energy, and measuring the subsequent absorption spectra. It is analogous to nuclear magnetic resonance (NMR), whereas NMR measures the spin of unpaired atomic nuclei. This technique was used in CHAPTER 4 in the investigation on top electrode material, to identify and quantify both native and radiation-induced defects. However, it is mentioned here because it is a powerful tool for identifying and quantifying the presence of oxygen vacancies, especially those modified by ionizing radiation and resulting in degradation of ferroelectric responses (Figure 12-9). In the future, EPR can be used in conjunction with the phenomenological model and estimates for the number of radiation-induced trapped charges introduced per ionizing radiation dose (see Section 5.7.8 for estimates). In its current state, the proposed phenomenological model quantifies radiation-induced defect interactions in relation to functional material response. However, when complemented by EPR results and estimates of defect creation per radiation dose, a more in-depth and comprehensive quantification of defects and defect-defect interactions in ferroelectric materials could be achieved, effectively estimating the number of induced interactions per TID. These results could be further expanded to diverse

radiation sources, new functional material systems, and a host of measurement and processing conditions.

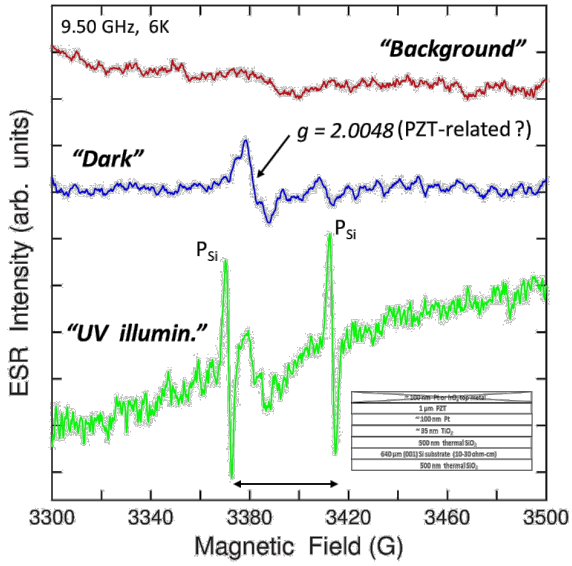

Figure 12-9 Electron paramagnetic resonance (EPR) of pre-irradiation PZT material stack. The "dark" signal with a g-value of ~2.005 and FWHM of ~10 G is very similar to the values reported in the literature for singly-ionized oxygen vacancies in powdered PZT samples.[175] The "P_{Si}" show spectra associated with shallow phosphorous donors in the Si substrate. Data and figure courtesy of Evan R. Glaser, US Naval Research Laboratory.

12.2.10 Ionic and Electronic Conductivity Measurements

Impedance spectroscopy measurements are commonly used to measure ionic and electronic conductivity across a range of temperatures and oxygen partial pressures in functional oxide materials, including ferroelectrics.[289] Information on defect concentration, defect mobility, defect association/dissociation energies, defect-dipole formation, and electron-hole transfer are available.[289] Impedance spectroscopy methods can be leveraged to measure changes to defect population and mobility in irradiated ferroelectric thin films.

As discussed at length in this thesis, ionizing radiation has been shown to substantially modify oxygen vacancies and their mobility in the ferroelectric material. These changes can be, to some extent, quantified via impedance spectroscopy methods measuring ionic conductivity and motion in the samples, and correlated to TID trends in future and ongoing studies. Such quantification could be used to improve the phenomenological model and more effectively quantify defect interactions in irradiated ferroelectric materials.

Going forward, significant practical advances and meaningful contributions to the science of ferroelectric materials and related defect interactions are likely to be obtained from a rigorous focus on radiation-ferroelectric interactions. It is expected that focused efforts on this approach will continue to facilitate significant discoveries regarding the fundamental interaction of radiation with ferroelectric materials, and pave the way for the engineering of radiation-tolerant, high performance MEMS and microelectronics devices.

REFERENCES

1. Trolier-McKinstry S, Muralt P. Thin film piezoelectrics for MEMS. *Journal of Electroceramics.* 2004;12(1-2):7-17.

2. Kholkin A, Pertsev N, Goltsev A. Piezoelectricity and Crystal Symmetry. In: Safari A, Akdogan E, eds. *Piezoelectric and Acoustic Materials for Transducer Applications*: Springer; 2008.

3. Hall D. Review of nonlinearity in piezoelectric ceramics. *Journal of Materials Science.* 2001;36(19):4575-4601.

4. Damjanovic D. Ferroelectric, dielectric and piezoelectric properties of ferroelectric thin films and ceramics. *Reports on Progress in Physics.* 1998;61(9):1267-1324.

5. Martin LW, Rappe AM. Thin-film ferroelectric materials and their applications. *Nature Reviews Materials.* 2016;2.

6. Dawber M, Rabe KM, Scott JF. Physics of thin-film ferroelectric oxides. *Reviews of Modern Physics.* 2005;77(4):1083-1130.

7. Stengel M, Vanderbilt D, Spaldin NA. Enhancement of ferroelectricity at metal-oxide interfaces. *Nature Materials.* 2009;8(5):392-397.

8. Fang D, Li F, Liu B, Zhang Y, Hong J, Guo X. Advances in Developing Electromechanically Coupled Computational Methods for Piezoelectrics/Ferroelectrics at Multiscale. *Applied Mechanics Reviews.* 2013;65(6).

9. [Anonymous]. An American national standard - IEEE standard definitions of primary ferroelectric terms. *IEEE Transactions on Ultrasonics Ferroelectrics and Frequency Control.* 1991;38(6):7-21.

10. Zhu X, Liu Z, Ming N. Perovskite oxide nanotubes: synthesis, structural characterization, properties and applications. *Journal of Materials Chemistry.* 2010;20(20):4015-4030.

11. Bolten D, Bottger U, Waser R. Reversible and irreversible piezoelectric and ferroelectric response in ferroelectric ceramics and thin films. *Journal of the European Ceramic Society.* 2004;24(5):725-732.

12. Benedek N, Fennie C. Why Are There So Few Perovskite Ferroelectrics? *Journal of Physical Chemistry C.* 2013;117(26):13339-13349.

13. Trolier-McKinstry S, Gharb N, Damjanovic D. Piezoelectric nonlinearity due to motion of 180° domain walls in ferroelectric materials at subcoercive fields: A dynamic poling model. *Applied Physics Letters.* 2006;88(20).

14. Bassiri-Gharb N. *Dielectric and piezoelectric nonlinearities in oriented $Pb(Yb_{1/2}Nb_{1/2})O_3$-$PbTiO_3$ thin films*: Materials Science and Engineering, The Pennsylvania State University; 2005.

15. Zhuang Z, Haun M, Jang S, Cross L. Composition and Temperature-Dependence of the Dielectric, Piezoelectric and Elastic Properties of Pure PZT Ceramics. *IEEE Transactions on Ultrasonics Ferroelectrics and Frequency Control.* 1989;36(4):413-416.

16. Ang C, Yu Z. Dielectric behavior of PbZr0.52Ti0.48O3 thin films: Intrinsic and extrinsic dielectric responses. *Applied Physics Letters.* 2004;85(17):3821-3823.

17. Vonhippel A. Ferroelectricity, Domain Structure, and Phase Transitions of Barium Titanate. *Reviews of Modern Physics.* 1950;22(3):221-237.

18. Poplavko Y, Tsykalov V, Molchano V. Microwave dielectric dispersion of ferroelectric and paralectric phases of barium titanate. *Soviet Physics Solid State, USSR.* 1969;10(11):2708-&.

19. Kersten O, Hofmann M, Schmidt G. Dielectric-Dispersion of Mn-doped Ceramics. *Ferroelectrics Letters Section.* 1986;6(3):75-80.

20. Bottger U, Arlt G. Dielectric Microwave Dispersion in PZT Ceramics. *Ferroelectrics.* 1992;127(1-4):95-100.

21. Herbiet R, Tenbrock H, Arlt G. The aging behavior of the complex material parameters - ε, d, and s in ferroelectric PZT ceramics. *Ferroelectrics.* 1987;76(3-4):319-326.

22. Arlt G, Dederichs H, Herbiet R. 90-Degrees-Domain Wall Relaxation in Tetragonally Distorted Ferroelectric Ceramics. *Ferroelectrics.* 1987;74(1-2):37-53.

23. Carl K, Hardtl K. Electrical Aftereffects in Pb(Ti,Zr)O3 Ceramics. *Ferroelectrics.* 1978;17(3-4):473-486.

24. Bassiri-Gharb N, Fujii I, Hong E, Trolier-McKinstry S, Taylor DV, Damjanovic D. Domain wall contributions to the properties of piezoelectric thin films. *Journal of Electroceramics.* 2007;19(1):49-65.

25. Li SP, Cao WW, Cross LE. The Extrinsic Nature of Nonlinear Behavior Observed in Lead Zirconate Titanate Ferroelectric Ceramic. *Journal of Applied Physics.* 1991;69(10):7219-7224.

26. Hall D. Rayleigh behaviour and the threshold field in ferroelectric ceramics. *Ferroelectrics.* 1999;223(1-4):319-328.

27. Rayleigh L. Notes on electricity and magnetism: On the behaviour of iron and steel under the operation of feeble magnetic forces. *Philosophical Magazine Series 5.* 1887(142).

28. Kronmuller H. Theory of rayleigh law in magnetically multiaxial and uniaxial crystals. 1971;32 (C1):C1-390-C391-391.

29. Damjanovic D, Demartin M. The Rayleigh law in piezoelectric ceramics. *Journal of Physics D-Applied Physics.* 1996;29(7):2057-2060.

30. Taylor D, Damjanovic D. Evidence of domain wall contribution to the dielectric permittivity in PZT thin films at sub-switching fields. *Journal of Applied Physics.* 1997;82(4):1973-1975.

31. Damjanovic D, Taylor D. Contributions to the nonlinear dielectric and piezoelectric response of ferroelectric thin films and ceramics. *Ferroelectrics.* 1999;221(1-4):137-146.

32. Brewer S, Deng C, Callaway C, et al. Effect of top electrode material on radiation-induced degradation of ferroelectric thin film structures. *Journal of Applied Physics.* 2016;120(2).

33. Li SP, Bhalla AS, Newnham RE, Cross LE. Quantitative-evaluation of extrinsic contribution to piezoelectric coefficient d_{33} in ferroelectric PZT ceramics. *Materials Letters.* 1993;17(1-2):21-26.

34. Hall DA, Stevenson PJ. High field dielectric behaviour of ferroelectric ceramics. *Ferroelectrics.* 1999;228(1-4):139-158.

35. Xu F, Trolier-McKinstry S, Ren W, Xu B, Xie Z, Hemker K. Domain wall motion and its contribution to the dielectric and piezoelectric properties of lead zirconate titanate films. *Journal of Applied Physics.* 2001;89(2):1336-1348.

36. Griggio F, Trolier-McKinstry S. Grain size dependence of properties in lead nickel niobate-lead zirconate titanate films. *Journal of Applied Physics.* 2010;107(2).

37. Shaw TM, Trolier-McKinstry S, McIntyre PC. The properties of ferroelectric films at small dimensions. *Annual Review of Materials Science.* 2000;30:263-298.

38. Cao W, Randall C. Grain size and domain size relations in bulk ceramic ferroelectric materials. *Journal of Physics and Chemistry of Solids.* 1996;57(10):1499-1505.

39. Holz S, Kiricenko S, Rissing L, et al. Integration of PVDF (polyvinylidene fluoride) in MEMS Production. *ECS Transactions.* 2014;64(1):189-195.

40. Graham JT, Brennecka GL, Ferreira P, et al. Neutron irradiation effects on domain wall mobility and reversibility in lead zirconate titanate thin films. *Journal of Applied Physics.* 2013;113(12).

41. Horikawa T, Mikami N, Mamkita T, et al. Dielectric Properties of (Ba,Sr)TiO3 Thin-Films Deposited by RF-Sputtering. *Japanese Journal of Applied Physics Part 1-Regular Papers Short Notes & Review Papers.* 1993;32(9B):4126-4130.

42. Smith GL, Pulskamp JS, Sanchez LM, et al. PZT-Based Piezoelectric MEMS Technology. *Journal of the American Ceramic Society.* 2012;95(6):1777-1792.

43. Radiation belt probes may help predict space weather [press release]. Rice News: Rice University News and Media2012.

44. Dey SK, Budd KD, Payne DA. Thin-film ferroelectrics of PZT by sol-gel processing. *IEEE Transactions on Ultrasonics Ferroelectrics and Frequency Control.* 1988;35(1):80-81.

45. Araujo E, Lima E, Guerra J, dos Santos A, Cardoso L, Kleinke M. Evidence for the monoclinic-tetragonal phase coexistence in $Pb(Zr_{0.53}Ti_{0.47})O_3$ thin films. *Journal of Physics-Condensed Matter.* 2008;20(41).

46. Heitmann AA, Rossetti GA. Thermodynamics of Ferroelectric Solid Solutions with Morphotropic Phase Boundaries. *Journal of the American Ceramic Society.* 2014;97(6):1661-1685.

47. Woodward D, Knudsen J, Reaney I. Review of crystal and domain structures in the PbZrxTi1-xO3 solid solution. *Physical Review B.* 2005;72(10).

48. Damjanovic D, Demartin M. Contribution of the irreversible displacement of domain walls to the piezoelectric effect in barium titanate and lead zirconate titanate ceramics. *Journal of Physics-Condensed Matter.* 1997;9(23):4943-4953.

49. Zhang S, Xia R, Shrout T. Lead-free piezoelectric ceramics vs. PZT? *Journal of Electroceramics.* 2007;19(4):251-257.

50. Mabud S. The Morphotropic Phase Boundary in PZT Solid Solutions. *Journal of Applied Crystallography.* 1980;13(JUN):211-216.

51. Marincel DM, Zhang HR, Britson J, et al. Domain pinning near a single-grain boundary in tetragonal and rhombohedral lead zirconate titanate films. *Physical Review B.* 2015;91(13):134113.

52. Amin A, Newnham R, Cross L. Effect of Elastic Boundary Conditions on Morphotropic Pb(Zr,Ti)O3 Piezoelectrics. *Physical Review B.* 1986;34(3):1595-1598.

53. Cheng J, Zhu W, Li N, Cross L. Electrical properties of sol-gel-derived $Pb(Zr_{0.52}Ti_{0.48})O_3$ thin films on a $PbTiO_3$-coated stainless steel substrate. *Applied Physics Letters.* 2002;81(25):4805-4807.

54. Oh S, Jang H. Ferroelectric phase transitions and three-dimensional phase diagrams of a $Pb(Zr,Ti)O_3$ system under a hydrostatic pressure. *Journal of Applied Physics.* 1999;85(5):2815-2820.

55. Oh S, Jang H. Epitaxial $Pb(Zr,Ti)O_3$ thin films with coexisting tetragonal and rhombohedral phases. *Physical Review B.* 2001;63(13).

56. Du X, Zheng J, Belegundu U, Uchino K. Crystal orientation dependence of piezoelectric properties of lead zirconate titanate near the morphotropic phase boundary. *Applied Physics Letters.* 1998;72(19):2421-2423.

57. Aggarwal S, Jenkins IG, Nagaraj B, et al. Switching properties of $Pb(Nb, Zr, Ti)O_3$ capacitors using $SrRuO_3$ electrodes. *Applied Physics Letters.* 1999;75(12):1787-1789.

58. Alexe M, Harnagea C, Hesse D, Gosele U. Polarization imprint and size effects in mesoscopic ferroelectric structures. *Applied Physics Letters.* 2001;79(2):242-244.

59. Bornand V, Trolier-McKinstry S, Takemura K, Randall C. Orientation dependence of fatigue behavior in relaxor ferroelectric-PbTiO3 thin films. *Journal of Applied Physics.* 2000;87(8):3965-3972.

60. Dawber M, Scott JF. A model for fatigue in ferroelectric perovskite thin films. *Applied Physics Letters.* 2000;76(8):1060-1062.

61. Du X, Chen I. Fatigue of $Pb(Zr_{0.53}Ti_{0.47})O_3$ ferroelectric thin films. *Journal of Applied Physics.* 1998;83(12):7789-7798.

62. Genenko Y, Glaum J, Hoffmann M, Albe K. Mechanisms of aging and fatigue in ferroelectrics. *Materials Science and Engineering B-Advanced Functional Solid-State Materials.* 2015;192:52-82.

63. Gruverman A, Tanaka M. Polarization retention in SrBi2Ta2O9 thin films investigated at nanoscale. *Journal of Applied Physics.* 2001;89(3):1836-1843.

64. Kang BS, Kim DJ, Jo JY, et al. Polarization retention in $Pb(Zr_{0.4}Ti_{0.6})O_3$ capacitors with IrO_2 top electrodes. *Applied Physics Letters.* 2004;84(16):3127-3129.

65. Lee JS, Joo SK. Enhanced fatigue and data retention characteristics of $Pb(Zr,Ti)O_3$ thin films by the selectively nucleated lateral crystallization method. *Japanese Journal of Applied Physics Part 1-Regular Papers Short Notes & Review Papers.* 2001;40(1):229-233.

66. Lee KM, An HG, Lee JK, et al. Enhanced retention characteristics of Pb(Zr, Ti)O_3 capacitors by ozone treatment. *Japanese Journal of Applied Physics Part 1-Regular Papers Short Notes & Review Papers.* 2001;40(8):4979-4983.

67. Lee JS, Park JH, Yun JI, Kim CS, Joo SK. Fatigue and data retention characteristics of single-grained Pb(Zr,Ti)O_3 thin films. *Journal of the Korean Physical Society.* 2001;39(1):184-188.

68. Lou X. Effects of porosity on electric fatigue behavior in PLZT and PZT ferroelectric ceramics. *Journal of Applied Physics.* 2009;105(2).

69. Lou X. Polarization fatigue in ferroelectric thin films and related materials. *Journal of Applied Physics.* 2009;105(2).

70. Mihara T, Watanabe H, de Araujo C. Polarization Fatigue Characteristics of Sol-Gel Ferroelectric Pb(Zr0.4Ti0.6)O3 Thin-Film Capacitors. *Japanese Journal of Applied Physics Part 1-Regular Papers Short Notes & Review Papers.* 1994;33(7A):3996-4002.

71. Nakamura T, Nakao Y, Kamisawa A, Takasu H. Preparation of Pb(Zr,Ti)O_3 Thin-Films on Electrodes Including IrO_2. *Applied Physics Letters.* 1994;65(12):1522-1524.

72. Scott JF, Dawber M. Oxygen-vacancy ordering as a fatigue mechanism in perovskite ferroelectrics. *Applied Physics Letters.* 2000;76(25):3801-3803.

73. Yoo IK, Desu SB. Fatigue Modeling of Lead Zirconate Titanate Thin-Films. *Materials Science and Engineering B-Solid State Materials for Advanced Technology.* 1992;13(4):319-322.

74. Duiker H, Beale P, Scott J, et al. Fatigue and Switching in Ferroelectric Memories - Theory and Experiment. *Journal of Applied Physics.* 1990;68(11):5783-5791.

75. Scott J, Araujo C, Melnick B, McMillan L, Zuleeg R. Quantitative measurement of space-charge effects in lead zirconate-titanate memories. *Journal of Applied Physics.* 1991;70(1):382-388.

76. Yoo I, Desu S. Mechanism of Fatigue in Ferroelectric Thin-Films. *Physica Status Solidi a-Applied Research.* 1992;133(2):565-573.

77. Mihara T, Watanabe H, De Araujo C. Characteristic change due to polarization fatigue of sol-gel ferroelectric Pb($Zr_{0.4}Ti_{0.6}$)O_3 thin-film capacitors. *Japanese Journal of Applied Physics Part 1-Regular Papers Short Notes & Review Papers.* 1994;33(9B):5281-5286.

78. Warren W, Dimos D, Tuttle B, et al. Polarization Suppression in Pb(Zr,Ti)O3 Thin-Films. *Journal of Applied Physics.* 1995;77(12):6695-6702.

79. Seebauer E, Noh K. Trends in semiconductor defect engineering at the nanoscale. *Materials Science & Engineering R-Reports.* 2010;70(3-6):151-168.

80. Weston TB, Webster AH, McNamara VM. Lead Zirconate-Lead Titanate Piezoelectric Ceramics with Iron Oxide Additions. *Journal of the American Ceramic Society.* 1969;52(5):253-&.

81. Aggarwal S, Ramesh R. Point defect chemistry of metal oxide heterostructures. *Annual Review of Materials Science.* 1998;28:463-499.

82. Gerson R. Variation in Ferroelectric Characteristics of Lead Zirconate Titanate Ceramics Due to Minor Chemical Modifications. *Journal of Applied Physics.* 1960;31(1):188-194.

83. Bai W, Meng X, Lin T, et al. Effect of Fe-doping concentration on microstructure, electrical, and magnetic properties of $Pb(Zr_{0.5}Ti_{0.5})O_3$ thin films prepared by chemical solution deposition. *Journal of Applied Physics.* 2009;106(12).

84. Aleem M, Nawaz H, Shuaib M, et al. Piezoelectric and pyroelectric properties of Sr-doped PZT (PSZT) with minor manganese additions. *6th Vacuum and Surface Sciences Conference of Asia and Australia (Vasscaa-6).* 2013;439.

85. Slouka C, Kainz T, Navickas E, et al. The Effect of Acceptor and Donor Doping on Oxygen Vacancy Concentrations in Lead Zirconate Titanate (PZT). *Materials.* 2016;9(11).

86. Majumder S, Roy B, Katiyar R, Krupanidhi S. Effect of acceptor and donor dopants on polarization components of lead zirconate titanate thin films. *Applied Physics Letters.* 2001;79(2):239-241.

87. Fowler JF. X-Ray Induced Conductivity in Insulating Materials. *Proceedings of the Royal Society of London Series a-Mathematical and Physical Sciences.* 1956;236(1207):464-480.

88. Oen OS, Holmes DK. Cross Sections for Atomic Displacements in Solids by Gamma-Rays. *Journal of Applied Physics.* 1959;30(8):1289-1295.

89. Sickafus K, Grimes R, Valdez J, et al. Radiation-induced amorphization resistance and radiation tolerance in structurally related oxides. *Nature Materials.* 2007;6(3):217-223.

90. Glower DD, Hester DL, Warnke DF. Effects of Radiation-Induced Damage Centers in Lead Zirconate Titanate Ceramics. *Journal of the American Ceramic Society.* 1965;48(8):417-&.

91. Gao J, Zheng L, Duo X, et al. Total dose radiation effects of Au/PbZr0.52Ti0.48O3/YBa2Cu3O7-δ capacitors. *Thin Solid Films.* 1999;340(1–2):132-136.

92. Gao J, Zheng L, Song Z, et al. Characteristics of Au/PbZr0.52Ti0.48O3/YBa2Cu3O7−δ capacitors fabricated on LaAlO3 and Y2O3-stabilized ZrO2 substrates during irradiation. *Philosophical Magazine Part B*. 1999;79(6):829-838.

93. Yang SA, Kim BH, Lee MK, Lee GJ, Lee N-H, Bu SD. Gamma-ray irradiation effects on electrical properties of ferroelectric PbTiO3 and Pb(Zr0.52Ti0.48)O3 thin films. *Thin Solid Films*. 2014;562:185-189.

94. Baturin I, Menou N, Shur V, et al. Influence of irradiation on the switching behavior in PZT thin films. *Materials Science and Engineering B*. 2005;120(1–3):141-145.

95. Menou N, Castagnos A-M, Muller C, et al. Degradation and recovery of polarization under synchrotron x-rays in $SrBi_2Ta_2O_9$ ferroelectric capacitors. *Journal of Applied Physics*. 2005;97(4):044106.

96. Scott JF, Araujo CA, Meadows HB, McMillan LD, Shawabkeh A. Radiation effects on ferroelectric thin-film memories: Retention failure mechanisms. *Journal of Applied Physics*. 1989;66(3):1444-1453.

97. Bastani Y, Cortes-Pena AY, Wilson AD, et al. Effects of high energy x-ray and proton irradiation on lead zirconate titanate thin films' dielectric and piezoelectric response. *Applied Physics Letters*. 2013;102(19).

98. Henriques A, Graham JT, Landsberger S, et al. Crystallographic changes in lead zirconate titanate due to neutron irradiation. *AIP Advances*. 2014;4(11).

99. Toacsan M, Ioachim A, Nedelcu L, Alexandru H. Accelerate ageing of PZT-type ceramics. *Progress in Solid State Chemistry*. 2007;35(2-4):531-537.

100. Proie RM, Polcawich RG, Cress CD, et al. Total Ionizing Dose Effects in Piezoelectric MEMS Relays. *Ieee Transactions on Nuclear Science*. 2013;60(6):4505-4511.

101. Leray J, Musseau O, Paillet P, Autran J, Sodi D, Coic Y. Radiation effects in thin-film ferroelectric PZT for non-volatile memory applications in microelectronics. *Journal De Physique Iii*. 1997;7(6):1227-1243.

102. Gao J, Zheng L, Zeng J, Lin C. gamma-ray total dose radiation effects of Pt/PbZr0.52Ti0.48/Pt and Au/PbTiO3/YBa2Cu3O7-delta ferroelectric capacitors. *Japanese Journal of Applied Physics Part 1-Regular Papers Short Notes & Review Papers*. 1998;37(9B):5126-5127.

103. Kim B, Yang S, Kang S, et al. Change of electrical properties of (K0.5Na0.5)(Mn0.005Nb0.995)O-3 thin films induced by gamma-ray irradiation. *Current Applied Physics*. 2016;16(5):539-544.

104. Medhi N, Nath A. Gamma Ray Irradiation Effects on the Ferroelectric and Piezoelectric Properties of Barium Titanate Ceramics. *Journal of Materials Engineering and Performance.* 2013;22(9):2716-2722.

105. Nath A, Medhi N. Effect of gamma ray irradiation on the ferroelectric and piezoelectric properties of barium stannate titanate ceramics. *Radiation Physics and Chemistry.* 2013;91:44-49.

106. Zhang G, Sun P, Zou Q, et al. Dose rate dependence of electrical characteristics of lead zirconate titanate capacitors. *Japanese Journal of Applied Physics Part 1-Regular Papers Short Notes & Review Papers.* 2003;42(10):6491-6495.

107. Solovev SP, Zakurkin VV, Kuzmin II, Dudarev VJ. X-ray and Dielectric Studies of Irradiated Perovskite Type Compounds. *Journal De Physique.* 1972;33(4):443-&.

108. Budd KD, Dey SK, Payne DA. Sol-gel processing of PbTiO3, PbZrO3, PZT, and PLZT thin films. *British Ceramic Proceedings.* 1985;36:107-121.

109. Budd KD, Payne DA. Sol-Gel Processing of Thin-Layer Dielectrics in Lead-Titanate-Based Systems. *Institute of Physics Conference Series.* 1989(103):13-22.

110. Assink RA, Schwartz RW. ^{1}H and ^{13}C NMR Investigations of $Pb(Zr,Ti)O_3$ Thin-Film Precursor Solutions. *Chemistry of Materials.* 1993;5(4):511-517.

111. Bassiri-Gharb N, Bastani Y, Bernal A. Chemical solution growth of ferroelectric oxide thin films and nanostructures. *Chemical Society Reviews.* 2014;43(7):2125-2140.

112. Schwartz R, Voigt J, Tuttle B, Payne D, Reichert T, DaSalla R. Comments on the effects of solution precursor characteristics and thermal processing conditions on the crystallization behavior of sol-gel derived lead zirconate titanate thin films. *Journal of Materials Research.* 1997;12(2):444-456.

113. Ho I, Xu Y, Mackenzie J. Electrical and optical properties of MgO thin film prepared by sol-gel technique. *Journal of Sol-Gel Science and Technology.* 1997;9(3):295-301.

114. Shibata J, Yamamoto H, Kulinich S, et al. Transmission electron microscopic studies of LiNb0.5Ta0.5O3 films deposited on sapphire substrates by thermal plasma spray CVD (microstructure of LiNb0.5Ta0.5O3 films deposited by thermal plasma spray CVD). *Materials Transactions.* 2002;43(7):1517-1524.

115. Kim S, Kim D, Im J, Kim C, Kingon A. Ferroelectric properties of new chemical solution derived SBT thin films for non-volatile memory devices. *Journal of Sol-Gel Science and Technology.* 1999;16(1-2):57-63.

116. Lakeman CDE, Payne DA. Processing Effects in the Sol-Gel Preparation of PZT Dried Gels, Powders, and Ferroelectric Thin-Layers. *Journal of the American Ceramic Society.* 1992;75(11):3091-3096.

117. Jia C, Urban K, Hoffmann S, Waser R. Microstructure of columnar-grained SrTiO3 and BaTiO3 thin films prepared by chemical solution deposition. *Journal of Materials Research.* 1998;13(8):2206-2217.

118. Schwartz R, Clem P, Voigt J, et al. Control of microstructure and orientation in solution-deposited BaTiO3 and SrTiO3 thin films. *Journal of the American Ceramic Society.* 1999;82(9):2359-2367.

119. Lange F. Chemical solution routes to single-crystal thin films. *Science.* 1996;273(5277):903-909.

120. Schwartz R. Chemical solution deposition of perovskite thin films. *Chemistry of Materials.* 1997;9(11):2325-2340.

121. Waser R. Microstructure of ceramic thin films. *Current Opinion in Solid State & Materials Science.* 1996;1(5):706-714.

122. Kuo Y, Tseng T. Preparation and characterization of PLZT thin films by sol-gel processing. *Journal of Materials Science.* 1996;31(23):6361-6368.

123. Langjahr P, Wagner T, Ruhle M, et al. Epitaxial growth and structure of cubic and pseudocubic perovskite films on perovskite substrates. *Epitaxial Oxide Thin Films Ii.* 1996;401:109-114.

124. Hoffmann S, Hasenkox U, Waser R, et al. Chemical solution deposited BaTiO3 and SrTiO3 thin films with columnar microstructure. *Epitaxial Oxide Thin Films Iii.* 1997;474:9-14.

125. Park C, Lee J, Lee S, Jun S, Kim H. Effect of excess PbO on microstructure and orientation of PZT(60/40) films. *Journal of Electroceramics.* 2010;25(1):20-25.

126. Lakeman C, Xu Z, Payne D. On the Evolution of Structure and Composition in Sol-Gel-Derived Lead-Zirdonate-Titanate Thin-Layers. *Journal of Materials Research.* 1995;10(8):2042-2051.

127. Schwartz R, Schneller T, Waser R. Chemical solution deposition of electronic oxide films. *Comptes Rendus Chimie.* 2004;7(5):433-461.

128. Brennecka G, Ihlefeld J, Maria J, Tuttle B, Clem P. Processing Technologies for High-Permittivity Thin Films in Capacitor Applications. *Journal of the American Ceramic Society.* 2010;93(12):3935-3954.

129. Wolf R, Trolier-McKinstry S. Temperature dependence of the piezoelectric response in lead zirconate titanate films. *Journal of Applied Physics.* 2004;95(3):1397-1406.

130. Bastani Y. *Ferroelectric Thin and Ultrathin Films for MEMS Applications* Atlanta, GA: Mechanical Engineering, Georgia Institute of Technology; 2013.

131. Sanchez LM, Potrepka DM, Fox GR, et al. Optimization of PbTiO3 seed layers and Pt metallization for PZT-based piezoMEMS actuators. *Journal of Materials Research.* 2013;28(14):1920-1931.

132. Potrepka DM, Fox GR, Sanchez LM, Polcawich RG. Pt/TiO_2 growth templates for enhanced PZT films and MEMS devices. *MRS Proceedings*; 2011.

133. Aoki K, Fukuda Y, Numata K, Nishimura A. Effects of Titanium Buffer Layer on Lead-Zirconate-Titanate Crystallization Processes In Sol-Gel Deposition Technique. *Japanese Journal of Applied Physics Part 1-Regular Papers Short Notes & Review Papers.* 1995;34(1):192-195.

134. Dai C, Xiao F, Lee C, Cheng Y, Chang P, Chang S. Thermal effects in PZT: diffusion of titanium and recrystallization of platinum. *Materials Science and Engineering a-Structural Materials Properties Microstructure and Processing.* 2004;384(1-2):57-63.

135. Kim S, Kim C, Oh Y. Influence of Al2O3 diffusion barrier and PbTiO3 seed layer on microstructural and ferroelectric characteristics of PZT thin films by sol-gel spin coating method. *Thin Solid Films.* 1997;305(1-2):321-326.

136. Ihlefeld J, Kotula P, Gauntt B, et al. Solution Chemistry, Substrate, and Processing Effects on Chemical Homogeneity in Lead Zirconate Titanate Thin Films. *Journal of the American Ceramic Society.* 2015;98(7):2028-2038.

137. Bhamidipati K, Didari S, Harris T. Slot die coating of polybenzimiazole based membranes at the air engulfment limit. *Journal of Power Sources.* 2013;239:382-392.

138. Didari S, Ahmad Z, Veldhorst J, Harris T. Wetting behavior of the shear thinning power law fluids. *Journal of Coatings Technology and Research.* 2014;11(1):95-102.

139. Furiouslettuce. BraggPlaneDiffraction.svg. 2009.

140. Furushima R, Tanaka S, Kato Z, Uematsu K. Orientation distribution-Lotgering factor relationship in a polycrystalline material as an example of bismuth titanate prepared by a magnetic field. *Journal of the Ceramic Society of Japan.* 2010;118(1382):921-926.

141. Lotgering F. Topotactical reactions with ferrimagnetic oxides having hexagonal crystal structures 1. *Journal of Inorganic & Nuclear Chemistry.* 1959;9(2):113-&.

142. Joseph J, Vimala T, Sivasubramanian V, Murthy V. Structural investigations on $Pb(Zr_xT_{1-x})O_3$ solid solutions using the x-ray Rietveld method. *Journal of Materials Science.* 2000;35(6):1571-1575.

143. Frantti J, Lappalainen J, Eriksson S, et al. Neutron diffraction studies of $Pb(Zr_xTi_{1-x})O_3$ ceramics. *Ferroelectrics.* 2001;261(1-4):857-862.

144. Cox D, Noheda B, Shirane G. Low-temperature phases in PbZr0.52Ti0.48O3: A neutron powder diffraction study. *Physical Review B.* 2005;71(13).

145. Rooksby H, Lewis B. Relations between the structures of phases in the system platinum molybdenum. *Journal of the Less-Common Metals.* 1964;6(6):451-460.

146. Eppelsheimer D, Penman R. Accurate determination of the lattice of β-titanium at 900° C. *Nature.* 1950;166(4231):960-960.

147. Weirich T, Winterer M, Seifried S, Hahn H, Fuess H. Rietveld analysis of electron powder diffraction data from nanocrystalline anatase TiO_2. *Ultramicroscopy.* 2000;81(3-4):263-270.

148. Ono S. PDF 00-058-0335, Iridium Oxide Cubic. University College London, England: Department of Earth Sciences; 2007.

149. Bolzan A, Fong C, Kennedy B, Howard C. Structural studies of rutile-type metal dioxides. *Acta Crystallographica Section B-Structural Science.* 1997;53:373-380.

150. Davey W. Precision measurements of lattice constants in abundant metals. *Zeitschrift Fur Kristallographie.* 1926;63(3/4):316-317.

151. Guo H, Tan X, Zhang S. In situ TEM study on the microstructural evolution during electric fatigue in $0.7Pb(Mg_{1/3}Nb_{2/3})O_3$-$0.3PbTiO_3$ ceramic. *Journal of Materials Research.* 2015;30(3):364-372.

152. Mortazavi N, Esmaily M, Halvarsson M. The capability of Transmission Kikuchi Diffraction technique for characterizing nano-grained oxide scales formed on a FeCrAl stainless steel. *Materials Letters.* 2015;147:42-45.

153. Bolten D, Lohse O, Grossmann M, Waser R. Reversible and irreversible domain wall contributions to the polarization in ferroelectric thin films. *Ferroelectrics.* 1999;221(1-4):251-257.

154. GmbH aS. Manual: aixDBLI, Research Line. In: GmbH aS, ed. 1.5.1.0 ed: aixACCT Systems GmbH; 2012:73

155. Brewer S, Deng C, Callaway C, Kalinin S, Vasudevan R, Bassiri-Gharb N. Piezoelectric response enhancement in the proximity of grain boundaries of relaxor-ferroelectric thin films. *Applied Physics Letters.* 2016;108(24).

156. Tertib64. Piezoresponse of parallel and antiparallel domains.png. *Piezoresponse Force Microscopy.* 2009.

157. Rodriguez B, Callahan C, Kalinin S, Proksch R. Dual-frequency resonance-tracking atomic force microscopy. *Nanotechnology.* 2007;18(47).

158. Jesse S, Kalinin S, Proksch R, Baddorf A, Rodriguez B. The band excitation method in scanning probe microscopy for rapid mapping of energy dissipation on the nanoscale. *Nanotechnology.* 2007;18(43).

159. Jesse S, Baddorf A, Kalinin S. Switching spectroscopy piezoresponse force microscopy of ferroelectric materials. *Applied Physics Letters.* 2006;88(6).

160. Kang C, Lee S, Jung I, Jung P, Hwang S, Ko J. The fabrication of patternable silicon nanotips using deep reactive ion etching. *Journal of Micromechanics and Microengineering.* 2008;18(7).

161. Menou N, Castagnos A-M, Muller C, et al. Degradation and recovery of polarization under synchrotron x rays in SrBi2Ta2O9 ferroelectric capacitors. *Journal of Applied Physics.* 2005;97(4):044106.

162. Merz WJ. Domain Formation and Domain Wall Motions in Ferroelectric Batio3 Single Crystals. *Physical Review.* 1954;95(3):690-698.

163. Kim S, Koo J, Shin S, Park Y. Improvement of retention loss in $Pb(Zr,Ti)O_3$ capacitors using $Ir/SrRuO_3$ top electrodes. *Applied Physics Letters.* 2005;87(21):212910.

164. Lee KM, An HG, Lee JK, et al. Enhanced retention characteristics of Pb(Zr, Ti)O-3 capacitors by ozone treatment. *Japanese Journal of Applied Physics Part 1-Regular Papers Short Notes & Review Papers.* 2001;40(8):4979-4983.

165. Schloss LF, McIntyre PC, Hendrix BC, Bilodeau SM, Roeder JF, Gilbert SR. Oxygen tracer studies of ferroelectric fatigue in $Pb(Zr,Ti)O_3$ thin films. *Applied Physics Letters.* 2002;81(17):3218-3220.

166. Chen Y, McIntyre PC. Effects of chemical stability of platinum/lead zirconate titanate and iridium oxide/lead zirconate titanate interfaces on ferroelectric thin film switching reliability. *Applied Physics Letters.* 2007;91(23):232906.

167. Stengel M, Aguado-Puente P, Spaldin NA, Junquera J. Band alignment at metal/ferroelectric interfaces: Insights and artifacts from first principles. *Physical Review B.* 2011;83(23):235112.

168. Wang Y, Niranjan MK, Janicka K, et al. Ferroelectric dead layer driven by a polar interface. *Physical Review B.* 2010;82(9):094114.

169. Hartmann AJ, Neilson M, Lamb RN, Watanabe K, Scott JF. Ruthenium oxide and strontium ruthenate electrodes for ferroelectric thin-films capacitors. *Applied Physics a-Materials Science & Processing.* 2000;70(2):239-242.

170. Magee C, Harrington W, Botnick E. On the use of CsX+ cluster ions for major element depth profiling in secondary ion mass-spectrometry. *International Journal of Mass Spectrometry and Ion Processes.* 1990;103(1):45-56.

171. Jaffe B, Cook WR, Jaffe HL. *Piezoelectric ceramics.* London, New York: Academic Press; 1971.

172. Taylor JR. *An Introduction to Error Analysis: The Study of Uncertainties in Physical Measurements.* 2nd ed. Sausalito, Calif.: University Science Books; 1997.

173. Sherrit S, Vannice D, Graham J, et al. Domain-wall motion in piezoelectric materials under high-stress. Proceedings Paper presented at the Eighth IEEE International Symposium on Applications of Ferroelectrics (ISAF); 1992.

174. Masys A, Ren W, Yang G, Mukherjee B. Piezoelectric strain in lead zirconate titante ceramics as a function of electric field, frequency, and dc bias. *Journal of Applied Physics.* 2003;94(2):1155-1162.

175. Longo V, Silva M, de Figueiredo A, et al. Photoluminescence in quasi-amorphous Pb0.8X0.2Zr0.53Ti0.47O3 (X = Ca, Sr and Ba) powders: An optical and structural study. *Chemical Physics Letters.* 2009;475(1-3):96-100.

176. Pramanick A, Damjanovic D, Daniels J, Nino J, Jones J. Origins of Electro-Mechanical Coupling in Polycrystalline Ferroelectrics During Subcoercive Electrical Loading. *Journal of the American Ceramic Society.* 2011;94(2):293-309.

177. Park C, Chadi D. Microscopic study of oxygen-vacancy defects in ferroelectric perovskites. *Physical Review B.* 1998;57(22):R13961-R13964.

178. Damjanovic D. Chapter 4 - Hysteresis in Piezoelectric and Ferroelectric Materials. In: Mayergoyz I, ed. *The Science of Hysteresis*. Oxford: Academic Press; 2006:337-465.

179. Pandey S, Thakur O, Kumar A, Prakash C, Chatterjee R, Goel T. Study of pinched loop characteristics of lead zirconate titanate (65/35). *Journal of Applied Physics.* 2006;100(1):014104.

180. Robert G, Damjanovic D, Setter N. Preisach modeling of ferroelectric pinched loops. *Applied Physics Letters.* 2000;77(26):4413-4415.

181. Kohli M, Muralt P, Setter N. Removal of 90 degrees domain pinning in (100) $Pb(Zr_{0.15}Ti_{0.85})O_3$ thin films by pulsed operation. *Applied Physics Letters.* 1998;72(24):3217-3219.

182. Ke Q, Kumar A, Lou X, Zeng K, Wang J. Origin of the enhanced polarization in La and Mg co-substituted BiFeO3 thin film during the fatigue process. *Applied Physics Letters.* 2012;100(4):042902.

183. Dawber M, Scott JF. Models of electrode-dielectric interfaces in ferroelectric thin-film devices. *Japanese Journal of Applied Physics Part 1-Regular Papers Short Notes & Review Papers.* 2002;41(11B):6848-6851.

184. Chen MC, Chang TC, Tsai CT, et al. Influence of electrode material on the resistive memory switching property of indium gallium zinc oxide thin films. *Applied Physics Letters.* 2010;96(26):262110.

185. Aggarwal S, Perusse SR, Madhukar S, et al. Rapid thermal annealing of oxide electrodes for nonvolatile ferroelectric memory structures. *Journal of Electroceramics.* 1998;2(3):171-179.

186. Wall J, Burke E. Gamma-Dose Distributions at and Near the Interface of Different Materials. *Ieee Transactions on Nuclear Science.* 1970;NS17(6):305-&.

187. Weast RC. *CRC Handbook of Chemistry and Physics* - Vol 1, 1987.

188. Hubbell JH, Seltzer SM. Tables of x-ray mass attenuation coefficientsand mass energy-absorption coefficientsfrom 1 keV to 20 MeV for elements z = 1 to 92 and 48 additional substances of dosimetric interest. 1996.

189. Brewer SJ, Cress CD, Williams SW, et al. Phenomenological Model for Defect Interactions in Irradiated Functional Materials. *Scientific Reports.* 2017;7(5308).

190. Yoshida Y, Langouche G. *Defects and Impurities in Silicon Materials: An Introduction to Atomic-Level Silicon Engineering.* Tokyo: Springer; 2015.

191. McColgin W, Shantharama L, Lavine J, et al. Defect engineering in CCD image sensors. *Defect and Impurity Engineered Semiconductors and Devices Iii.* 2002;719:119-124.

192. Foltyn S, Civale L, Macmanus-Driscoll J, et al. Materials science challenges for high-temperature superconducting wire. *Nature Materials.* 2007;6(9):631-642.

193. Taylor F, Buckeridge J, Catlow C. Defects and Oxide Ion Migration in the Solid Oxide Fuel Cell Cathode Material LaFeO3. *Chemistry of Materials.* 2016;28(22):8210-8220.

194. Boser O. Statistical theory of hysteresis in ferroelectric materials. *Journal of Applied Physics.* 1987;62(4):1344-1348.

195. Taylor D, Damjanovic D. Domain wall pinning contribution to the nonlinear dielectric permittivity in $Pb(Zr,Ti)O_3$ thin films. *Applied Physics Letters.* 1998;73(14):2045-2047.

196. Wu Z, Sayer M, Liu M, Safari A, Kingon A, Haertling G. Defect Structures and Fatigue in Ferroelectric PZT Thin Films. *Proceedings of the Eighth Ieee International Symposium on Applications of Ferroelectrics.* 1992:244-247.

197. Ohnishi T, Shibuya K, Yamamoto T, Lippmaa M. Defects and transport in complex oxide thin films. *Journal of Applied Physics.* 2008;103(10).

198. Saremi S, Xu R, Dedon LR, et al. Enhanced Electrical Resistivity and Properties via Ion Bombardment of Ferroelectric Thin Films. *Advanced Materials.* 2016.

199. Clark G, Marwick A, Koch R, Laibowitz R. Effects of radiation-damage in ion-implanted thin films of metal-oxide superconductors. *Applied Physics Letters.* 1987;51(2):139-141.

200. Kalinin S, Spaldin N. Functional Ion Defects in Transition Metal Oxides. *Science.* 2013;341(6148):858-859.

201. Bibes M, Barthelemy A. Multiferroics: Towards a magnetoelectric memory. *Nature Materials.* 2008;7(6):425-426.

202. Van de Walle C. Defect analysis and engineering in ZnO. *Physica B-Condensed Matter.* 2001;308:899-903.

203. Lin Y, Fang S, Su D, Brinkman K, Chen F. Enhancing grain boundary ionic conductivity in mixed ionic-electronic conductors. *Nature Communications.* 2015;6.

204. Medvedev D, Lyagaeva J, Gorbova E, Demin A, Tsiakaras P. Advanced materials for SOFC application: Strategies for the development of highly conductive and stable solid oxide proton electrolytes. *Progress in Materials Science.* 2016;75:38-79.

205. Wee S, Zuev Y, Cantoni C, Goyal A. Engineering nanocolumnar defect configurations for optimized vortex pinning in high temperature superconducting nanocomposite wires. *Scientific Reports.* 2013;3.

206. Shikama T, Katsui H, Nagata S, et al. *Radiation Effects in Functional Materials for Nuclear Fusion Application.* International Atomic Energy Agency (IAEA)2013.

207. Lucchese M, Stavale F, Ferreira E, et al. Quantifying ion-induced defects and Raman relaxation length in graphene. *Carbon.* 2010;48(5):1592-1597.

208. Imai H, Hirashina H. Intrinsic-Defect and Extrinsic-Defect Formation in Silica Glasses by Radiation. *Journal of Non-Crystalline Solids.* 1994;179:202-213.

209. Galeener FL, Kerwin DB, Miller AJ, Mikkelsen JC. X-ray Creation and Activation of Electron-Spin-Resonance in Vitreous Silica. *Physical Review B.* 1993;47(13):7760-7779.

210. Chang S, Kim J, Phatak C, et al. X-ray Irradiation Induced Reversible Resistance Change in Pt/TiO2/Pt Cells. *Acs Nano.* 2014;8(2):1584-1589.

211. Haugsrud R, Norby T. Proton conduction in rare-earth ortho-niobates and ortho-tantalates. *Nature Materials.* 2006;5(3):193-196.

212. Crandall RS. Defect relaxation in amorphous silicon: Stretched exponentials, the Meyer-Neldel rule, and the Staebler-Wronski effect. *Physical Review B.* 1991;43(5):4057-4070.

213. Avrami M. Kinetics of phase change 1: General theory. *Journal of Chemical Physics.* 1939;7(12):1103-1112.

214. Paunovic V, Mitic V, Miljkovic M, Pavlovic V, Zivkovic L. Ho2O3 Additive Effects on BaTiO3 Ceramics Microstructure and Dielectric Properties. *Science of Sintering.* 2012;44(2):223-233.

215. Daniels J, Majkut M, Cao Q, et al. Heterogeneous grain-scale response in ferroic polycrystals under electric field. *Scientific Reports.* 2016;6.

216. Gao J, Zheng L, Huang B, et al. Total dose radiation effects of Pt/PZT/Pt ferroelectric capacitors fabricated by PLD method. *Semiconductor Science and Technology.* 1999;14(9):836-839.

217. Brewer S, Zhou H, Williams S, et al. Effect of Microstructure on Irradiated Ferroelectric Thin Films. *Journal of Applied Physics.* 2017;121(244102).

218. Claeys CL, Simoen E. *Radiation effects in advanced semiconductor materials and devices.* Berlin ; New York: Springer; 2002.

219. Uberuaga B, Vernon L, Martinez E, Voter A. The relationship between grain boundary structure, defect mobility, and grain boundary sink efficiency. *Scientific Reports.* 2015;5.

220. Dey S, Mardinly J, Wang Y, et al. Irradiation-induced grain growth and defect evolution in nanocrystalline zirconia with doped grain boundaries. *Physical Chemistry Chemical Physics.* 2016;18(25):16921-16929.

221. Shen T. Radiation tolerance in a nanostructure: Is smaller better? *Nuclear Instruments & Methods in Physics Research Section B-Beam Interactions With Materials and Atoms.* 2008;266(6):921-925.

222. Theissmann R, Schmitt L, Kling J, et al. Nanodomains in morphotropic lead zirconate titanate ceramics: On the origin of the strong piezoelectric effect. *Journal of Applied Physics.* 2007;102(2).

223. Lucuta PG, Teodorescu V, Vasiliu F. SEM, SAED, and TEM investigations of domain structure in PZT ceramics at morphotropic phase boundary. *Applied Physics a-Materials Science & Processing.* 1985;37(4):237-242.

224. Berger MJ, Coursey JS, Zucker MA, Chang J. Stopping-Power & Range Tables for Electrons, Protons, and Helium Ions. *NISTIR 4999*: NIST Physical Measurement Laboratory; 1998.

225. Ziegler JF. Interactions of Ions with Matter. http://www.srim.org2017/.

226. Berger MJ*ea*. NIST Standard Reference Database 8 (XGAM). *NIST Physical Measurement Laboratory*1998.

227. Oldham T, McLean F. Total ionizing dose effects in MOS oxides and devices. *Ieee Transactions on Nuclear Science.* 2003;50(3):483-499.

228. Setter N, Damjanovic D, Eng L, et al. Ferroelectric thin films: Review of materials, properties, and applications. *Journal of Applied Physics.* 2006;100(10).

229. Chang C, Tang C. An integrated pyroelectric infrared sensor with a PZT thin film. *Sensors and Actuators a-Physical.* 1998;65(2-3):171-174.

230. Otsuki T, Arita K. Quantum jumps in FeRAM technology and performance. *Integrated Ferroelectrics.* 1997;17(1-4):31-43.

231. Schwartz R, Reichert T, Clem P, Dimos D, Liu D. A comparison of diol and methanol-based chemical solution deposition routes for PZT thin film fabrication. *Integrated Ferroelectrics.* 1997;18(1-4):275-286.

232. Clem P, Tuttle B, Ruffner J, et al. Investigation of PZT/LSCO/Pt/aerogel thin film composites for uncooled pyroelectric IR detectors. *MRS Proceedings Journal.* 1999;541:661-666.

233. Brennecka G, Parish C, Tuttle B, Brewer L. Multilayer thin and ultrathin film capacitors fabricated by chemical solution deposition. *Journal of Materials Research.* 2008;23(1):176-181.

234. Song Z, Lin C. Microstructure and electrical properties of PbZr0.48Ti0.52O3 ferroelectric films on different Pt bottom electrodes. *Applied Surface Science.* 2000;158(1-2):21-27.

235. Mhin S, Nittala K, Lee J, et al. Phase and Texture Evolution in Chemically Derived PZT Thin Films on Pt Substrates. *Journal of the American Ceramic Society.* 2014;97(9):2973-2979.

236. Eitel R, Shrout T, Randall C. Nonlinear contributions to the dielectric permittivity and converse piezoelectric coefficient in piezoelectric ceramics. *Journal of Applied Physics.* 2006;99(12).

237. ASTM. Standard test methods for determining average grain size. *Designation: E112 − 12*2013.

238. Gleiter H. Grain boundaries as point defect sources or sinks: Diffusional creep. *Acta Metallurgica.* 1979;27(2):187-192.

239. Dollar M. Grain-boundaries as sinks or sources for point-defects. *Scripta Metallurgica.* 1986;20(7):1059-1060.

240. Singh BN, Foreman AJE. Calculated grain size-dependent vacancy supersaturation and its effect on void formation. *Philosophical Magazine.* 1974;29(4):847-857.

241. Ovid'ko I, Sheinerman A. Irradiation-induced amorphization processes in nanocrystalline solids. *Applied Physics a-Materials Science & Processing.* 2005;81(5):1083-1088.

242. Tagantsev A, Stolichnov I, Colla E, Setter N. Polarization fatigue in ferroelectric films: Basic experimental findings, phenomenological scenarios, and microscopic features. *Journal of Applied Physics.* 2001;90(3):1387-1402.

243. Randall C, Kim N, Kucera J, Cao W, Shrout T. Intrinsic and extrinsic size effects in fine-grained morphotropic-phase-boundary lead zirconate titanate ceramics. *Journal of the American Ceramic Society.* 1998;81(3):677-688.

244. Ihlefeld J, Harris D, Keech R, Jones J, Maria J, Trolier-McKinstry S. Scaling Effects in Perovskite Ferroelectrics: Fundamental Limits and Process-Structure-Property Relations. *Journal of the American Ceramic Society.* 2016;99(8):2537-2557.

245. Marincel DM, Zhang H, Jesse S, et al. Domain Wall Motion Across Various Grain Boundaries in Ferroelectric Thin Films. *Journal of the American Ceramic Society.* 2015;98(6):1848-1857.

246. Ihlefeld J, Shelton C. Chemical homogeneity effects on the nonlinear dielectric response of lead zirconate titanate thin films. *Applied Physics Letters.* 2012;101(5).

247. Brewer S, Williams S, Deng C, et al. Functional and structural effects of layer periodicity in chemical solution-deposited $Pb(Zr,Ti)O_3$ thin films *Journal of the American Ceramic Society.* 2017(00):1-12.

248. Karthik J, Mangalam R, Agar J, Martin L. Large built-in electric fields due to flexoelectricity in compositionally graded ferroelectric thin films. *Physical Review B.* 2013;87(2).

249. Mangalam RVK, Karthik J, Damodaran AR, Agar JC, Martin LW. Unexpected Crystal and Domain Structures and Properties in Compositionally Graded PbZr1-xTixO3 Thin Films. *Advanced Materials.* 2013;25(12):1761-1767.

250. Anbusathaiah V, Kan D, Kartawidjaja FC, et al. Labile Ferroelastic Nanodomains in Bilayered Ferroelectric Thin Films. *Advanced Materials.* 2009;21(34):3497-+.

251. Ban Z, Alpay S, Guo R, et al. Lattice misfit as a design parameter for enhanced dielectric response and tunability in epitaxial barium strontium titanate films. *Morphotropic Phase Boundary Perovskites, High Strain Piezoelectrics, and Dielectric Ceramics.* 2003;136:333-343.

252. Roytburd A, Zhong S, Alpay S. Dielectric anomaly due to electrostatic coupling in ferroelectric-paraelectric bilayers and multilayers. *Applied Physics Letters.* 2005;87(9).

253. Vrejoiu I, Zhu YL, Le Rhun G, Schubert MA, Hesse D, Alexe M. Structure and properties of epitaxial ferroelectric PbZr0.4Ti0.6O3/PbZr0.6Ti0.4O3 superlattices grown on SrTiO3 (001) by pulsed laser deposition. *Applied Physics Letters.* 2007;90(7).

254. Pontes F, Longo E, Leite E, Varela J. Improvement of the dielectric and ferroelectric properties in superlattice structure of $Pb(Zr,Ti)O_3$ thin films grown by a chemical solution route. *Applied Physics Letters.* 2004;84(26):5470-5472.

255. Lee H, Christen H, Chisholm M, Rouleau C, Lowndes D. Strong polarization enhancement in asymmetric three-component ferroelectric superlattices. *Nature.* 2005;433(7024):395-399.

256. Wang C, Fang Q, Zhu Z, et al. Dielectric properties of $Pb(Zr_{20}Ti_{80})O_3/Pb(Zr_{80}Ti_{20})O_3$ multilayered thin films prepared by RF magnetron sputtering. *Applied Physics Letters.* 2003;82(17):2880-2882.

257. Zhou Z, Xue J, Li W, Wang J, Zhu H, Miao J. Heterolayered lead zirconate titanate thin films of giant polarization. *Journal of Applied Physics.* 2004;96(10):5706-5711.

258. Cooper V, Johnston K, Rabe K. Polarization enhancement in short period superlattices via interfacial intermixing. *Physical Review B.* 2007;76(2).

259. Bungaro C, Rabe K. Epitaxially strained [001]-$(PbTiO_3)1(PbZrO_3)1$ superlattice and $PbTiO_3$ from first principles. *Physical Review B.* 2004;69(18).

260. Tian W, Jiang J, Pan X, et al. Structural evidence for enhanced polarization in a commensurate short-period BaTiO3/SrTiO3 superlattice. *Applied Physics Letters.* 2006;89(9).

261. Kornev IA, Bellaiche L. Unusual thermodynamic properties and nonergodicity in ferroelectric superlattices. *Physical Review Letters.* 2003;91(11).

262. Cross L. Flexoelectric effects: Charge separation in insulating solids subjected to elastic strain gradients. *Journal of Materials Science.* 2006;41(1):53-63.

263. Ahluwalia R, Tagantsev A, Yudin P, Setter N, Ng N, Srolovitz D. Influence of flexoelectric coupling on domain patterns in ferroelectrics. *Physical Review B.* 2014;89(17).

264. Brooks K, Reasney I, Klissurska R, Huang Y, Bursill L, Setter N. Orientation of Rapid Thermally Annealed Lead Zirconate Titanate Thin Films on (111) Pt Substrates. *Journal of Materials Research.* 1994;9(10):2540-2553.

265. Calame F, Muralt P. Growth and properties of gradient free sol-gel lead zirconate titanate thin films. *Applied Physics Letters.* 2007;90(6).

266. Schuller IK. New Class of Layered Materials. *Physical Review Letters.* 1980;44(24):1597-1600.

267. Bao DH, Scholz R, Alexe M, Hesse D. Growth, microstructure, and ferroelectric properties of $Pb(Zr_{0.4}Ti_{0.6})O_3/PbZrO_3$ superlattices prepared on $SrTiO_3$ (100) substrates by pulsed laser deposition. *Journal of Applied Physics.* 2007;101(5).

268. de la Peña F, Ostasevicius T, Fauske VT, et al. HyperSpy 1.1.2. Zenodo; 2017.

269. Cliff G, Lorimer G. Quantitative analysis of thin specimens. *Journal of Microscopy-Oxford.* 1975;103(MAR):203-207.

270. Muralt P. Texture control and seeded nucleation of nanosize structures of ferroelectric thin films. *Journal of Applied Physics.* 2006;100(5).

271. Vasudevan R, Khassaf H, Cao Y, et al. Acoustic Detection of Phase Transitions at the Nanoscale. *Advanced Functional Materials.* 2016;26(4):478-486.

272. Haun M, Furman E, Jang S, Cross L. Thermodynamic theory of the lead zirconate-titanate solid solution system, 1: Phenomenology. *Ferroelectrics.* 1989;99:13-25.

273. Haun MJ, Furman E, Jang SJ, Cross LE. Thermodynamic theory of the lead zirconate-titanate solid-solution system, 5: Theoretical calculations. *Ferroelectrics.* 1989;99:63-86.

274. Berfield T, Ong R, Payne D, Sottos N. Residual stress effects on piezoelectric response of sol-gel derived lead zirconate titanate thin films. *Journal of Applied Physics.* 2007;101(2).

275. Morozovska A, Golovina I, Lemishko S, Andriiko A, Khainakov S, Eliseev E. Effect of Vegard strains on the extrinsic size effects in ferroelectric nanoparticles. *Physical Review B.* 2014;90(21).

276. Kumar A, Kalinin S, Kim Y. Exploring electro-chemo-mechanical phenomena on the nanoscale using scanning probe microscopy. *Electro-Chemo-Mechanics of Solids*: Springer; 2017.

277. Araujo E, Lima E, Bdikin I, Kholkin A. Thickness dependence of structure and piezoelectric properties at nanoscale of polycrystalline lead zirconate titanate thin films. *Journal of Applied Physics.* 2013;113(18).

278. Bastani Y, Schmitz-Kempen T, Roelofs A, Bassiri-Gharb N. Critical thickness for extrinsic contributions to the dielectric and piezoelectric response in lead zirconate titanate ultrathin films. *Journal of Applied Physics.* 2011;109(1).

279. de la Cruz J, Joanni E, Vilarinho P, Kholkin A. Thickness effect on the dielectric, ferroelectric, and piezoelectric properties of ferroelectric lead zirconate titanate thin films. *Journal of Applied Physics.* 2010;108(11).

280. Welsh A, Wilke R, Hickner M, Trolier-McKinstry S. Low-Cost, Damage-Free Patterning of Lead Zirconate Titanate Films. *Journal of the American Ceramic Society.* 2013;96(9):2799-2805.

281. Brennecka G, Tuttle B. Fabrication of ultrathin film capacitors by chemical solution deposition. *Journal of Materials Research.* 2007;22(10):2868-2874.

282. Wang L, Ren W, Yao K, Shi P, Wu X, Yao X. Effects of thickness on structures and electrical properties of K0.5Na0.5NbO3 thick films derived from polyvinylpyrrolidone-modified chemical solution. *Ceramics International.* 2012;38:S291-S294.

283. Nguyen M, Dekkers M, Vu H, Rijnders G. Film-thickness and composition dependence of epitaxial thin-film PZT-based mass-sensors. *Sensors and Actuators a-Physical.* 2013;199:98-105.

284. Zhong C, Wang X, Fang J, Li L. Investigation of Thickness Dependence of Structure and Electric Properties of Sol-Gel-Derived BiScO3-PbTiO3 Thin Films. *Journal of the American Ceramic Society.* 2010;93(10):3305-3311.

285. Bowen C, Kim H, Weaver P, Dunn S. Piezoelectric and ferroelectric materials and structures for energy harvesting applications. *Energy & Environmental Science.* 2014;7(1):25-44.

286. Bastani Y, Bassiri-Gharb N. Enhanced dielectric and piezoelectric response in PZT superlattice-like films by leveraging spontaneous Zr/Ti gradient formation. *Acta Materialia.* 2012;60(3):1346-1352.

287. Benedetto J, Moore R, McLean F, Brody P, Dey S. The Effect of Ionizing Radiation on Sol-Gel Ferroelectric PZT Capacitors. *Ieee Transactions on Nuclear Science.* 1990;37(6):1713-1717.

288. Alford N, Petrov P, Gagarin A, et al. Enhanced electrical properties of ferroelectric thin films by ultraviolet radiation. *Applied Physics Letters.* 2005;87(22).

289. Boukamp B, Pham M, Blank D, Bouwmeester H. Ionic and electronic conductivity in lead-zirconate-titanate (PZT). *Solid State Ionics.* 2004;170(3-4):239-254.

290. Brewer S, Williams S, Griffin L, et al. Enhanced radiation tolerance in Mn-doped ferroelectric thin films. *Applied Physics Letters.* 2017;111(2).

291. Scott J, De Araujo C. Ferroelectric Memories. *Science.* 1989;246(4936):1400-1405.

292. Sayyah R, Macleod T, Ho F. Radiation-Hardened Electronics and Ferroelectric Memory for Space Flight Systems. *Ferroelectrics.* 2011;413:170-175.

293. Joshi V, Ohno M, Ida J, Nagatomo Y, Strauss K, IEEE. Integrated silicon on insulator-ferroelectric capacitor process for radiation hard non volatile universal memory applications. *2005 Non-Volatile Memory Technology Symposium, Proceedings.* 2005:39-40.

294. Sanchez L, Wu S, Naik I. Observations of Ferroelectric Polarization Reversal in Sol-Gel Processed Very Thin Lead Zirconate Titanate Films. *Applied Physics Letters.* 1990;56(24):2399-2401.

295. Augustine G, Rohatgi A, Jokerst N. Base Doping Optimization for Radiation-hard Si, GaAs, and InP Solar Cells. *Ieee Transactions on Electron Devices.* 1992;39(10):2395-2400.

296. Sellin P, Vaitkus J. New materials for radiation hard semiconductor dectectors. *Nuclear Instruments & Methods in Physics Research Section a-Accelerators Spectrometers Detectors and Associated Equipment.* 2006;557(2):479-489.

297. Bruzzi M, Adey J, Al-Ajili A, et al. Radiation-hard semiconductor detectors for SuperLHC. *Nuclear Instruments & Methods in Physics Research Section A - Accelerators Spectrometers Detectors and Associated Equipment.* 2005;541(1-2):189-201.

298. Xin H, Ren W, Wu X, Shi P. Effect of Mn doping on structures and properties of chemical solution deposited lead zirconate titanate thick films with (100) preferential orientation. *Journal of Applied Physics.* 2013;114(2).

299. Wei H, Chen Y. Ferroelectric and pyroelectric properties of Mn-doped lead zirconate titanate ceramics. *Ceramics International.* 2015;41(5):6158-6163.

300. Zhang Q. Effects of Mn doping on the ferroelectric properties of PZT thin films. *Journal of Physics D: Applied Physics.* 2003;37(1).

301. Zhang Q, Whatmore R. Improved ferroelectric and pyroelectric properties in Mn-doped lead zirconate titanate thin films. *Journal of Applied Physics.* 2003;94(8):5228-5233.

302. Zhang Q, Whatmore R. Improved ferroelectric properties in Mn-doped PZT thin films. *Integrated Ferroelectrics.* 2003;52:73-84.

303. Ng Y, Alexander S. Structural Studies of Manganese-Stabilized Lead Zirconate Titanate. *Ferroelectrics.* 1983;51(1-2):81-86.

304. Kamiya T, Suzuki T, Tsurumi T, Daimon M. Effects of manganese addition on piezoelectric properties of $Pb(Zr_{0.5}Ti_{0.5})O_3$. *Japanese Journal of Applied Physics Part 1-Regular Papers Short Notes & Review Papers.* 1992;31(9B):3058-3060.

305. Krogstad J. Is there room for porosity in nuclear ceramics? What we can learn from dynamic microstructures in extreme conditions. *American Ceramic Society Bulletin.* 2017;96(1):30-34.

306. Bednyakov P, Sluka T, Tagantsev A, Damjanovic D, Setter N. Formation of charged ferroelectric domain walls with controlled periodicity. *Scientific Reports.* 2015;5.

307. Shvartsman V, Kholkin A, Verdier C, Yong Z, Lupascu D. Investigation of fatigue mechanism in ferroelectric ceramic via piezoresponse force microscopy. *Journal of the European Ceramic Society.* 2005;25(12):2559-2561.

308. Jeon Y, Kim D, No K, Kim S, Chung J. Residual stress analysis of Pt bottom electrodes on $ZrO_2/SiO_2/Si$ and SiO_2/Si substrates for $Pb(ZrTi)O_3$ thick films. *Japanese Journal of Applied Physics Part 1-Regular Papers Short Notes & Review Papers.* 2000;39(5A):2705-2709.

309. Griggio F, Jesse S, Kumar A, et al. Substrate Clamping Effects on Irreversible Domain Wall Dynamics in Lead Zirconate Titanate Thin Films. *Physical Review Letters.* 2012;108(15).

310. Kushima A, Yildiz B, Singhal S, Yokokawa H. Role of lattice strain and defect chemistry on the oxygen vacancy migration at the $(8.3\%Y_2O_3\text{-}ZrO_2)/SrTiO_3$ hetero-interface: A first principles study. *Solid Oxide Fuel Cells 11 (SOFC - XI).* 2009;25(2):1599-1609.

311. Kubicek M, Cai Z, Ma W, Yildiz B, Hutter H, Fleig J. Tensile lattice strain accelerates oxygen surface exchange and diffusion in $La_{1-x}Sr_xCoO_{3-\delta}$ Thin Films. *ACS Nano.* 2013;7(4):3276-3286.

312. Kim C, Yoon D, Lee J, Choi C, No K. Effects of Substrate and Bottom Electrodes on the Phase-Formation of Lead-Zirconate-Titanate Thin-Films Prepared by the Sol-Gel Method. *Japanese Journal of Applied Physics Part 1-Regular Papers Short Notes & Review Papers.* 1994;33(5A):2675-2678.

313. Chandran M, Tiwari B, Kumaran C, Samji S, Bhattacharya S, Rao M. Integration of perovskite PZT thin films on diamond substrate without buffer layer. *Journal of Physics D-Applied Physics.* 2012;45(20).

314. Reshmi R, Natarajan V, Jayaraj M. Effect of Buffer Layer on the Properties of Laser Ablated PZT Thin Films. *Integrated Ferroelectrics.* 2010;117:104-109.

315. Masuda A, Yamanaka Y, Tazoe M, Yonezawa Y, Morimoto A, Shimizu T. Highly-Oriented Pb(Zr,Ti)O3 Thin-Films Prepared by Pulsed-Laser Ablation on GaAs and Si Substrates with MgO Buffer Layer. *Japanese Journal of Applied Physics Part 1-Regular Papers Short Notes & Review Papers.* 1995;34(9B):5154-5157.

316. Liou B, Yu C, Chou C. Low temperature preparation of PZT thin films on different substrates by CO2 laser annealing. *Ferroelectrics.* 2007;357:228-232.

317. Helms CR, Deal BE. The physics and chemistry of SiO_2 and the Si-SiO_2 interface. Electrochemical Society Meeting; 1988; New York.

318. Pobedinskas P, Bolsee J, Dexters W, et al. Thickness dependent residual stress in sputtered AlN thin films. *Thin Solid Films.* 2012;522:180-185.

319. Corkovic S, Whatmore R, Zhang Q. Development of residual stress in sol-gel derived $Pb(Zr,Ti)O_3$ films: An experimental study. *Journal of Applied Physics.* 2008;103(8).

320. Feng X, Huang Y, Rosakis A. On the Stoney formula for a thin film/substrate system with nonuniform substrate thickness. *Journal of Applied Mechanics - Transactions of the ASME.* 2007;74(6):1276-1281.

321. Ong R, Payne D, Sottos N. Processing effects for integrated PZT: Residual stress, thickness, and dielectric properties. *Journal of the American Ceramic Society.* 2005;88(10):2839-2847.

322. Stoney G. The tension of metallic films deposited by electrolysis. *Proceedings of the Royal Society of London Series a-Containing Papers of a Mathematical and Physical Character.* 1909;82(553):172-175.

323. Williamson G, Hall W. X-ray Line Broadening From Filed Aluminium and Wolfram. *Acta Metallurgica.* 1953;1(1):22-31.

324. Ogilvie R, Kaminaga U, Sugiyama H, Nicolich J. X-ray Stress Analysis Employing the Lattice Parameter Ellipsoid. JCPDS-International Centre for Diffraction Data2007:145-149.

325. Frantti J, Lantto V. Structural studies of Nd-modified lead zirconate titanate ceramics between 11 and 680 K at the morphotropic phase boundary. *Physical Review B.* 1997;56(1):221-236.

326. Yagnamurthy S, Chasiotis I, Lambros J, Polcawich R, Pulskamp J, Dubey M. Mechanical and Ferroelectric Behavior of PZT-Based Thin Films. *Journal of Microelectromechanical Systems.* 2011;20(6):1250-1258.

327. Garino TJ, Harrington M. Residual stress in PZT thin films and its effect on ferroelectric properties. 1991; MRS Proceedings, 243, 341.

328. Brennecka G, Huebner W, Tuttle B, Clem P. Use of stress to produce highly oriented tetragonal lead zirconate titanate (PZT 40/60) thin films and resulting electrical properties. *Journal of the American Ceramic Society.* 2004;87(8):1459-1465.

329. Lee J, Park C, Kim M, Kim H. Effects of residual stress on the electrical properties of PZT films. *Journal of the American Ceramic Society.* 2007;90(4):1077-1080.

330. Liu C, Fei W, Li W. Effects of texture and residual stress on the transition of ferroelectric perovskite thin films with C-axis polarization. *Thin Solid Films.* 2008;516(6):1265-1270.

331. Liu C, Li W, Fei W, Zhang S, Wang J. Influence of phase transition induced by residual stress on ferroelectric properties of highly (100)-oriented $Pb(Zr_{0.52}Ti_{0.48})O_3$ thin films. *Journal of Alloys and Compounds.* 2010;493(1-2):499-501.

332. Zhou Y, Yang Z, Zheng X. Residual stress in PZT thin films prepared by pulsed laser deposition. *Surface & Coatings Technology.* 2003;162(2-3):202-211.

333. Freund LB, Suresh S. *Thin Film Materials: Stress, Defect Formation, and Surface Evolution.* 1st ed. Cambridge, England; New York: Cambridge University Press; 2009.

334. van Spengen W. MEMS reliability from a failure mechanisms perspective. *Microelectronics Reliability.* 2003;43(7):1049-1060.

335. Sabate N, Vogel D, Gollhardt A, et al. Residual stress measurement on a MEMS structure with high-spatial resolution. *Journal of Microelectromechanical Systems.* 2007;16(2):365-372.

336. Shepard J, TrolierMcKinstry S, Hendrickson M, et al. The effects of biaxial stress on the ferroelectric characteristics of PZT thin films. *Materials For Smart Systems Ii.* 1997;459:47-51.

337. Chung I, Yoo I, Lee W, et al. Electrode stress effects on electrical properties of PZT thin film capacitors. *Proceedings of the 1994 IEEE International Symposium on Applications of Ferroelectrics (ISAF).* 1994:527-530.

338. Zhu H, Chu D, Fleck N, Rowley S, Saxena S. Polarization change in ferroelectric thin film capacitors under external stress. *Journal of Applied Physics.* 2009;105(6).

339. Kelman M, McIntyre P, Hendrix B, Bilodeau S, Roeder J. Effect of applied mechanical strain on the ferroelectric and dielectric properties of $Pb(Zr_{0.35}Ti_{0.65})O_3$ thin films. *Journal of Applied Physics.* 2003;93(11):9231-9236.

340. Catalan G, Sinnamon L, Gregg J. The effect of flexoelectricity on the dielectric properties of inhomogeneously strained ferroelectric thin films. *Journal of Physics-Condensed Matter.* 2004;16(13):2253-2264.

341. Catalan G, Noheda B, McAneney J, Sinnamon L, Gregg J. Strain gradients in epitaxial ferroelectrics. *Physical Review B.* 2005;72(2).

342. Suzuki H, Ohno T, Fu D, Sakamoto N. Domain switching control of CSD--derived ferroelectric thin films by residual stress. Paper presented at: 14th US-Japan Seminar on Dielectric and Piezoelectric Materials, 2009; Welches, Oregon, United States.

343. Griggio F, Jesse S, Kumar A, et al. Mapping piezoelectric nonlinearity in the Rayleigh regime using band excitation piezoresponse force microscopy. *Applied Physics Letters.* 2011;98(21).

344. Bintachitt P, Jesse S, Damjanovic D, et al. Collective dynamics underpins Rayleigh behavior in disordered polycrystalline ferroelectrics. *Proceedings of the National Academy of Sciences of the United States of America.* 2010;107(16):7219-7224.

345. Sridhara Rao DVM, K., Humphreys CJ. TEM specimen preparation techniques. In: Mendez-Vilas A, Diaz J, eds. *Microscopy: Science, Technology, Applications and Education.* Vol 2. Badajoz, Spain: Formatex Research Center; 2010:1232-1244.

346. Lee J, Yoon K, Hwang K, Park J, Ahn S, Kim T. Label free novel electrical detection using micromachined PZT monolithic thin film cantilever for the detection of C-reactive protein. *Biosensors & Bioelectronics.* 2004;20(2):269-275.

347. Zhang Q, Djuth F, Zhou Q, Hu C, Cha J, Shung K. High frequency broadband PZT thick film ultrasonic transducers for medical imaging applications. *Ultrasonics.* 2006;44:E711-E715.

348. Jonnalagadda K, Chasiotis I, Yagnamurthy S, et al. Experimental Investigation of Strain Rate Dependence of Nanocrystalline Pt Films. *Experimental Mechanics.* 2010;50(1):25-35.

349. Brantley W. Calculated elastic constants for stress problems associated with semiconductor devices. *Journal of Applied Physics.* 1973;44(1):534-535.

350. Ding H, Lee X, Chen W. Analytical solutions for a uniformly loaded circular plate with clamped edges. *Journal of Zhejiang University Science.* 2005;6A(10):1163-1168.

351. Agar J, Damodaran A, Okatan M, et al. Highly mobile ferroelastic domain walls in compositionally graded ferroelectric thin films. *Nature Materials.* 2016;15(5):549.

352. Gebhardt S, Partsch U, Schonecker A. PZT Thick Films for MEMS. *2008 17th Ieee International Symposium on the Applications of Ferroelectrics.* 2008:412-413.

353. Zhang Y, Ishimaru M, Varga T, et al. Nanoscale engineering of radiation tolerant silicon carbide. *Physical Chemistry Chemical Physics.* 2012;14(38):13429-13436.

354. Rudy R, Grove K, Rivas M, et al. Total Ionizing Dose Effects on Piezoelectric Thin-Film Cantilevers with Oxide Electrodes. *IEEE Trans Ultrason Ferroelectr Freq Control.* 2017;64(7):1135-1143.

355. Dash B, Dash P, Rath H, et al. Swift heavy ion irradiation induced modification of BiFeO3 thin films prepared by sol-gel method. *Indian Journal of Physics.* 2010;84(10):1315-1320.

356. Angadi B, Victor P, Jali V, Lagare M, Kumar R, Krupanidhi S. High energy Li ion irradiation effects in ferroelectric PZT and SBT thin films. *Thin Solid Films.* 2003;434(1-2):40-48.

357. Piazza G, Stephanou P, Pisano A. Piezoelectric aluminum nitride vibrating contour-mode MEMS resonators. *Journal of Microelectromechanical Systems.* 2006;15(6):1406-1418.

358. Pulskamp J, Bedair S, Polcawich R, et al. Electrode-shaping for the excitation and detection of permitted arbitrary modes in arbitrary geometries in piezoelectric resonators. *IEEE Transactions on Ultrasonics Ferroelectrics and Frequency Control.* 2012;59(5):1043-1060.

359. Nishide M, Matsuoka M, Tai T, et al. Rapid and high sensitive structure evaluation of ferroelectric films using micro-Raman spectroscopy: In-situ observation of stress accumulation and release in PbTiO3 films during first cooling process. *3rd International Congress on Ceramics (Icc3): Advances in Electro Ceramics.* 2011;18.

360. Nishide M, Kuzuhara M, Tai T, et al. In-situ observation of a MEMS-based $Pb(Zr,Ti)O_3$ micro cantilever using micro-Raman spectroscopy. *Journal of the Ceramic Society of Japan.* 2010;118(1380):644-647.

361. Nishida K, Osada M, Sakai J, et al. Oxygen vacancies in PbTiO3 thin films probed by resonant Raman spectroscopy. *Journal of the Ceramic Society of Japan.* 2013;121(1416):598-601.

362. Bastani Y, Bassiri-Gharb N. Processing Optimization of Lead Magnesium Niobate-Lead Titanate Thin Films for Piezoelectric MEMS Application. *Journal of the American Ceramic Society.* 2012;95(4):1269-1275.

363. Park J, Xu F, Trolier-McKinstry S. Dielectric and piezoelectric properties of sol-gel derived lead magnesium niobium titanate films with different textures. *Journal of Applied Physics.* 2001;89(1):568-574.

364. Cross L. *Relaxor Ferroelectrics.* Vol 114. Piezoelectricity: Evolution and Future of a Technology: Springer; 2008.

365. Angadi B, Jali V, Lagare M, Bhat V, Umarji A, Kumar R. Radiation resistance of PFN and PNM-PT relaxor ferroelectrics. *Radiation Measurements.* 2003;36(1-6):635-638.

366. Dunn S, Tiwari D. Influence of ferroelectricity on the photoelectric effect of $LiNbO_3$. *Applied Physics Letters.* 2008;93(9).

367. Kalinin S, Bonnell D, Alvarez T, et al. Atomic polarization and local reactivity on ferroelectric surfaces: A new route toward complex nanostructures. *Nano Letters.* 2002;2(6):589-593.

368. Favia P, Gonzales M, Simoen E, Verheyen P, Klenov D, Bender H. Nanobeam Diffraction: Technique Evaluation and Strain Measurement on Complementary Metal Oxide Semiconductor Devices. *Journal of the Electrochemical Society.* 2011;158(4):H438-H446.

369. Surowiak Z, Kupriyanov M, Czekaj D. Properties of nanocrystalline ferroelectric PZT ceramics. *Journal of the European Ceramic Society.* 2001;21(10-11):1377-1381.

370. Bernal A, Tselev A, Kalinin S, Bassiri-Gharb N. Free-Standing Ferroelectric Nanotubes Processed via Soft-Template Infiltration. *Advanced Materials.* 2012;24(9):1160-1165.

371. Gubinyi Z, Batur C, Sayir A, Dynys F. Electrical properties of PZT piezoelectric ceramic at high temperatures. *Journal of Electroceramics.* 2008;20(2):95-105.

372. Gao Z, Lu C, Wang Y, Yang S, Yu Y, He H. Super Stable Ferroelectrics with High Curie Point. *Scientific Reports.* 2016;6.

373. Li Q, Wei J, Cheng J, Chen J. High temperature dielectric, ferroelectric and piezoelectric properties of Mn-modified BiFeO3-BaTiO3 lead-free ceramics. *Journal of Materials Science.* 2017;52(1):229-237.

374. Harrington S, Zhai J, Denev S, et al. Thick lead-free ferroelectric films with high Curie temperatures through nanocomposite-induced strain. *Nature Nanotechnology.* 2011;6(8):491-495.

375. Rivera R, Hejazi M, Safari A. Ferroelectric and dielectric properties of bismuth ferrite based thin films by pulsed laser deposition. 2012 IEEE International Symposium on Applications of Ferroelectrics; 2012.

376. Barala S, Banerjee N, Kumar M. Effect of gamma ray irradiation on epitaxial $Pb(Zr,Ti)O_3/SrRuO_3$ tunable varactor devices. *Journal of Electronic Materials*. 2016;45(8):4122-4128.